Links between metamorphism and deformation in feldspar at mid-crustal conditions

Thesis submitted in accordance with the requirements of The University of Liverpool for the degree of Doctor of Philosophy by

Joseph Daniel Gardner

January 2019

This work is dedicated to the memory of

Emily Paige Short

Happy the man whose lot it is to know
The secrets of the Earth
He hastens not to work his fellows' hurt by unjust deeds
But with rapt admiration contemplates
Immortal Nature's ageless harmony
~ EURIPIDES
(c. 485 – 406 BC)

Abstract

Feldspar is the most common mineral in the Earth's mid-to-lower crust, and therefore exerts fundamental controls on crustal strength. However, due to the relatively complex chemistry of the feldspar series, particularly its temperature dependence on composition, interactions between metamorphism and deformation, and thus overall deformation behaviour, remain poorly understood. Metagabbroic rocks from a crustal-scale shear zone were studied using electron backscatter diffraction and transmission electron microscopy, to investigate the deformation behaviour of plagioclase at greenschist facies. Numerical modelling was also employed to characterise the microstructural evolution of features observed in the natural samples, specifically the effect that large grains have on the evolution of a fine-grained matrix. The results of this study showed that mm–cm-scale albite grains were formed through fluid-assisted, interface-coupled replacement reactions, which produced a high dislocation density in those grains through a chemical, rather than mechanical, mechanism. Small albite grains of the same composition were formed either through classical precipitation mechanisms, or by growth from strain-free nuclei that consumed the large grains, in response to the stored strain energy in the large grains. The reduction in grain size led to fluid-assisted diffusion creep (pressure solution) becoming the dominant deformation mechanism that accommodated high strains in the samples. Despite this deformation being expected to destroy crystallographic preferred orientation, or texture, preferred orientation domains are preserved to high strains in the albite-rich matrix of the rocks. Metagabbroic samples with five different strain levels were studied, to show how albite grain size, aspect ratio, and texture strength, and second phase abundance, evolved and interacted during deformation. Although the secondary phases produced during metamorphic reactions are reported to inhibit grain growth, which promotes GSS creep, the results of this study show their presence may also limit texture modification by inhibiting the rotations normally associated with diffusion creep and grain boundary sliding, to preserve CPO domains to high strain. The modelling results showed that large grains can have a significant effect on the microstructural evolution of a fine-grained matrix undergoing diffusion creep. In particular, rotations of matrix grains were strongly influenced by the rotation direction and velocity of the large grain. The study also showed that the rotation direction of large grains does not have to be simply either synthetic or antithetic; rotation directions changed due to interactions with the matrix. The model output also showed that large grains create stress heterogeneities that focus the effects of diffusion creep. The stress heterogeneities resulted in the alignment of grain boundaries, and led to a profound drop in strength of the deforming material. These results show the microstructural evolution of rocks undergoing (fluid-assisted) diffusion creep is complex and requires further study.

List of Abbreviations

BSE – backscattered electron

CCD – charge-coupled device

CL - cathodoluminescence

CPO – crystallographic preferred orientation. This phrase is preferred to the commonly interchanged *lattice preferred orientation* (LPO), as a crystal lattice is a construct used to help understand repetition in the ordered pattern of atoms that make up a crystal, not a physical entity. Thus, it is preferable to describe the actual alignment of crystals rather than the alignment of hypothetical lattices.

DisGBS – dislocation-accommodated grain boundary sliding

DPC – dissolution-precipitation creep.

EBSD – electron backscatter diffraction

EDS – energy dispersive spectroscopy

FIB – focused ion beam

GBM – grain boundary migration

GBS – grain boundary sliding

GND – geometrically necessary dislocations

GSI – grain size-insensitive

GSS – grain size-sensitive

GSR – grain size reduction

GSZ – Gressoney shear zone

HAGB – high-angle grain boundary

HR-EBSD – high angular resolution EBSD

IPF – inverse pole figure

OPPG – one point per grain (related to data used for the construction of pole figures)

MAD – misorientation angle distribution

MAD$_1$ – mean angular deviation

MI – misorientation index

SAD – selected area diffraction

SDD – silicon drift detector

SE – secondary electron

SEM – scanning electron microscopy

SIP – species identification protocol

SPO – shape-preferred orientation

TEM – transmission electron microscopy

WBV – Weighted Burgers Vector

Contents

Acknowledgements

My sincere thanks first go to my PhD supervisors, John Wheeler and Betty Mariani, who started off as supervisors but have ended up as friends (hopefully they feel the same…). John, your support, understanding and flexibility when I was going through the most difficult of times will not be forgotten. It has been a privilege and a pleasure to work with someone of such academic prowess, even if I did occasionally fear my mind might collapse under the weight of some of the more nuanced ideas we shared. Your sense of humour, penchant for 'post-match analysis' and unbridled enthusiasm for science have enriched my PhD experience no end, and I look forward to many collaborations – both scientific and social – in the future. Betty, it has been a privilege to work with someone so continually enthusiastic about seeking the answers to the secrets that the rocks we study hold, and don't always give away freely. Your support and care throughout my studies have been second to none and again, I hope we share many years of future collaboration.

Special mention should go to those who helped me with data collection and processing throughout this study. Thanks go to Dave and Lars for inviting me down to Oxford and getting me involved in all the HR-EBSD nonsense. A crisp pilsner or two somewhere in continental Europe is massively overdue. Thanks also go to James and Richard for use of their QEMSCAN facility, and to Karl in NiCaL for helping me with the TEM analysis, which were both fundamental to the study.

Los culitos – Johnio, Júju, Mikey, Cata and Jaslin – you are all total legends. You have provided so many laughs, been there through difficult times, and enhanced my PhD experience no end. We meet a lot of people during the course of our PhDs, but not everyone becomes a friend for life. I look forward with great happiness to the many more days we will share together in the future!

To the many other people in the department who have provided fun, support and inspiration over the years – in particular Cazmatazz, Pam, Felix, Dan, Gaz, Anthony, Becky, Jenny, Pablo, JVH, but there are many others – thank you all.

Liverpool would not be the same without its thriving and creative social scene. For my introduction to this and to some of the loveliest people I have ever met, huge thanks go to Laurie Crombie. Thank you for inviting me into the fold Loz, it's been great and I'm looking forward to having time to maybe pursue some more creative ideas with you in the future! To the rest of the Kazimier/Wind Factory crew – Bex, Léon, Sam, Anna, Dan, Emily, Venya, Maria, Sophie, Luci, Alex, Liam, Amy, Seb, Hannah, Mike, George, Howard, Joe, Emily, Joel, Kev, Lynton, Laura, Rich, Luís, Guro, Mina, Nick,

Charlie, Steph, Ulysses, Anna, and all the rest of you beautiful ones – thank you all for making the last few years so much fun: I wanna be with you everywhere.

Another special mention must go to Nawal, and of course Sisi, not only for providing a creative and inspiring to place to write in the last few weeks of my PhD, but also for your infectious social enthusiasm, indomitable spirit, and refreshingly unique view on the world.

Davey G, Hema, Lisa, Tom and Debbie – it's hard to stay in touch with people when you leave a place behind. With you guys it's been effortless, and I can't thank you enough for the friendship, love and support you've given me over the past four years.

Finally, thanks go to my mum and dad, and the rest of my family, for keeping me grounded by showing a complete and unwavering lack of interest in the subject matter of this study. Ma and Pa, thank you for always offering me unconditional love and support, and giving me the freedom to find my own way in the world.

Chapter 1 Introduction

1.1 Crustal deformation

1.1.1 Deformation in the crust and the development of shear zones

The Earth's crust can be separated into different regimes depending on its principal deformation behaviour. The upper crust is brittle, and dominantly deforms by brittle faulting and cataclastic flow (Sibson, 1994). In the middle and lower crust, the viscous deformation of crustal rocks is governed by their rheology, which describes a rock's material properties through constitutive equations that link stress (σ) and strain rate ($\dot{\varepsilon}$). Rock rheology is fundamental to understanding plate tectonics, which occurs because of the relative strength of overlying lithospheric plates compared to the underlying weaker asthenosphere (Bürgmann and Dresen, 2008). The Earth's crust deforms in response to tectonic stresses. Strain does not develop uniformly, but is localised into discrete regions. The reasons behind the initiation of strain localization remain elusive, and this topic remains the focus of intense research activity (e.g., Czaplińska et al., 2015; Gardner et al., 2017; Getsinger et al., 2013; Hansen et al., 2012; Viegas et al., 2016). In the upper crust, brittle fault zones are produced, and, at the higher temperatures and pressures of the mid-to-lower crust, viscous shear zones form (Passchier and Trouw,

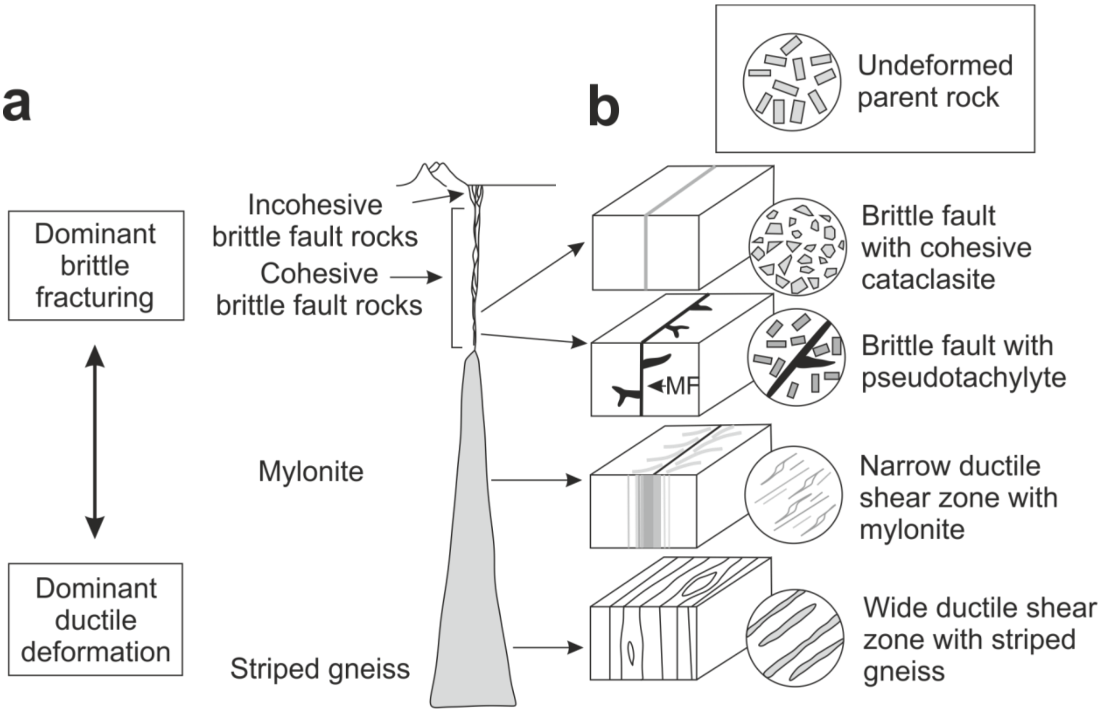

Figure 1.1 *a) Schematic representation of the structure of shear zones in the Earth's crust. b) Dominant mode of deformation and typical rock type. After Passchier and Trouw (2005), Fig. 5.2.*

2005). The largest shear zones, which occur at plate tectonic boundaries, have both brittle and viscous components (Fig.1.1). The depth of the brittle-viscous transition depends on many factors, such as lithology, fluid pressure and bulk strain rate.

Movement on faults in the brittle upper crust generates earthquakes, and the loading of faults to failure occurs by viscous flow in the lower crust and mantle, so understanding how rocks deform viscously in the mid to lower crust is fundamental to understanding brittle behaviour of fault zones and the associated seismic hazard (Bürgmann and Dresen, 2008).

Rocks in shear zones are commonly observed to have undergone a grain size reduction when compared to undeformed neighbouring rocks (e.g., De Bresser et al., 2001; Fitz Gerald and Stünitz, 1993; Kilian et al., 2011; Rutter and Brodie, 1988; Viegas et al., 2016). Grain size reduction is thus understood to be critical to localising strain and the development of shear zones (e.g., Tullis et al., 1990). A reduction in grain size can occur due to cataclasis, dynamic recrystallization or the nucleation of new phases, or by a combination of these processes.

1.1.2 Deformation mechanisms in shear zones

Different mechanisms accommodate strain in rocks depending on changes in ambient conditions (in particular temperature and pressure) of deformation with crustal depth. In the brittle regime of the upper crust, where low temperature and low lithostatic pressure dominate, rocks deform by brittle fracture and cataclasis during frictional sliding at high strain rates (Passchier and Trouw, 2005). The frictional strength of rocks increases with depth, due to the increase in lithostatic pressure (Bürgmann and Dresen, 2008). A transition between dominantly frictional and dominantly viscous behaviour is defined by thermally- (and fluid-) activated creep mechanisms in mid to lower crust (Fig 1.1). The transition occurs over a temperature range of ~300–500 °C, which translates to a depth of around 10–15 km assuming a geothermal gradient of ~30 °C/km (Bürgmann and Dresen, 2008).

In the viscous regime of the mid to lower crust, non-recoverable deformation is accommodated by two competing mechanisms – grain size-sensitive diffusion creep, or grain size-insensitive dislocation creep. Constitutive equations that describe both creep mechanisms take the form of an Arrhenius equation:

$$\dot{\varepsilon} = Ae^{\frac{-Q}{RT}}\frac{\sigma^n}{d^m}$$

where $\dot{\varepsilon}$ is the strain rate (s^{-1}), σ is the differential stress (MPa), n is the stress exponent, d is the grain size (m), m is the grain size exponent, A is a material constant, Q is the activation energy of the particular mechanism (kJ mol^{-1}), R is the gas constant and T is the absolute temperature (K) (Poirier, 1985). In dislocation creep, flow is mainly sensitive to stress, and material strength is insensitive to grain size, so the exponents n and m are experimentally determined to be ~3 (although this can vary substantially, e.g., Hacker and Christie (1990) observed n ~3.7 in amphibolite deforming by dislocation creep) and 0, respectively. During diffusion creep, which is more sensitive to grain size, n and m have been determined to be ~1 (i.e., strain rate increases linearly with stress), and 3 (i.e., the strength of a material deforming by diffusion creep reduces by three orders of magnitude, with each order of magnitude drop in grain size), respectively. Experimentally-derived values for these parameters can be used to construct deformation mechanism maps (Fig. 1.2; Rybacki and Dresen, 2004b).

1.1.2.1 Dislocation creep

Deformation by creep occurs due to lattice defects in crystalline materials (Hull and Bacon, 2011). Point defects exist either as extra atoms (interstitials) or unfilled atomic sites (vacancies) in the lattice. Line defects, known as dislocations, are the ends of extra half planes of atoms within the lattice (edge dislocations) or other linear defects accommodating lattice mismatch (screw and mixed dislocations; Poirier, 1985). During dislocation glide, non-recoverable (plastic) strain is accommodated by the movement of atoms on specific crystallographic planes, without fracture of the lattice (Hull and Bacon, 2011). Shape change occurs by dislocation lines migrating through a lattice across one row of atoms at a time. Dislocations can tangle or meet impurities/second phases and strain hardening can occur, which, at low temperatures, can promote brittle fracturing (Tullis and Yund, 1987). At higher temperatures, which activate the lattice diffusion of vacancies that can untangle locked dislocations, climb of dislocations onto new slip planes can occur, and viscous deformation can proceed (Hull and Bacon, 2011). Collectively, the processes of glide and climb are known as dislocation creep (Hirth and Tullis, 1992).

Active slip systems can be defined for dislocation creep, comprised of the crystallographic plane on which slip occurs (e.g. (001) and the crystallographic direction movement occurs in (known as the Burger's vector, e.g. [010]; Hull and Bacon, 2011). Dislocation creep on a dominant slip system can lead to the development of a crystallographic preferred orientation (CPO), because it changes the shape of a crystal and elongate grains become aligned with the kinematic axes of bulk flow, similar to a pile of books sliding on a shelf (Passchier and Trouw, 2005). Pole figures can be used to identify the dominance of a specific slip system, as dominant slip planes tend to align with sample foliation, and the dominant Burger's vector with the sample lineation (Law, 1990; Passchier and Trouw, 2005).

Mineral grains are loaded with dislocations under applied stress, and plastically deformed grains contain high dislocation densities (Wheeler et al., 2009). Because dislocations distort the crystal lattice, they are surrounded by a stress field, which increases the internal energy of that grain (Hull and Bacon, 2011). Recovery processes work to minimise this energy, by reordering dislocations into low energy configurations to form subgrain boundaries (Bestmann et al., 2005; Piazolo et al., 2006). Increasing densities of dislocations in a subgrain boundary leads to an increase in misorientation across the boundary, leading to the production of small new grains by subgrain rotation recrystallization (Drury and Urai, 1990). The growth of strain-free grains by migration of high-angle grain boundaries can also be driven by gradients in dislocation density across boundaries, with new, strain-free grains growing at the expense of their more distorted neighbours, which leads to an overall decrease in the internal energy of the system (Drury and Urai, 1990).

1.1.2.2 Diffusion creep

Diffusion creep is a fundamental process in the Earth's crust (Kilian et al., 2011; Rosenberg and Stünitz, 2003; Rybacki and Dresen, 2000; Rybacki et al., 2006) and mantle (Hiraga et al., 2010; Hirth and Kohlstedt, 1995; Karato and Wu, 1993). Diffusion creep relies on the presence of lattice vacancies, which diffuse through the crystal lattice (Nabarro-Herring creep), and/or the presence of grain boundaries which may allow relatively easy diffusion (Coble creep), to create non-recoverable shape change. The concentration of vacancies in a crystal varies with stress. At sites (or interfaces) under high stress, the vacancy concentration will be lower than those under low stress. This disparity creates a vacancy concentration—or chemical potential—gradient which drives diffusion. Under constant loading this gradient will persist, which drives continual, stress-driven grain shape change during Nabarro-Herring creep (Fig. 1.3). In grains under anisotropic stress, grain boundaries of different orientations will have different normal stress values, so chemical potential will vary from face to face. This induces diffusion of material along the grain boundary network, leading to grain shape change during Coble creep (Wheeler, 1992). In the presence of water, grain boundary diffusion creep is termed pressure solution (Menegon et al., 2008; Rutter, 1976; Rutter, 1983; Wheeler, 1992; Wintsch and Yi, 2002), but it is equivalent to Coble creep (Elliott, 1973). Diffusion creep always occurs in conjunction with grain boundary

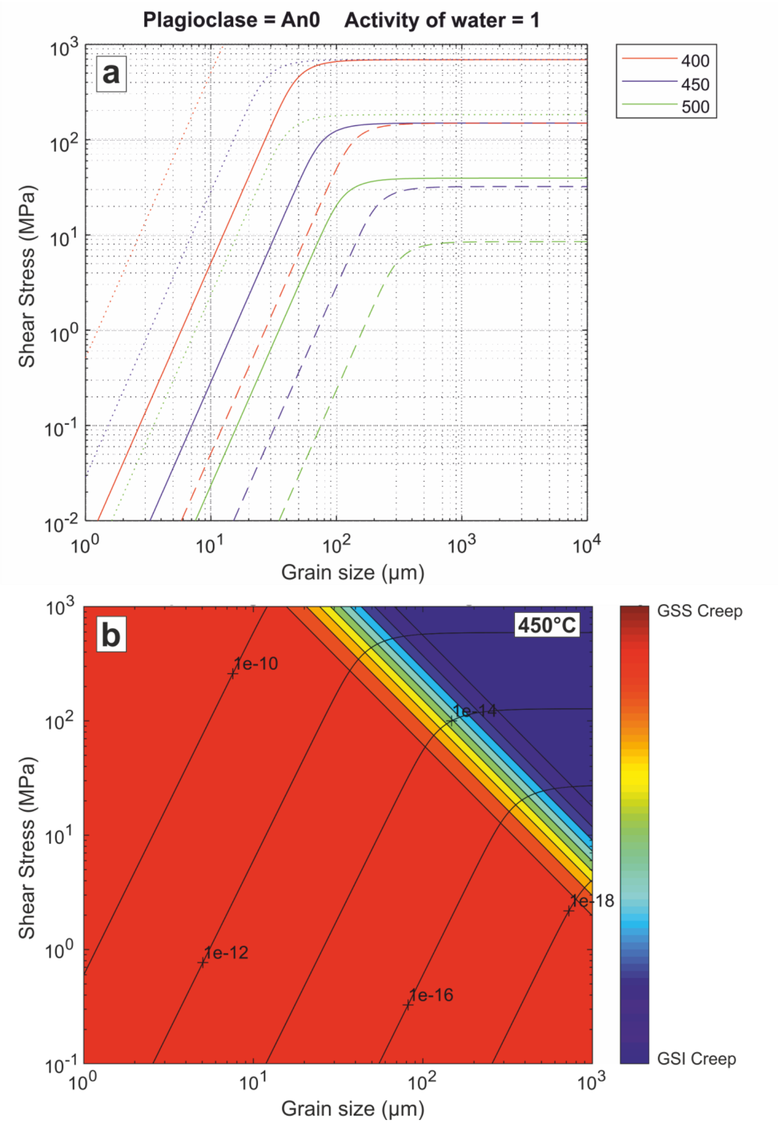

Figure 1.2 *Deformation mechanism maps produced by code supplied by Mark Pearce, CSIRO, based on the parameters of Rybacki and Dresen (2004b). The maps indicate albite grains in the samples deformed in the boundary zone between grain size-sensitive (GSS) and grain size-insensitive (GSI) creep, if a T of ~450 °C, natural strain rates (Bürgmann and Dresen, 2008), reasonable crustal stresses (see list in appendix of Wheeler 2014), and hydrous conditions (evidence for hydrous fluid infiltration and hydrous reaction products are seen everywhere in all samples) are assumed. a) At 500 °C, stresses of around 30 MPa and a strain rate of* 10^{-14} s^{-1}*, the transition from GSI to GSS creep occurs at the observed grain sizes of tens to hundreds µm. Strain rates: solid line =* 10^{-14} s^{-1}*, dashed line =* 10^{-16} s^{-1}*, dotted line =* 10^{-12} s^{-1}*. b) Contours in the transition zone between GSI and GSS creep are spaced at 10% increments. At 450 °C, stresses of around 100 MPa and a grain size of around 50 µm, GSS creep contribution to deformation of around 10–20% would be expected; i.e., although some signatures of dislocation creep may be present in the microstructure, it would not be expected to dominate deformation.*

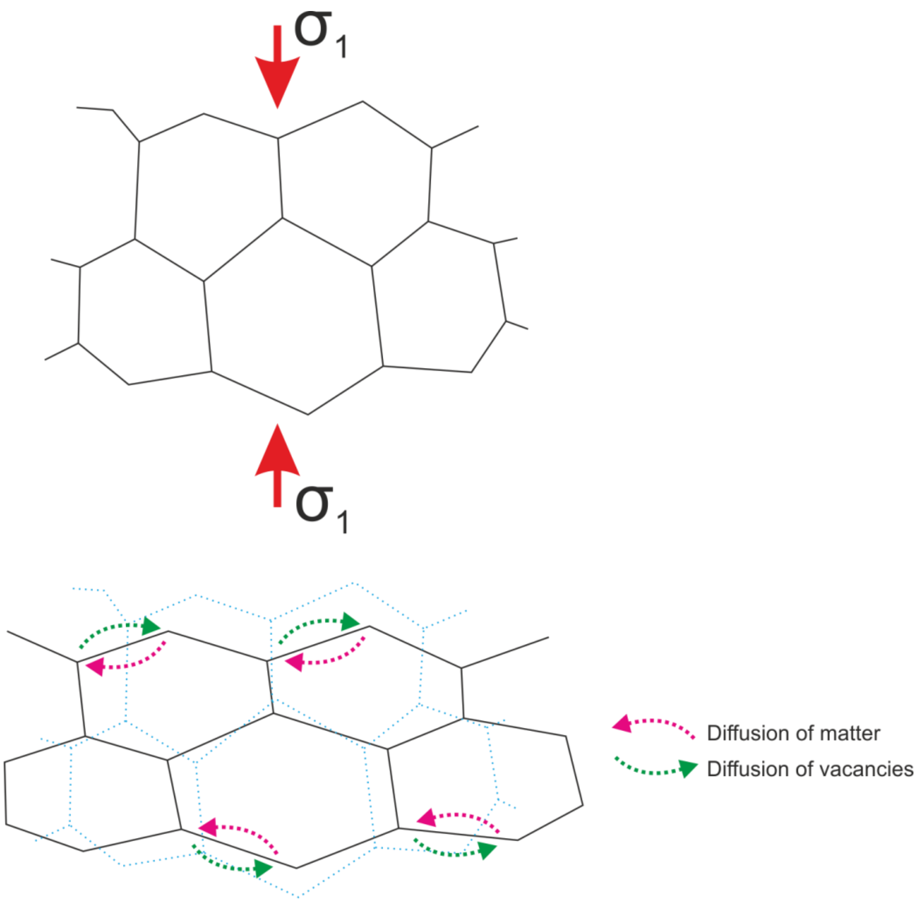

Figure 1.3 *Schematic diagram showing shape change caused by differential stress during diffusion creep. After Fossen (2016), Fig. 10.7.*

sliding (GBS) and grain rotations, to maintain continuity during shape change (Elliott, 1973). Because of this, diffusion creep is traditionally reported to weaken or destroy any pre-existing CPO (e.g., Kilian et al., 2011; Menegon et al., 2008), although other work has shown this may not always be the case (Wheeler, 2009), as explained below.

1.1.3 The importance of texture development and microstructural evolution in rock deformation studies

The study and interpretation of microstructures developed in naturally deformed rocks, on the grain and subgrain scale, plays an important role in unravelling the history and dynamics of tectonic processes recorded in the Earth's crust (Bestmann et al., 2005). Experimental studies of rock deformation yield information that allows us to construct deformation mechanism maps and understand the rheology of Earth materials, but results have to be extrapolated over time and space scales that differ by several orders of magnitude e.g., typically cm-scale samples will be deformed during high temperature experiments at strain rates of 10^{-4} to 10^{-6} s^{-1}, compared to strain rate estimates of 10^{-9} to 10^{-13} s^{-1} in natural shear zones (Bürgmann and Dresen, 2008). Because of this, experimental results must be compared against field data in some way, to confirm the experiments accurately approximate natural processes. Comparisons between these two types of data are carried out using microstructural analysis.

The microstructure of a polycrystalline material controls its mechanical behaviour during deformation. For example, the flow stress and strength anisotropy of a polycrystalline aggregate depend on grain size and grain shape distribution, and on texture strength, in the aggregate. Grain size reduction leads to strain localisation across thin section-to-lithospheric length-scales (Passchier and Trouw, 2005). During dislocation creep, many dislocations form on the same slip plane, and if movement of the leading dislocation is inhibited for any reason, the other dislocations will 'pile up' behind it. If dislocation pile-ups occur at grain boundaries during diffusion creep (the Hall-Petch effect), the length scale across which the pile-ups occur (i.e., the grain size) determines the bulk flow stress of the deforming material. Likewise, deformation by diffusive mass transfer is strongly dependent on grain size, as smaller grains result in shorter diffusion pathways. In polyphase samples, grain growth can be inhibited to preserve the lifetime of diffusion creep (Pearce and Wheeler, 2011). The rearrangement of phases into interconnected weak layers can lead to macroscale weakening of a material.

Studying texture evolution during deformation helps to understand the dynamic environment of an evolving microstructure (Engler and Randle, 2009). A crystallographic preferred orientation (CPO, or texture) is commonly reported to be produced by relatively high temperature dislocation creep. CPOs can yield information about which slip systems were active during crystal plastic deformation (Law, 1990; Passchier and Trouw, 2005). However, CPOs from many natural samples cannot be interpreted unambiguously as current understanding of the physical processes controlling texture development remains incomplete (Jiang et al., 2000; Wenk and Christie, 1991). For example, Getsinger and Hirth (2014) showed CPO development in amphibole can occur by oriented grain growth and rigid grain rotation during experiments, and suggested that CPOs could develop by the same mechanisms in natural lower crustal shear zones. Bulk CPO measurements cannot tell us anything about the processes that affect intergrain and intragrain domains, and in particular those that affect grain boundaries (Wheeler et al., 2003). As grain boundaries are the interfaces across which all granular interactions must be accommodated, they are vital to our understanding of deformation processes (Wheeler et al., 2001).

Initially strong CPOs, regardless of the mechanism of CPO formation, can be weakened or destroyed during diffusion creep, as it is geometrically necessary for grain boundary sliding and grain rotations to occur to maintain continuity during grain shape change (Elliott, 1973). Thus a dominance of diffusion creep is often inferred in deformed rocks lacking a strong texture and other microstructural indicators. However, recent work has shown diffusion creep may modify microstructure in unexpected ways. Imon et al. (2004) suggested that dissolution-precipitation creep (DPC) produced a CPO observed in amphibolites, by preferential dissolution of original amphibole at grain boundaries sub-parallel to foliation and nucleation and anisotropic growth of new amphibole in a stress field. Bons and den Brok (2000) showed numerically that DPC can produce CPOs when grain dissolution and growth rates are anisotropic and rigid-body rotation works in parallel with DPC.

Jiang et al. (2000) showed an inherited CPO can be preserved to high strain during diffusion creep. Wheeler (2009) used a numerical model to show that seismic anisotropy could be preserved during diffusion creep, due to grain elongation inhibiting rotations during deformation. Thus, as CPOs can be inherited and maintained even at high strains during diffusive mass transfer, they are not always a reliable indicator of dominant deformation mechanisms in natural samples. Misorientation analysis can help to resolve this, and in some cases may be a more accurate guide (Jiang et al., 2000). Mineral grains that have grown via subgrain rotation from the same parent will have a crystallographic relationship (Wheeler et al., 2001). Different phases that share a common parent, e.g. have nucleated from the same lattice, may show similar relationships. The difference in orientation between two grains can be quantified using a misorientation axis (a crystallographic direction) and a misorientation angle. The misorientation axis defines the direction, and the misorientation angle defines the magnitude, of the rotation either crystal must move through to be brought into congruence with the other (Jiang et al., 2000; Wheeler et al., 2001). Histograms plotting the misorientation angle distribution (MAD) for a set of grains can be produced, and misorientations between neighbouring (correlated) and random (uncorrelated) grains can be compared (Wheeler et al., 2001). A statistically significant difference between the two distributions suggests neighbouring grains have physically interacted with each other and/or have inherited their orientations from a pre-existing microstructure (Wheeler et al., 2001). Such analyses can be used to reveal the deformation history of a rock, and which deformation mechanisms were dominant during strain accommodation, and thus allow insight into the rheology of the Earth’s crust.

1.1.4 Nature of the problem

Feldspar is the most common mineral in the Earth's continental crust (Tullis, 2002). How feldspar responds to tectonic stresses therefore exerts controls on crustal rheology, and controls fundamental geological processes within the crust, such as mountain building and the loading of brittle faults to failure (Cowie et al., 2013). However, the deformation behaviour of plagioclase is not well understood. A particular complication in understanding plagioclase deformation is the complex physical and chemical interactions that can occur during deformation (Rosenberg and Stünitz, 2003; Stünitz, 1998). As plagioclase exists across a solid solution in which the stable species is temperature dependent, vertical movement in the crust can lead to grain size reduction by the crystallisation of new grains of different composition (Fitz Gerald and Stünitz, 1993; Stünitz, 1998; Stünitz and Tullis, 2001). Because plagioclase exhibits two excellent cleavages, brittle grain size reduction can occur across a range of P–T conditions (Kruse et al., 2001; Stünitz, 1993). Grain size reduction can also occur by dynamic recrystallization (Kruse and Stünitz, 1999; Kruse et al., 2001; Rosenberg and Stünitz, 2003; Stünitz et al., 2003). On grain size reduction, the grain size-sensitive mechanism of (fluid-assisted) grain boundary diffusion creep can dominate deformation (Jiang et al., 2000; Prior and Wheeler, 1999; Stünitz, 1993). Previous work on deformed metagabbros from the Gressoney Shear Zone (GSZ) has revealed ambiguous microstructures in an albite-rich matrix (Jiang et al., 2000; Prior and Wheeler, 1999). The mechanism of grain size reduction in the metagabbros is yet to be determined. CPO domains are observed although conditions of deformation make it unlikely that dislocation creep dominated deformation. Grain size in the matrix suggests deformation to high strains occurred predominantly by fluid-assisted diffusion creep subsequent to grain size reduction, but this mechanism is commonly expected to significantly weaken or destroy any pre-existing texture, so the observed CPO domains are hard to explain.

1.1.5 Thesis aims

This study builds on the work of Prior and Wheeler (1999) and Jiang et al. (2000) by focusing on chemical and physical changes that occurred in the metamorphosed gabbros from the GSZ. Grain boundary diffusion creep (Coble creep and pressure solution) remains a poorly understood phenomenon, as it characteristically leaves no signature microstructures, so the observation of CPO domains in the albite matrix of the metagabbros provides an opportunity to track microstructural evolution during diffusion creep in natural rocks. Specifically, the work in this thesis aims to address the following research questions:

1) What caused the observed distortion in mm-scale albite porphyroclasts, which deformed at P–T conditions too low for dislocation creep to have dominated deformation?
2) What was the mechanism by which observed CPO domains were inherited in the albite-rich matrix of the metagabbros?
3) How did different grain size reduction mechanisms combine to produce the fine-grained albite matrix?
4) How did the CPO domains observed in the fine-grained albite matrix evolve with increasing strain, during fluid-assisted diffusion creep (pressure solution)?
5) How were the CPO domains preserved to high strain during fluid-assisted diffusion creep, given that the grain rotations associated with diffusion creep should have destroyed any shared grain alignment?
6) What effect do porphyroclastic grains have on the microstructural evolution of a fine-grained matrix during diffusion creep?

The answers to these questions will provide insight into how metamorphism and deformation interact in feldspar, and the effects these interactions have on the strength and deformation behaviour of the Earth's crust. The answers will also provide a greater understanding of the effects of (fluid-assisted) diffusion creep, a fundamental deformation mechanism that is commonly interpreted to leave no signature, on microstructural evolution, which will help diffusion creep become better recognised in naturally-deformed materials and therefore facilitate a wider understanding of the influence of this fundamental process.

1.2 Plagioclase

This thesis primarily concerns metamorphic and deformation processes that are observed to occur in plagioclase feldspar, so a review of the important characteristics of plagioclase is included here. Feldspar also exists across the Na-K potassium feldspar solid solution, but as K-feldspar is not an important component of this thesis, it is not included in the review. The likely consequences of this study's findings to the K-feldspar system are briefly discussed within the main chapters.

1.2.1 Plagioclase chemistry and structure

Plagioclase feldspar is a framework silicate that exists across a solid solution from the pure Na end-member albite ($NaAlSi_3O_8$) and the pure Ca end-member anorthite ($CaAl_2Si_2O_8$). The solid solution is split into six arbitrary subdivisions based on anorthite percentage:

- Albite	An 0–10
- Oligoclase	An 10–30
- Andesine	An 30–50
- Labradorite	An 50–70
- Bytownite	An 70–90
- Anorthite	An 90–100

Si and Al comprise the tetrahedral framework of plagioclase, with Na^{2+} and Ca^{+} ions filling interstitial sites. Because of the difference in charge on sodium and calcium ions, a coupled substitution occurs in the transition from albite to anorthite, where Ca content of plagioclase varies with Al content.

The unit cell of anorthite is twice the length of that of albite, due to the ordering of Al in tetrahedral sites. Al-O-Al bonds are energetically unfavourable (Loewenstein, 1954), and as Al ions inhabit two tetrahedral sites in anorthite (compared to one in albite), the repeating pattern of atoms occurs over ~14 Å rather than ~7 Å (Fig. 1.4, Table 1.1; Deer et al., 2013). Variations in Al–Si ordering below ~800 °C lead to a series of structural changes and exsolution behaviour, termed the low temperature series. At higher temperatures, structures are more disordered and form the high temperature series (Deer et al., 2013).

Plagioclase exhibits a number of miscibility gaps across its solid solution that are temperature-dependent. At the greenschist facies conditions of the middle crust, where the Gibbs free energy of mixing is low compared to higher temperatures, the peristerite gap occurs between albite and oligoclase. Plagioclase compositions of An5–20 are not observed (Maruyama et al., 1982). Albite is the most stable phase, and is often observed to contain fine lamellae of oligoclase e.g. Yund (1986). At amphibolite facies conditions, intermediate compositions are found, suggesting closure of the solvus occurs somewhere close to 600 °C (Carpenter, 1994).

Property	High Albite	Low Albite	Anorthite
a (Å)	8.16	8.14	8.17
b (Å)	12.87	12.79	12.87
c (Å)	7.11	7.16	14.17
α (°)	93.5	94.3	93.1
β (°)	116.4	116.6	115.9
γ (°)	90.3	87.7	91.3

Table 1.1 *Unit cell parameters of end member plagioclase feldspars.*

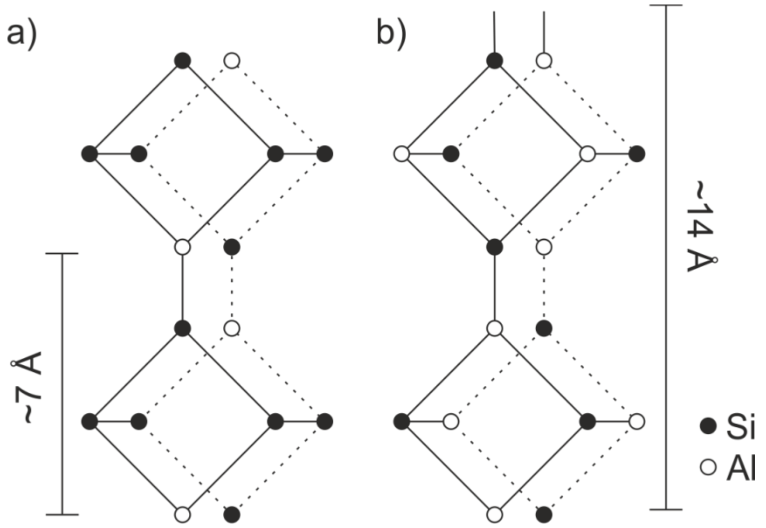

Figure 1.4 *Si (black) and Al (white) ordering in the tetrahedral framework of a) fully-ordered albite and b) anorthite. The c-axis of the unit cell in anorthite is approximately twice the length of that in albite. After Deer et al. (2013), Fig. 199.*

Compositional change in plagioclase is dependent on lattice diffusion. Because Na and Ca are charge-balanced by Si and Al, respectively, lattice diffusion in plagioclase is particularly slow, as it involves the exchange of relatively highly charged, tetrahedrallycoordinated cations (Cherniak, 2010). The interdiffusion coefficient over the temperature range 1100–1400 °C, at 0.1 MPa, has been measured experimentally, and is found to follow the Arrhenius relation $D = 1.099 \times 10^{-3} \exp(-517 \pm 21 \text{ kJ/mol}) \text{ m}^2 \text{ s}^{-1}$ under anhydrous conditions (Grove et al., 1984). At 1100 °C this yields a D of $\sim 10^{-23} \text{ m}^2 \text{ s}^{-1}$. At the lower temperatures of the middle crust, diffusion coefficients would be lower, so zoning would be expected to be preserved, and is commonly observed, in plagioclase grains that were originally Ca-bearing e.g. Pearce et al. (2011).

1.2.2 Deformation behaviour of plagioclase feldspar

Feldspar is dominantly observed to deform by brittle fracture at the temperatures and pressures of the mid-crust. In granitic rocks, which comprise the majority of the continental crust, it is commonly the strongest phase (Fitz Gerald and Stünitz, 1993; Simpson, 1985; Stünitz and Fitz Gerald, 1993; Viegas et al., 2016). In metabasic rocks, at medium to high metamorphic grades, it is often the softest mineral (compared to amphibole and pyroxene), so accommodates much of the strain during deformation (Brodie and Rutter, 1985).

Microcracking is commonly observed in natural feldspar samples that have deformed at greenschist facies conditions (Fitz Gerald and Stünitz, 1993; Stünitz, 1993; Stünitz and Fitz Gerald, 1993). Fracture is promoted along its two good cleavages on (010) and (001), meaning microcracking can still be significant at much higher grades, where dislocation creep may be expected to be active (Fitz Gerald and Stünitz, 1993; Menegon et al., 2008; Menegon et al., 2013; Stünitz et al., 2003). This is, in part, dependent on the orientation of mineral grains with respect to the kinematic reference frame – in ‘hard’ orientations, microfracturing is promoted, whereas in ‘soft’ orientations, where grains are aligned preferentially to activate slip on (010)[001], subgrain rotation recrystallization can occur (Kruse et al., 2001).

Experimental observations also show microcracking dominates deformation in albite at low temperatures ($T \leq 500$ °C, $P = 1.0$–1.5 GPa, $\dot{\varepsilon} = 10^{-6} \text{ s}^{-1}$) (Hacker and Christie, 1990). Grains that have undergone intense microfracturing can display features reminiscent of intracrystalline deformation, such as subgrains and patchy extinction (Tullis and Yund, 1987). Pervasive (micro)fracturing followed by movement on the two good cleavage planes simulates crystal plastic slip on those planes, and can result in grain flattening and the development of CPOs (Tullis and Yund, 1987). Care, then, is needed in interpreting microstructural observations in plagioclase. TEM analysis can help to distinguish between small-scale brittle fractures and networks of dislocations (Tullis and Yund, 1987).

In natural samples deformed at higher grades, crystal plastic processes are observed to accommodate strain (Hacker and Christie, 1990; Kruse et al., 2001; Rosenberg and Stünitz, 2003; Tullis, 2002). At upper amphibolite facies, feldspar is observed to undergo subgrain rotation recrystallization, and shows evidence of grain boundary migration, as well as microstructural evolution by diffusion-accommodated grain boundary sliding (Rosenberg and Stünitz, 2003), and grain shape change accommodated by diffusive mass transfer (Gower and Simpson, 1992). Anorthite in leucogabbros deformed at mid to lower crustal conditions (T = 675–700 °C, P = 350–450 MPa) shows evidence for initial grain size reduction occurring by subgrain rotation recrystallization, with a possible transition to dislocation-accommodated grain boundary sliding (DisGBS; Svahnberg and Piazolo, 2010). A transition from dislocation creep to DisGBS is also observed in oceanic gabbroic mylonites deformed at amphibolite facies (Miranda et al., 2016). At granulite facies, both dislocation creep and diffusion creep can be active in feldspar (Martelat et al., 1999). The dominant recrystallization mechanism at high grade (T ~ 700 °C, P < 900 MPa) in feldspar has been shown to be dependent on crystallographic orientation, where 'soft' orientations in which the dominant slip system [001](010) is aligned favourably with respect to the kinematic reference frame recrystallize by subgrain rotation, whereas 'hard' orientations deform by microfracturing and nucleation of new grains from fragments (Kruse et al., 2001). In layered gabbro mylonites deformed at ~800–900 °C, plagioclase was observed to develop strong crystallographic preferred orientations (CPOs) and therefore is inferred to have deformed by dislocation creep in monomineralic layers, whereas finer-grained layers of two-phase plagioclase-pyroxene mixtures show evidence they deformed by diffusion creep (Mehl and Hirth, 2008).

Dynamic recrystallization is concomitant on the presence of dislocations, and their ability, and/or the ability of high angle boundaries, to move. Experiments have shown that the movement of dislocations by glide in feldspar is inhibited by the fact that most are partials associated with stacking faults (i.e. their Burgers vectors are not translation vectors of the lattice; Hacker and Christie, 1990). This means that the climb of dislocations is difficult to achieve as the stacking faults themselves have to migrate by diffusion, and vacancy diffusion is extremely sluggish in feldspar at lower temperatures (Hacker and Christie, 1990; Tullis, 2002). This suppression of climb can lead to strain hardening and thus promote fracture. Grain size reduction by crystal plastic mechanisms is observed in experimentally deformed plagioclase at high temperatures (≥ 800 °C; Hacker and Christie, 1990; Tullis and Yund, 1985; Tullis and Yund, 1987), but dislocation creep is predominantly accommodated by bulging recrystallization and the migration of high-angle grain boundaries, rather than dislocation climb-dependent recovery and the formation of subgrains (Tullis, 2002). Experimentally deformed (300 MPa confining pressure, temperatures between 1140 and 1480 K, stresses from 30 to 600 MPa, strain rates between 2×10^{-6} and 1×10^{-3} s^{-1}) fine-grained synthetic anorthite shows a transition from dislocation creep to diffusion creep dependent on stress, with samples deformed at stresses > 120 MPa yielding a stress exponent of 3, whereas at lower stresses, stress exponents of 1 are observed, indicating diffusion creep (Rybacki and Dresen, 2000). In both stress regimes, the addition of water significantly lowers activation energies for creep in the samples, with a corresponding decrease in strength of anorthite in both the dislocation and diffusion creep regimes (Rybacki and Dresen, 2000). Dimanov et al. (1999) also observed weakening of synthetic anorthite aggregates with the addition of water, which when extrapolated to natural conditions yields a difference in strength of 3–4 orders of magnitude between wet and dry samples. From these and other experimental data (see studies listed in Table 1 of Rybacki and Dresen, 2004b), deformation mechanism maps for feldspar rocks have been constructed, which show that grain-boundary diffusion creep and dislocation creep regimes are separated by a transition zone that is extremely grain-size sensitive. For grain sizes on the order of 10–50 μm, the maps predict that grain-boundary diffusion creep will dominate deformation in wet plagioclase from greenschist facies to granulite facies (Fig. 1.2; Rybacki and Dresen, 2004b).

A transition from dominantly brittle behaviour to dominantly grain-size sensitive creep behaviour is observed in feldspar at sufficiently small grain sizes (Jiang et al., 2000; Menegon et al., 2008; Prior and Wheeler, 1999; Stünitz, 1993; Stünitz and Fitz Gerald, 1993; Viegas et al., 2016; Wintsch and Yi, 2002), regardless of the grain size reduction mechanism. Strain accommodation occurs by pressure solution or Coble creep, depending on the presence of fluid and temperature of deformation (*op cit*). Experimental evidence suggests the presence of a small amount of water (~0.9 wt%) enhances grain boundary diffusion so that, depending on temperature and strain rate, a transition directly from cataclastic flow to grain boundary diffusion creep can be achieved (Tullis and Yund, 1991).

1.2.3 Chemical grain size reduction in plagioclase

Chemical disequilibrium is important when considering recrystallization and grain size reduction in feldspar. As plagioclase composition varies across a solid solution in which the stable species is temperature dependent, there is abundant evidence, from both nature and experiment, that syn-deformational reactions, driven by chemical disequilibrium, can produce fine-grained feldspar of a new composition (reequilibration at lower grade conditions generally produces feldspar of more albitic composition) in the middle crust (Brodie and Rutter, 1985; Fitz Gerald and Stünitz, 1993; Stünitz, 1998; Stünitz and Fitz Gerald, 1993; Stünitz and Tullis, 2001). This process is sometimes termed neocrystallisation (Stünitz, 1998). In addition, much endeavour has recently been focused on identifying and characterising fluid-mediated, interface-coupled, mineral replacement reactions, which occur when a metastable solid phase comes into contact with a fluid, leading to dissolution of that phase and the precipitation of a new, stable phase from the dissolved components (Putnis, 2002; Putnis, 2009; Putnis and Putnis, 2007). Mineral replacement reactions are often pseudomorphic, so although new small grains can be produced, the replacement process does not necessarily lead to an overall grain size reduction (Putnis, 2009). Feldspar has been shown to undergo replacement reactions in both nature (Engvik et al., 2008; Mukai et al., 2014; Plümper et al., 2017; Plümper and Putnis, 2009) and experiment (Hövelmann et al., 2009), with albite commonly being produced. Indeed, regional-scale albitization across tens of km^2 is observed in nature (Engvik et al., 2008; Plümper et al., 2017). The products of such reactions contain a high defect density, which is attributed to non-perfect topotactic growth during replacement (Engvik et al., 2008; Hövelmann et al., 2009; Plümper et al., 2017).

1.3 Thesis structure

The data analysis in this thesis is presented as four distinct but interrelated chapters, which are intended to be submitted to internationally-recognised peer-reviewed journals. References for all chapters can be found at the end of this thesis.

Chapter 2: Methods. This chapter describes the methods used for analysis in this thesis. Sample preparation for scanning electron microscopy (SEM) and transmission electron microscopy (TEM) work are described, followed by a description of the SEM and TEM techniques used. Electron backscatter diffraction (EBSD) is the main analytical tool used in chapters 3, 4 and 6 of this study, so EBSD data acquisition, processing and analysis is then described. Finally, the numerical model used for simulation of microstructural evolution during diffusion creep in Chapter 5 is described.

Chapter 3: Mineral replacement reactions as a precursor to grain size reduction in a feldspar rich shear zone: A new link between metamorphism and deformation. In the lowest strain samples of the Gressoney metagabbros, large albite porphyroclasts coexist with small albitic matrix grains. EBSD reveals that small grains neighbouring porphryoclasts share their orientation, so are likely derived from them. Therefore, this chapter describes the grain size reduction mechanisms that are likely to have occurred to produce the CPO domains observed in the matrix at higher strains (Chapter 4). Multiple types of fluid-rock interaction are probably responsible for the overall grain size reduction, and which one dominates locally is probably dependent on the degree of fracturing, and consequent fluid availability. Where fracturing and fluids are least abundant, interface-coupled replacement reactions appear to load product porphyroclasts with a high defect density, allowing grain growth from strain-free nuclei to eventually consume large porphyroclasts. This process is driven by internal strain energy produced by chemical not mechanical means, and occurs at crustal conditions where grain boundary migration would not normally be expected to be significant in plagioclase.

Chapter 4: Evolution of microstructure and texture along a strain gradient during diffusion creep. This chapter describes the evolution of texture in the albitic matrix at increasingly higher strain during fluid-assisted diffusion creep. Texture strength is quantified using the M-Index in MTEX, a MatLab®-based toolbox for texture analysis. Misorientation analysis is also carried out using MTEX. Texture strength is shown to decrease with increasing strain, and misorientation angle distributions tend towards random. The effect of a second phase on albite grain size and shape, and texture strength is also quantified. The results suggest that although a second phase inhibits grain growth, which could lead to increased deformation by diffusion creep, grain rotations may also be inhibited with increased second phase abundance, thereby preserving an inherited texture to high strains.

Chapter 5: The influence of porphyroclasts on microstructural evolution during diffusion creep. Diffusion creep is a fundamental deformation in the Earth, but remains poorly understood. In this chapter, we present numerical simulations of diffusion creep which investigate the influence of porphyroclasts on microstructural evolution in both pure and simple shear. The models are run in DiffForm, a MatLab®-based platform specifically designed to simulate deformation during diffusion creep. The results show that the evolution of grain rotations and angular velocities depends on interactions between the porphyroclast and matrix grains, and these interactions affect the strength of the model. Grain rotations in simple shear also result in the partitioning of initial grain orientations into smaller subsets of shared grain orientation, which may be analogous to the formation of small CPO domains observed in Chapter 4.

Chapter 6: Application of the Weighted Burgers Vector algorithm to high-angular resolution EBSD datasets. New techniques allow for ever more detailed information to be gathered by EBSD. In this chapter, we show how high-angular resolution EBSD (HR-EBSD) datasets can be used in conjunction with the Weighted Burgers Vector (WBV) technique to extract information about the interactions between dislocation sets that cannot be gathered by either technique independently, or by other methods using 2D EBSD map data. We suggest that combining the two techniques in future studies may yield significant steps forward in our understanding of dislocation activity in deformed crystals.

Chapter 7: Synthesis and future work. The final chapter of this thesis pulls together all the main findings of the previous chapters, and explains the implications of our findings in terms of understanding deformation in the Earth. Future research directions are also suggested.

1.4 Status of manuscripts and co-author contributions

At the time of thesis submission, none of the chapters of this thesis have been submitted for peer review. Intended target journals and co-author contributions for each chapter are listed below. Mark Pearce is thanked for supplying MATLAB® code to produce the deformation mechanism maps presented in Fig. 1.2.

Chapter 3: Mineral replacement reactions as a precursor to grain size reduction in a feldspar rich shear zone: A new link between metamorphism and deformation.

Target journal: Journal of Metamorphic Geology

Co-author contributions:

Joe Gardner – Principal investigator, primary author, data collection, data analysis

John Wheeler – Data analysis, manuscript review, discussion

Elisabetta Mariani – Data analysis, manuscript review, discussion

Karl Dawson – TEM data collection, data analysis

Chapter 4: Evolution of microstructure and texture along a strain gradient during diffusion creep.

Target journal: Lithos

Co-author contributions:

Joe Gardner – Principal investigator, primary author, data collection, data analysis

John Wheeler – Data analysis, manuscript review, discussion

Elisabetta Mariani – Data analysis, manuscript review, discussion

Chapter 5: The influence of porphyroclasts on microstructural evolution during diffusion creep.

Target journal: Journal of Structural Geology

Co-author contributions:

Joe Gardner – Principal investigator, primary author, data collection, data analysis

John Wheeler – Data analysis, manuscript review, discussion

Chapter 6: Application of the Weighted Burgers Vector algorithm to high-angular resolution EBSD datasets.

Target journal: Ultramicroscopy

Co-author contributions:

Joe Gardner – Principal investigator, primary author, data collection, data analysis

John Wheeler – Data analysis, manuscript review, discussion

David Wallis – Data collection (albite dataset), provision of olivine dataset

Chapter 2 Methods

2.1 Introduction

The following chapter details all methods that were employed during the course of this study. The majority of data presented in this study were collected in the Electron Microscopy Laboratory, Department of Earth, Ocean and Ecological Sciences, University of Liverpool. FIB-preparation of electron transparent samples and TEM imaging were carried out at the Imaging Centre at Liverpool (ICaL), University of Liverpool. High-angular resolution EBSD data were collected and processed in the Department of Earth Sciences, University of Oxford.

2.2 Sample preparation

Samples collected from the Gressoney Shear Zone at the localities detailed in Figure 3.1 were cut into billets ready for thin section preparation in the Earth Science department at the University of Liverpool. Thin sections were manufactured from the billets by Paul Hands of Hands On Thin Sections Ltd.

2.2.1 Sample preparation for SEM

As EBSD was the principal analytical technique employed in the study, all thin sections were prepared to a standard at which reliable EBSD data could be acquired. EBSD requires a high-quality surface polish to facilitate clear diffraction pattern collection. Patterns are collected from the top 10–50 nm of the specimen surface, so this part of the sample should be representative of the region from which crystallographic orientation data is required (Engler and Randle, 2009). Thin sections were initially manufactured with a high quality ¼ µm diamond polish by Paul Hands of Hands On Thin Sections. This finish was improved with a final chemo-mechanical polish for 2–3 hours using 0.005–0.006 µm grit size colloidal silica (SYTON®) in the Electron Microscopy Laboratory at the University of Liverpool. As silicate materials are non-conducting, charge from an electron beam can build up on the sample surface during data acquisition. To avoid this, as a final step samples were carbon coated, also in the Electron Microscopy Laboratory at the University of Liverpool.

2.2.2 Sample preparation for TEM

Electron-transparent samples suitable for TEM analysis were prepared using the FIB method in the Imaging Centre at Liverpool (ICaL) at the University of Liverpool. An FEI Helios 600i dual-beam focussed ion beam (FIB) instrument was used to prepare the samples via a lift out method (Giannuzzi and Stevie, 1999; Tomus and Ng, 2013). Orientation contrast images were used to determine targets for foil preparation using a

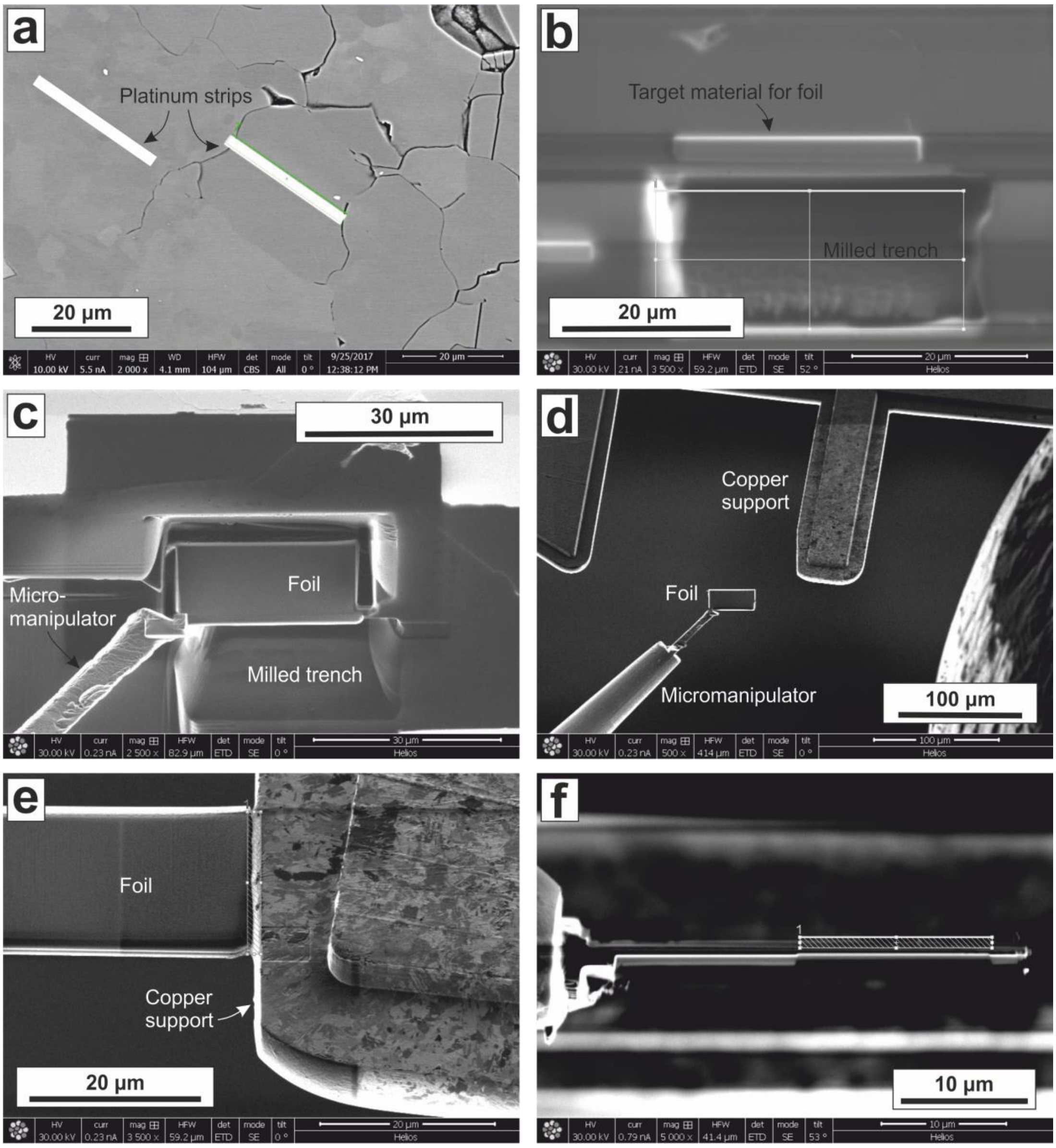

Figure 2.1 *FIB preparation of electron transparent samples for TEM. a) Orientation contrast image showing where TEM foils were collected from. The white strips are platinum that was laid on the sample surface to protect regions of interest during milling. The left hand strip was placed over part of a distorted porphyroclast, which displays a mottled texture in the orientation contrast image. The right hand strip was laid on a distortion-free, recrystallized grain. b) Trenches were milled either side of a region of interest using a beam of gallium ions to generate 1 µm thick foils. c) Foils were attached to a micromanipulator using beam-induced Pt deposition and extracted from the bulk sample. d–e) Foils were attached to Cu supports, using beam-induced Pt deposition. f) Foils were finally milled to approximately 100 nm to achieve electron transparency.*

retractable concentric back scattered electron detector fitted to the FIB instrument, using operating conditions of 10 kV accelerating voltage and 5.5 nA probe current (Fig. 2.1a). Platinum strips were laid on the sample surface to protect regions of interest during milling (white strips in Fig. 2.1a). Trenches were milled either side of a region of interest using a beam of gallium ions with an accelerating voltage of 30 kV and a high beam current (21–65 nA) to produce foils 1 μm thick (Fig. 2.1b). Foils were attached to a micromanipulator using beam-induced Pt deposition and extracted from the bulk sample (Fig. 2.1c). The foils were then attached to Cu supports, again using beam-induced Pt deposition (Fig. 2.1d & e), before further milling to approximately 100 nm to achieve electron transparency (Fig. 2.1f), using a 30 kV Ga ion beam with reduced currents (80 pA–2.5 nA), and finished with a low kV (2–8 kV) polish.

2.3 Scanning electron microscopy

2.3.1 Energy Dispersive Spectroscopy

Energy Dispersive Spectroscopy (EDS) was used to characterise the chemical composition of a material. When electrons carrying a few tens of kilo electron volts (keV) interact with a specimen, electrons from atoms within the specimen are ejected. Vacant electron sites are filled by electrons from higher electron shells with a higher energy state, and as they drop to the lower energy state, X-rays with an energy characteristic to the atoms present in the material are emitted (Champness, 1977; Humphreys et al., 2014).

The X-ray detectors used in EDS analysis are normally made of semiconducting silicon. As X-rays cannot be deflected by magnets, the X-ray detector must be in the line of sight of the specimen. When incoming X-rays hit the detector they excite a number of electrons in the silicon, leaving positively charged holes in the outer electron shells. The number of electrons excited, and thus the number of resultant holes, is proportional to the energy of the X-ray. If a voltage is applied across the semiconductor, the magnitude of the current that flows as an X-ray is absorbed will be exactly proportional to the energy of the X-ray (Humphreys et al., 2014). Each ‘pulse’ produced by an X-ray is amplified, and overall data are collected and presented as a histogram of cumulative counts at each energy level (Fig. 2.2).

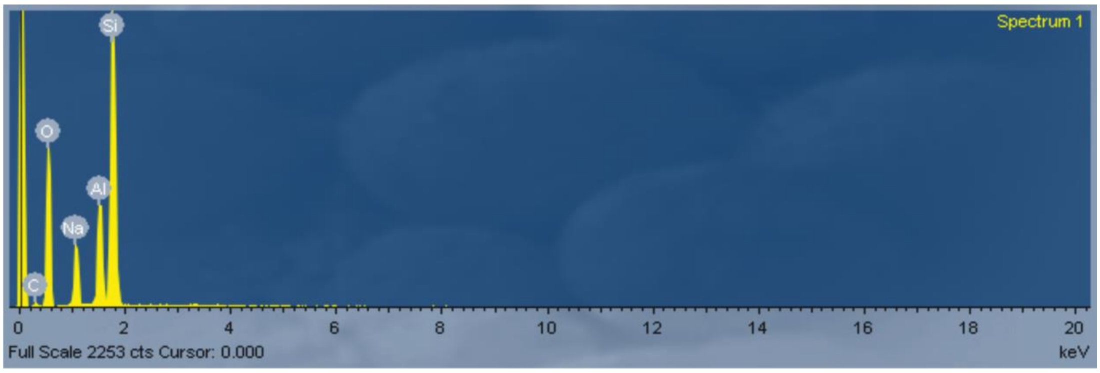

Figure 2.2 *Example of chemical spectrum generated by EDS. The x-axis records the energy (keV) of incoming X-rays, which is characteristic to the element the X-rays are generated from. The y-axis records the intensity of the signal (number of X-ray counts).*

EDS analyses presented in this study were performed on a Philips XL30 tungsten filament SEM in the Electron Microscopy Laboratory at the University of Liverpool. The XL30 at Liverpool is fitted with an array of detectors in addition to EDS: backscatter electron (BSE), secondary electron (SE), electron backscatter diffraction (EBSD), and cathodoluminescence (CL). In this study, the XL30 was used to collect BSE images and EDS data. Typical operating conditions used in this study were 20 kV accelerating voltage, 60–80 μA beam current and 5 nm spot size.

2.3.2 Electron Backscatter Diffraction

Electron Backscatter Diffraction (EBSD) is a well-established tool for characterising microtexture in crystalline materials. The technique works by rastering an electron beam across a sample surface to generate Kikuchi diffraction patterns, which can be used to derive crystallographic orientation of the target grains (Fig. 2.3). During data collection, the sample surface is tilted at an angle of ~20° to the electron beam, which reduces the path length of electrons entering the specimen, allowing more of them to undergo diffraction and escape the specimen, resulting in well-resolvable diffraction patterns (Figs. 2.3 and 2.4) (Engler and Randle, 2009).

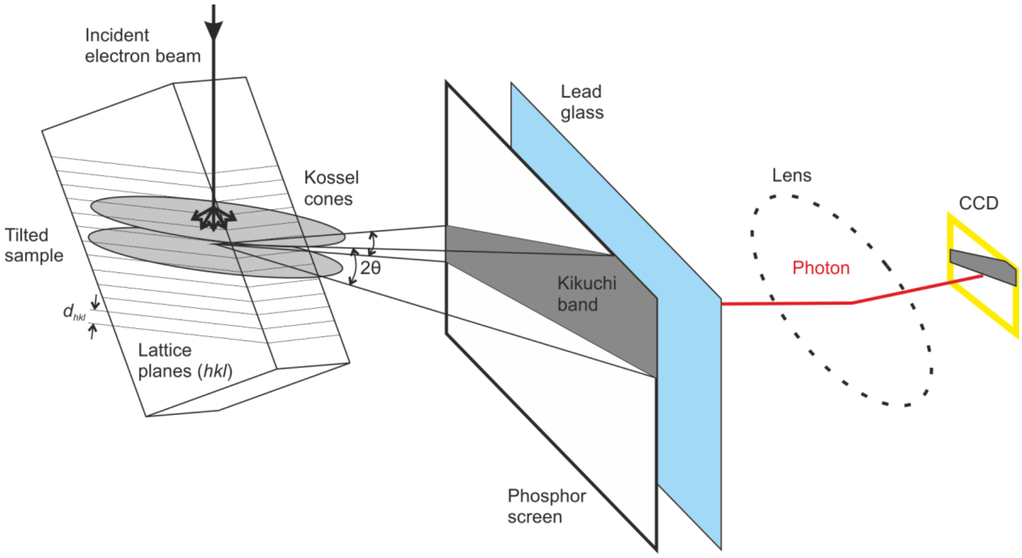

Figure 2.3 *Schematic diagram showing the generation of Kikuchi diffraction bands and basic set up of an EBSD data acquisition system. Electrons from the incoming electron beam are scattered by interaction with atoms on specific lattice planes. Backscattered electrons are deflected to intersect a phosphor screen. The pattern generated by the backscattering depends on which lattice planes are intersected by the electron beam. Patterns are captured by the generation of photons from the phosphor screen, which are captured by a charge-coupled device (CCD; i.e. a camera) that amplifies the photon signal and records output as an image, similar to the one shown in Figure 2.4a.*

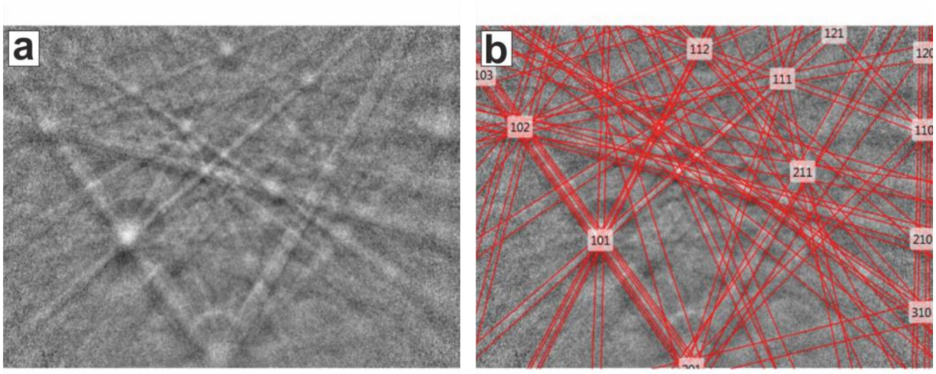

Figure 2.4 *Example of an albite Kikuchi diffraction pattern. a) raw electron backscatter pattern; b) indexed electron backscatter pattern with labelled zone axes.*

Backscattered electrons are diffracted by crystal lattice planes, according to Bragg's Law:

$$n\lambda = 2d\ sin\theta$$

where n is an integer that states the order of reflection, λ is the wavelength, and d is the spacing between atomic planes. Bragg showed that diffraction occurs on atomic planes, i.e., lattice planes $\{hkl\}$, as follows (Engler and Randle, 2009).

Consider a crystal lattice with three atomic layers, A, B and C (Fig. 2.5). Incoming rays intersect the atomic planes in the direction XY at an angle θ. Some radiation is reflected off atomic plane A at an angle 2θ, but most travels into the lattice to be reflected off deeper planes, also at an angle of 2θ. The line X–X_2, which is perpendicular to the incident beam, represents the crest of an in phase wave. For the beam to be diffracted, the outgoing waves must also be in phase, along the line Z–Z_2, which is achieved if the path length of beams diffracted by successive atomic planes is equal to an integral number of wavelengths, i.e. the distance I–Y_1–J is one or a multiple of wavelengths, λ. As $IY_1 = Y_1J = d\ \sin\theta$, the condition at which beams will be diffracted from any atomic plane can be summarised as $n\lambda = 2d\ sin\theta$, which is Bragg's Law.

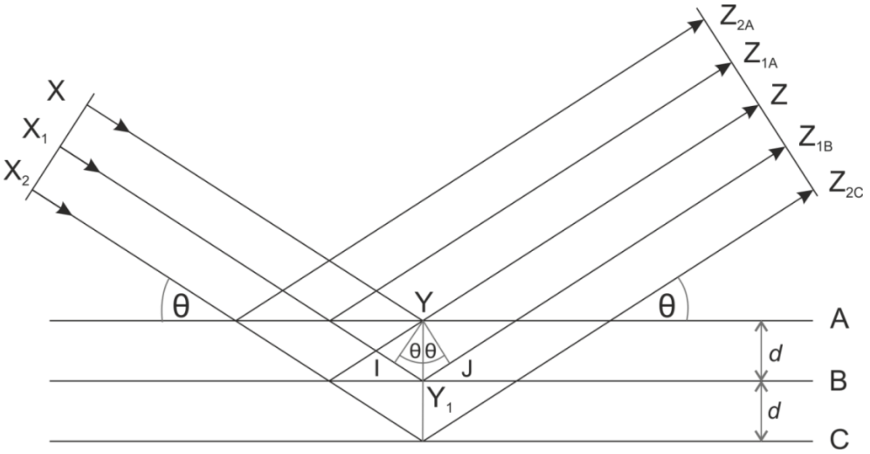

Figure 2.5 *Schematic of principles behind Bragg's Law of diffraction by crystallographic planes. Incoming rays intersect atomic planes A, B, and C in the direction XY, at angle θ. Some radiation is reflected off atomic plane A at an angle 2θ, but most travels into the lattice to be reflected off deeper planes, also at an angle 2θ. The line X–X_2, which is perpendicular to the incident beam, represents the crest of an in phase wave. For the beam to be diffracted, outgoing waves must also be in phase, along the line Z–Z_2. This condition is achieved if the path length of beams diffracted off successive atomic planes is equal to an integral number of wavelengths. As $IY_1 = Y_1J = d\ sin\theta$, the condition at which beams will be diffracted from any atomic plane can be summarised as $n\lambda=2d\ sin\theta$, which is Bragg's Law.*

When electrons enter a crystalline solid, they are scattered in all directions, so some electrons intersect every atomic plane at the Bragg angle. Because diffraction occurs in all directions, a pair of cones of diffracted electrons is formed by each set of diffracting crystallographic planes (Fig. 2.3). Diffraction patterns are deflected onto a fluorescent phosphor screen, and the resulting luminescence is captured by a low-light Charge-Coupled Device (CCD) camera (Fig. 2.3), to produce images such as those shown in Figure 2.4. Camera sensitivity is improved by the technique of 'binning' groups of pixels together, which also reduces diffraction pattern collection time (Randle, 2009).

The diffraction pattern is composed of Kikuchi bands, which are the traces of the large-angle cones projected onto a two-dimensional surface (Fig. 2.3). Solving Kikuchi patterns to determine the crystallographic orientation of the sampled region requires that i) the pattern is correctly indexed i.e. that the bands are correctly attributed to the crystallographic planes that generated them, and ii) the relative position of the bands is determined with respect to an external reference frame, to determine the crystal orientation (Engler and Randle, 2009). In high symmetry crystals, at three bands or zone axes (where bands, i.e. crystallographic planes, intersect) are required to determine crystallographic orientation, although more may be required for unambiguous indexing, particularly for materials with lower symmetry. The current study utilised at least eight bands per diffraction pattern for unambiguous determination of orientation in feldspar.

Spatial resolution limits of the EBSD technique depend on such factors as the type (atomic number) of material being studied, microscope set-up, accelerating voltage and probe current used, and the quality of diffraction patterns. Limits for most materials fall in the tens of nm range (Randle, 2009). The smallest step size used in this study was 0.2 μm, an order of magnitude greater than generally accepted spatial resolution limits, because these length scales were adequate for imaging all intracrystalline deformation features of interest.

The angular resolution limit of EBSD depends on the precision of diffraction pattern indexing, which itself depends on system calibration and diffraction pattern quality. As modern EBSD systems are set up to automatically derive crystallographic orientations from diffraction patterns, the accuracy of this solve-routine affects angular resolution (Randle, 2009). The generally accepted angular resolution of conventional EBSD sits between 0.5–1°. Recent advances in this area using the technique of high-angular resolution EBSD (HR-EBSD) show vast potential to gather important information about elastic stresses, elastic strains and lattice rotations (Britton et al., 2013) in deformed crystalline materials, and is discussed further in sections 2.4.5 and 6.2.1.

2.3.3 CamScan X500 CrystalProbe field emission gun SEM

Almost all EBSD data presented in this study were collected in the Electron Microscopy Laboratory, University of Liverpool on a CamScan X500 CrystalProbe field emission gun (FEG) SEM. The electron beam in the X500 CrystalProbe is generated by thermionic field emission from a tungsten single crystal tip coated with ZrO_2 (Seward et al., 2002). Field emission works on the quantum mechanical principle of tunnelling, whereby when a large electrical field is generated between a cathode and an anode, the classical energy barriers that inhibit the liberation of free electrons from a material are removed (i.e. the electrons can 'tunnel' through said barriers), so a beam of free electrons can easily be generated. The beam of electrons is highly focused, resulting in a smaller activation volume, which can be used to collect data with a high spatial resolution.

The X500 CrystalProbe was designed with the column (i.e. electron beam) inclined at 70° to the conventional vertical position used in most SEMs (Fig. 2.6). This geometry allows specimens to remain horizontal whilst also creating a 20° incidence angle between the electron beam and sample surface (the ideal angle to generate backscattered electrons, as mentioned above). This geometry improves accuracy of specimen positioning, as a horizontal rather than tilted stage removes the need for constant vertical adjustment of the stage, which also reduces the time required to achieve accurate stage positioning. The X500 was designed to perform in-situ deformation experiments (none were performed in this study), so the horizontal stage also means there is no risk of samples moving or flowing away during such experiments. Because of the tilted column, the SEM chamber can be split into two (upper and lower) domains, meaning a heat shield that separates the upper and lower domains could be integrated into the X500, which reduces the effect of radiation on the detectors during in-situ heating experiments. The SE detector is positioned as it would be on a conventional SEM and is not affected by the inclined gun column geometry. The BSE detector is in a slightly different position than normal to provide distance between itself and the additional heating apparatus. The phosphor screen is coated with a thin film of aluminium to filter infra-red and low energy electrons, so it deflects heat and enhances the sharpness of the Kikuchi diffraction bands (Seward et al., 2002).

The CamScan X500 is fitted with an F+ Nordlys EBSD detector, and EBSD data were collected using Oxford Instruments' AZtec acquisition system. The CCD camera fitted to the CamScan has a 1344 × 1024 resolution, and is capable of digitising Kikuchi diffraction patterns at a speed of 640 Hz (i.e. 640 patterns per second). Simultaneous

EDS data acquisition can be performed during EBSD mapping as the CamScan is also equipped with Oxford Instruments’ X-Max 50 mm^2 silicon drift detector (SDD), which is also processed using the AZtec acquisition system. Typical operating conditions used in this study were 20 kV accelerating voltage, 20–30 nA beam current and 5.5 nm spot size.

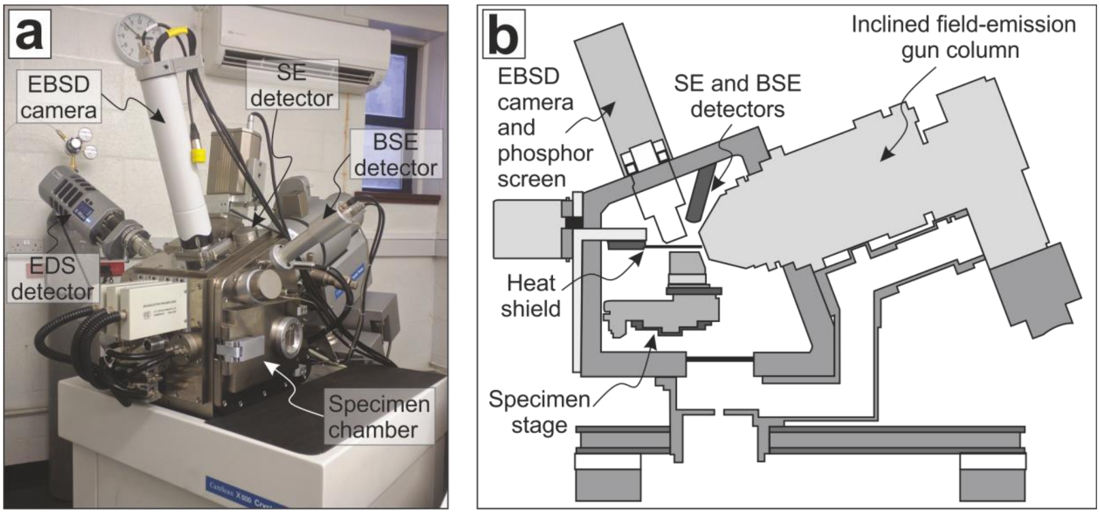

Figure 2.6 *Main features of the CamScan X500 CrystalProbe FIB-SEM. a) Photograph showing position of the main detectors and the specimen chamber; b) schematic cross-section showing the geometry of detectors with respect to the chamber, stage and inclined field-emission gun column.*

2.3.4 Quantitative evaluation of minerals by scanning electron microscopy

The quantitative evaluation of minerals by scanning electron microscopy, or QEMSCAN®, is an SEM method developed by CSIRO and FEI to provide automated and rapid, repeatable quantification of mineral content for the mining industry. The Diagenesis Research Group in the Department of Earth, Ocean and Ecological Sciences at the University of Liverpool uses an FEI WellSite Qemscan SEM equipped with a tungsten filament two Bruker light-element energy dispersive X-ray (EDS) spectrometers, which collect X-ray spectra from the surfaces of polished thin sections or blocks at a rate of c.10 ms per pixel (Pirrie et al., 2004).

Spectra are compared against a database of common mineralogical spectra to allow for rapid identification of mineral phases. EDS data for each pixel are compared to pixel brightness in a BSE image, which increases accuracy of identification (Qian et al., 2015). The QEMSCAN® database is made up of Species Identification Protocols (SIPs), each designed to optimise measurements of different types of geological materials e.g. ore deposits. An existing SIP can be modified or bespoke SIPs can be

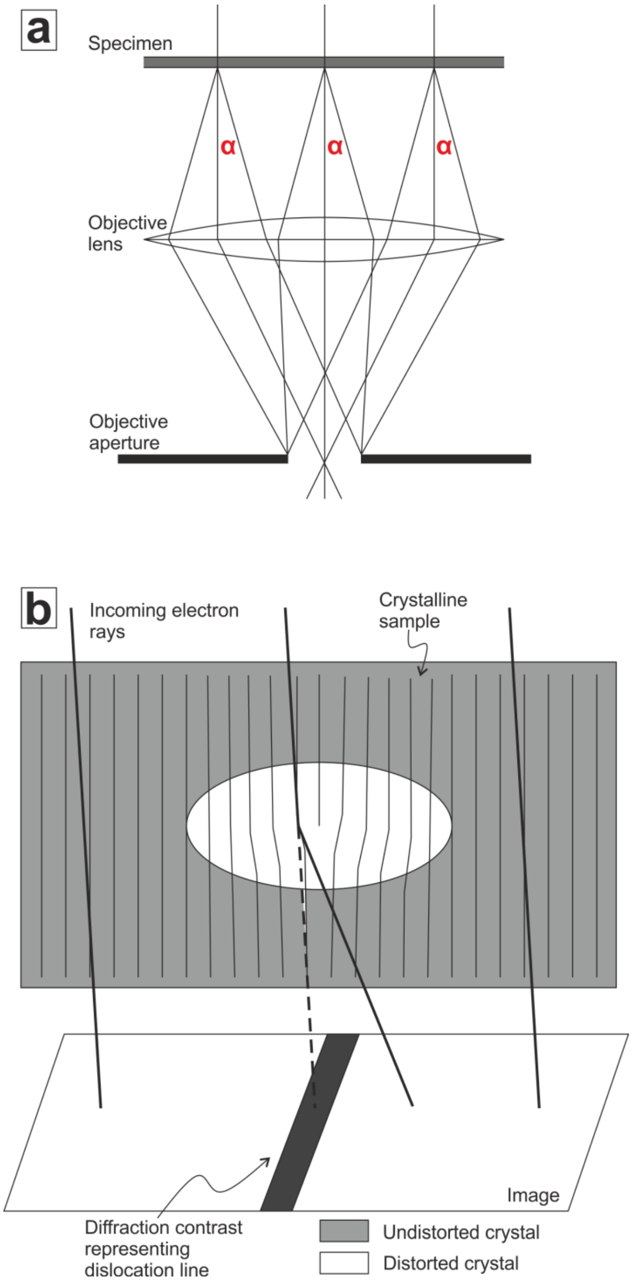

Figure 2.7 *a) Schematic of main principles of TEM diffraction. Redrawn from Fig. 4.8, Humphreys et al. (2014). Electrons are diffracted as they pass through an electron transparent sample. An objective lens behind the sample re-focuses diffracted electrons to form an image. An objective aperture in the back focal plane can be inserted to prevent all electrons that have been scattered through an angle larger than α from being collected in the image; b) Schematic of generation of dislocation lines in bright-field TEM images. Diffraction contrast can be used to visualise any feature which alters the planes that cause Bragg diffraction, such as dislocations and other crystal defects. Dislocations appear as dark lines in bright field images, because lattice planes become the most distorted when they are closest to a dislocation core, meaning rays are diffracted to an angle greater than α, and so dark lines are created in a bright field image. Redrawn from Fig. 4.27, Humphreys et al. (2014).*

constructed from scratch. The SIP parameters used for the analysis presented in Chapter 4 can be found in Appendix 1.

2.4 Transmission electron microscopy

Transmission electron microscopes (TEMs) work on similar principles to SEMs (e.g. a beam of electrons is generated by thermionic emission, controlled by magnets, and directed to interact with the atoms of a sample of interest to generate images and other data), except that samples of interest are prepared to be electron transparent, by methods such as those detailed in section 2.2.2 above. TEM can be used to generate selected area diffraction (SAD) patterns, which can provide information about intracrystalline distortion or shared orientation of crystal grains (Humphreys et al., 2014). The technique can also be used to generate images of intracrystalline features based on contrast. Such features will appear light or dark in a TEM image, depending on which contrast mechanism is at work.

TEM employs lenses to focus electrons that have been diffracted on their journey through the sample. An objective lens behind the sample re-focuses diffracted electrons to form an image. An objective aperture in the back focal plane can be inserted to prevent all electrons that have been scattered through an angle larger than α (Fig. 2.7a). This results in all areas of the sample which lack specimen appearing bright in an image, and so is called bright field imaging. Those regions of specimen that are thicker, or have a greater density, scatter electrons more strongly, so fewer electrons will pass through the aperture, and those regions will appear dark in the image (Humphreys et al., 2014).

In crystalline materials, diffraction of the electron beam is greatly increased in particular orientations, meaning strong contrast between features that diffract weakly or strongly can be observed in images. Diffraction contrast can be used to visualise any feature which alters the planes that cause Bragg diffraction, such as dislocations and other crystal defects. Dislocations appear as dark lines in bright field images as lattice planes are bent the most closest to a dislocation core, meaning rays are diffracted to an angle greater than α, and so will appear as a dark line in a bright field image (Fig. 2.7b; Humphreys et al. (2014).

Bright field TEM images were collected at the Imaging Centre at Liverpool (ICaL) at the University of Liverpool. A 200 kV JEOL 2000FX instrument operating in conventional TEM mode (Fig. 3.11a), and a probe aberration corrected JEOL 2100FCs S/TEM instrument operating at 200 kV in bright field scanning TEM (BF-STEM) mode (Fig. 3.11b), were used for image collection.

2.5 EBSD acquisition, processing and analysis

2.5.1 Data acquisition

Indexing in AZtec occurs within Oxford Instruments' HKL® software. Kikuchi diffraction patterns are transformed to Hough space, essentially meaning individual bands are converted into points (peaks) in a 2D space (Wilkinson and Britton, 2012). The Hough transform makes it easier for the software to locate peak positions to facilitate accurate indexing. In this way the diffraction patterns are matched by best-fit solutions within the HKL database to calculate most likely mineral phase and orientation from a user-defined list of expected phases. Accuracy of match is assessed by the quantity of Mean Angular Deviation (MAD_1) and the number of bands identified. Pattern refinement was carried out on points with an MAD_1 of < 0.4. 2 x 2 binning was used to speed up pattern processing and enhance generated Kikuchi diffraction patterns. Gain was set to 8 and exposure time was automatically optimised by AZtec.

2.5.2 Data cleaning and processing in CHANNEL 5®

Inherent in all EBSD datasets are spurious data points related to the misindexing or non-indexing of the Kikuchi diffraction pattern generated at a given point. Post-processing or 'cleaning' procedures can be used to remove such points and smooth EBSD data. Caution must be exercised so as not to introduce errors by over-processing of data. Oxford Instruments' Tango application in its Channel 5® software was used to clean all EBSD data, following the procedure outlined below.

Figure 2.8a shows a band contrast map of EBSD data collected primarily from an albite-rich area of the metagabbros analysed in this study. Pixels with poor band contrast are dark, and mostly reveal grain boundaries or holes in the samples. Pixels with improved band contrast are progressively lighter in the grayscale image. Figure 2.8b shows raw (unprocessed) EBSD data. Albite grains are coloured using the All-Euler colour scheme, and all other grains are not plotted. The upper white arrow points to a grain that contains systematic misindexing, and the lower white arrow to an adjacent grain that contains a number of non-indexed pixels. A misorientation profile drawn through the grain containing systematic misindexing shows the misindexing occurs due to a 180° rotation about the <201> (or <−20−1>) axis (Fig. 2.8c). This is a common misindexing problem in plagioclase and happens because the solutions about this rotation angle-axis pair are so similar the program cannot easily distinguish between the two.

During noise reduction, orientations of zero solutions (i.e. non-indexed pixels) are extrapolated using between 1 and 8 nearest neighbours. This can lead to problems of over-extrapolation, where grains ‘grow’ into holes or other regions in a spurious manner. To avoid this, band contrast maps can be used to threshold only those pixels above a user-defined grey-scale (i.e. holes, grain boundaries, and other non-crystalline features are removed), to which the extrapolation procedure is then applied. Figure 2.8d shows an example of the same map, in which most low grey-scale value pixels have been removed. Noise reduction is then applied to this data subset, and zero solutions are calculated from four nearest neighbours. Individual pixels with a different orientation to surrounding pixels (wild spikes) are also removed. The zero solution algorithm is then applied to the entire dataset using six nearest neighbours, resulting in the map shown in Figure 2.8e. Most zero solutions within grains have disappeared, without producing spurious growth into holes etc. Systematic misindexing can be removed by defining an angle-axis pair about which to rotate misindexed data. Pixels within 5° of a 180° misorientation about the <201> and <–20–1> planes were rotated. Figure 2.8f shows the data when systematic spikes have been removed.

Pole figures presented in Chapter 3 were plotted using Oxford Instruments’ Mambo pole figure software. Contours were calculated with a half width of 15° and cluster size of 5°. Some of the All-Euler plots presented in Chapter 4 (as documented in figure captions) were plotted in Oxford Instruments’ Tango software.

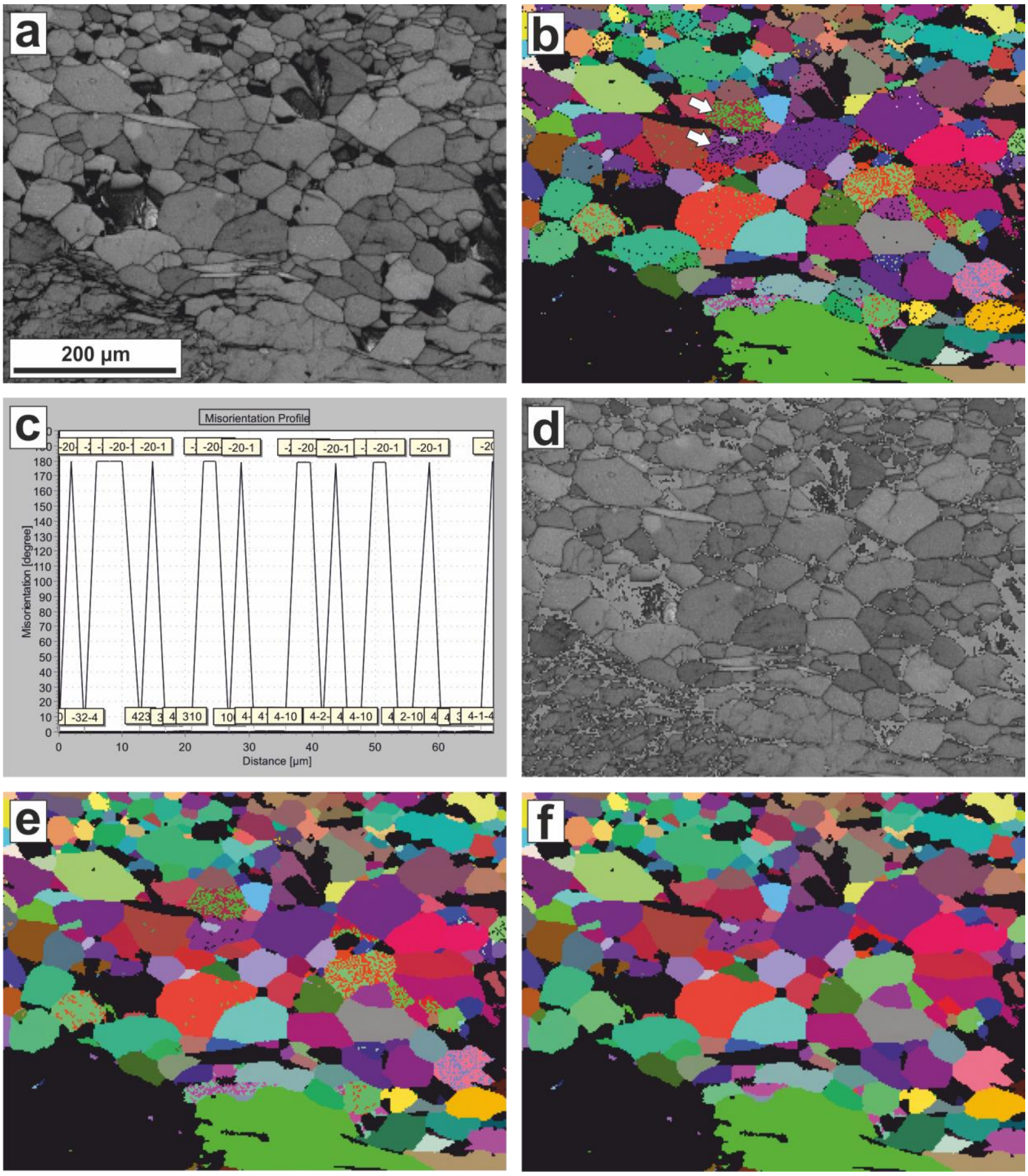

Figure 2.8 *Data cleaning in Channel 5®. a) Raw band contrast image; b) raw All-Euler data showing grains with systematic misindexing (top arrow) and unindexed pixels (bottom arrow); c) misorientation profile drawn through grain with systematic misindexing (top arrow in (b)), showing all misindexing occurs around a common angle-axis pair; d) band contrast image, which has been thresholded to remove all pixels with low band contrast values, i.e. where data is lacking (holes) or poor quality (grain boundaries, poorly indexed phases). The extrapolation of data to fill gaps with nearest neighbour orientations is applied to this data subset, so that grains are not extrapolated into holes or across grain boundaries; e) the same EBSD data after grain extrapolation and the removal of wild spikes (unreliable single pixel orientations) has been performed; f) the same EBSD data after the removal of systematically misindexed pixels within grains, performed by pixel rotation around common misindexing angles and axes.*

2.5.3 CrystalScape

CrystalScape is a MatLab®-based program used to process EBSD data written by Prof. John Wheeler at the University of Liverpool. CrystalScape was used to calculate grain boundary misorientations and plot most of the All-Euler EBSD maps presented in Chapters 3, 4 and 5. It was also used to calculate the Weighted Burgers Vector, as detailed below.

2.5.4 The Weighted Burgers Vector

The Weighted Burgers Vector (WBV) algorithm can be used to obtain 3D information (magnitude and direction) about the dominant Burgers vectors in dislocation populations of distorted crystals using orientation gradients in 2D EBSD map data (Wheeler et al., 2009). As lattice curvature measured by EBSD captures information about populations of geometrically necessary dislocations (GNDs) (Ashby, 1970; Wallis et al., 2016; Wheeler et al., 2009), the WBV algorithm can be used to constrain both a lower bound magnitude of the dislocation density tensor, and the directions of the Burgers vectors most likely to make up the GND population. Further explanation of how the WBV is calculated can be found in section 3.4.5.

2.5.5 MTEX

MTEX is a MatLab®-based toolbox for texture analysis (Bachmann et al., 2010; Mainprice et al., 2014). MTEX was used to plot pole figures, to calculate texture strength (M-index; see Table 4.1), to plot misorientation angle distribution histograms, and to calculate grain parameters (Table 4.2) in Chapter 4. The MatLab® scripts used in MTEX can be found in Appendix 2.

2.5.6 High-angular resolution EBSD

High-angular resolution EBSD (HR-EBSD) is a relatively new EBSD data processing technique that can increase angular resolution of the data by two orders of magnitude, from ~0.5° to ~0.006° (Britton et al., 2013). HR-EBSD works by the direct comparison of two or more Kikuchi diffraction patterns using cross-correlation (Britton and Hickey, 2018). Diffraction patterns are decomposed into multiple regions of interest to which the cross-correlation procedure is applied. Changes in Kikuchi band width from pattern to pattern can be correlated to changes in the width between crystallographic planes due to stored elastic strain, and changes in the orientations of the bands across different patterns can be correlated to crystal rotations caused by the presence of geometrically necessary dislocations (GNDs), and so can be used to estimate a lower bound estimate of dislocation density (Britton and Hickey, 2018). Stored elastic strains and rotations are measured with respect to a user-defined reference point, which ideally is not strained.

The HR-EBSD technique was developed with a focus on analysing the results of nanoindentation tests, where unstrained sample surface lies within a few μm of the strained surface of interest (Wilkinson et al., 2006b). Unstrained parts of a sample are much harder to come across in naturally deformed rocks. If the entire sample is deformed, calculated strains are relative not absolute.

HR-EBSD relies on the input of known Burgers vectors to calculate dislocation density of plastically-deformed material. As the albite studied here i) is not inferred to have been plastically deformed, and ii) contains uncommon Burgers vectors (as calculated by the WBV; see Chapter 3), it was decided that the calculated dislocation densities were not reliable, so they are not included in this thesis. Chapter 6 details a comparison of information obtained by the WBV algorithm when applied to conventional and HR-processed EBSD data.

2.6 Numerical modelling

DiffForm is a MatLab®-based program developed by Prof. John Wheeler, which is used for modelling microstructural evolution during diffusion creep (Berton et al., 2006; Ford et al., 2004; Ford et al., 2002). As diffusion creep is driven by differences in stress on grain boundaries (depending on how the interface is oriented with respect to σ_1), the model works by calculating diffusive fluxes, that are driven by chemical potential (which is dependent on stress), along interface segments. By calculating the current (i.e. flux x interface width) along an interface, growth and dissolution rates, and hence grain shape change, can be derived (Wheeler and Ford, 2008). A rigorous treatment of the fundamental mathematics which DiffForm utilised to model microstructural evolution in diffusion creep can be found in Wheeler (2009). A non-mathematical description of the principles behind the model can be found in Section 5.3 of this thesis.

Chapter 3 Mineral replacement reactions as a precursor to grain size reduction in a feldspar rich shear zone: A new link between metamorphism and deformation

3.1 Abstract

Grain size reduction is an important process that leads to rheological weakening and strain localisation in the earth. In this chapter, evidence is presented for a hybrid mechanism of grain size reduction in feldspar, the most common mineral in the middle and lower crust. Multiple types of fluid-rock interaction occur depending on local variation in degree of fracturing, which opens fluid pathways. Electron backscatter diffraction and transmission electron microscopy is used to show that fluid-mediated, interface-coupled replacement of Ca-bearing plagioclase by albite can form product grains with a high dislocation density (and associated plastic strain), due to the presence of growth defects produced during replacement. Critically, this is a chemical not mechanical mechanism for increasing plastic strain energy in mineral grains. In a subsequent stage of evolution, this strain energy provides a driving force for growth by boundary migration of new, strain-free grains, which leads to an overall reduction in grain size. The grain size reduction is associated with a switch from dominantly brittle to dominantly viscous behaviour, which leads to creep by diffusive mass transfer. As feldspar dictates the strength of the middle and lower crust, the fact that interface coupled replacement reactions driven by fluid-rock interaction can lead to mechanical weakening in feldspar means these reactions may exert fundamental controls on crustal deformation behaviour. Grain size reduction is a key component of strain localisation in the viscous crust, which in turn dictates where and how much brittle deformation (i.e. earthquakes) occurs in the upper crust. As such, these reactions warrant further investigation in nature, theory and experiment.

3.2 Introduction

The overall strength of the lithosphere is greatly influenced by the localisation of strain into discrete zones of deformation. Grain size reduction is an important feature of strain localisation in the Earth (De Bresser et al., 2001; Kilian et al., 2011; Platt and Behr, 2011; Tullis and Yund, 1985; Warren and Hirth, 2006). It can be achieved by three main mechanisms: cataclasis (Simpson, 1985), the production of new phases during metamorphic reactions (Brodie and Rutter, 1985; Newman et al., 1999; Stünitz and Tullis, 2001) and dynamic recrystallization (Platt and Behr, 2011). The dominant deformation behaviour of any mineral is dependent on local variables such as temperature, pressure, bulk mineral assemblage, grain size, and strain rate during deformation.

3.2.1 Deformation in plagioclase feldspar

Feldspar, the most common constituent of the Earth's middle to lower crust, has been observed to undergo dominantly brittle grain size reduction at mid-crustal conditions, particularly in rocks of granitic composition, where it is commonly the strongest phase (Fitz Gerald and Stünitz, 1993; Simpson, 1985; Stünitz and Fitz Gerald, 1993; Viegas et al., 2016). Plagioclase is weaker than pyroxene and amphibole at lower crustal levels, so accommodates most of the strain in metabasic rocks deformed at medium to high metamorphic grades (Brodie and Rutter, 1985)

Microcracking (small, high-aspect-ratio cracks that form in rocks due to differential stress; Anders et al., 2014) is commonly observed to dominate deformation of natural feldspar samples at greenschist facies conditions (Fitz Gerald and Stünitz, 1993; Stünitz, 1993; Stünitz and Fitz Gerald, 1993), but can still be significant at much higher grades (Fitz Gerald and Stünitz, 1993; Menegon et al., 2008; Menegon et al., 2013; Stünitz et al., 2003). This behaviour is primarily due to its two good cleavages on (010) and (001). Experimentally, microcracking has also been observed to be the dominant deformation mechanism in albite at low temperatures ($T \leq 500$ °C, $P = 1.0$–1.5 GPa, $\dot{\varepsilon} = 10^{-6}$ s^{-1}; Hacker and Christie, 1990). Fragmented crystals can exhibit intracrystalline deformation features, including subgrain and patchy extinction features, although TEM reveals these are due to small-scale brittle fractures rather than networks of dislocations (Tullis and Yund, 1987). In addition, pervasive (micro)fracturing and subsequent movement on the two good cleavage planes simulates crystal plastic slip on those planes and can result in grain flattening and the development of CPOs (Tullis and Yund, 1987).

Dynamic recrystallization has been observed to occur in feldspar, but relies on the presence of dislocations and their ability to move (Tullis, 2002). Dislocation glide is inhibited in feldspar as most dislocations occur as stacking faults, and climb is inefficient because vacancy diffusion is slow in feldspar at low temperatures (Hacker and Christie, 1990; Tullis, 2002). Suppression of climb leads to strain hardening and promotes fracture. Where it occurs, dislocation creep tends to be accommodated by bulging recrystallization (where grain boundaries migrate into crystals with the highest dislocation density; Passchier and Trouw, 2005) and (high-angle) boundary migration rather than climb-dependent recovery and subgrain formation (Tullis, 2002). The transition from the dislocation creep regime to the grain-boundary diffusion creep regime has been shown to be extremely grain-size sensitive. For grain sizes on the order of 10–50 μm, deformation mechanism maps predict that grain-boundary diffusion creep will dominate deformation in wet plagioclase from greenschist facies to granulite facies (Fig. 1.2; Rybacki and Dresen, 2004b).

A transition from dominantly brittle behaviour to dominantly grain-size sensitive creep behaviour (pressure solution or Coble creep, depending on the presence of fluid and temperature of deformation) has also been observed in feldspar at sufficiently small grain sizes (Jiang et al., 2000; Menegon et al., 2008; Prior and Wheeler, 1999; Stünitz, 1993; Stünitz and Fitz Gerald, 1993; Viegas et al., 2016; Wintsch and Yi, 2002). The effect of even a small amount of water (~0.9 wt%) is to enhance grain boundary diffusion so that, depending on temperature and strain rate, a transition directly from cataclastic flow to grain boundary diffusion creep can be achieved (Tullis and Yund, 1991).

3.2.2 The role of feldspar chemistry in grain size reduction

As outlined in section 1.2.3, chemical disequilibrium has consequences for recrystallization and grain size reduction in feldspar. The stable composition of plagioclase is temperature-dependent, due to changes in lattice structure and the ordering of Si and Al. Studies of both nature and experiment show that syn-deformational reactions, driven by chemical disequilibrium, can produce fine-grained feldspar of a new composition (lower grade conditions produce plagioclase with increasingly high Na content) in the middle crust (Brodie and Rutter, 1985; Fitz Gerald and Stünitz, 1993; Stünitz, 1998; Stünitz and Fitz Gerald, 1993; Stünitz and Tullis, 2001).

The relatively recent identification of fluid-mediated, interface-coupled, mineral replacement reactions, appear to be relatively common in plagioclase, having been observed in both nature (Engvik et al., 2008; Mukai et al., 2014; Plümper et al., 2017; Plümper and Putnis, 2009) and experiment (Hövelmann et al., 2009). These reactions occur when a metastable solid phase comes into contact with a fluid, leading to dissolution of that phase and the precipitation of a new, stable phase from the dissolved components (Putnis, 2002; Putnis, 2009; Putnis and Putnis, 2007). Mineral replacement reactions are often pseudomorphic, so although new small grains can be produced, the replacement process does not always lead to an overall grain size reduction (Putnis, 2009). Albite is commonly produced during replacement reactions in plagioclase, with regional-scale albitization across tens of km^2 being observed in nature (Engvik et al., 2008; Plümper et al., 2017). The products of such reactions contain a high defect density, which is attributed to non-perfect topotactic growth during replacement (Engvik et al., 2008; Hövelmann et al., 2009; Plümper et al., 2017).

Thus, feldspar may undergo grain size reduction by a combination of physical and chemical processes. The interplay between these two processes is not well understood, despite the resulting grain size reduction ultimately being a major control on crustal strength. In this contribution, the causes of grain size reduction in albite following the pseudomorphic replacement of Ca-bearing plagioclase in a mid-crustal metagabbro were investigated. The aims of this study were i) to characterise intracrystalline distortion observed in albite porphyroclasts and explain its origins and role in subsequent stages of deformation; and ii) to determine the primary mechanism of feldspar grain size reduction (i.e. process of mylonitization) in the metagabbros, so as to elucidate the role interface-coupled replacement reactions can play in crustal-scale deformation and strain localisation.

3.3 Geological setting

The Gressoney Shear Zone (GSZ) is a km-wide extensional shear zone responsible for unroofing eclogite facies rocks in the internal zones of the Western Alps (Wheeler and Butler, 1993). The GSZ itself lies mostly within the Combin Zone, although its lower boundary sits against eclogite facies rocks in the Zermatt-Saas and Monte Rosa (Reddy et al., 1999). Together, the Combin and Zermatt-Saas zones make up the Piemonte Unit, which has been identified as relict oceanic crust that was sandwiched between the Sesia Zone (overriding southern continent) and the European basement (e.g. the Monte Rosa, Dora Maira and Gran Paradiso massifs) during the Alpine orogeny (Wheeler and Butler, 1993). Rb–Sr dating has been used to show the GSZ was active for 9 Ma, between 45–36 Ma (Reddy et al., 1999).

A variety of lithologies are found within the GSZ. Km-scale outcrops of metagabbro are inferred to be pre-Alpine (ca. 250 Ma) as no basic magmatism has been recorded in the Western Alps during the Alpine orogeny (see Wheeler and Butler (1993) and references therein). Within the Piemonte unit, all lithologies carry greenschist facies grade assemblages, and there is no evidence that the rocks of the GSZ ever experienced a higher grade of metamorphism. Crucially for this study, the metagabbros detailed below appear to have experienced a single phase of metamorphism and deformation in the greenschist facies (Prior and Wheeler, 1999; Wheeler and Butler, 1993), conditions at which crystal plastic mechanisms are not expected to be operative in feldspar. Prior and Wheeler (1999) provided a detailed description of the mineral assemblage in the samples, showing the feldspar in the metagabbros has been completely albitised (An_0), with Ca below the detectability limit of microprobe analysis in feldspar grains, and the Ca-bearing phase clinozoisite having been produced. Albitisation is common in feldspar (Engvik et al., 2008; Hövelmann et al., 2009; Plümper and Putnis, 2009) due to the abundance of Na-rich crustal fluids (Bucher and Stober, 2010). The albite grains therefore exhibit a complete lack of chemical zoning.

The samples in this study come from an outcrop of metagabbro found close to the base of the Combin Zone (UTM coordinates: 4042730 E, 5069723 N, Fig. 3.1), approximately 2 km north of Estoul in the Val d'Ayas. The outcrop shows variation in strain on the sub-metre scale, with cm-wide shear bands anastomosing around less-deformed pods (tens of cm) of the same material. Here, the results of a microstructural analysis of porphyroclastic grains of albite found in the least-deformed samples, as well as a mm-scale albite pseudomorph from a higher strain sample that was protected from deformation by inclusion in a pyroxene porphyroclast, are presented.

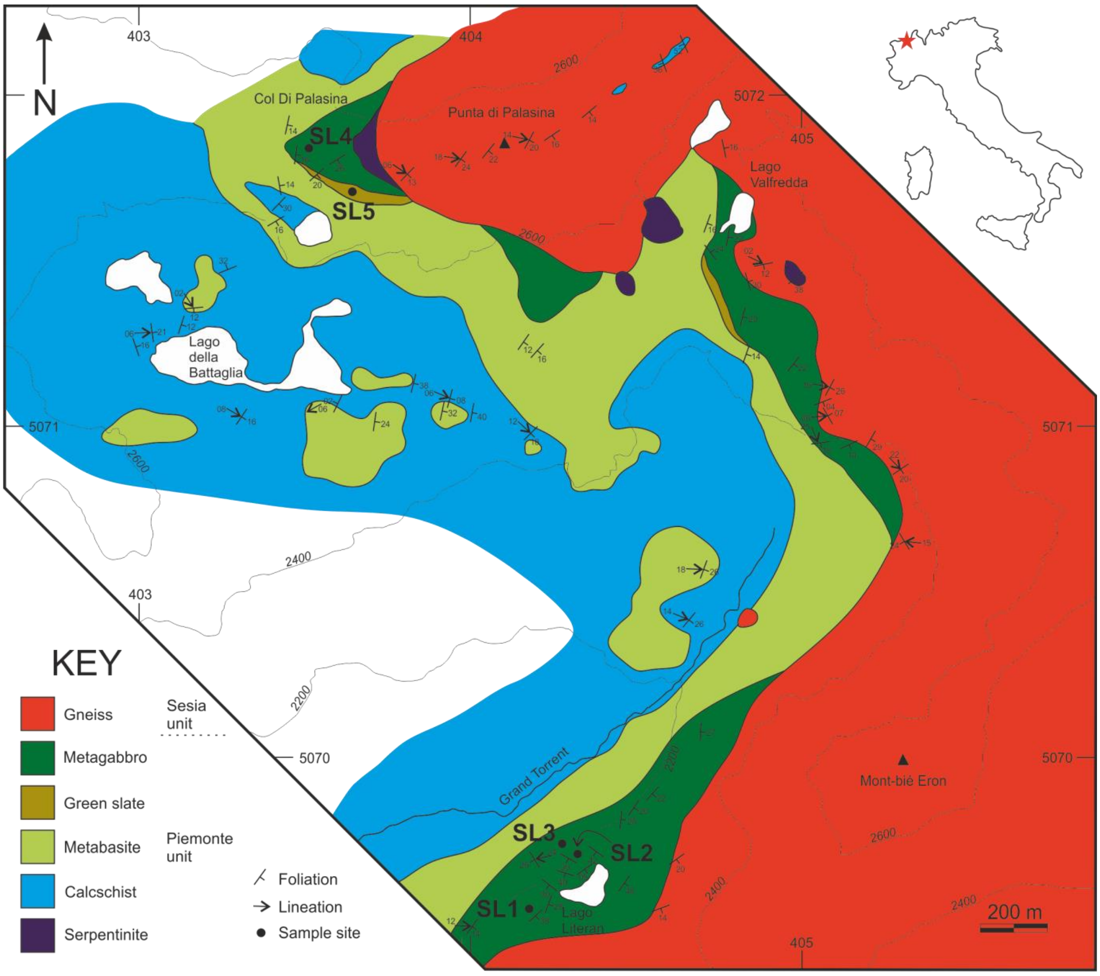

__Figure 3.1__ Geological map of part of the Gressoney Shear Zone (GSZ), which is composed of a suite of greenschist-facies lithologies. Inset shows location within the NW Italian Alps. Localities of samples collected for analysis in chapters 3 and 4 are identified.

3.4 Methods

Deformation in the metagabbros was primarily studied using polarized light and electron microscopy. Samples were prepared as thin sections cut perpendicular to foliation and parallel to lineation (i.e. the X–Z kinematic plane), where these features could be identified.

3.4.1 Optical images

The polarized light images and whole thin section scans in Figure 3.2a & b, and Figure 3.3b were collected using a Leica DM2500P microscope equipped with a Leica DFC295 camera (3 mega pixel resolution) and the Leica Application Suite software. Single images were acquired in capture mode, and whole thin section scans were acquired using live mode (up to 25 frames per seconds), which stitches together live images as the microscope stage is moved manually. The XPL image in Figure 3.3a was collected using a Lumenera Infinity 4 camera connected to a Meiji Techno MT9000 polarized microscope.

3.4.2 Scanning electron microscopy

Thin sections were polished for 2–3 hours using 0.05 μm colloidal silica, and carbon coated prior to collection of backscatter electron (BSE) images and electron backscatter diffraction (EBSD) data.

3.4.3 BSE imaging

BSE imaging was used to analyse phase distribution and chemistry on the μm-scale. BSE images were collected on a Philips XL30 SEM with a tungsten filament in the Earth Science department at the University of Liverpool. Data were collected using an accelerating voltage of 20 kV, beam current of 60–90 μA and a working distance of 13 ± 0.1 mm.

3.4.4 Electron backscatter diffraction (EBSD)

EBSD was used to obtain quantitative crystallographic orientation data from albite porphyroclasts and matrix grains. EBSD data were collected on a CamScan X500 CrystalProbe FEG-SEM equipped with a Nordlys F+ detector in the Department of Earth Science at the University of Liverpool (see section 2.3.3; Fig. 2.6). Data were collected with a working distance of 25 mm, accelerating voltage of 20 kV, and a beam current of ~30 nA. Automated runs were set up using the Oxford Instruments AZtec© software with 2 × 2 pattern binning. Step size for collection varied between 0.35 and 1.5 μm (see figure captions for step size used to collect each specific map) to allow a statistically reliable number of data points to be collected in even the smallest grains

(Humphreys, 2001; Randle, 2009; Wilkinson and Britton, 2012). Analyses of EBSD data were carried out in Oxford Instruments' Channel 5© software package. Band contrast data were used to threshold only the most reliable data points based on clarity of diffraction patterns (Hildyard et al., 2009). Subsequent data cleaning followed the routine that was set out in Prior et al. (2002) and Bestmann and Prior (2003). Nearest neighbours were used to fill in missing data points. Single pixel rotations ('wild spikes') within grains were removed. A systematic misindexing error of 180° rotation about the [201] axis that is common in feldspar was also removed (see section 2.5.2). Pole figures derived from EBSD data were plotted in both upper and lower hemispheres because, in triclinic feldspar, opposite crystallographic directions (e.g. [100] and [$\bar{1}$00]) are not symmetrically equivalent. Pole figures were plotted using Oxford Instruments' Channel 5® software.

3.4.5 The Weighted Burgers Vector

All EBSD maps (except those shown in Figs. 3. 4 & 3.14, which were plotted in Channel 5®) were plotted using CrystalScape, a Matlab®-based toolbox for quantitative analysis of EBSD data developed by Prof. John Wheeler at the University of Liverpool. The Weighted Burgers Vector (WBV) is a quantity that can be calculated in CrystalScape from orientation gradients in 2D EBSD map data (Wheeler et al., 2009). It uses the sole assumption that large-scale elastic strains are negligible, so lattice curvature can be entirely attributed to the presence of distributed dislocations. As dislocation structures such as dipoles can cancel out and therefore do not contribute to measured lattice curvature, EBSD captures information about populations of geometrically necessary dislocations (GNDs; Ashby, 1970; Wallis et al., 2016; Wheeler et al., 2009). The WBV algorithm can be used to constrain both a lower bound magnitude of the dislocation density tensor, and the directions of the Burgers vectors most likely to make up the GND population. The scalar magnitude of the WBV is defined as

$$W = \rho b l_3 \tag{1}$$

where ρ is the scalar density of dislocations, b is the Burgers vector, and l_3 is the sine of the angle that a given dislocation line has, relative to the plane of the map. Thus l_3 weights the dislocation density, by the angle at which dislocations intersect with the map plane, between 1 (perpendicular to map plane) and 0 (parallel to map plane). The derived value for W will therefore be less than the magnitude of the dislocation density tensor, D (which is equal to ρb), by a stereological factor between 1 and 0 dependent on how dislocation lines are oriented with respect to the sample surface. Averaged over many grains, the most likely value for l_3 can be shown to be 0.5, and thus $W = D/2$, and

W will be of the same order of magnitude as *D* (Wheeler et al., 2009). The WBV at each pixel can be approximated to a crystallographic direction using Miller Index notation, and visualised on inverse pole figure (IPF) plots. Thus, with knowledge of the length of the specific Burgers vector(s), *b*, identified in the microstructure and the average magnitude of the Weighted Burgers Vector, *W*, for a region of an EBSD map, a lower bound for the dislocation density (weighted by a value between 1 and 0 by l_3) can be estimated by rearranging equation (1) to solve for ρ.

3.4.6 Transmission Electron Microscopy

Transmission electron microscopy (TEM) was used to investigate the dislocation structure produced by the replacement reaction. Electron-transparent samples were produced for transmission electron microscopy (TEM) analysis in the Imaging Centre at Liverpool (ICaL) at the University of Liverpool using an FEI Helios 600i dual-beam focussed ion beam (FIB) instrument via a lift out method (Giannuzzi and Stevie, 1999; Tomus and Ng, 2013). Orientation contrast images were used to determine targets for foil preparation using a retractable concentric back scattered electron detector fitted to the FIB instrument using an accelerating voltage of 10 kV and a probe current of 5.5 nA (Fig. 2.1a). Trenches were milled either side of a region of interest using a beam of gallium ions with an accelerating voltage of 30 kV and a high beam current (21–65 nA) to produce foils 1 μm thick (Fig. 2.1b). Foils were then extracted from the bulk sample and attached to Cu supports before further milling to approximately 100 nm to achieve electron transparency, using a 30 kV Ga ion beam with reduced currents (80 pA–2.5 nA), and finished with a low kV (2–8 kV) polish (Figs. 2.1c–f). Bright field TEM images were collected at ICaL, using a 200 kV JEOL 2000FX instrument operating in conventional TEM mode, and a probe aberration corrected JEOL 2100FCs S/TEM instrument operating at 200 kV in bright field scanning TEM (BF-STEM) mode.

3.5 Results

3.5.1 General observations

The low strain metagabbros contain mm-scale porphyroclasts of albite that are surrounded by matrix grains of the same composition that have a grain size on the order of tens of μm diameter (Fig. 3.2a). The metagabbros also contain mafic phases. Large (mm- to cm-scale) clinopyroxene porphyroclasts show abundant evidence for brittle behaviour, commonly fracturing along cleavage planes, and minor hornblende porphyroclasts are also present (Fig. 3.2a). Albite precipitate can locally be observed within fractures in the clinopyroxene grains. Fractures can be tracked across multiple porphyroclasts, indicating all phases present in the original gabbro underwent some degree of brittle fracture (Fig. 3.2b). As previously observed (Wheeler and Butler, 1993), the hornblende is not foliated and therefore appears to be of pre-Alpine, late magmatic origin. Both the clinopyroxene and hornblende porphyroclasts have undergone reaction to actinolite and minor chlorite at their rims, and along fractures and cleavage planes. Neither clinopyroxene or hornblende occur as fine grains. Clinozoisite often occurs in bands or clumps that lie between the clinopyroxene porphyroclasts and the albite porphyroclasts/matrix; fine-grained albite and clinozoisite grains do not tend to be mixed in the matrix. Chlorite most commonly occurs in fractures within the clinopyroxene. Fine scale distribution of secondary phases is described in more detail below. Fracture patterns on the thin section scale follow the geometrical relationship commonly observed in fault rocks. R_1, R_2, P, Y and X fracture arrays can all be observed (Figs. 3.2c & d; Logan et al., 1992), plus cracking along cleavage planes, which is most evident in clinopyroxene porphyroclasts (Figs. 3.2a & b).

3.5.2 Porphyroclastic albite grains

The albite porphyroclasts exhibit a faint sweeping optical extinction pattern, and subgrains can be observed in places. Sections of the porphyroclasts go into extinction at different orientations, so are slightly rotated with respect to one another (Fig. 3.3a). The sections are locally separated by bands of small grains (Fig. 3.3a; see below). The porphyroclasts lack any evidence for zoning, with all grains analysed by semi-quantitative EDS yielding a composition of An_0 (see Appendix 3). This concurs with previous microprobe analysis of grains in higher strain samples that lack porphyroclasts (Prior and Wheeler, 1999). Chemical maps collected during EBSD data collection also show a complete lack of zoning in the porphyroclasts (Fig. 3.4).

Albite porphyroclasts tend to contain abundant reaction products common to greenschist facies metamorphism (clinozoisite, actinolite, and chlorite), although distribution can be variable. These (hydrous) secondary phases, in particular clinozoisite, often grow elongate parallel to twin planes (Fig. 3.3b, black arrows). In the parts of porphyroclast cores where secondary phases are less abundant, the signature of transient microporosity can commonly (but not ubiquitously) be observed, in the form of secondary phase product inclusions, particularly clinozoisite (e.g. Figs. 3.3b & c). The signature of transient microporosity mainly occurs in regions of the porphyroclasts that lack twinning or evidence for fracturing (Fig. 3.3b, white arrow). Bands of secondary phase reaction products, that do not appear to be associated with any specific cleavage plane, can be observed in the porphyroclasts (Fig. 3.3d – note 'curvature' of band, which suggests that this feature is not associated with a crystallographic plane).

This band of second phase inclusions runs through a single albite porphyroclast, and is not associated with a band of smaller albite grains, such as those represented in Fig. 3.5, so does not appear to have formed as a result of fluid influx and precipitation into a fracture in the classical sense.

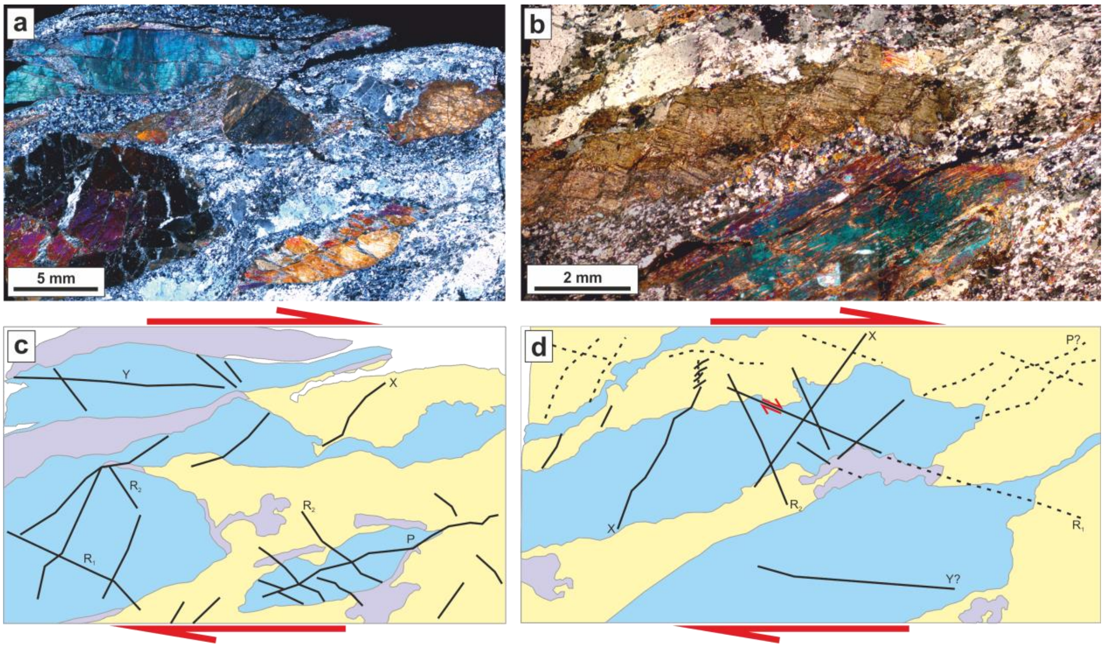

Figure 3.2 *XPL images showing thin-section scale brittle features. a) Large clinopyroxene porphyroclasts and slightly smaller albitic feldspar porphyroclasts dominate the samples. Hornblende is locally present, most often occurring as reaction rims on the clinopyroxene. Actinolite occurs as reaction rims and in between pulled-apart clinopyroxene porphyroclasts. Albite occurs in a bimodal distribution – mm–cm porphyroclasts are surrounded by smaller matrix grains, of the same* An_0 *composition. The fine-grained albite forms part of a mostly two-phase matrix with clinozoisite. The clinozoisite and albite are not well mixed; clinozoisite appears in clumps, often in between clinopyroxene porphyroclasts, or between clinopyroxene and albite porphyroclasts, suggesting fine-grained albite may have been dissolved at sites of highest stress. Albite precipitate occurs within fractures (dilatant sites) in the clinopyroxene porphyroclasts. b) detail of adjacent clinopyroxene and albite porphyroclasts shows through-going fractures across phase boundaries, suggesting all phases in the original coarse-grained gabbro underwent brittle fracture. c) and d) are overlays of a) and b), respectively, showing that the observed fractures follow typical geometries of fracture sets, after Rutter et al. (1986). The coarse distribution of albite (yellow), clinozoisite (purple), and mafic phases (blue) is shown.*

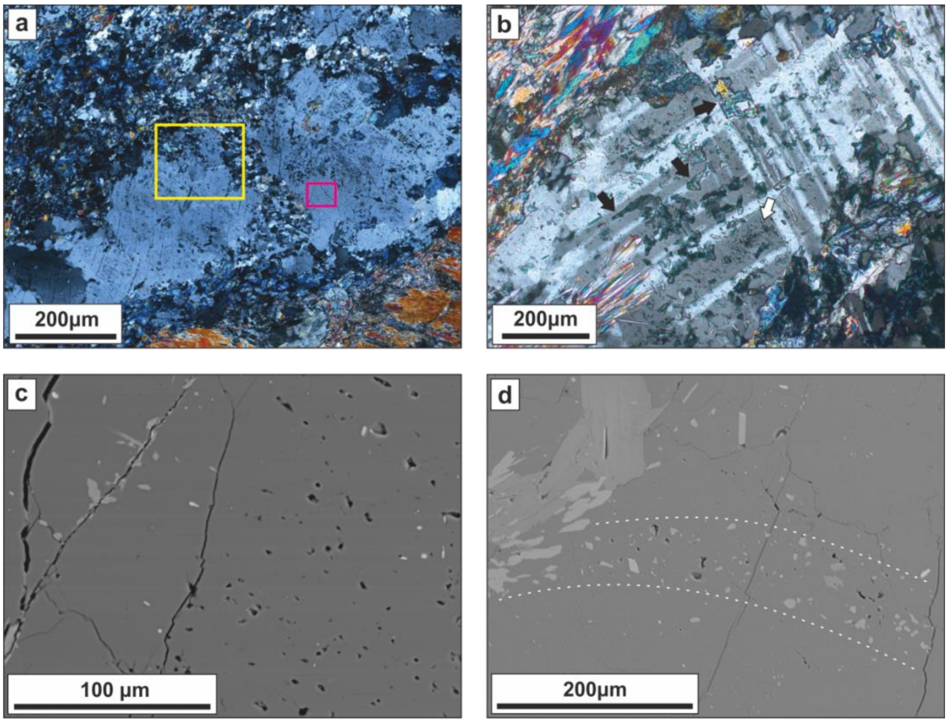

Figure 3.3 *a) Overview of an albite porphyroclast detailed in later figures (yellow box is region shown in Figs. 3.5, 3.6, 3.8 & 3.9; fuchsia box is region shown in Figs. 3.7 & 3.11). Sections of the porphyroclast go into extinction at different times showing they have been rotated with respect to one another, possibly due to through-going brittle fracture. A band of small grains some 100 μm wide cross-cuts the porphyroclast, and abundant inclusions of greenschist-facies reaction products (clinozoisite, actinolite, chlorite) can be observed. A cluster of clinozoisite sits directly below the albite porphyroclast, filling the region between that and a clinopyroxene porphyroclast. XPL; b) Close-up of sets of intersecting twins within an albite porphyroclast, showing secondary phase inclusions (mostly clinozoisite, with some actinolite) that are aligned parallel to and elongate in the direction of the twin planes (black arrows), suggesting that growth of these phases may have exploited cleavage planes (microfractures) in the albite porphyroclast to transport the necessary mafic components (probably in solution). Where twin segments are wider, secondary phase inclusions are observed to be scattered through the segment, recording the existence of transient microporosity within the segment (white arrow). XPL; c) Distributed intragranular microporosity in a large albite porphyroclast, characteristic of interface-coupled replacement reaction products, particularly within feldspars, e.g. Putnis (2015). Some of these 'pores' probably contained second phase inclusions that were plucked during sample polishing. BSE image; d) Curved(?) band of secondary phases (clinozoisite, actinolite) running through the centre of a large albite porphyroclast. Small albite grains are not associated with this band so its genesis is different to the band of small albite grains running through the centre of the porphyroclast in (a). The band is likely to record a fluid infiltration pathway into the original gabbroic (Ca-bearing) feldspar. BSE image.*

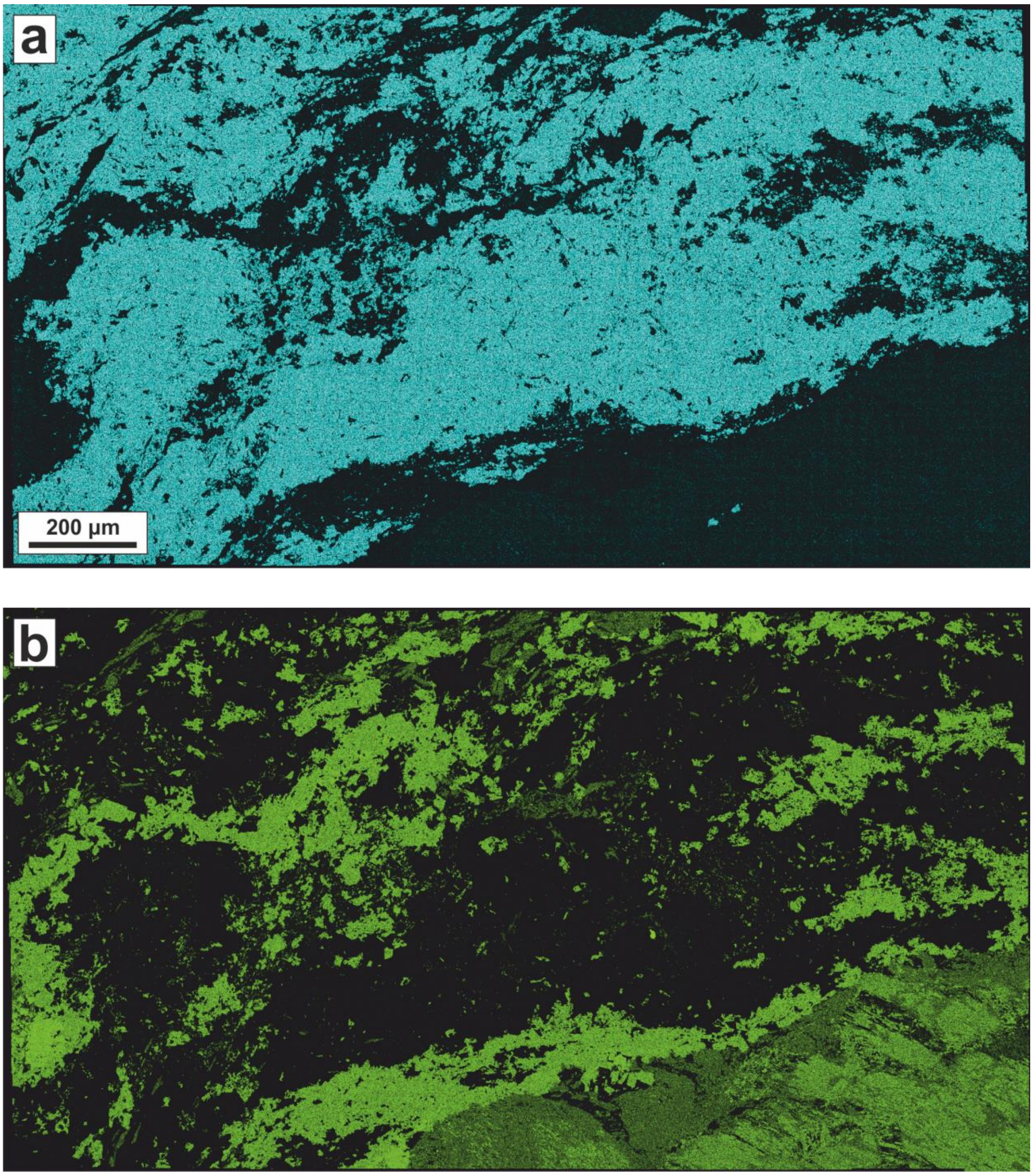

Figure 3.4 *Chemical maps of a) Na and b) Ca distribution in the metagabbros. Compare with Fig. 3.3a and Fig. 3.5 for further details. Note in particular i) the complete lack of chemical zonation in a mm-scale grain, and ii) that the bands of small grains that cross-cut their parent are of exactly the same composition as the parent.*

3.5.2.1 Porphyroclast One

EBSD maps of the porphyroclasts reveal the presence of lattice distortion within those grains. Figure 3.5 shows part of porphyroclast one, which itself contains both wide and fine bands of small grains (see yellow box in Fig. 3.3a; small grains are discussed in detail below). In both types of band, the small grains are primarily bordered by high-angle grain boundaries (fuchsia > 15°; Fig. 3.5). In the core of porphyroclast one, a network of low angle boundaries can be observed (yellow > 2°, lime green > 5°, blue > 10°; Fig. 3.5). 180° twin boundaries plotted in white show distribution of albite twinning (about [010]) within the porphyroclast and small grain population. The low angle boundaries locally create distinct subgrains, but more often occur as a distributed network of subgrain walls that is observed to be pervasive in all analysed porphyroclasts and porphyroclast fragments. Despite the intracrystalline distortion and associated small amount of spread in the distribution, the orientation of porphyroclast one plots as essentially a single crystal on a pole figure (Fig. 3.6a).

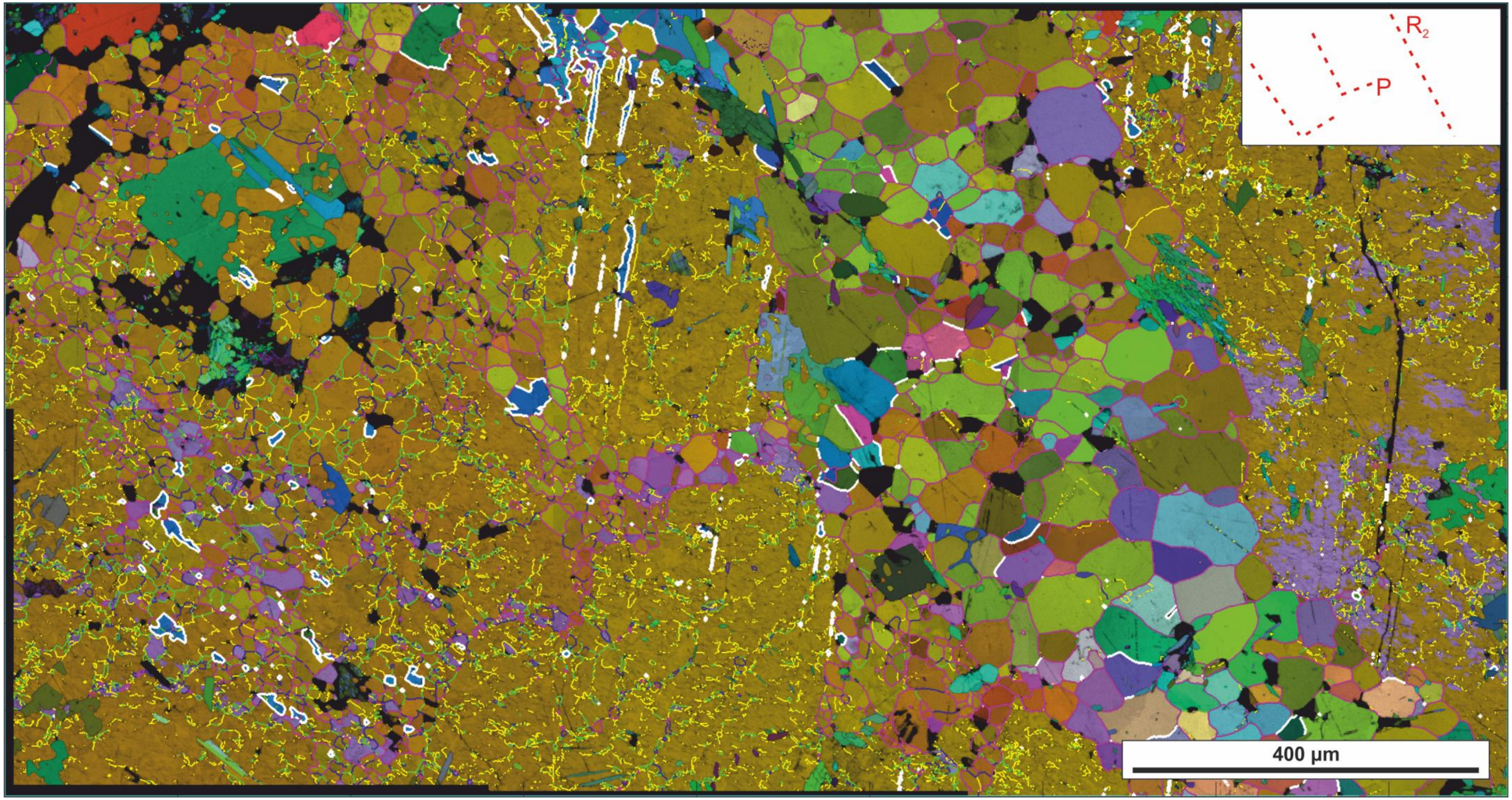

Figure 3.5 *EBSD map of the region identified by the large yellow box in Fig. 3.3a. All-Euler colour scheme. (Sub)grain boundaries are coloured with respect to misorientation across the boundary (yellow > 2°, lime green > 5°, blue > 10°, fuchsia > 15°, white > 160° (which picks out the albite twin)). The core of the sandy-brown porphyroclast is littered with subgrain boundaries with misorientations of 10° or less. The boundaries can be linked to form discrete subgrains, but also occur as distributed networks. Subgrains are most abundant in the top left quadrant of the image. Within the porphyroclast, discrete bands of small grains can be observed; these bands are arranged in orientations associated with the thin section fracture patterns of P and* R_2*, as per the schematic inset. Nearly all the small grains in the bands are surrounded by high-angle grain boundaries.*

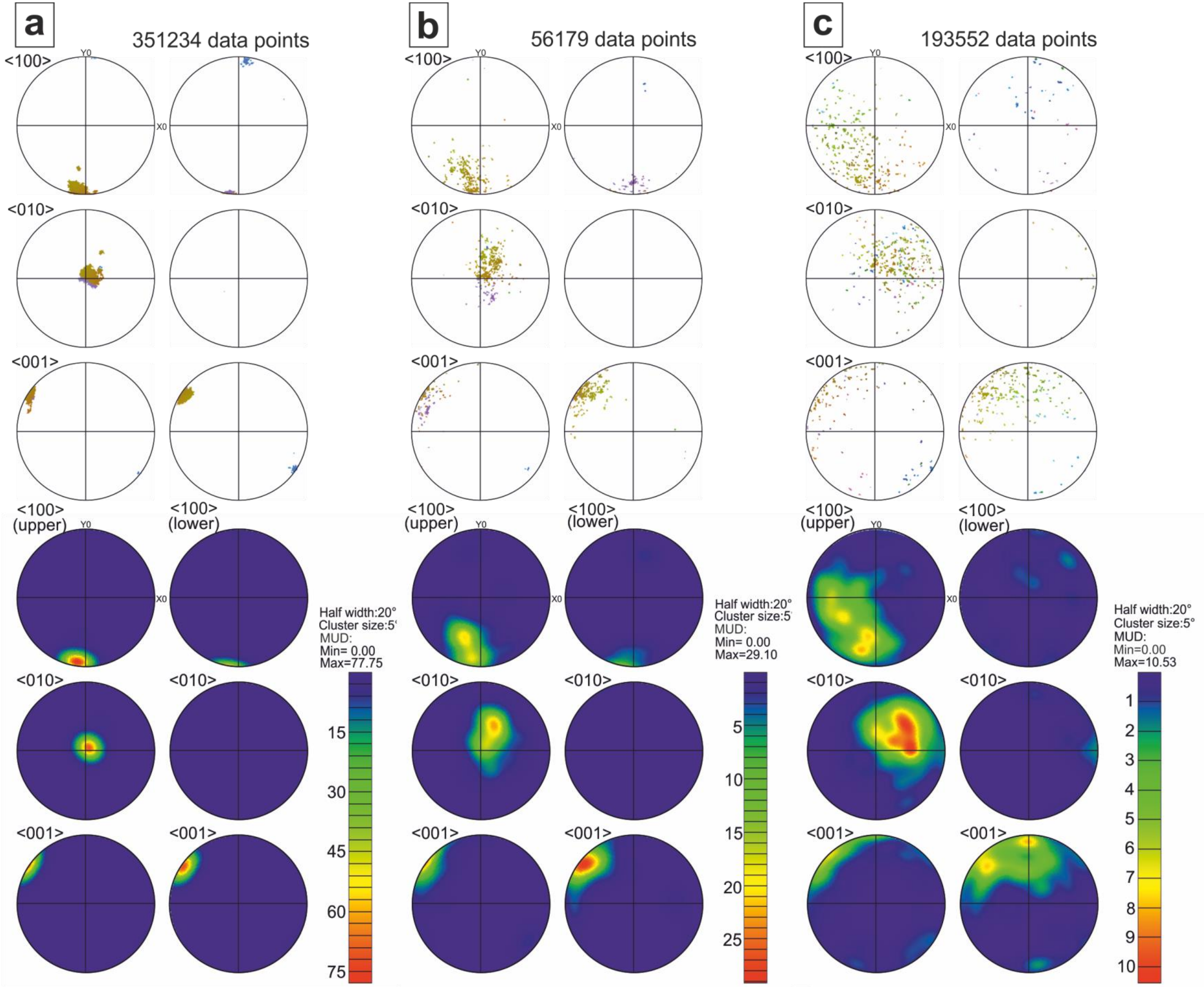

***Figure 3.6** Pole figures showing the orientation relationships between (a) the porphyroclast, (b) the narrow band with right-angle geometry, and (c) the wider band to the right of the field of view in Fig. 3.6a. Upper and lower hemispheres of the principal crystallographic directions are plotted. Directions of each region can be seen to inhabit the same hemispheres and broadly the same quadrants of the pole figures, with dispersion away from a single crystal distribution in the porphyroclast increasing from the smaller to larger band.*

The texture component map shown in Figure 3.7 is taken from the core of porphyroclast one, in a region that lacks bands of fine grains (Fig. 3.3a, fuchsia box), and shows quantitatively the high intragranular distortion observed in all porphyroclasts and porphyroclast fragments. Misorientation occurs over very low angles, often less than a degree, but with some larger steps of a few degrees (i.e. subgrain walls; Fig. 3.7).

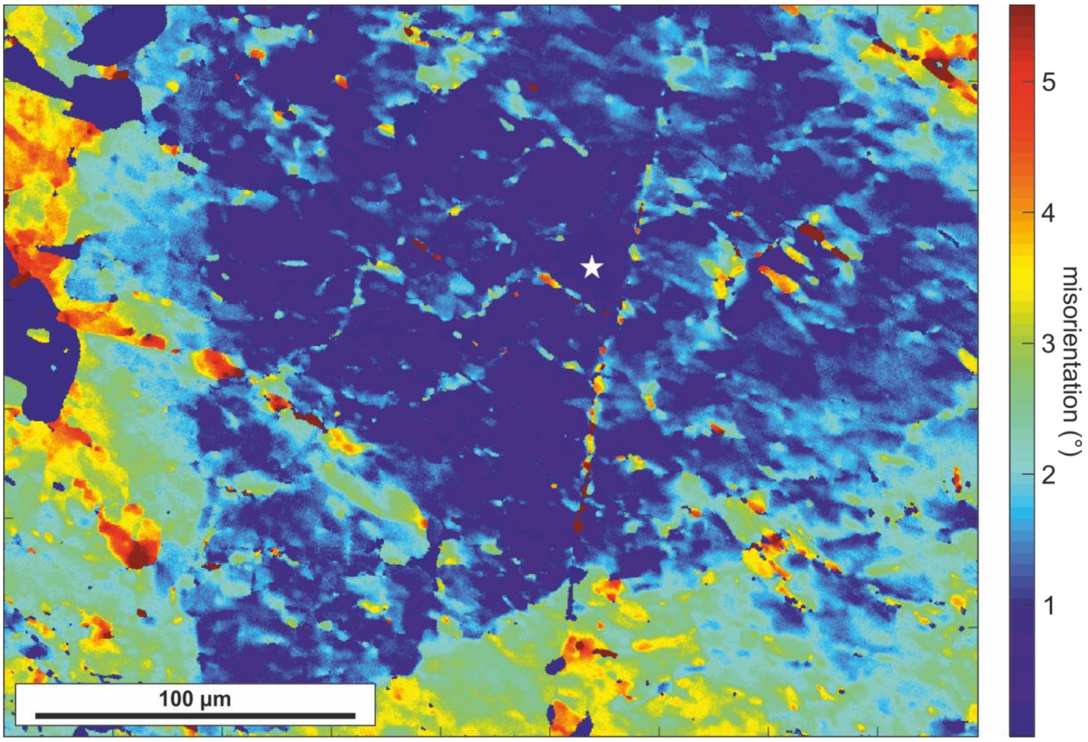

Figure 3.7 *Texture Component map of the region outlined by the fuchsia box in Fig. 3.3a. Misorientation calculated with respect to white star. Dark blue grains to left of field of view are secondary phases.*

Lattice distortion in the porphyroclasts can be quantified by applying the Weighted Burgers Vector (WBV) algorithm to EBSD data (Wheeler et al., 2009). Figure 3.8 displays the calculated magnitude of the WBV, which can be taken as a proxy for dislocation density (note that units for dislocation density and WBV are different; see Wheeler et al. (2009) for details), in a part of porphyroclast one containing bands of new grains (same region as shown in Fig. 3.5; small grains are discussed below). The shortest WBVs are related to the smallest misorientations between pixels, which can be caused by errors in the original sampling. As they are prone to error (Wheeler et al., 2009) the shortest measurements have been removed, so the WBV magnitude displayed is thresholded between 0.008 and 0.036 μm^{-1}. Grain boundaries with misorientations greater than 5° are marked in white. The WBV values in the core of porphyroclast one range between about 0.01 and 0.035 μm^{-1}.

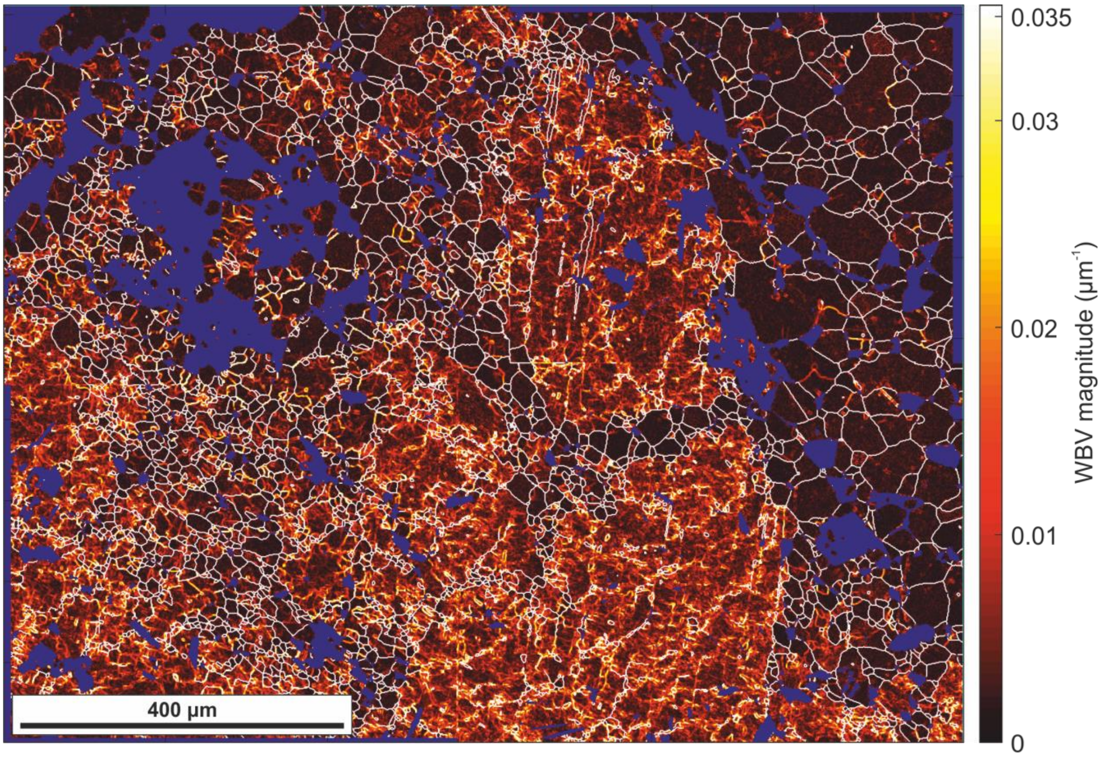

Figure 3.8 *EBSD map showing the magnitude of the Weighted Burgers Vector in all albite grains for the same field of view as Fig. 3.5. Other phases are coloured blue. Grain boundaries with misorientations > 5° are shown in white. The difference in WBV magnitude, which is a proxy for dislocation density, between the porphyroclast and all small grains can clearly be observed.*

An advantage of the WBV method is that possible Burgers vectors of GNDs can be constrained with minimal assumptions (Wheeler et al., 2009). Figure 3.9 shows an EBSD band contrast map of the same field of view as Figure 3.7 (core of porphyroclast one), overlain with WBV crystallographic directions, for those pixels with a WBV magnitude greater than 0.025 µm^{-1}. The map shows a dominance of green pixels, with significant blue pixels also apparent (a range of other pixel colours, i.e. WBV orientations, are also present, as to be expected in a 3D network of dislocations; Fig. 3.10). Pixels in the image have been coloured with respect to crystallographic directions using the IPF colour scheme. Green in this colour scheme indicates the presence of Burgers vectors with a [100] crystallographic direction, and blue indicates [010] (see IPF key, Fig. 3.9 inset, and Fig. 3.10 for IPF plots of the individual lines).

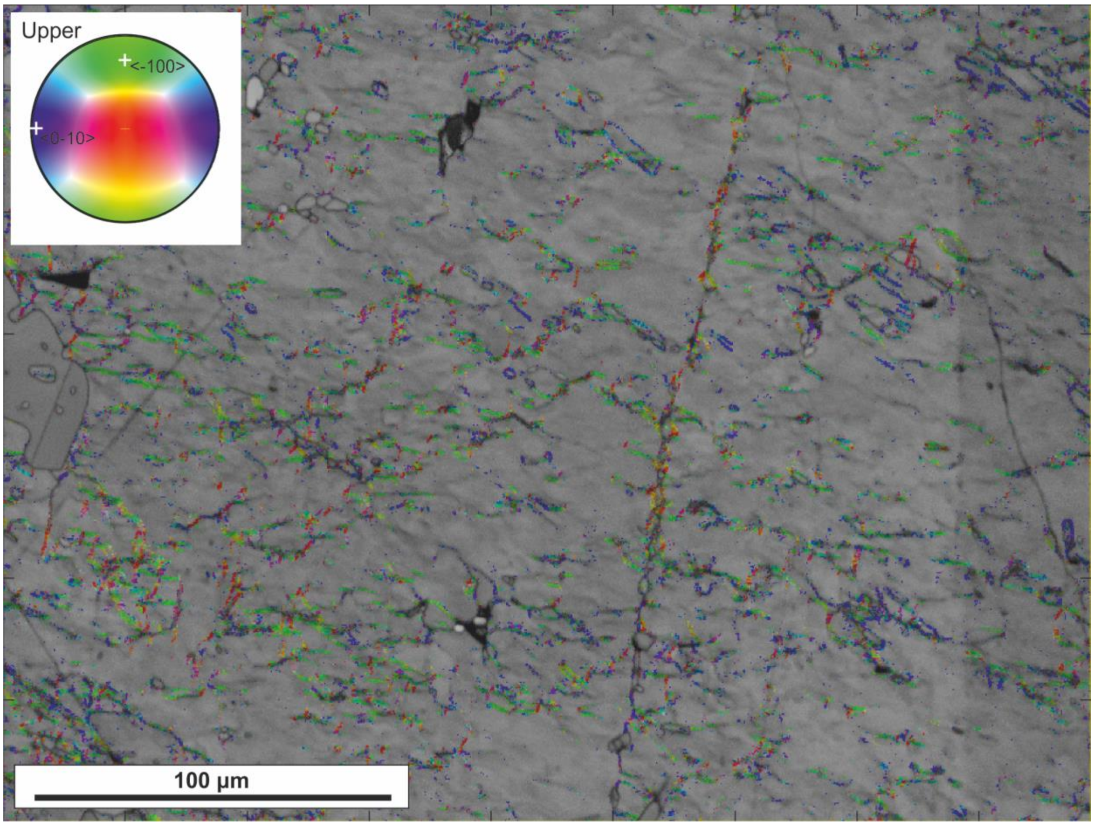

Figure 3.9 *Band contrast map of the core of an albite porphyroclast (fuchsia box in Fig. 3.3a), with directions of most likely Burgers vectors in dislocation structures coloured using the IPF colour scheme. The smallest magnitude pixels have been removed as they are prone to the highest errors. A clear dominance of the [001] and [010] directions can be seen by the abundance of green and blue pixels, respectively. The [010] direction has never been identified as a slip direction in plagioclase feldspar, so the presence of [010] Burgers vectors is taken as evidence that the dislocation population was not produced by slip on crystallographic planes; rather it is believed to develop due to imperfect lattice matchup across the interface during the replacement reaction.*

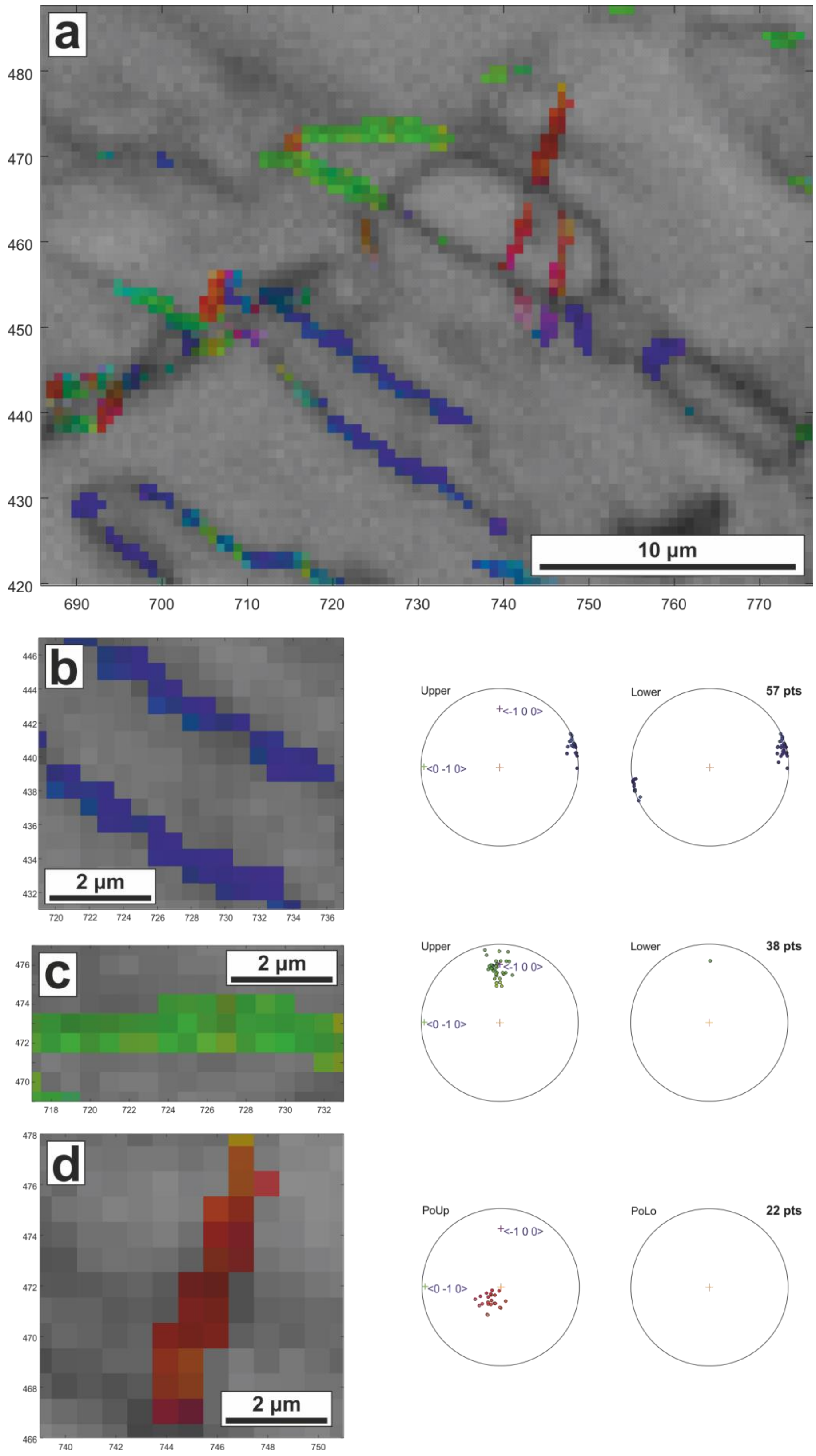

Figure 3.10 *Zoomed EBSD maps showing a) individual lines within the WBV direction plot shown in Fig. 3.9; b) Blue lines correspond to the [010] crystallographic direction; c) Green lines correspond to the [100] crystallographic direction; d) Red lines correspond to the [001] crystallographic direction.*

Two TEM foils were collected from adjacent regions in porphyroclast one; one foil was extracted from the distorted porphyroclast core adjacent to the fine-grained band with dog-leg geometry (see Fig. 3.5), and the other from a distortion-free grain within the band of new grains. Bright-field TEM images show the presence of a high density of dislocations, to which the measured misorientation in the porphyroclast core can be attributed (Fig. 3.11a). Figure 3.11b shows an atypical grain boundary microstructure, where a network of straight, perpendicular grain boundaries (black arrows) are linked to subgrain wall structures (white arrows), which are identifiable as the boundary features made up of rows of repeating small lines.

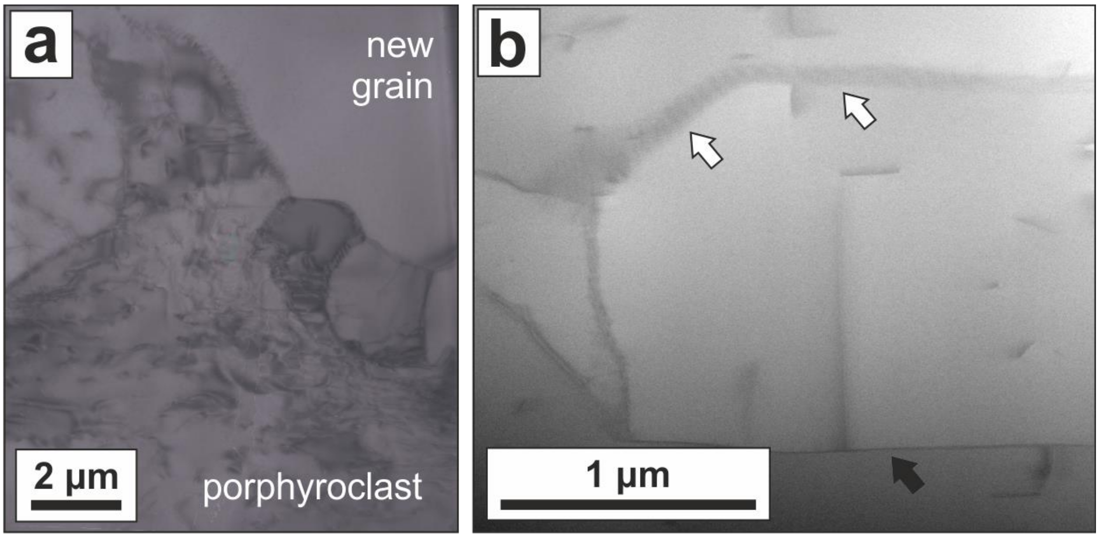

Figure 3.11 *Bright-field TEM images. Foils were cut from the core of the albite porphyroclast in Fig. 3.5, and adjacent small grains. a) A high dislocation density can be observed in the porphyroclast core (lower part of image), compared with a low dislocation density in the small grains. Some boundaries between the grains are composed of ordered dislocations (i.e. subgrain walls). b) Characteristically long and straight disruptions to the lattice in the core of the porphyroclast are indicative of growth defects (Matthews and Blakeslee, 1974), rather than those produced by crystal plastic deformation. Straight grain boundaries with perpendicular geometries (black arrow), and subgrain boundaries that have the same geometries can be observed.*

3.5.2.2 Porphyroclast Two

Albite porphyroclast two is oriented such that the [001] direction is perpendicular to the EBSD map plane, and displays albite twins (twin planes also more or less perpendicular to map plane) that have been disrupted by brittle fracture (Fig. 3.12a). Segments of both

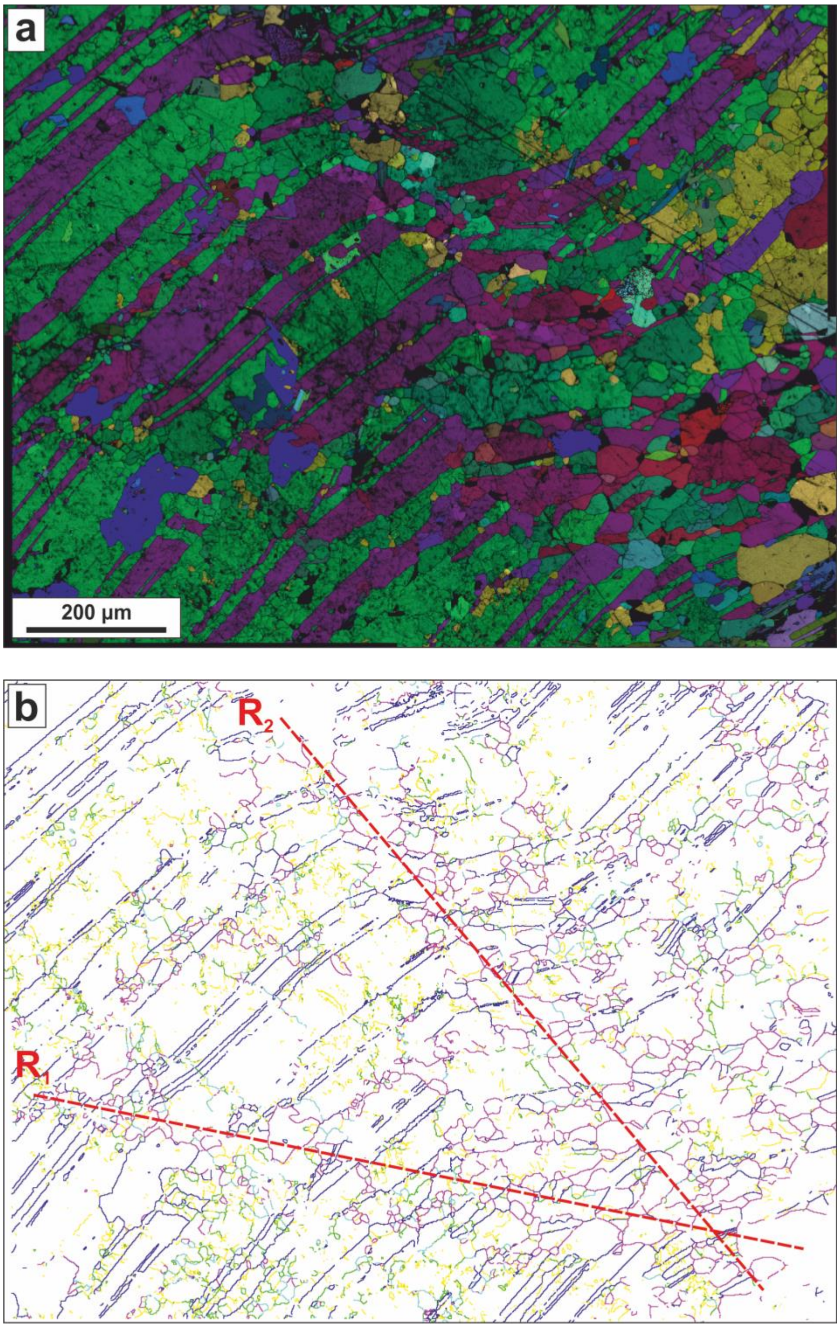

Figure 3.12 *a) EBSD map showing albite porphyroclast two, which displays twin segments that are offset and rotated with respect to one another. The twin segments are separated by small, nominally strain-free, recrystallized grains that inherit the orientation of the parent grain. b) A plot of grain boundaries in the same field of view as (a) shows that bands of small grains, which have high angle grain boundaries, follow a distribution that can be related to the geometry of fracturing at the thin section scale. Where fracture traces intersect, a higher density of small grains with high angle boundaries can be observed. Rows of grains with high angle boundaries are also occasionally present along twin boundary traces.*

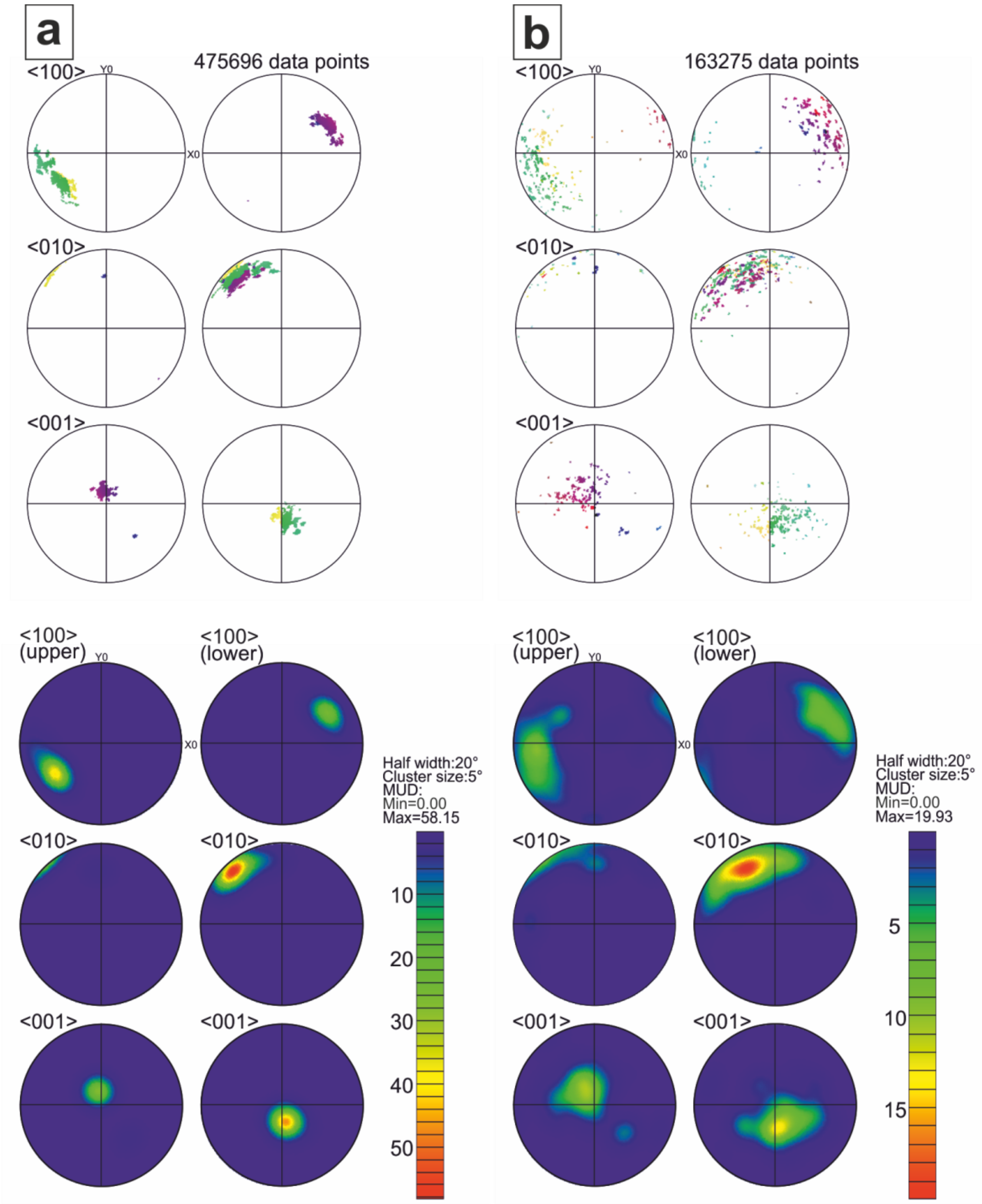

Figure 3.13 *Pole figures constructed from a) porphyroclast two (including rotated fragments), and b) the small grains, shown in Fig. 3.12. The pole figures show an arcuate distribution for the main porphyroclast, due to rotation of fragments produced by brittle fracture, which is broadly followed by the small grain population, with a wider spread. The small grains are thought to be derived from the porphyroclast in this case, so can be seen to inherit the orientation of the parent clast.*

the green and purple twins (coloured with the All-Euler scheme) are offset and rotated with respect to the main NE–SW twin orientations. Bands of small grains (discussed below) mark the boundaries of offset segments. The orientations of these bands of offset are sub-parallel to the R_1 and R_2 trends identified at the thin section scale (Fig. 3.12b). Pole figures constructed from porphyroclast two reflect the offset/rotation observed in the twins, showing an arcuate distribution of the [010] and [100] directions (Fig. 3.13).

3.5.2.3 Porphyroclast Three

Albite porphyroclast three is also twinned, and has escaped through-going fracture by its inclusion in a larger clinopyroxene porphyroclast (Fig. 3.14). Although there are no large fractures in this pseudomorphic region, porphyroclast three has undergone fine-scale fragmentation, or crushing, as best seen in the band contrast map (Fig. 3.14a). Notably, although twin boundaries are not offset in the same way as the grain in Figure 3.12, they do show some evidence of curvature, i.e. migration, into adjacent twin segments (Fig. 3.14b & d). Porphyroclast three has a 'tail' of grains (to the right of the field of view) that appear to have evolved in relation a fracture in the clinopyroxene grain, where clinopyroxene has been fragmented, and relatively large chlorite grains have grown. This tail probably formed from fragments of porphyroclast three, as a signature of the twin orientations can be seen in the population of fine grains (Fig. 3.14b). An actinolite reaction rim that has grown at the original plagioclase-clinopyroxene boundary is a single crystal coloured brown and purple in the all-Euler colour scheme (Fig. 3.14c; the difference in orientation between these two colours is very sight, and is an artefact of the Euler colour scheme). The map shows the single crystal also grows within/through the albite pseudomorph which, because actinolite is a hydrous mineral that only forms in the presence of fluid, may record growth in an interconnected network of pores, microfractures or grain boundaries that were exploited during growth (Noiriel et al., 2010). Clinozoisite has grown throughout the albite pseudomorph, sometimes inheriting and growing aligned to the original plagioclase twin plane (Fig. 3.14d; white arrow). A WBV analysis shows that some segments of the grain display the same kind of intragranular distortion as other albite porphyroclasts (Fig. 3.14e). A strain-free population of small grains within the porphyroclast can also be observed.

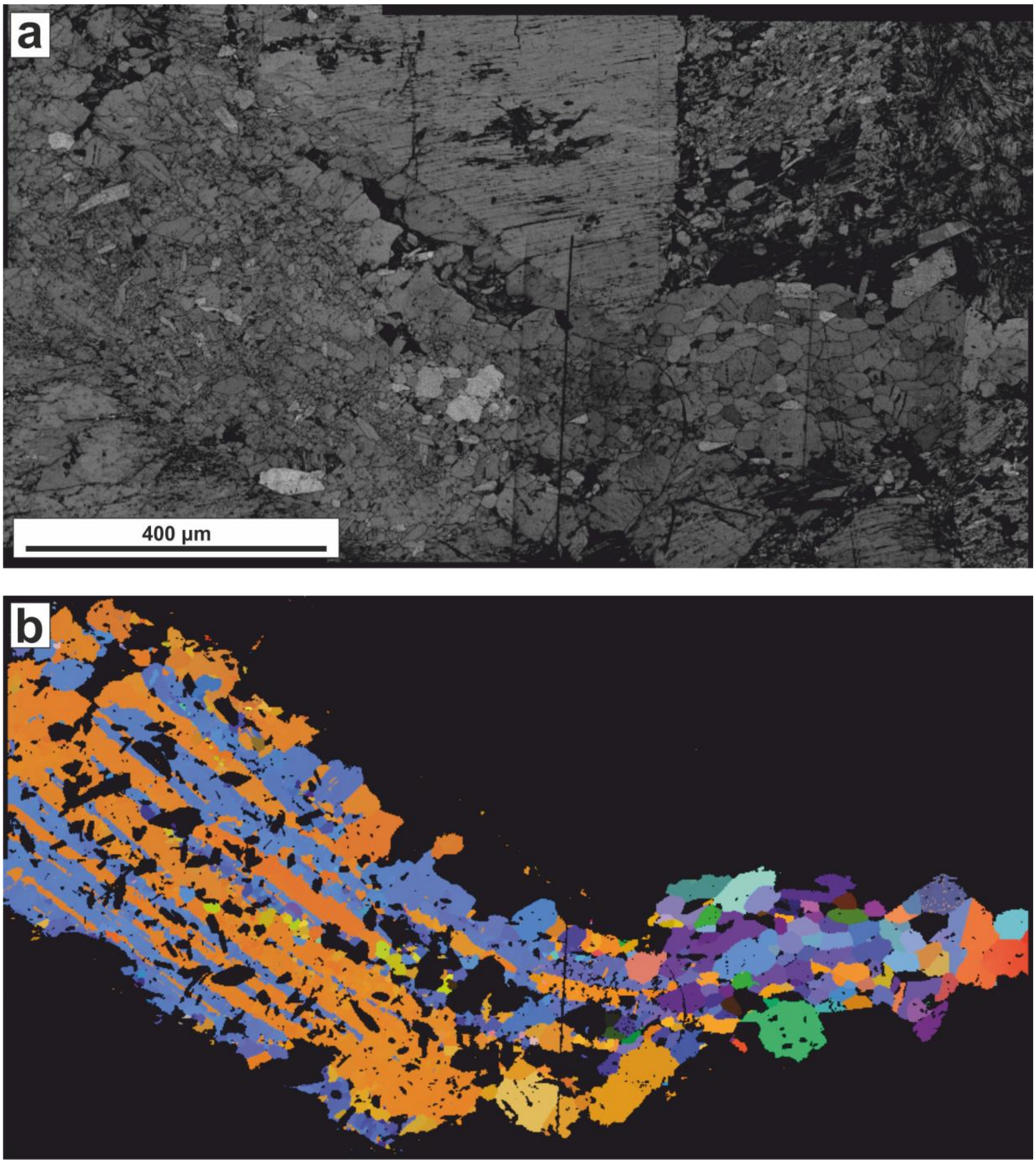

Figure 3.14 *EBSD maps showing a pseudomorphically-replaced feldspar grain with an inherited twinning pattern. The resultant albite is a collection of smaller grains, as seen in (a) the band contrast map and (b) the All-Euler map of albite. The bulk of the grain is protected from deformation by inclusion in a large clinopyroxene porphyroclast, but has a more deformed 'tail', where a dilatant fracture opened in the clinopyroxene. The signature of original twinning can be followed into the tail. Twin boundaries are no longer straight suggesting slight boundary migration has occurred. Continued on next page.*

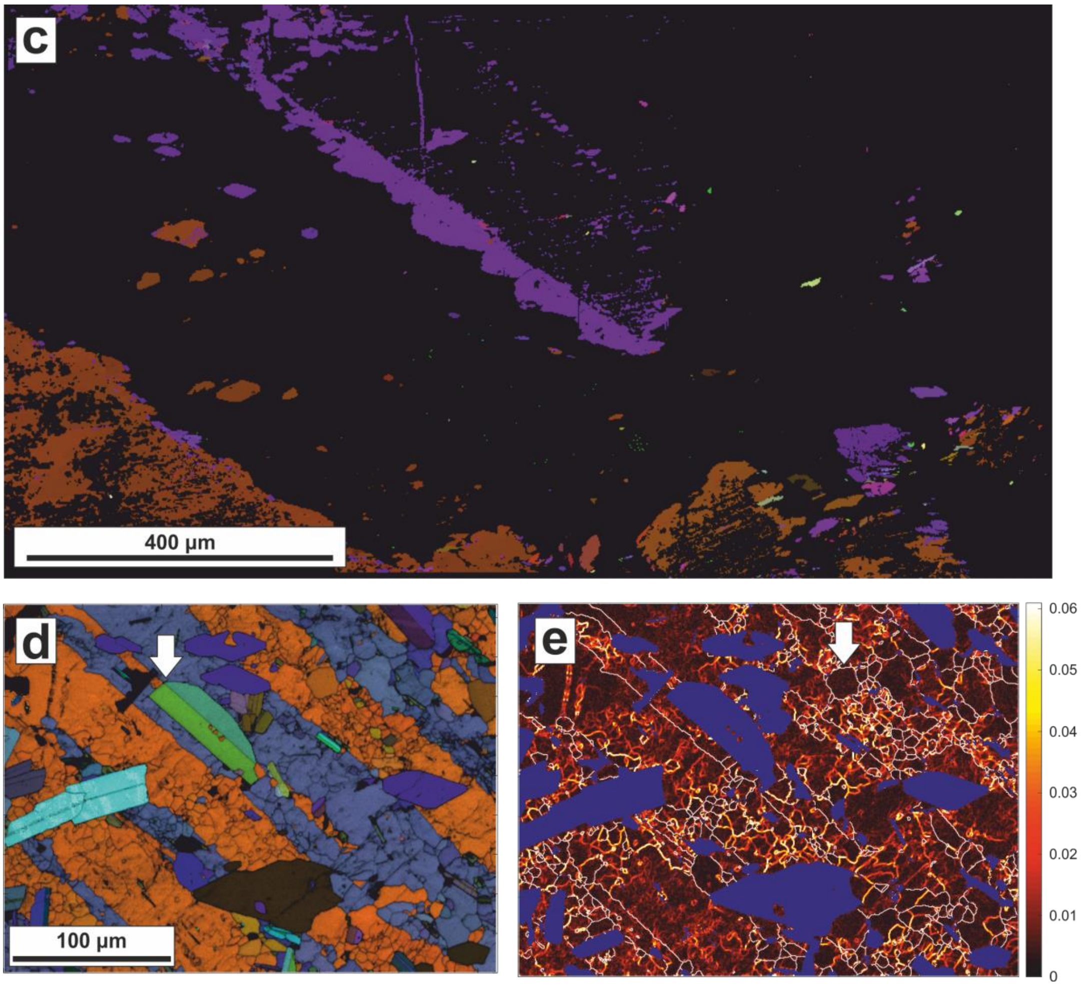

Figure 3.14 continued *c) An EBSD All-Euler map showing only actinolite, which formed as a reaction rim marking the original boundary between the clinopyroxene grain and its feldspathic inclusion. The shared Euler colours show the actinolite is a single crystal that has grown within the albite (colour jump between purple and brown is an artefact of the colour scheme, and only represents a change in orientation of a few degrees max), suggesting the actinolite may have exploited an interconnected pore network (characteristic of interface-coupled replacement reactions) during growth. d) In the All-Euler map, a twinned, green-coloured clinozoisite grain can be observed to inherit the twin plane of the original feldspar (white arrow). Overall the clinozoisite grains do not show any significant SPO within the pseudomorph. e) A WBV magnitude map of the same area as (d) shows higher distortion in parts of the pseudomorph that have not fragmented, and low distortion in small new grains (e.g. white arrow).*

In regions where porphyroclasts have experienced slightly higher strains, they begin to break down. Figure 3.15 shows a field of view in which multiple fragments of the same porphyroclast can be identified by their shared orientation, coloured purple in the All-Euler colour scheme. The fragments contain the same high distortion as other porphyroclastic grains, as identified by the common intragranular network of low angle boundaries (yellow > 2°, green > 5°, blue > 10°; Fig. 3.15a), and high WBV magnitudes (Fig. 3.15b). The fragments are separated by small grains, which, due to their abundance, are no longer constrained to discrete bands. Detailed views show that, where boundary segments of the porphyroclast fragments lie adjacent to small grains with low WBV magnitudes (a proxy for dislocation density), the boundary segment geometry is almost always concave into grains with higher distortion (e.g. white arrows, Fig. 3.16), suggestive of boundary migration driven by stored strain energy.

3.5.3 Small grains

Bands of fine-grained albite and local subgrains, of about the same average size as the matrix grains (mean diameter in bands ~29 μm, mean diameter in matrix ~41 μm), can be observed to cross-cut some albite porphyroclasts (Figs. 3.3a, 3.5 & 3.12). Isolated small grains also locally occur within the porphyroclasts (Figs. 3.5 & 3.12). There is no measureable difference in composition between porphyroclasts and small grains using EDS (Fig. 3.4).

A relatively wide (300–400 μm) band of small grains can be seen to run through the centre of porphyroclast one (Fig. 3.5), which contains small grains with a diameter of up to ~100 μm. In this band, grains are rather equant (i.e. have aspect ratios close to one), and typically exhibit lobate boundaries and 120° triple junctions, suggesting that textural coarsening/growth by boundary migration has occurred. Misorientation profiles across the wide band show that misorientation increases, with respect to porphyroclast orientation, to the centre of the band.

A smaller (50–70 μm-wide) band, with a right-angled bend, runs from the centre-left of the larger band to the top left corner of the field of view (Fig. 3.5). These grains exhibit the same annealed boundary geometries as those in the wider band, but have a smaller grain size, with an average diameter of 30–50 μm. Both bands of grains are predominantly surrounded by high-angle boundaries (> 15°, coloured fuchsia). High angle boundaries that separate small grains from the porphyroclast, defining the edges of both bands, predominantly show curvature into the porphyroclast.

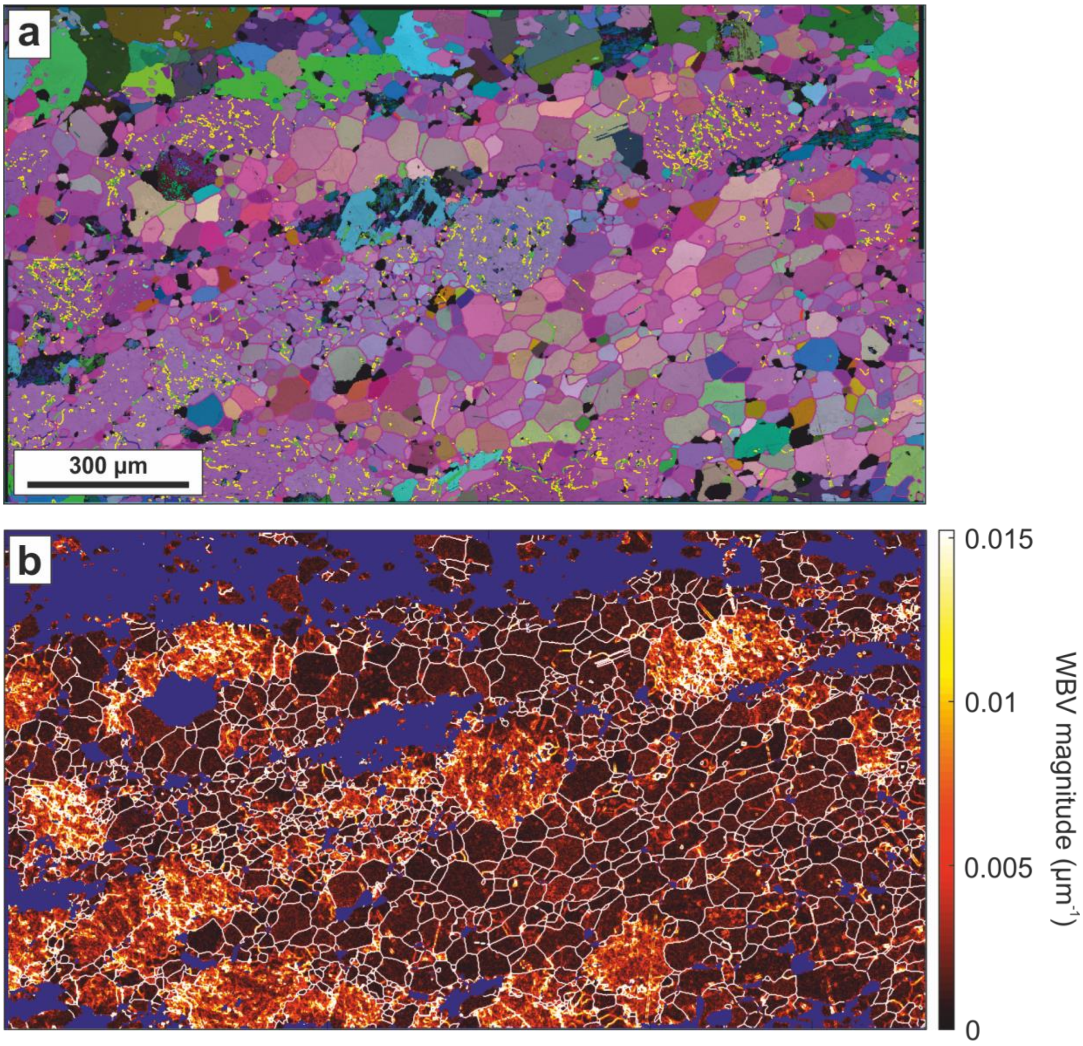

Figure 3.15 *EBSD maps showing the breakdown of albite porphyroclasts to smaller grains. Some porphyroclasts have apparently been dismembered, probably as a result of experiencing higher local strains. a) The All-Euler colour scheme shows that porphyroclast fragments share an original orientation (purple in the colour scheme), and the small grains inherit that orientation similarly to previous examples. b) A WBV magnitude map of the same area reveals high distortion in the fragments . Small grains lack the high WBV values. Detail of the relationship between small grains and porphyroclast fragments is shown in Fig. 3.16.*

The orientations of the traces of the bands of new grains in Figure 3.5 are not associated with common cleavage planes in feldspar. The porphyroclast is oriented such that the (010) plane is parallel to the plane of the map, and the (001) plane runs approximately NE–SW (see pole figures in Fig. 3.9). However, the wide band and two finer bands of small grains are sub-parallel, and oriented so that they may originally have been related to R_2 fractures associated with right-lateral shear deformation (compare with Figs. 3.2a–d) (Logan et al., 1992). The bands that run at an angle of ~90° to the main bands, creating a dog-leg geometry, could be associated with P-orientation fractures (see inset and compare to Figs. 3.2a–d).

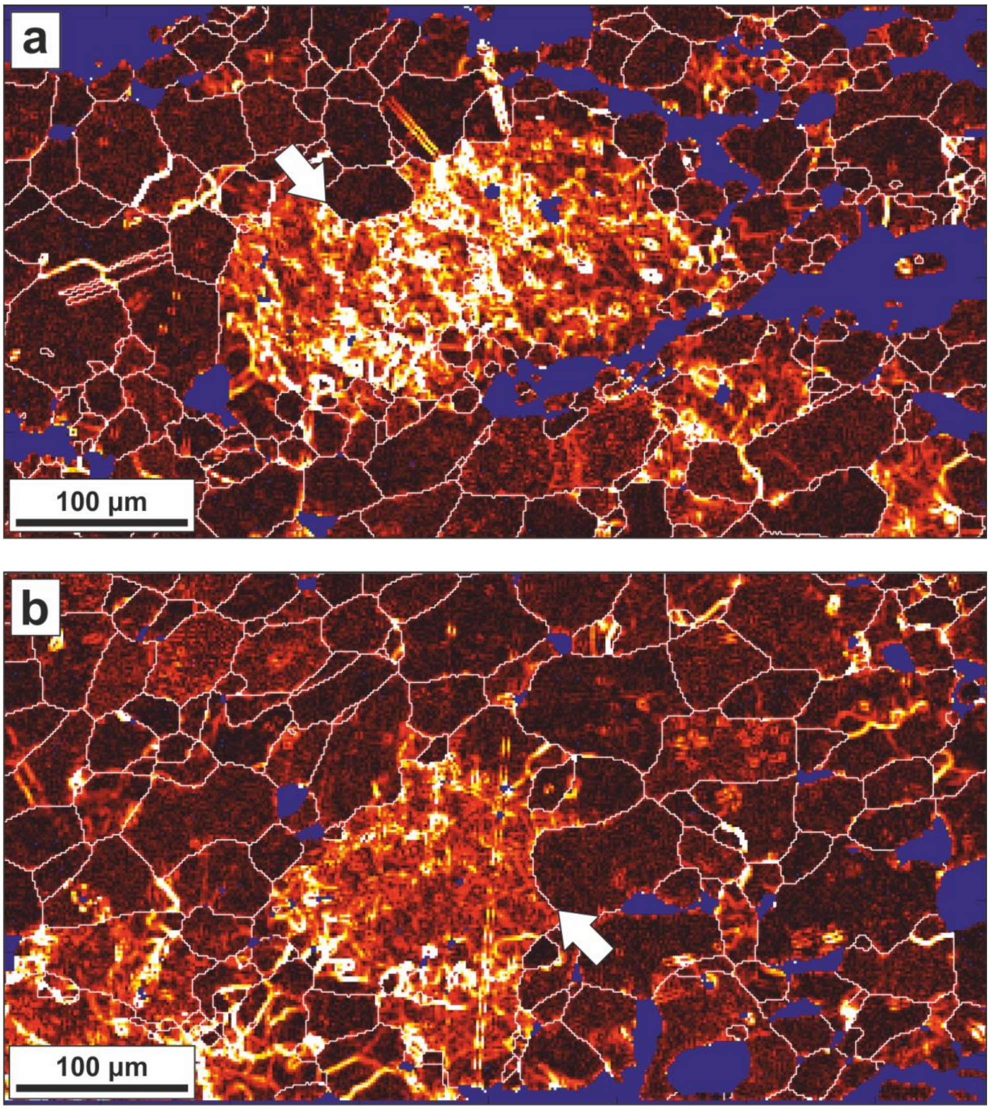

Figure 3.16 *WBV magnitude plots showing detail of two of the albite porphyroclast fragments shown in Fig. 3.15. Nearly every boundary segment shared between a fragment and a new grain is concave into the fragment, suggesting boundary migration driven by a difference in free energy between the highly distorted fragments and mostly strain-free small grains.*

Pole figures constructed from a) the bulk porphyroclast, b) the finer band of small grains and c) the wide band of small grains in Figure 3.5 show the smaller grains broadly share an orientation relationship with the porphyroclast (Fig. 3.6). The clusters of each of the principal crystallographic directions plot in the same quadrant and hemisphere in each set of pole figures (triclinic minerals do not share symmetry across hemispheres). The porphyroclast (Fig. 3.6a) shows a single crystal distribution, which is to be expected, as although they exhibit substantial internal distortion, porphyroclasts remain single large fragments. Small grains in the fine band (Fig. 3.6b) show a spread in orientations away from the porphyroclast orientation, particularly in the [100] and [010] plots. Grains in the wide band (Fig. 3.6c) show a greater dispersion of the clusters in the plots of all three crystallographic directions, but overall orientation geometry is maintained. The twin orientation that occurs in the porphyroclast in Fig. 3.5 can also be seen in, and has probably been inherited by, the small grain population.

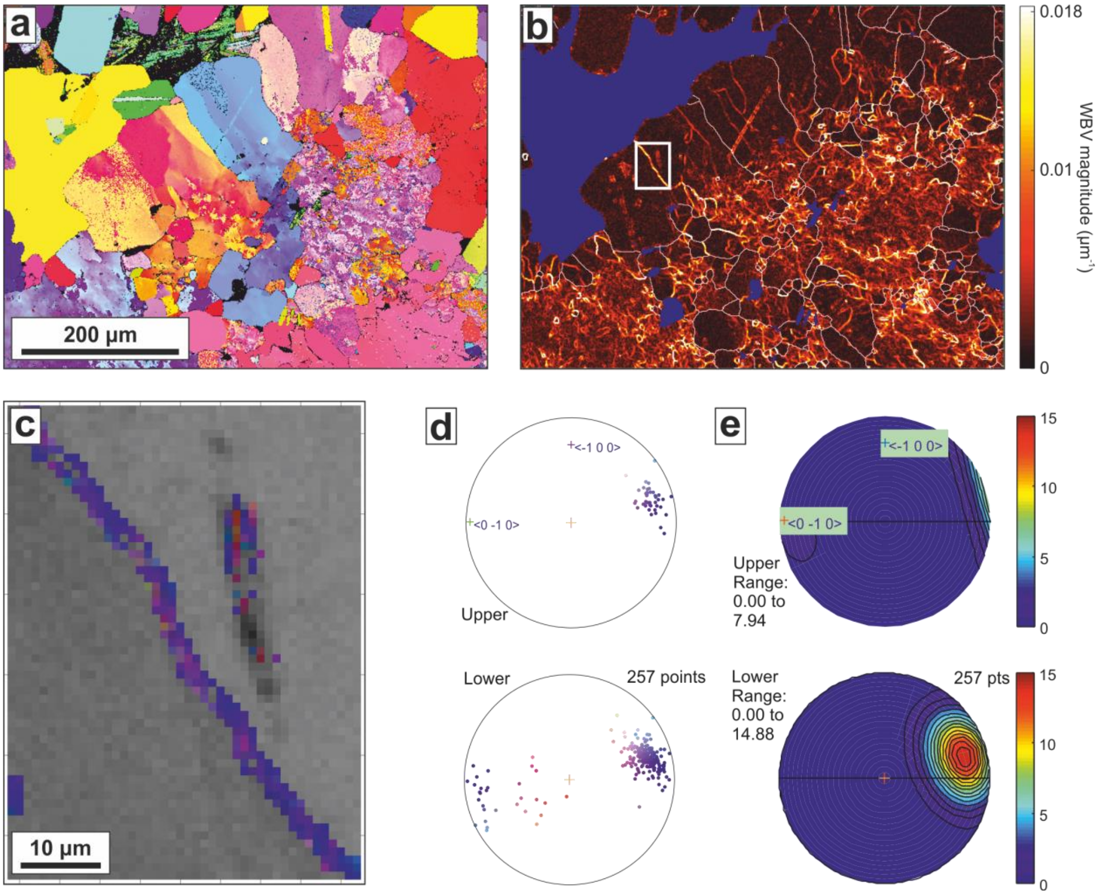

Figure 3.17 *EBSD maps showing growth of albite (sub)grains at porphyroclast grain boundaries. a) Unprocessed IPFZ map and b) WBV magnitude map show the intense distortion in the porphyroclast (mottled colours in a) in general does not continue into new growth at the grain edge, although original grain boundaries and rare subgrain boundaries do propagate into the new growth. c) Subgrain walls are dominated by dislocations with [010] Burgers vectors, most easily visualised in d) point or e) contoured IPF plots.*

In other porphyroclasts, bands of small grains can be observed, although the boundaries of the bands tend not to be as sharply defined (i.e. look less like precipitate-filled dilatant sites). Figure 3.12 shows a porphyroclast whose twins have been right-laterally offset, with portions of twins having been rotated during the shear event associated with brittle fracture. A map plotting only grain boundaries shows that bands of small grains, with high-angle misorientations, separate the rotated twin fragments (Fig. 3.12b). The bands of small grains in the map follow R_1 and R_2 geometries, and where they intersect there is a higher abundance of small grains. Pole figures constructed from this field of view show the small grain population inherits the parent clast orientation, following the same arcuate distribution (which is produced by rotation of twin fragments), but with a wider spread (Fig. 3.13).

Small albite grains and subgrains can be observed to line the borders of porphyroclastic grains (e.g. top left corner of Fig. 3.5; Fig. 3.17). The lattice distortion observed in the porphyroclast in IPF maps (Fig. 3.17a), and in the WBV magnitude plot (Fig. 3.17b) is typically absent in the smaller grains. The fringe of new (sub)grains appears to grow from the distorted porphyroclast shown in Figure 3.17 with little or no misorientation at the contact (i.e. epitaxially), and the grains have the elongate blocky character produced by syntaxial growth in veins (Bons et al., 2012). The [010] Burgers vector dominates the dislocation population that comprises subgrain walls within the grains (Figs. 3.17c–e), which look to have propagated into the new grains during growth on the surface of a distorted parent (Spruzeniece et al., 2017).

In the region of higher strain shown in Figure 3.15, which contains the fragmented porphyroclasts , small grains are significantly more abundant than other regions. Small grains exhibit a weak shape-preferred orientation (mean aspect ratio = 1.6), with long axes oriented in a trace rotated ~30° away from the foliation plane. Porphyroclast fragments are offset along the same trend, which is subparallel to the P fracture trace observed elsewhere in the samples. Two distinct populations of small grains can be distinguished. Between porphyroclast fragments, mostly equant (aspect ratios close to one), small grains (mean diameter ~18 μm) that share a closer orientation to the porphyroclasts and contain some subgrain boundaries can be observed. Slightly larger grains (mean diameter ~29 μm) in the other population are free of the subgrain network, have very low measured WBV magnitudes, and tend to be more elongate, with aspect ratios of 1.5 or above, which may indicate flattening by pressure solution (Figs. 3.15 & 3.16; Wheeler, 2009).

TEM reveals that small grains are relatively dislocation free in comparison to the porphyroclasts (Fig. 3.8). WBV analysis confirms this quantitatively across each data set, with nearly all small grains consistently yielding values $<< 0.01\ \mu m^{-1}$ (Figs. 3.9, 3.14, 3.15, 3.16 & 3.17). Localised isolated small grains also occur within the porphyroclasts. They tend to be smaller than the grains arranged in bands but are surrounded by high angle grain boundaries. The isolated grains yield a similarly low WBV magnitude, which indicates they are nominally strain-free (Wheeler et al., 2009).

3.6 Discussion

3.6.1 Evidence for brittle deformation

Evidence from nature and experiment overwhelmingly points to the fact that (micro)fracturing in feldspar at mid-crustal conditions is ubiquitous (e.g., Kruse et al., 2001; Menegon et al., 2008; Menegon et al., 2013; Stünitz, 1993; Stünitz and Fitz Gerald, 1993; Tullis et al., 1990; Tullis and Yund, 1987; Viegas et al., 2016). At the thin-section scale, multiple features show that albite porphyroclasts in the low strain metagabbros underwent some degree of brittle deformation during shear. The presence of fractures that can be traced across porphyroclast boundaries of different phases (Fig. 3.2) suggests a brittle response in all phases during initial deformation (D_1). The fact that some fractures can be tracked across multiple porphyroclasts shows that overall relative movement of porphyroclastic fragments was limited during deformation (e.g. Figs. 3.2b & d), although the presence of pull-apart structures shows more significant movement occurred in some places (e.g. Figs. 3.2a & c; Fig. 3.15). The fact that the sections of the porphyroclast shown in Figure 3.3a are only slightly rotated with respect to one another, again suggests that although through-going fracture occurred in the albite grains, further rotation of albite fragments was limited at low strains. In other porphyroclasts, rotation of fragments may have been greater, as suggested by twin fragments in Figure 3.12, and associated arcuate distribution in pole figures of this region (Fig. 3.13), where deformation looks to have produced a semi-brittle shear zone. Fragment rotation was probably accommodated without a loss of cohesion through pressure solution processes (see Chapter 4). The largest offsets are accommodated on Y shears, although many fractures show limited movement on this plane. This suggests that comminution by grinding on fracture planes may have been limited and although some fragmentation must have occurred on those planes, this may not be the only method of grain size reduction in the bulk samples.

The pseudomorphic region shown in Figure 3.14 shows evidence for penetrative grain-scale fragmentation (this is best seen in the band contrast image) with little further movement of the fragments, thus preserving the bulk twinning pattern of the parent. Movement of the fragments of the pseudomorph appears to have been restricted by inclusion within the surrounding clinopyroxene porphyroclast, to keep the twin pattern intact. In comparison, where the clinopyroxene itself contains a dilatant fracture, on the right hand side of the map, the albite grains become smeared out into a tail with a much weakened, although still identifiable, twin signature. The penetrative fragmentation is similar to the 'microcrushing' produced experimentally by Tullis and Yund (1987), where the influence of feldspar's two good cleavages promotes ubiquitous grain-scale microfractures. This type of crushing, with limited movement, may also be responsible for producing the relative distribution of phases in microstructures produced by higher strains, where large clinozoisite crystals grow around fragmented albite, with the albite fragment orientations preserving an original twin pattern (Fig. 4.12). Notably, the crushed texture observed in porphyroclast three looks significantly different to the cores of more coherent porphyroclasts, e.g., porphyroclast one (Fig. 3.5), which shows a mottled pattern in a large single grain, as opposed to many small grain fragments (compare Fig. 3.9 with Fig. 3.14a).

3.6.2 Multiple fluid-rock interaction processes

Initial fracturing in plagioclase created pathways for fluid infiltration. Healed fractures (Fig. 3.3d, Fig. 3.5), micro-shears (Fig. 3.12) and cleavage (Fig. 3.3b) all served as fluid pathways. These were heterogeneously distributed, as evidenced by the similarly-heterogeneous distribution of small albite grains and second phase inclusions such as clinozoisite, which were produced by fluid-rock interaction. During initial fracturing, the plagioclase was Ca-bearing, and thus out of equilibrium at greenschist-facies conditions, e.g. Stünitz (1998). Complete replacement to albite must have been relatively fast (see section 3.6.2.1), as no zoning has been preserved in mm-scale albite grains (Fig. 3.4). It is therefore likely that the Ca-plagioclase reacted with Na-rich crustal fluid (Bucher and Stober, 2010) to produce both the large albite porphyroclasts with high internal distortion *and* the population of small grains (Na-rich albite, and Ca-Al-rich clinozoisite). The amount of fluid available via any particular pathway appears to have had a profound effect on the type of fluid-rock interaction that has occurred. The genesis of each grain population is now discussed in turn.

3.6.2.1 Genesis of (distortion in) porphyroclasts

EBSD and TEM results show that the lattices of porphyroclasts are highly distorted (Figs. 3.5, 3.7, 3.8, 3.9, 3.11a, 3.12, 3.15 & 3.16). Whether or not lattice distortion of this kind can be produced by dislocation creep at greenschist facies conditions is an unresolved issue, but the general consensus from nature (Kruse et al., 2001; Menegon et al., 2008; Menegon et al., 2013; Viegas et al., 2016; Wintsch and Yi, 2002) and experiment (Stünitz et al., 2003; Tullis, 2002; Tullis and Yund, 1992; Tullis and Yund, 1987) is that evidence for active slip systems in feldspar is rare at mid-crustal (T ~350–500 °C, P ~400–500 MPa) conditions. However, the parameters outlined in Rybacki and Dresen (2004b), and the observation that albite in the middle crust is commonly ‘wet’ (i.e. the middle crust will have a high water activity; Yardley and Bodnar, 2014), suggest a more complex picture. Deformation mechanism maps for wet albite constructed using the parameters in Rybacki and Dresen (2004b) suggest that for the conditions i) grain sizes greater than a few hundred μm, ii) common differential stresses in the crust (on the order of tens to hundreds of MPa; see table in appendix of Wheeler, 2014), and iii) natural strain rates (10^{12}–10^{-16} s^{-1}), dislocation creep can contribute towards deformation in feldspar at 400–500 °C (Fig. 1.2). Shigematsu and Tanaka (2000) presented evidence for low temperature (below 500 °C) plasticity in ultramylonitic feldspar from the Hatagawa fault zone in NE Japan. However, they based their argument for crystal plasticity primarily on the observation of CPOs, but it has been shown that CPOs can develop via other mechanisms such as microfracturing in feldspar (Tullis and Yund (1987); see also Chapter 4). The distributed dislocations in the metagabbroic samples, which have not been rearranged into low energy configurations, suggest dislocation climb (and therefore mobility) was restricted in our samples, and so dislocation creep played only a minor role in deformation.

The generation of dislocations by microfracturing in plagioclase has been described in detail by Stünitz et al. (2003). Those authors suggested some deformation bands with a high dislocation density could represent healed cracks, due to the observation of nanoscale pores associated with the bands observed in TEM. In addition, glissile dislocations are reported to be able to propagate into a bulk crystal from high dislocation density regions around fractures, and may help catalyse the transition from brittle to plastic deformation in plagioclase. The TEM investigations in this study did not record porosity in regions of high dislocation density. However, the TEM foils degraded quickly under beam energy so we cannot completely rule out the presence of porosity. In addition, the signature of transient microporosity (i.e. intragranular product phase inclusions not associated with fractures) was observed in some regions of the porphyroclasts using optical microscopy (Fig. 3b–c), although this does not tend to be associated with obvious fracturing, and is interpreted to have been generated during the replacement of Ca-bearing plagioclase with albite (see below).

The lattice distortion in the large albite grains is not interpreted to be inherited from deformation at higher grades as i) there is no evidence that the rocks of the GSZ ever experienced higher deformation conditions than greenschist facies (Prior and Wheeler, 1999; Wheeler and Butler, 1993), and ii) there has been a metamorphic transition from Ca-bearing plagioclase to pure albite at greenschist facies, which is expected to erase any pre-existing lattice distortion. The WBV technique resolved the presence of the [010] crystallographic direction in the Burgers vector population (Fig. 3.11; Fig. 3.17c). This is not a direction that has previously been identified in plagioclase slip systems e.g. (Stünitz et al., 2003), so is taken as further evidence that the dislocation network is not derived from crystal plasticity. The geometries of (sub)grain boundaries observed using TEM (Fig. 3.11b), that are long and straight, and intersect at an angle of 90°, also suggest they did not form by crystal plasticity.

A complete lack of zoning in the porphyroclasts (Fig. 3.4) suggests that the removal of Ca from plagioclase was efficient and relatively fast, and indicates a different genesis for the large, distorted albite porphyroclasts. Lattice diffusion of Ca can be discounted as an explanation for the lack of zoning, due to the extremely low value of the interdiffusion coefficient, D, for CaAl-NaSi coupled substitution (required in the transition from Ca-bearing plagioclase to albite), at mid-crustal conditions. Experimentally derived values for this interdiffusion coefficient over the temperature range 1100–1400 °C, and at 0.1 MPa, are found to follow the Arrhenius relation $D = 1.099 \times 10^{-3} \exp(-517 \pm 21 \text{ kJ/mol})$ $\text{m}^2\ \text{s}^{-1}$ under anhydrous conditions (Grove et al., 1984). At 1100 °C, this yields a D of $\sim 10^{-23}$ $\text{m}^2\ \text{s}^{-1}$, and this temperature is substantially higher than the 350–500 °C temperature range of the middle crust, meaning lattice interdiffusion would be more sluggish at greenschist facies conditions (Cherniak, 2010). Thus, lattice interdiffusion preserves zoning in grains of μm to mm size over tens of Ma timescales (the timescale over which the Gressoney Shear Zone was active; Reddy et al., 1999), so we discount it as a viable mechanism for albitisation of the original plagioclase porphyroclasts.

Fast chemical equilibration in the fluid-rich conditions of the middle crust, and the presence of intragranular lattice distortion not derived by crystal plastic processes, suggest that the porphyroclastic grains have formed by a fluid-assisted interface-coupled dissolution-precipitation reaction (Putnis, 2002; Putnis, 2009; Putnis and Putnis, 2007). When metastable solids come into contact with fluids, dissolution can occur, causing the fluid to become supersaturated with respect to a more stable solid phase, which, depending on nucleation kinetics, may then precipitate. Nucleation is favoured (i.e. the energy budget is lower) when a product phase shares a similar crystallographic structure to the parent phase, so that new grains can nucleate on the surface of the dissolving parent grain (Putnis and John, 2010; Putnis and Putnis, 2007). This process is termed epitaxy (i.e. crystal growth on a crystal substrate that determines orientation; Matthews, 1975), and leads to the product inheriting the orientation of the parent, as we see in the pseudomorphic grain (Fig. 3.14). As the product phase precipitates, components of the solute are removed from the fluid, which increases the driving force for dissolution of the parent. Enhanced dissolution of the parent leads to enhanced precipitation of the product, until a steady state dissolution-precipitation rate is reached (Putnis and Putnis, 2007), and a topotactic replacement (i.e. the conversion of an existing single crystal into a crystal product which shares a crystallographic orientation with respect to the original crystal; Shannon and Rossi, 1964) occurs. Experimental replacement of oligoclase and labradorite (i.e. Ca-bearing plagioclase) to pure Na end-member albite has been performed in an ^{18}O-enriched Na- and Si-bearing solution (Hövelmann et al., 2009). Oxygen isotope redistribution during these experiments has shown that the original Ca-bearing plagioclase framework breaks down entirely during replacement and new albite grains precipitate from the fluid, as opposed to the rearrangement of cations via some mechanism of enhanced ionic diffusion through an intact lattice. A Ca-bearing phase, pectolite ($NaCa_2Si_3O_8OH$), is also produced (Hövelmann et al., 2009), similar to the clinozoisite produced in the natural samples of this study.

For the reaction to proceed and go to completion, fluid pathways to the reaction interface must be kept open. Transient porosity is therefore a key control in the evolution of fluid-assisted reactions. Porosity can be generated by two means. Firstly, if the replacement is pseudomorphic, i.e. the original shape and dimensions are preserved, but the new phase has a smaller molar volume, as a necessity, porosity will be generated (e.g. Fig. 3.7; Putnis, 2009). External dimensions and crystallographic orientations across replacement interfaces have been observed to be preserved in feldspar reactions (Engvik et al., 2008; Hövelmann et al., 2009; Putnis, 2002; Putnis and Putnis, 2007), and there is a small molar volume decrease from Ca-bearing plagioclase to albite, relative to a fixed number of oxygens, e.g. for comparison, the molar volumes of anorthite and albite are 100.73 ± 0.15 and 100.21 ± 0.19 $cm^3\ mol^{-1}$, respectively (Smith, 1956). In fact, the balancing of replacement reactions depends on which elements are considered to be mobile. For the transition from oligoclase to albite, Al is generally assumed to be immobile (Putnis, 2009), so can be written:

$$Ca_{0.22}Na_{0.74}K_{0.04}Al_{1.22}Si_{2.78}O_8 + 0.59Na^+_{(aq)} + 0.59OH^- + 1.21SiO_2$$

$$\rightarrow 1.22NaAlSi_3O_8 + 0.11NaCa_2Si_3O_8OH + 0.04K^+_{(aq)} + 0.04OH^- + 0.22H_2O$$

but in reality, this would lead to a large volume increase, so pseudomorphism would not be maintained. It is possible to rewrite this equation so the volume is balanced, if more material is lost to fluid, as:

$$Ca_{0.22}Na_{0.74}K_{0.04}Al_{1.22}Si_{2.78}O_8 + 0.59Na^+_{(aq)} + 0.59OH^- + 0.55SiO_2 + 0.22H_2O$$

$$\rightarrow NaAlSi_3O_8 + 0.11NaCa_2Si_3O_8OH + 0.22NaAl(OH)^0_4 + 0.04K^+_{(aq)} + 0.04OH^-$$

(both versions of the reaction are taken from Putnis et al., 2009). In either case, experiments that use ^{18}O to track how intact the plagioclase crystal lattice remains during interface-coupled reactions suggest the entire lattice breaks down and is reconstructed during replacement, meaning Al is not immobile. Growth of product grains could therefore fill all pores, so a second mechanism of porosity generation during replacement reactions is required. If more solid is dissolved than precipitated, then this will also result in development of porosity (Putnis and Putnis, 2007). It is likely the dominant mechanism of transient porosity generation was more solid being dissolved than precipitated in the studied samples.,

Replacement can occur across tens of km^2 if the reactions proceed by either or both of these porosity-generating mechanisms (Plümper et al., 2017). In the cores of porphyroclasts in the samples, where fewer secondary phases are present (indicating less fracture), intragranular microporosity, and intragranular product phase inclusions that record transient porosity, characteristic of interface-coupled replacement reactions is observed (Figs. 3.3b, white arrow, & 3.3c; Putnis, 2015). In addition, the actinolite grain that has grown as a single crystal, wrapping around and through the twinned albite pseudomorph, suggests that a network of interconnected pores existed in that grain during the replacement of Ca-bearing plagioclase to albite, which the actinolite crystal exploited for growth (Fig. 3.14c). Some porphyroclastic grains show only small regions of microporosity (tens of μm; Fig. 3.3b), others can be quite large (hundreds of μm; Fig. 3.3c). The extent of microporosity appears to depend on the amount of (micro)fracturing that occurred in each region, i.e. where fracture was common, fluid availability was high so traditional dissolution and precipitation occurred, and where fracture was rare, less fluid was available, so interface-coupled replacement in a nm-thin film of fluid occurred; hence the low-density cores of porphyroclasts tend to be where replacement reaction indicators are found. These observations suggest that the likely mechanism of porphyroclast formation in less fractured regions of the original plagioclase grains was via interface-coupled replacement reaction. The same reaction is concluded to have occurred in all porphyroclasts or porphyroclast fragments that escaped fracturing (thus limiting available fluid), including undamaged twin segments (Fig. 3.3b, Fig. 3.14e).

Dislocation generation in the replacement reaction scenario can be explained as a result of imperfect replacement, due to a lattice mismatch between Ca-bearing plagioclase and pure albite. This type of growth defect, which is characteristically long and straight (as those observed using TEM; Fig. 3.11b), are well-known in the materials science community, and are termed misfit dislocations e.g. (Matthews and Blakeslee, 1974). A lattice misfit during epitaxial/topotactic growth can be accommodated either by misfit dislocations, or by misfit elastic strain, or a combination of both (Jain et al., 1997; van der Merwe, 1991; Vdovin, 1999). Growth defects would effectively be ‘frozen in’ to the albite microstructure as slow diffusion rates restrict the climb (from one lattice plane to another), and recovery (rearrangement into low-energy configurations), of dislocations in feldspar at the formation conditions of the middle crust (Tullis, 2002).

Mukai et al. (2014) demonstrated that the initial fluid infiltration that is required for a replacement reaction can occur along phase boundaries in the absence of cracking. In this case, a reaction rim is commonly formed along the phase boundary, such as the actinolite rim observed in Figure 3.14. The distribution of clinozoisite between clinopyroxene and albite indicates initial fluid infiltration probably occurred by this mechanism (Fig. 3.2). Where second phases grow parallel to twin planes in porphyroclasts, it is likely that fluid exploited cleavage planes syn- or post- brittle deformation (Fig. 3.2d, Fig. 3.14d – white arrow). Hence, cleavage planes are likely to be the pathways that fed fluid, required for interface-coupled replacement reactions, to the centre of grains. However, replacement reactions did not occur along such pathways, as the presence of the pathways, and fluid flux within them, promoted traditional dissolution and precipitation. Interface-coupled replacement only occurred in the absence of (micro)fracture, by a nanoscale fluid film migrating through a coherent crystal. The migration of this reaction front preserved the parent plagioclase orientation topotactically, and left behind characteristic intragranular lattice distortion and signatures of transient microporosity.

In summary, despite the absence of a preserved reaction front due to reactions going to completion, the process of interface-coupled replacement was identified in the samples using the following criteria:

1. A lack of zoning in a phase where it is otherwise common, indicating ehanced reaction kinetics (Putnis, 2009; Fig. 3.4).
2. Observation of intragranular microporosity or the signature of transient microporosity (and second phase inclusions which share orientations with twin and cleavage planes of porphyroclasts) (Putnis and Putnis, 2007; Fig. 3.3; Fig. 3.14d).

3. The preservation of crystallographic orientation during complete replacement of parent grains (Hövelmann et al., 2009; Fig. 3.12; Fig. 3.14).
4. Observation of a highly distorted lattice when intracrystalline lattice distortion is not expected at the conditions of deformation (Engvik et al., 2008; Hövelmann et al., 2009; Fig. 3.5; Fig. 3.7; Fig. 3.14).
5. Unusual geometries of subgrain walls and Burgers vectors not identified as active in crystal-plastic deformation of the mineral under analysis (Fig. 3.9; Fig. 3.11).

These criteria can be applied to any other replacement system. Their application could allow the products of replacement reactions to be identified even when complete replacement on a regional scale (e.g., Plümper et al., 2017) has taken place.

3.6.2.2 The presence of subgrains

Optically, subgrain features can locally be observed. Tullis and Yund (1987) suggested microcrushing can lead to patchy extinction that resembles subgrains but dynamically recrystallised subgrains are not produced at low temperatures. The temperature of deformation suggests dislocation climb was not active in the albite porphyroclasts (Tullis and Yund, 1985), so that observed subgrain walls (upper left of Fig. 3.5, around the diamond-shaped, green-coloured clinozoisite inclusion; white arrows, Fig. 3.11b; Fig. 3.17) are unlikely to have formed by the reordering of distributed dislocations into lower-energy configurations (i.e. recovery; White, 1977). Instead, the subgrain structures could have been produced by two mechanisms:

(1) Fracturing of initial large feldspar grains may have resulted in the formation of fragments which have undergone a small amount of rotation, and then served as nuclei for a new population of small albite grains that have grown with low misorientations between them. Nucleation by small fragments has been proposed as a mechanism of dynamic recrystallisation in feldspar by Stünitz et al. (2003), but those authors did not observe subgrains being produced in this way, only grains with high-angle boundaries, and suggested that the process could explain a lack of host control on orientation in resultant small grain populations. It is conceivable, however, that limited movement on fracture planes may inhibit rotations, and low angle misorientations could form by this mechanism. Indeed, Tullis and Yund (1987) suggested that subgrains observed at low temperatures may have formed by cataclastic flow.

(2) The topotactic growth of two adjacent nuclei with a small difference in orientation has been shown to produce subgrains during experiments on interface-coupled replacement (Spruzeniece et al., 2017). It is conceivable, from the geometry of the subgrains shown in Figure 3.17, that subgrain boundaries have propogated into new grains during epitaxial growth on a distorted substrate. However, replacement reactions tend to leave behind intragranular microporosity and create lattice distortion during growth, as observed in the porphyroclastic grains, and neither of these features are observed in the grains shown in Figure 3.17. WBV magnitude maps also show low values for lattice distortion in the subgrains in Figure 3.8. These observations make it unlikely that the subgrains formed by interface-coupled replacement, and indicates at least two mechanisms of fluid-rock interaction happened in tandem during coupled metamorphism and deformation, to produce large distorted porphyroclasts and small, distortion free grains. The distribution of small grains with high angle boundaries provides greater insight into this and will now be discussed.

3.6.2.3 Genesis of small grains

Bands of small grains cross-cut many of the porphyroclasts (Figs. 3.3, 3.5, 3.6, 3.8, 3.11, 3.12 & 3.15). Such bands are features that have been observed in many other naturally deformed feldspar grains, often accompanied by a change in composition between porphyroclast and small grains e.g. Fitz Gerald and Stünitz (1993). Those authors suggested that the small grains represent fractures filled with precipitate associated with a chemical change, so they have formed by a classical nucleation mechanism (i.e. crystal nuclei forming to decrease the chemical free energy of the volume of the system; Vernon, 2018), as opposed to their formation via deformation-induced recrystallization. In the rocks of this study, however, there is no difference in composition between the two grain populations. The formation of small and large grains with the same composition could be achieved if the small grains formed by the mechanism just described, and other processes of chemical change (i.e. interface-coupled dissolution-precipitation in a thin fluid film) subsequently affected the transition to albite in the adjacent porphyroclasts. In this scenario, the switch in mechanism for the transition to albite would be dependent on the amount of fracturing and associated availability of fluid to catalyse the metamorphic reactions, as described in section 3.6.2.1.

The microstructure in the bands of small grains is not reminiscent of growth into dilatant sites (Bons et al., 2012), and the orientation relationships to the adjacent larger grains require explanation. The fine band in Figure 3.5 with the right-angle bend has smaller grains with orientations that are closer to the porphyroclast orientation than the orientation of grains in the wider band to the right of the same figure. This orientation relationship could be achieved if the small grains are formed from nuclei of fragments of the original parent (Stünitz et al., 2003), where more fragments are produced in larger cracks that accommodate more movement, leading to wider band formation and associated wider spread in orientations due to greater fragment rotation. This style of genesis would also explain the geometry of the bands with respect to expected fracture traces (see inset in Fig. 3.5). Differences in grain size can be explained by relative fluid flux in cracks that experienced different amounts of offset/dilatancy, with greater opening resulting in a larger fluid flux (so more available solute) and more space for grains to grow.

Bands of small grains sub-parallel to fracture traces in Figure 3.12 show that small grains do not only occur in dilatant sites. Rotation of twin fragments appears to have occurred without loss of cohesion in the grain (and the bulk rock); as such the microstructure displayed in Figure 3.12 is a semi-brittle shear zone. Semi-brittle deformation could occur if dissolution of Ca-plagioclase fragments and precipitation of albite occurred in fine grains surrounding the twin fragments, to accommodate rotation, i.e. if pressure solution was active in the rocks.

Fragments generated by cataclasis typically have straight edges, angular shapes, and a large spread in grain size distribution (Stünitz and Fitz Gerald, 1993). In the Gressoney metagabbros, grains in the bands do not exhibit these features, but instead show evidence for textural coarsening (120° triples, curved boundary segments, relatively equant grain shapes). These observations suggest that if the bands of small grains are derived from fragments, then complete dissolution of the fragments and precipitation of new albite must have occurred, whilst preserving host orientation. However, Stünitz et al. (2003) suggested that a lack of host control in small grains in fact indicates nucleation from fragments, not a shared orientation, which contradicts our observations. It is possible that true cataclastic flow did not occur in the metagabbros of this study, so the original orientation of fragments was maintained despite some degree of cataclasis taking place. The small grains do not exhibit the characteristic porosity (or reaction product inclusions that record transient porosity) and intragranular distortion of replacement reactions, so the transition is not likely to have occurred by that mechanism. In the bands discussed above, the boundary segments of nearly all small grains that intersect with the larger albite porphyroclasts show curvature into the clast, which suggests that the population of small grains grew into the larger grains. This is clearest in Figures 3.14 and 3.15, where small grain growth into the porphyroclast fragments occurs even in the absence of any fractures; although fragmentation of the original clast probably occurred by fracturing, fractures within the remaining fragments are not observed. Figure 3.15a shows a small grain (white arrow) growing at the expense of a porphyroclast fragment where no clear fractures are visible in the fragment, suggesting that growth did not occur by precipitation into a void. The driving force for small grains to grow at the expense of the porphyroclasts via boundary migration is provided by the lattice distortion in the clasts, which, in turn, is a consequence of imperfect growth of the albite porphyroclasts during interface-coupled replacement.

Tullis (2002) noted that during crystal plastic deformation of feldspar, dislocation climb is restricted by low diffusion rates, so recovery cannot occur and high dislocation densities can build up. Instead, local recrystallisation by bulging is promoted. Although the dislocation population in the albite porphyroclasts is interpreted to have been generated by imperfect growth during interface-coupled replacement, the restrictions on climb in feldspar are still pertinent to inhibiting recovery, and enhancing bulging and grain boundary migration, which is why evidence for migrated, scalloped boundaries is observed.

The production of small grains and complete consumption of porphyroclasts in this manner led to an overall grain size reduction, within the albite, of a few orders of magnitude, which has implications for the overall strength of the deforming metagabbros, as it could lead to a transition from dominantly brittle deformation, to dominantly viscous strain accommodation by fluid-assisted diffusion creep, or pressure solution (see Chapter 4). The transition from dominantly brittle to dominantly viscous deformation has been observed in other feldspar-rich lithologies; e.g. Stünitz and Fitz Gerald (1993) cite granular flow as the main deformation mechanism in mid-crustal metagranites, which requires grain boundary sliding accommodated by fluid-assisted diffusive mass transfer, and is essentially exactly the same process.

3.6.3 Energy considerations

The new, small grains appear to have grown at the expense of the porphyroclast in order to reduce the stored strain energy which developed due to imperfect growth during the reaction (Drury and Urai, 1990; Urai et al., 1986),. How does this driving force for recrystallisation compare to lattice distortion produced by plastic deformation? An estimate of GND density in the porphyroclasts can be derived from the WBV technique by rearranging equation (1), if values for Burgers vector length and l_3 are known. The length of the *b* lattice parameter, 12.79 Å (Deer et al., 2013), is used for the Burgers vector length in the estimate, although this is somewhat arbitrary as the lengths of both the *a* and *b* lattice parameters yield results of the same order of magnitude. The *b* parameter was chosen as it was consistently identified as a dominant Burgers vector in the WBV analyses (see section 3.5.2.1). The pole figures presented in Figure 3.6 show that the [010] direction is essentially perpendicular to the map plane in the porphyroclast shown in Figure 3.5, in which case l_3 has a value of unity (Wheeler et al., 2009). Using 0.02 as a value of W, estimated from the magnitude maps presented in Figure 3.6 (which converts to $2*10^4$/m), a first-order estimate of dislocation density in the porphyroclasts is therefore calculated as

$$\rho = \frac{W}{bl_3} = \frac{2 * 10^4}{1.28 * 10^{-9}} \cong 1.6 * 10^{13}\ m^{-2}$$

Significantly, this value is of the same order of magnitude expected to be produced by crystal plastic deformation (e.g., Stünitz, 1998, and references therein), reported dislocation densities in naturally and experimentally deformed minerals on the order of 10^{13}–10^{-14} m^{-2}). However, in the albite porphyroclasts of the Gressoney metagabbros, the high dislocation density is interpreted to have been produced primarily by a chemical (imperfect growth during interface-coupled replacement) as opposed to a mechanical process. Differences in dislocation density in adjacent grains are known to provide a driving force for grain growth by boundary migration in crystalline materials (Drury and Urai, 1990; Piazolo et al., 2006; Urai et al., 1986), and it is likely that small, strain free grains eventually consumed the porphyroclasts in more deformed samples (see Chapter 4).

3.6.4 Conceptual model

The theoretical constraints on this conceptual model are as follows: i) dislocations are relatively immobile in plagioclase feldspar at greenschist facies (Tullis, 2002); ii) the transition of Ca-bearing plagioclase to pure albite requires aqueous fluids because of the production of zoisite, and those fluids are also likely to have enhanced reaction rates. Six basic processes define the model, which must have occurred, to an extent, in parallel:

1) Brittle deformation occurred to create the fracture networks observed at thin-section scale (Fig. 3.2; Fig. 3.18a). Fluid infiltration occurred along all available fracture planes. Ca-bearing plagioclase from the original gabbro was out of equilibrium at greenschist facies conditions during the initial fracturing, providing a chemical driving force for transition to albite.

2) In through-going fractures, some of which then became dilatant, albite nucleated in a “classical” fashion, due to the chemical driving force (i.e. the lowering of Gibbs free energy) to change Ca-plagioclase to albite (Fig. 3.18b). Nuclei were related in orientation to the original grains, and may have been derived from Ca-plagioclase fragments, although the exact relationships were modified later and cannot be characterised in detail. Wider bands have a broader spread in orientation, which can be explained by greater rotation of original fragments, or by later shear accommodated by pressure solution, which would cause a variety of grain rotations (Wheeler 2009). Physical rotations are evident in twin fragments in Figure 3.12 for example, and could have occurred elsewhere in equant grain aggregates, where they are consequently less obvious.
3) The exact plagioclase breakdown reaction cannot be diagnosed as no Ca-bearing plagioclase remains, but as clinozoisite forms from the An component, the reaction must have followed the form:

   Ca-bearing plagioclase + Na^+ + $SiO_2(aq)$ + H_2O = albite + clinozoisite + H^+

   So, in parallel with (2), second phases (particularly clinozoisite) grew along cleavage planes, and in other places where microcracks formed. Second phase growth tended to occur elongate and parallel to twinning for this reason (Fig. 3.3b, Fig. 3.18c; twin planes are parallel to cleavage planes in plagioclase).

4) The parent Ca-bearing plagioclase did not undergo reaction everywhere by processes (2)/(3). In those regions that were devoid of fractures, hence where fluid flux was limited to grain and phase boundaries, the Ca-plagioclase to albite transition occurred by interface-coupled replacement, in a nanothin film of fluid (Fig. 3.18d). The replacement reaction generated intragranular microporosity (Fig. 3.3c), and intragranular distortion due to lattice mismatch during replacement (Fig. 3.8, Fig. 3.15b, Fig. 3.16). Processes (2) and (4) occurred simultaneously, resulting in the complete albitization of Ca-bearing plagioclase, and a bimodal grain size distribution of small (tens μm-scale), strain-free albite grains, and large (mm-scale), strained albite porphyroclasts.
5) Where small strain-free albite grains shared a boundary segment with the larger strained albite porphyroclasts (e.g., edges of bands of small grains in Fig 3.5; edges of distorted clast fragments in Figs. 3.14 & 3.15), grain boundary migration occurred, and small grains grew at the expense of the porphyroclasts (Fig. 3.18e). The driving force was provided by strain energy in the distorted

lattices of the porphyroclasts. This may have resulted in some porphyroclast fragments being entirely consumed by new strain-free grains (Fig. 3.18f).

6) Where new strain free grains were in contact with each other, growth was driven by grain boundary energy to produce equilibrated “foam” textures (e.g. large band in Fig. 3.3).

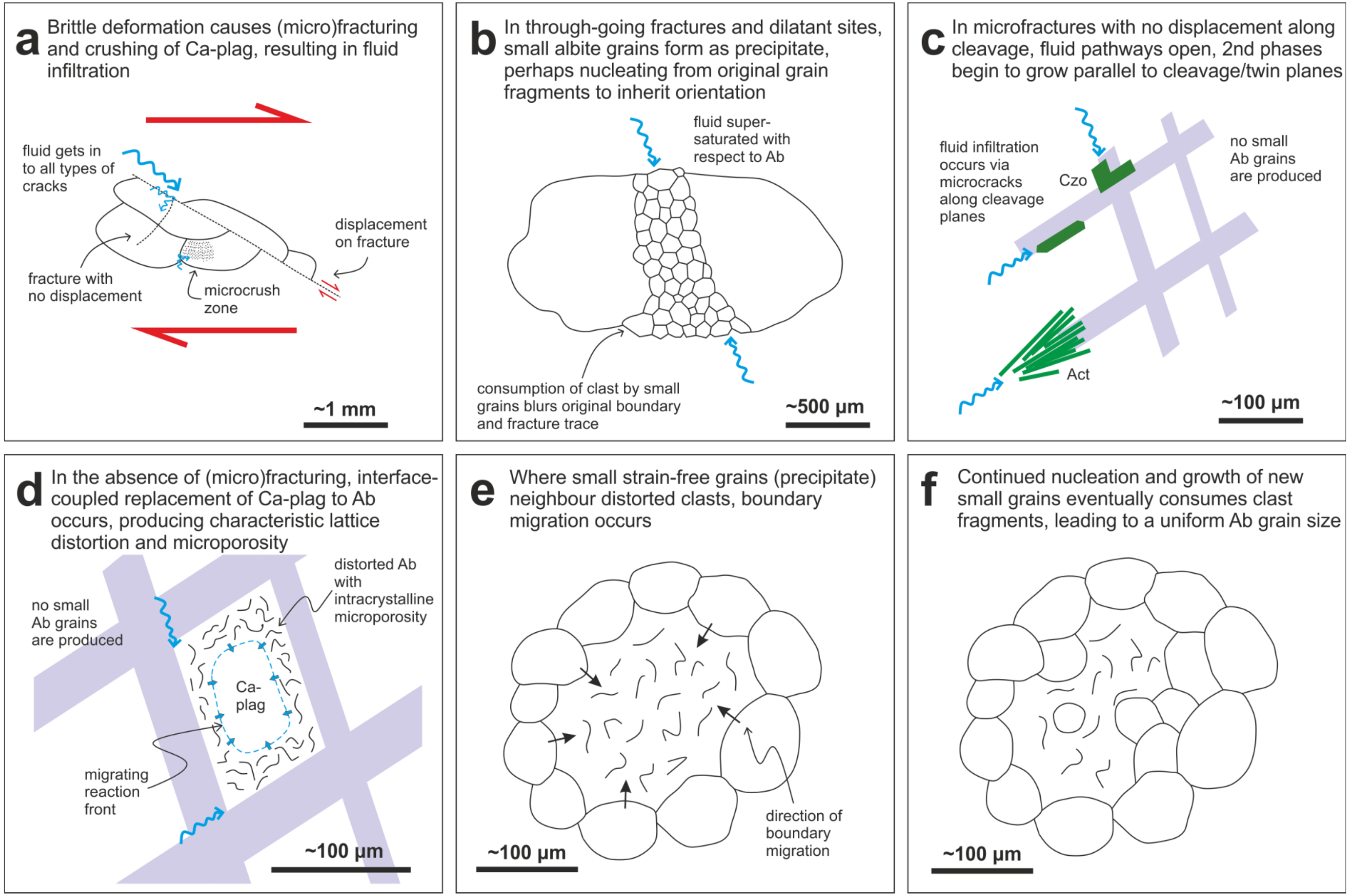

Figure 3.18 *Conceptual model of albite grain size reduction. The dominant process in each part of the model is described in each of the boxes (a)–(f). Ab = albite, Czo = clinozoisite.*

3.7 Conclusions

Evidence for three different microstructural settings, that result in three different types of fluid-rock interaction, was observed in the Gressoney metagabbros:

- dilatant cracks where, after fluid infiltration, fragmented Ca-plagioclase dissolved, and albite + clinozoisite (and sometimes other phases) precipitated, as evidenced by bands of small grains that cross-cut albite porphyroclasts. The magnitude of movement and dilation on individual cracks dictated the degree of host control on orientation, and the size of new small grains.
- (micro)cracks along cleavage planes, on which a very limited amount of movement or opening occurred, resulted in a drastically lower fluid flux. This led to the production of secondary phases which are often aligned along cleavage/twin planes.
- an absence of fracturing and associated lack of fluids resulted in the occurrence of interface-coupled replacement reactions, where reaction fronts migrated through parent Ca-plagioclase in a nanothin film of fluid. The replacement reactions generate intragranular microporosity, and high internal distortion due to imperfect growth during replacement.

Replacement of Ca-plagioclase to albite happened by two processes: i) dissolution of Ca-plagioclase, possibly transport, and precipitation of albite from solution (first generation of small grains); ii) interface-coupled replacement across a solid-to-solid reaction front (large distorted albite clasts). Large distorted porphyroclasts were then, in some cases, consumed by small grains. Grain boundary migration, driven by dislocation density contrasts, was the mechanism by which small unstrained nuclei grew to consume porphryoclasts.

The study here involved relatively low strain material, which underwent significant grain size reduction due to chemical instability of Ca-bearing plagioclase at mid-crustal conditions. The grain size reduction was catalysed by the influx of crustal fluids associated with fracturing. The grain size reduction mechanism outlined here is associated with a switch in the dominant mode of deformation from initial brittle behaviour to viscous, steady-state flow. Evidence of strain accommodation by viscous creep is observed in higher strain samples of the rocks (see Chapter 4), and other species of feldspar are known to deform by dissolution-precipitation creep in the middle crust at grain sizes of a similar magnitude (e.g. K-feldspar; Menegon et al., 2008). This grain size reduction mechanism may therefore play an important role in modifying the deformation response of the crust to applied tectonic stresses, and lead to a switch from dominantly frictional (i.e. the brittle strength of albite) to dominantly viscous (i.e. the strength of albite undergoing pressure solution) behaviour even at relatively low strains. Such a switch in deformation behaviour has major consequences, as viscous deformation redistributes stress non-seismically. so could lead to the cessation of earthquake generation. Conversely, grain size reduction can promote strain localization in the crust and the formation of shear zones, which can lead to the build-up of stresses in the upper crust that are capable of producing earthquakes (Thielmann et al., 2015; see also section 1.1.1)

Chapter 4 Evolution of microstructure and texture along a strain gradient during diffusion creep.

4.1 Abstract

Rock microstructures evolve during deformation, depending on the stress, pressure and temperature conditions they are exposed to. Such microstructural evolution is believed to exert fundamental controls on the strength of the lithosphere and the development of shear zones. However, an incomplete record of microstructural evolution is normally preserved in natural rocks. In particular, microstructural evolution during diffusion creep is difficult to decipher, as this fundamental deformation mechanism leaves very few indicators. Metagabbroic rocks from the Gressoney Shear Zone, NW Italy, that have been naturally deformed to high strains by fluid-assisted diffusion creep (pressure solution), are rich in fine albite grains that exhibit crystallographic preferred orientation domains. The orientation domains have been inherited from single crystals, so had a strong texture prior to deformation. This study uses electron backscatter diffraction to investigate the evolution of microstructure and rock texture with increasing strain during pressure solution, with the aim of understanding how diffusive mass transfer can modify an inherited texture. Metagabbroic samples with five different strain levels are used to show how albite grain size, aspect ratio, and texture strength, and second phase abundance, evolve and interact during deformation. Although the secondary phases produced during metamorphic reactions are reported to inhibit grain growth, which promotes GSS creep, this study shows their presence may also limit texture modification by inhibiting the rotations normally associated with diffusion creep and grain boundary sliding, to preserve CPO domains to high strain. This study shows a strong inherited CPO can be preserved to high strain by grain boundary diffusion creep, which implies that the interpretation of CPO domains must be treated with care, as their presence can be open to misinterpretation (i.e. dislocation creep activity may be assumed), without careful analysis.

4.2 Introduction

The microstructure of crystalline materials influences their mechanical properties (Humphreys, 2001), and the correct interpretation of microstructures observed in naturally deformed rocks allows insight into the geodynamic history of the Earth (Bestmann et al., 2005). Rock microstructures evolve during deformation, depending on the stress, pressure and temperature conditions they are exposed to, and microstructural evolution is believed to exert fundamental controls on the strength of the lithosphere and the development of shear zones (Montési and Hirth, 2003a; Mukai et al., 2014;

Platt and Behr, 2011). Natural rocks are nearly always polyphase materials, and the presence and distribution of secondary phases is regarded to influence their rheology during deformation (Czaplińska et al., 2015; Herwegh et al., 2011; Newman et al., 1999; Platt, 2015). The impact of phase-mixing during deformation is currently a much-debated topic in the rock deformation community, due to its potential role in limiting grain growth and strain localisation in the crust (Bercovici and Ricard, 2012; Cross and Skemer, 2017).

One particularly important parameter which defines the dominant deformation mechanism in viscously-deforming rocks is grain size (Kilian et al., 2011; Menegon et al., 2013; Stünitz, 1993); which in turn influences the rheology of those rocks (De Bresser et al., 2001; Montési and Hirth, 2003a; Rutter and Brodie, 1988; Rybacki and Dresen, 2004a). Grain size-reduction, as observed during the breakdown of the albite porphyroclasts in the samples, can result in a transition from dislocation creep to diffusion creep, which has been observed or modelled for many lithospheric materials e.g. quartz (Kilian et al., 2011), feldspar (Rybacki and Dresen, 2000; Rybacki and Dresen, 2004a), olivine (Karato et al., 1986). Grain growth can 'switch off' diffusion creep but is inhibited by the presence of secondary phases (Pearce and Wheeler, 2011).

Diffusion creep is a fundamental deformation mechanism in the Earth (Hiraga et al., 2010; Miyazaki et al., 2013; Wheeler, 1992; Wheeler, 2009). At low homologous temperatures (i.e. the temperature of a material as a fraction of its melting point temperature, in K) and in the presence of water, diffusive mass transfer occurs by pressure solution (Elliott, 1973; Menegon et al., 2008; Rutter, 1976; Rutter, 1983; Wheeler, 1992; Wintsch and Yi, 2002), but diffusion creep and pressure solution are equivalent processes (Elliott, 1973). Both diffusion creep and pressure solution involve strain accommodation by grain boundary sliding (GBS) (Ashby and Verrall, 1973), which depends on grain rotations to preserve continuity during grain shape change (Elliott, 1973; Wheeler, 2009). Diffusion creep has been reported to leave few microstructural indicators, as the diffusive exchange of material within and between grains tends to erase existing microstructures. Instead, indirect evidence such as the absence of a CPO in highly-strained, fine-grained mineral aggregates with equant grains is often used in support of the interpretation of diffusion creep or grain boundary sliding (Bestmann and Prior, 2003; Passchier and Trouw, 2005).

This study uses electron backscatter diffraction to investigate the evolution of microstructure and rock texture with increasing strain during pressure solution, with the aim of understanding how diffusive mass transfer modifies an inherited texture. Grain size and shape evolve during pressure solution so in this study these variables are compared to texture strength. Variation in grain size and shape is also compared to second phase content to assess the effect of phase mixing on texture evolution. The work presented here focuses on the fine-grained albitic matrix of highly-deformed metagabbros from the Gressoney Shear Zone (GSZ; Fig. 2.1) (Jiang et al., 2000; Prior and Wheeler, 1999; Reddy et al., 1999; Reddy et al., 2003; Wheeler and Butler, 1993). The albitic matrix of these metagabbros has previously been observed to exhibit CPO domains, each interpreted to be inherited from a single large parent grain during metamorphism at greenschist facies (Chapter 3; Jiang et al., 2000; Prior and Wheeler, 1999. Dislocation creep is not expected to dominate deformation in feldspar at greenschist facies (Tullis, 2002), although its potential influence is discussed below. The current study compares the microstructural characteristics of the fine-grained albitic matrix at five strain levels, to show how grain size, aspect ratio, second phase abundance and texture strength evolve and interact during deformation that is accommodated by diffusive mass transfer.

4.3 Geological setting

See section 3.3 of this thesis. Figure 3.1 details the field localities of all analysed samples.

4.4 Methods

Thin sections cut perpendicular to foliation and parallel to lineation (i.e. the x–z kinematic plane, where observed) were prepared. Samples were polished for 2–3 hours using 0.05 μm colloidal silica, and carbon coated prior to electron backscatter diffraction (EBSD) data collection.

The whole thin section scans shown in Figure 4.1 were collected using a Leica DM2500P microscope equipped with a Leica DFC295 camera (3 mega pixel resolution) and the Leica Application Suite software. Single images were acquired in capture mode, and whole thin section scans were acquired using live mode (up to 25 frames per seconds). Live images were stitched together by the software during manual movement of the microscope stage. The XPL images in Figure 4.2 were collected using a Lumenera Infinity 4 camera connected to a Meiji Techno MT9000 polarized microscope.

QEMSCANSEM-EDS data were collected by Mr. James Utley in the Department of Earth, Ocean and Ecological Sciences at the University of Liverpool using an FEI WellSite QEMSCAN SEM equipped with two Bruker light-element energy dispersive

X-ray (EDS) spectrometers, operating at 15 kV. The EDS spectrometers collect X-ray spectra from the surfaces of polished thin sections or blocks at a rate of c.10 ms per pixel (Pirrie et al., 2004). Collected spectra are compared against a database of common mineralogical spectra, which is user defined, to allow for rapid identification of mineral phases. The accuracy of identification of phases is increased by comparing EDS data for each pixel to pixel brightness in a BSE image (Qian et al., 2015). The QEMSCAN® database is made up of Species Identification Protocols (SIPs), which can be constructed to optimise the quantification of different types of geological material e.g., ore deposits, sediments. Images presented in Figure 4.3 were collected using a 20 μm step size. Images in Figure 4.4 were collected using a 2 μm step size.

EBSD data were collected on a CamScan X500 FEG-SEM fitted with an F+ Nordlys detector at the University of Liverpool, using the Aztec Oxford Instruments acquisition system. Multiple EBSD maps (automated montages) were collected from albite-rich areas of each sample (i.e. each strain level). Step size for collection ranged from 2 to 5 μm. Maps were individually processed to remove spurious pixels and fill non-indexed points following the procedure set out in Prior et al. (2002), and detailed in section 2.5.2 of this thesis. Systematic misindexing of pixels can occur when two (or more) different crystallographic orientations generate Kikuchi patterns that are so similar, the processing software (Aztec, in this case) cannot distinguish between them, so systematically chooses an incorrect orientation, leading to the mottled pattern that can be observed in some of the grains in Figure 2.8b & e. A common systematically misindexed 180° rotation about the [201] crystallographic axis was removed in the albite grains (see section 2.5.2).

A statistical analysis was carried out across all five strain levels to compare grain area and aspect ratio in albite, and clinozoisite abundance, in each map. The free MatLab® microstructural characterisation toolbox, MTEX, was used to generate grain morphology statistics and calculate texture strength (Mainprice et al., 2014). To accurately determine grain size and shape from EBSD data, the chosen step size for data point collection must be small enough that the change of missing grains or grain intercepts is small, otherwise the measured grain size will be larger than the true grain size (Humphreys, 2004). To obtain an accuracy of 10%, at least five pixels per grain should be collected, and for an accuracy of 5%, at least eight pixels per grain are required (Humphreys, 2001). In this study, grains smaller than 10 pixels were removed to improve the reliability of grain data. The code for each processing step used can be found in Appendix 2. Clinozoisite was chosen to be indicative of a ‘secondary phase’, as, in nearly all cases, the fine-grained matrix in the rocks is composed of an albite-clinozoisite two phase mixture. The goal of the analysis was to determine the effect of second phase abundance on the microstructural evolution of the albite grains undergoing pressure solution at increasing strains.

4.5 Results

4.5.1 Optical microscopy

4.5.1.1 Relative strain levels

The overall distribution of phases at the thin section scale (approx. 2 × 3 cm) helps to define five strain (i.e. deformation) levels in the suite of samples (SL 1–5; Fig. 4.1). At the lowest strains (SL1), large albite porphyroclasts are preserved but a population of fine-grained albite is also present (see Chapter 3; Fig. 4.1a). At every other strain level, large albite porphyroclasts are essentially absent (Fig. 4.1b–e). Localised albitic porphyroclast remnants, that tend to be only slightly larger than their unstrained counterparts, are found scattered through the matrix, most easily identified using EBSD by their high intergranular distortion. Relative strain levels subsequent to SL1 are defined by the evolution of mafic porphyroclasts. At SL2, mafic porphyroclasts (clinopyroxene and minor hornblende) are preserved, leading to the development of pressure shadows (see next paragraph; Fig. 4.1b). Mafic porphyroclast breakdown occurs at SL3, where mafic fragments tend to be strung out in rows (Fig. 4.1c), and by SL4, mafic fragments become isolated within the finer-grained matrix (Fig. 4.1d). At the final strain level (SL5; Fig. 4.1e), no mafic porphyroclasts are observed, although small grains of clinopyroxene, hornblende, actinolite and chlorite still occur. In hand specimen, the SL5 sample does not have a gabbroic texture and is categorised as "green slate" on the geological map (Fig. 2.1), so may have had a basaltic protolith, although the exact starting material remains unclear. In the field, all observed boundaries between green slate and metagabbro were sharp not gradational, possibly suggesting a different original grain size.

4.5.1.2 Albite

In the lowest strain samples, pressure shadows are not observed, although albite does occur in dilatant sites within fractured clinopyroxene (Fig. 4.1a). At SL2, pressure shadows that contain large (on the order of hundreds of μm diameter) albite grains have formed around clinopyroxene porphyroclasts (Fig. 4.1b). Largely monomineralic bands of relatively coarse-grained albite (minor actinolite is present) that are connected to the pressure shadows run through the samples. Due to the breakdown of mafic porphyroclasts with increasing strain, albitic pressure shadows are less apparent at higher strain levels.

4.5.1.3 Clinozoisite distribution

At the lowest strains, albite and clinozoisite are not well mixed in the fine-grained matrix. Clinozoisite tends to occur in clusters between albite and clinopyroxene grains (Fig. 4.1a & 4.2;

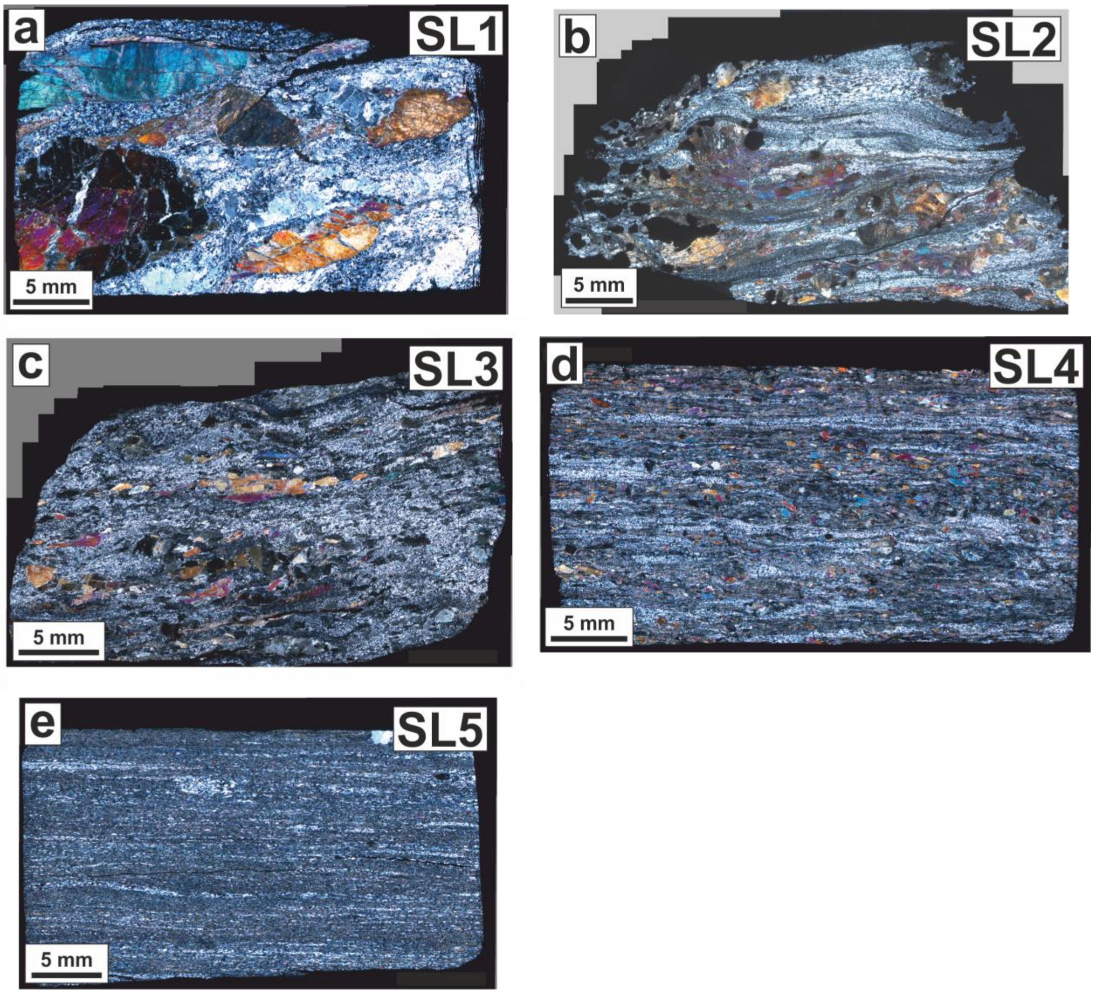

Figure 4.1 *Scans of whole thin sections used in this study. SL = strain level. a) SL1 – cm-scale mafic porphyroclasts (clinopyroxene and minor hornblende) are fractured but remain relatively intact. Cm-scale albite porphyroclasts and clusters on mm-scale clinozoisite are also present; b) SL2 – mm-scale mafic porphyroclasts remain, albite porphyroclasts are absent. Albite and clinozoisite are relatively-well mixed in the fine-grained (tens to hundreds μm) matrix; c) SL3 – mm-scale mafic clasts become boudinaged, with albite and clinozoisite remaining well-mixed; d) SL4 – grain size of mafic grains is significantly reduced, and albite and clinozoisite show some banding (i.e. separation); SL5 – grain size of all phases is homogeneous, and all phases are well mixed.*

see also Fig 3.2). At SL2, the fine-grained matrix is largely a two-phase mixture of albite and clinozoisite, although clinozoisite abundance varies spatially. The heterogeneous distribution of clinozoisite continues through strain levels 3 and 4. Clinozoisite-rich bands show up as dark streaks or patches in the matrix in cross-polarised light (Fig. 4.1a–d). By SL5, clinozoisite distribution becomes more homogeneous, although, at a fine (sub-mm) scale, banding between albite and clinozoisite is preserved. Clinozoisite can also be seen to form strain caps around mafic porphryoclasts at SL2, and locally occurs in monophase bands between mafic porphyroclasts, e.g. see Figures 4.4b and 4.9b for clear examples. Clinozoisite is commonly zoned, with more Fe-rich cores showing yellow-orange interference colours (Deer et al., 2013) zoning out to a characteristic anomalous blue (Fe-poor) in XPL (Fig. 4.2).

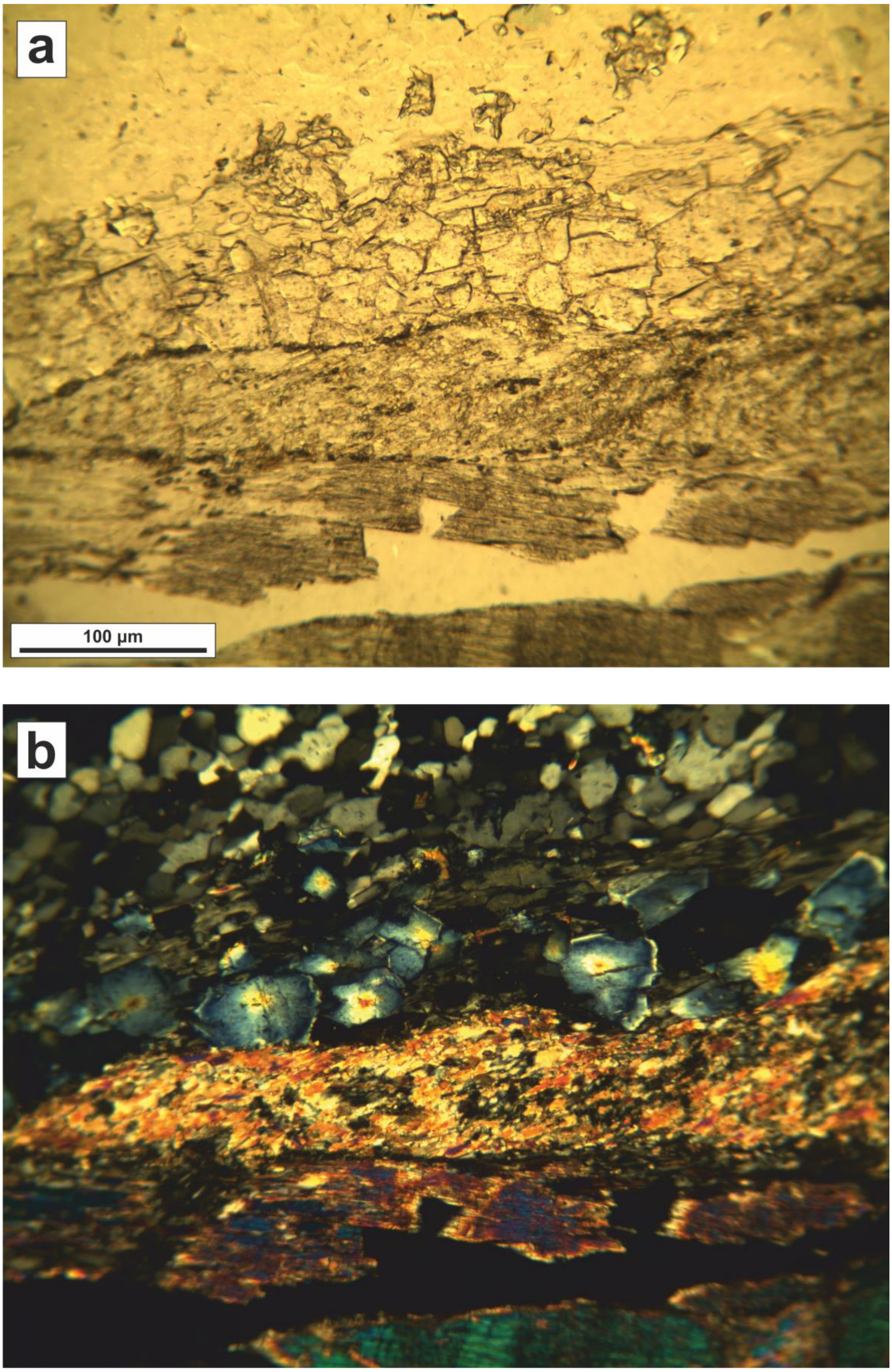

Figure 4.2 *Optical microscope images in a) plane-polarized and b) cross-polarized light showing clinozoisite distribution. Clinozoisite commonly occurs between albite bands and mafic porphyroclasts at SL1. See also Fig. 3.2. At SL1, clinozoisite also commonly exhibits yellow cores (Fe-rich) that zone out to an anomalous blue (Fe-poor).*

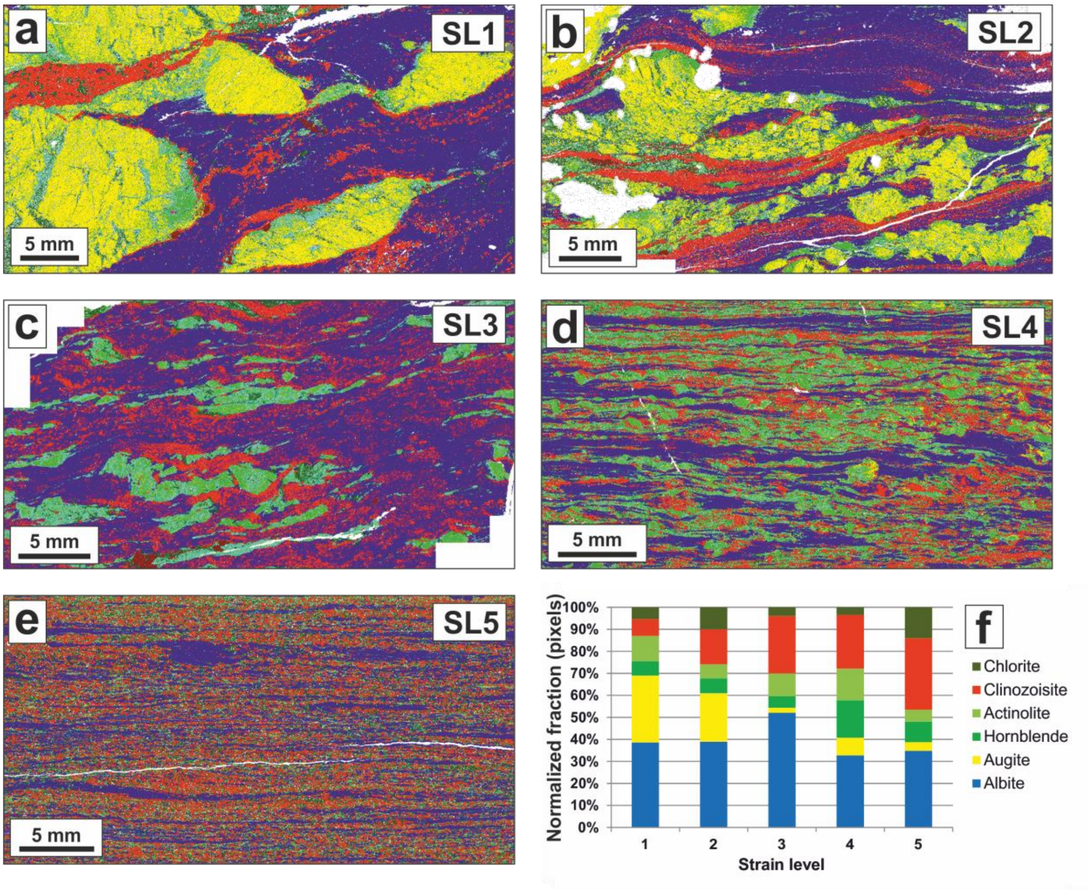

Figure 4.3 *Thin-section scale SEM-EDS scans produced by QEMSCAN. Strain level (SL) increases from a) to e) (see also Fig. 4.1). Albite = blue, clinopyroxene = yellow, hornblende = medium green, actinolite = light green, clinozoisite = red, chlorite = dark green. Albite content is relatively constant during strain evolution, whereas clinopyroxene content falls dramatically with breakdown to other mafic phases (see Fig. 4.4). Relative clinozoisite content increases with strain. Banding/separation of albite from other phases develops with strain, although albite band width also decreases with increased strain. See Appendix 1 for SIP parameters.*

4.5.2 QEMSCAN

SEM-EDS scanning of entire thin sections, using the QEMSCAN® method, allows an appraisal of the evolution of phase content and distribution with increasing strain (Pirrie et al., 2004). At SL1 (Fig. 4.3a), the large clinopyroxene porphyroclasts (yellow), that dominate the samples, largely occur as coherent grains, but decompose to actinolite and chlorite as fragments are pulled apart, and along fracture and cleavage surfaces (Fig. 4.4a). Clinozoisite predominantly lines clinopyroxene-Ab boundaries, but also occurs throughout the albite-dominated matrix. At SL2 (Fig. 4.3b), clinopyroxene porphyroclasts are significantly more fractured than SL1, and comprise a smaller area percentage of the thin section (Fig. 4.3f), with the increased fracturing accompanied by increased fluid influx probably leading to the generation of more chlorite. Both clinopyroxene and hornblende porphyroclasts are replaced by actinolite and chlorite, showing replacement of mafic phases occurred at conditions where hornblende was not stable (i.e. lower than amphibolite facies so 500 °C or less; Fig. 4.4b & c). Clinozoisite

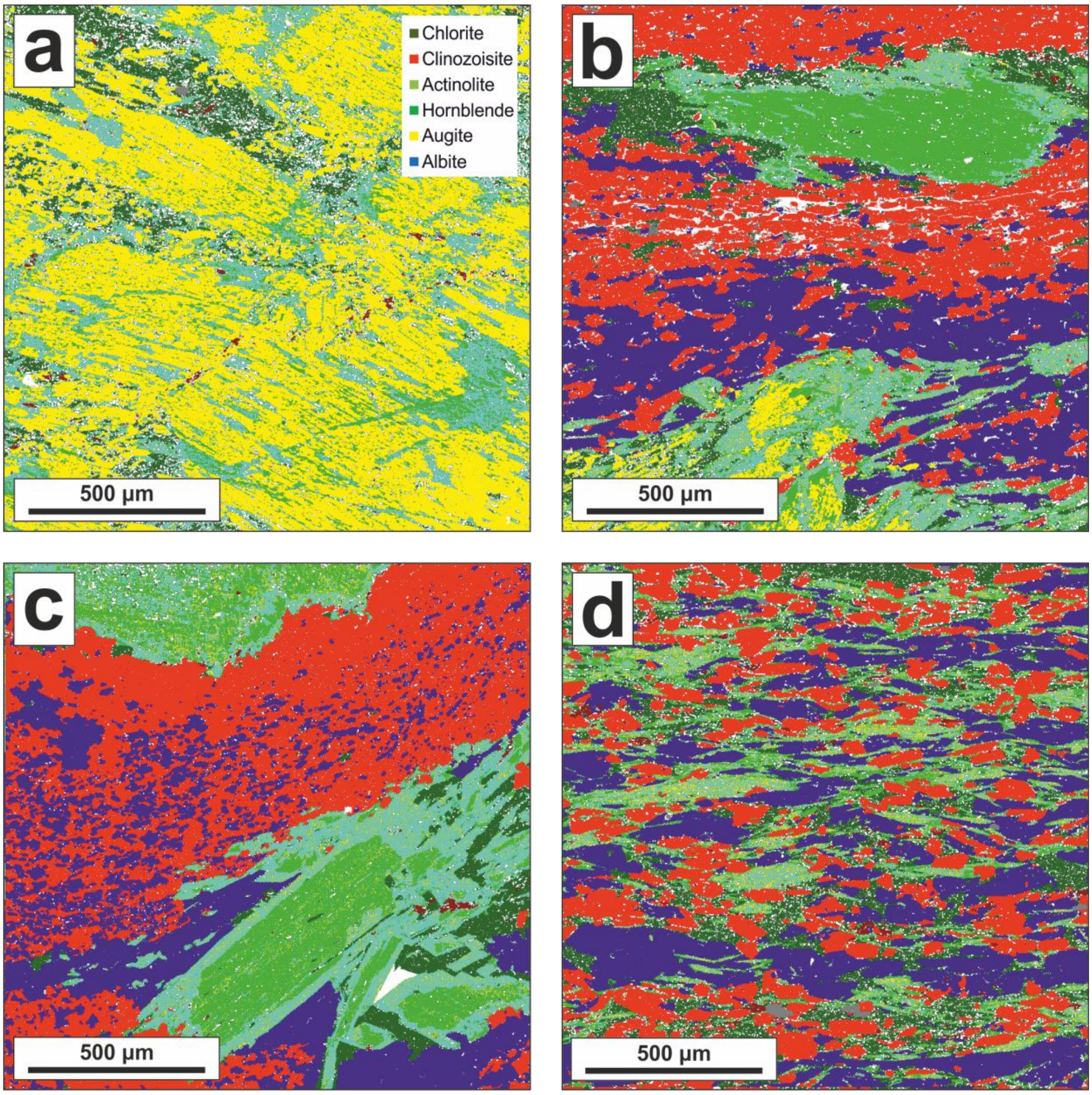

Figure 4.4 *QEMSCAN images showing reaction details in mafic phases. a) SL1; core of clinopyroxene (yellow) showing breakdown to actinolite (light green) and chlorite (dark green) along fracture and cleavage planes (related to fluid influx). b) SL2; both clinopyroxene and hornblende (medium green) have greenschist-facies reaction rims of actinolite and chlorite, supporting the idea that hornblende is igneous, rather than metamorphic (which would indicate amphibolite-facies metamorphism), as put forward by Prior and Wheeler (1999). c) SL3; replacement of hornblende to form euhedral crystals of actinolite and chlorite. Clinopyroxene is very rare by this stage. d) SL5; dominant mafic phases are actinolite or chlorite, no large porphyroclasts remain.*

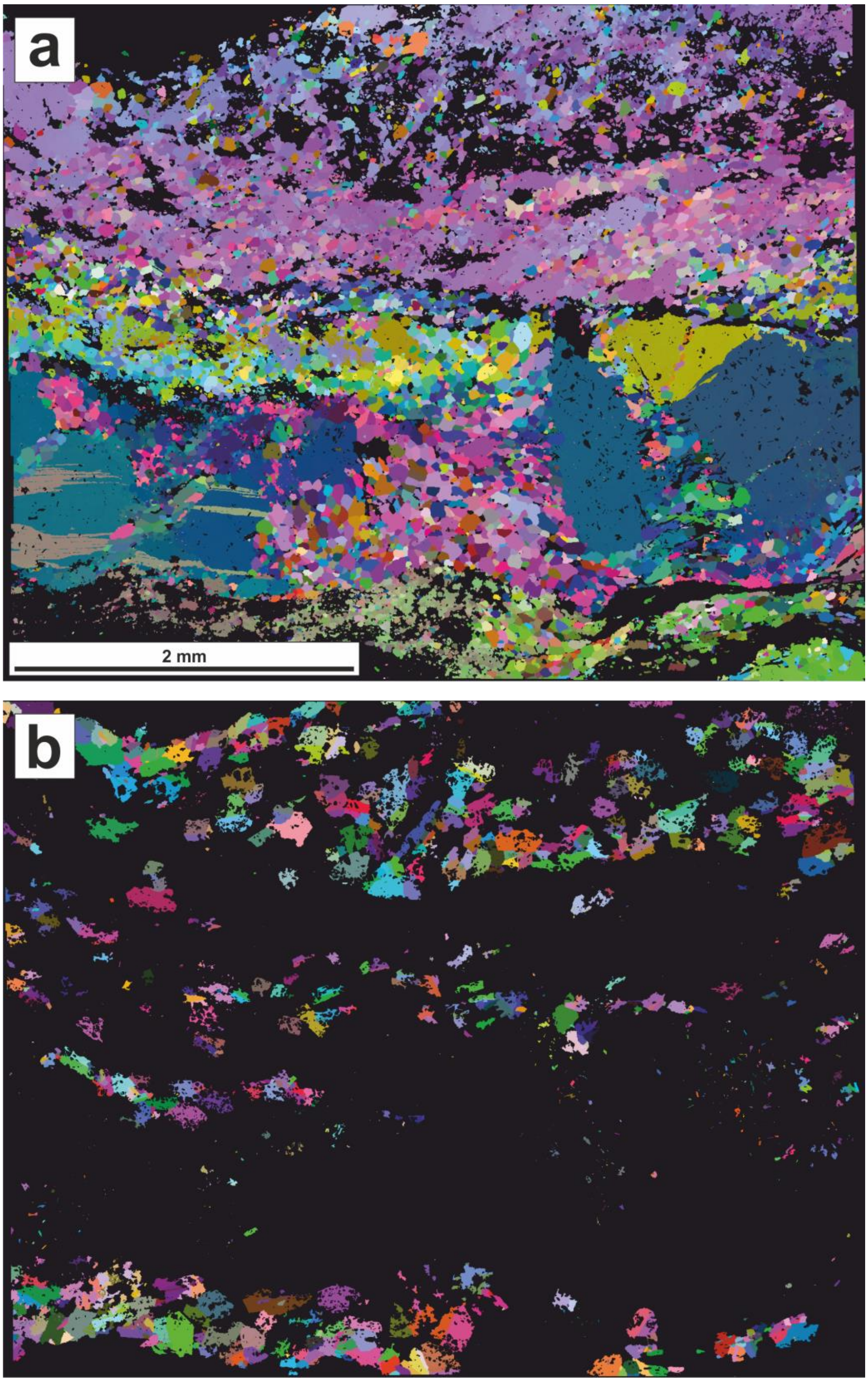

Figure 4.5 *All-Euler EBSD maps. a) Albite distribution at SL1. Albite grain population consists of porphyroclasts and fine grains. b) Clinozoisite distribution at SL1, same field of view. Grain shapes are equant and do not share a preferred orientation. In general, clinozoisite and albite are not well mixed. Clinozoisite tends to occur at albite-clinopyroxene phase boundaries, or CPO domain boundaries, which would originally have been plagioclase-plagioclase grain boundaries. Albite that precipitated within what was probably a through-going fracture in a porphyroclast (bottom right of (a)), is mixed with actinolite not clinozoisite.*

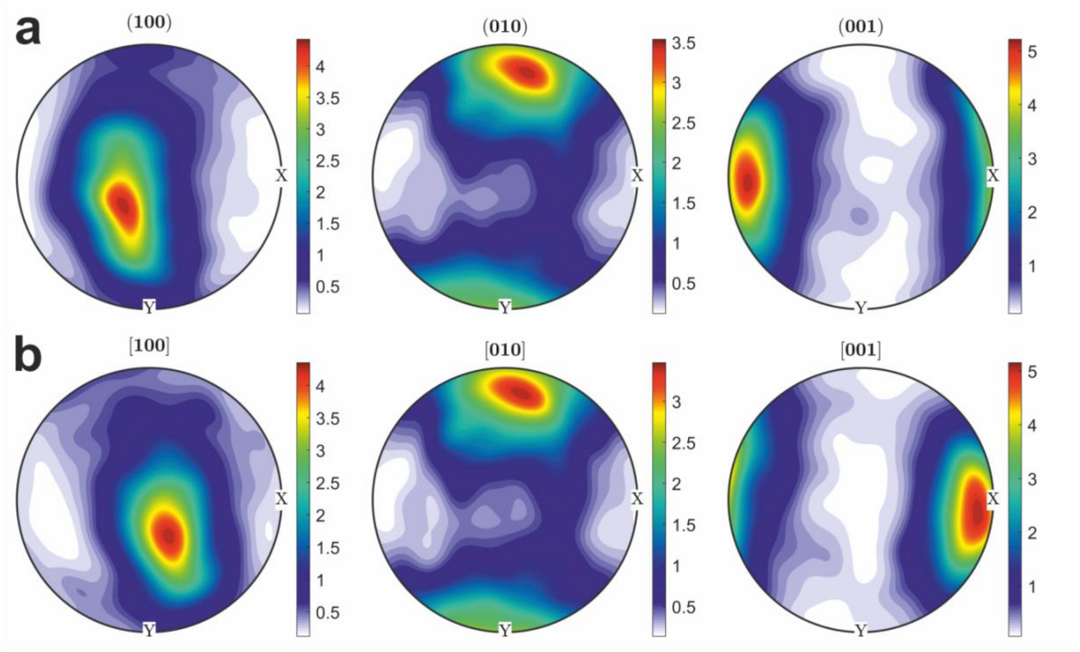

Figure 4.6 *Pole figures constructed from the purple band of Ab at the top of Fig. 4.5a. Halfwidth = 10°.*

streaks outline the sample foliation, wrapping around and between mafic porphyroclasts. From SL3 onwards, clinopyroxene becomes rare, and all phases become more mixed, although albite tends to occur in mostly monophase bands even at the highest strains (Fig. 4.3c–e, Fig. 4.4d). Albite content broadly remains at some 30–40% at all strain levels, but relative clinozoisite content increases with strain (Fig. 4.3f). The systematic decrease of clinopyroxene and increase of hydrous reaction products with increasing strain observed in Fig. 4.3f suggests that increasing strain was concomitant with an increase in fluid availability.

4.5.3 EBSD

4.5.3.1 Albite microstructures

EBSD data show that texture strength decreases significantly with increasing strain level in CPO domains observed in the albite matrix. At SL1, albite porphyroclasts are observed to be highly distorted, while the population of small grains are not. The potential origin of the strain in the porphyroclasts was discussed at length in Chapter 3, so will not be repeated here. In summary, small albite grains at SL1 are thought to be a new population of strain-free grains derived partly by precipitation from a supersaturated fluid, and partly by recrystallization mechanisms that worked to consume the highly strained porphyroclastic grains to reduce the overall free energy of the system. At SL1, bands of colour in All-Euler maps show albite porphyroclast remnants broadly share orientations with surrounding small grains (Fig. 4.5a). One point per grain (OPPG) pole figures for albite at SL1 show maxima in which the (010) plane lies close to the foliation plane, and the [001] direction is aligned to the rock lineation (Fig. 4.6; all samples were cut as close to the X–Z plane as possible). This is a common slip system in plagioclase (Stünitz et al., 2003), however, grains in individual CPO domains in these samples are random with respect to the kinematic axes of deformation, and are not well aligned for movement on common plagioclase slip planes (see also Jiang et al., 2000). Because most CPO domains are not aligned to the kinematic axes, the alignment observed in Figure 4.6 is interpreted to be coincidence, and dislocation creep is not interpreted to dominate deformation in these samples. MAD and pole figure data are taken from the purple band of grains close to the top of Figure 4.5a. Texture strength (quantified by the M-index, which ranges from 0, when grains completely lack a shared orientation, to 1, when all grains share an identical orientation; Skemer et al., 2005) calculated using MTEX in this region is relatively high, at 0.52 (Table 4.1), indicating the grains in the domain probably formed from a large single parent.

By strain level 2, albite porphyroclasts are no longer prominent in the microstructure, and albite grains are mainly present as part of a two-phase matrix, through which clear CPO domains streak (Fig. 4.7a). The CPO domains are interpreted to be inherited from mm- to cm-scale Ca-bearing plagioclase grains in the original gabbro that have undergone a grain size reduction during their transition to pure albite (see Chapter 3). Multiple mechanisms are interpreted to have operated in parallel to contribute to an overall grain size reduction of some 3–4 orders of magnitude (see section 3.6). The All-Euler map shows that overall CPO domain shapes have undergone readjustment during deformation, with the domain outlines becoming elongate parallel to foliation, and domain tails pinching out at their limits (e.g. light blue domain in Fig. 4.7a). One-point-per-grain (OPPG) pole figures from the individual CPO domains have maxima that show that the domain orientations are unrelated to any orientation that would be expected to have been produced by common plagioclase slip systems (Fig. 4.8; Satsukawa et al., 2013). Texture strength varies in the domains but is generally high (Table 4.1).

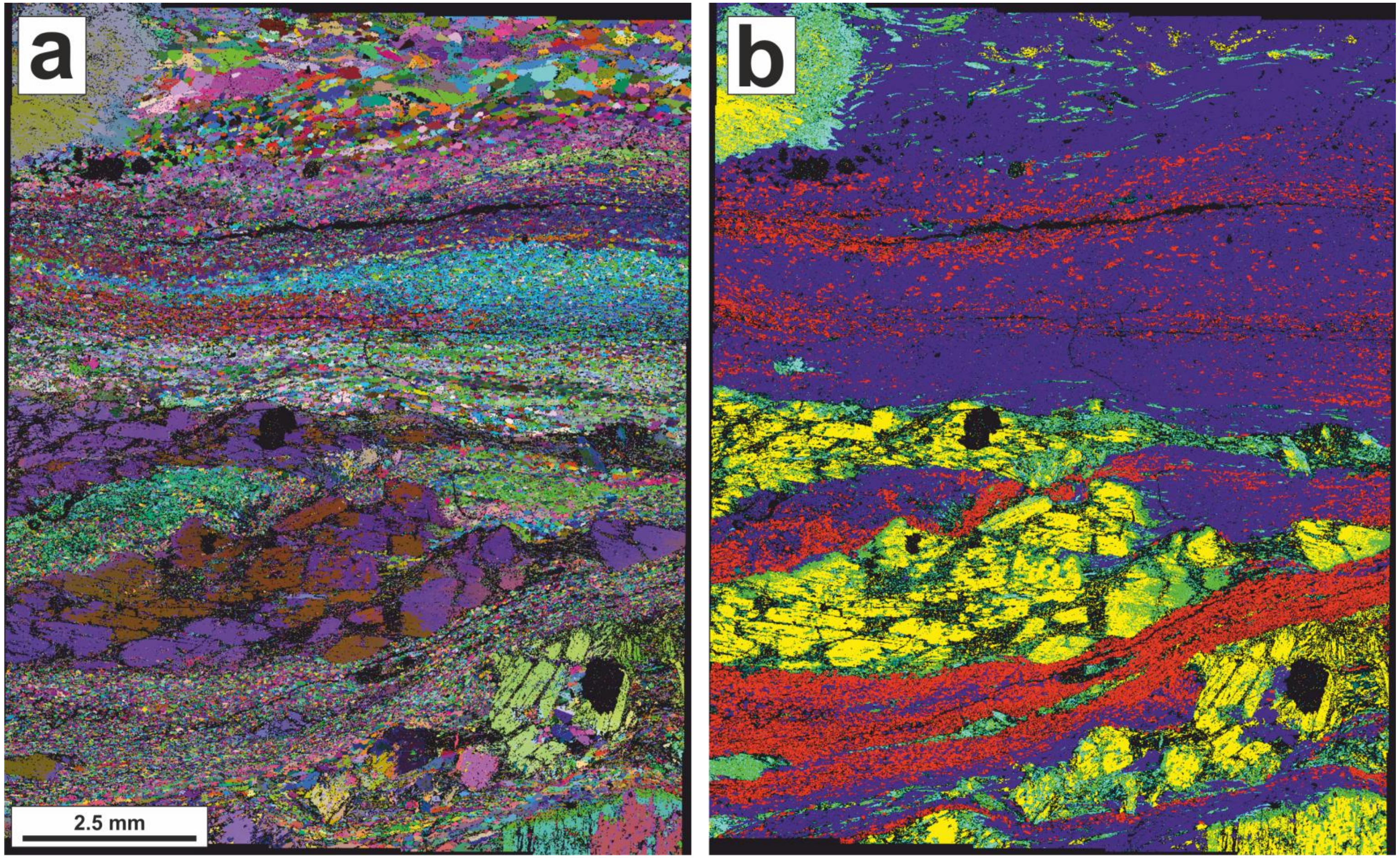

Figure 4.7 *a) All-Euler EBSD map showing streaked CPO domains in the fine-grained albite matrix at SL2. Large grains derived from a pressure shadow run across the top of the map, adjacent to a clinopyroxene porphyroclast. Pressure shadow grains (i.e. precipitate) are again mixed primarily with actinolite, which is noticeably different to the rest of the two-phase matrix that is composed primarily of albite and clinozoisite. Pressure shadow grains lack a preferred orientation. b) Phase map of the same area as (a). Blue = albite, red = clinozoisite, yellow = clinopyroxene, light green = amphibole, dark green = chlorite.*

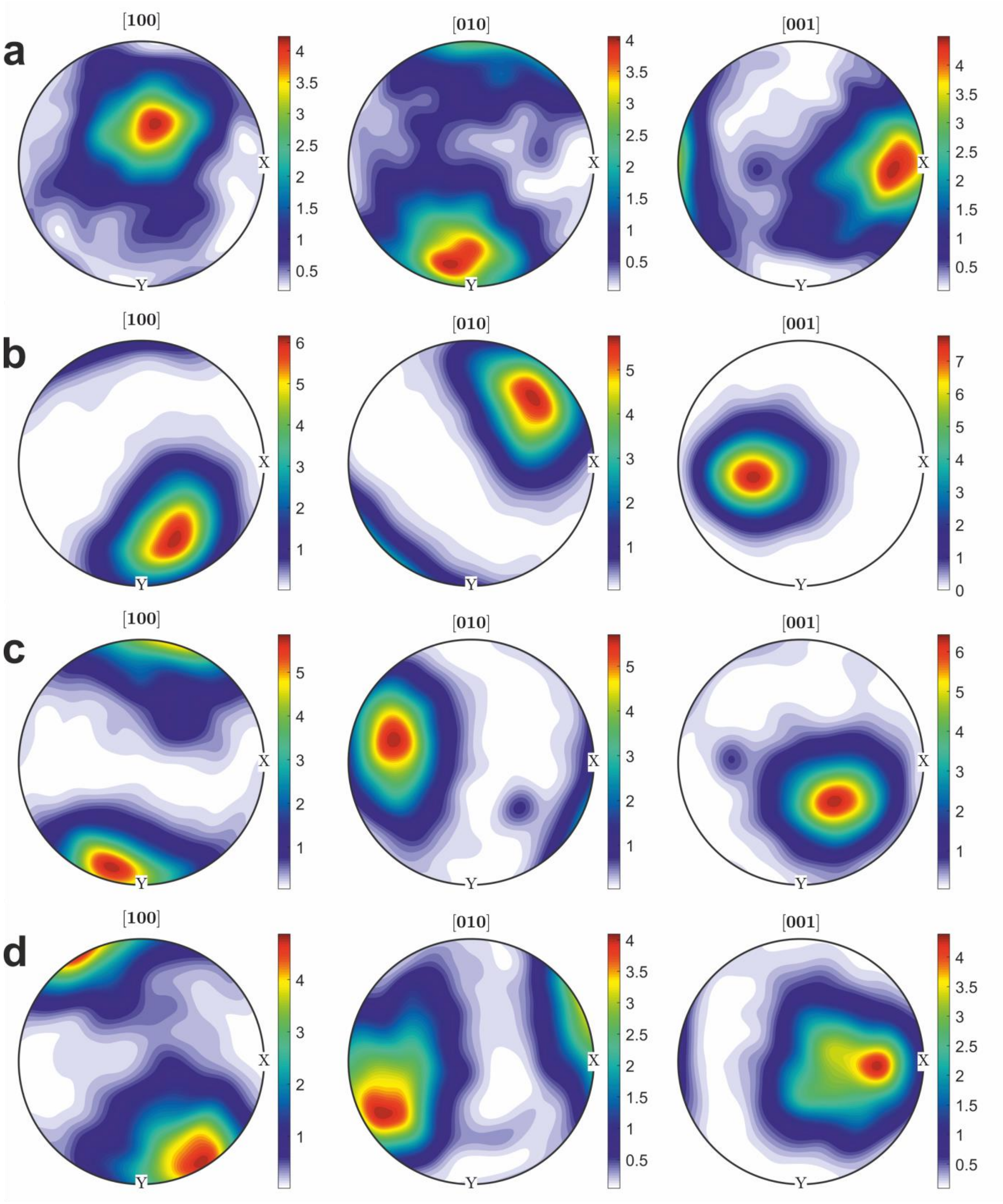

***Figure 4.8** Pole figures constructed from individual CPO domains observed at SL2. Half-width = 10°. a) Pole figure constructed from the light purple CPO domain that lies below pressure shadow grains in Figure 4.7; b) Pole figure constructed from the dark purple CPO domain in the top right of Figure 4.7; c) Pole figure constructed from the light blue CPO domain in the top right of Figure 4.7; d) Pole figure constructed from the pink CPO domain that merges with light blue domain to the top left of Figure 4.7.*

A distinct population of albite grains occurs at SL2 in pressure shadows related to stress heterogeneities around mafic porphyroclasts (top of Fig. 4.7, Fig. 4.9). Grain size is significantly larger in bands of grains derived by precipitation into pressure shadows than in the wider albite matrix, with grains commonly on the order of hundreds of microns in diameter (Fig. 4.9). At natural strain rates and stresses, the dominant deformation mechanism in such grains, at around 500 °C, is expected to be grain-size insensitive dislocation creep (see deformation mechanism maps, Fig. 1.2), and when grain boundaries, coloured with respect to misorientation angle, are plotted on EBSD maps, common evidence for subgrain walls (2–15°) in the large grains can be observed, suggesting that dislocations may have been mobile in these grains; i.e. recovery of dislocations into low-energy configurations (Drury and Urai, 1990) occurred. Strain accommodation by diffusive mass transfer is less likely to be dominant in these grains due to the increased length of diffusion pathways. Because these grains are interpreted to form by 'classic' precipitation, not interface-coupled replacement, subgrain formation by imperfect topotaxy is not interpreted to be the mechanism by which the observed subgrains have formed.

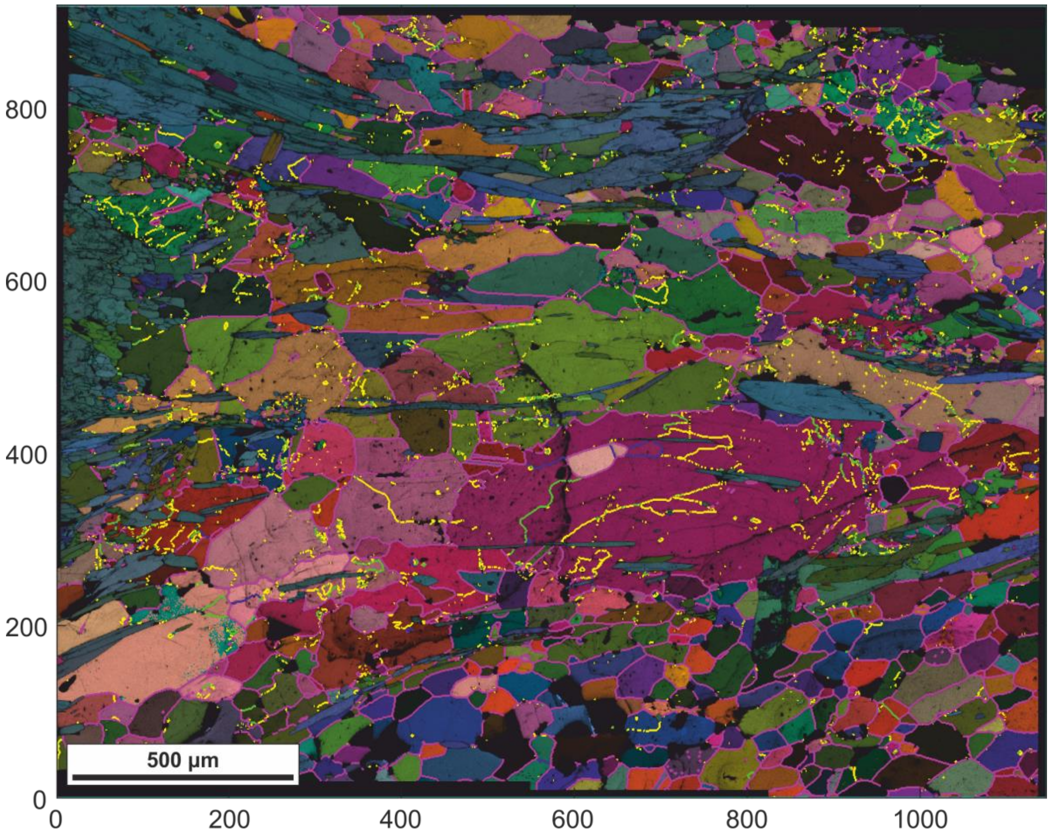

Figure 4.9 *Detail of albitic pressure shadow grains from SL2. Abundant subgrain walls can be observed within these hundreds of µm-scale grains. (Sub)grain boundaries are coloured with respect to misorientation: yellow > 2°, blue > 5°, light green > 10°, fuchsia > 15°.*

At SL3, distinct CPO domains can still be observed in the fine-grained albite matrix (Fig. 4.10), but texture strength within the domains is in general weaker than those calculated for CPO domains at SL2 (Table 4.1). MADs plotted for SL3 domains have a peak at around 50–60°, with a skew towards higher angles (i.e. more random). Pole figures for the domains are variable, although the [001] axis consistently plots in the z-direction, suggesting that grains rotated primarily around this axis (Fig. 4.11). Of note are the pole figures for the green-orange domain (Fig. 4.11c, which suggests these grains are aligned preferentially for slip on [010](100). The [010] direction commonly appears in Weighted Burgers Vector (WBV) analyses performed on these samples (see previous chapter; Wheeler et al., 2009). However, as previously stated, dislocation creep is not interpreted to have dominated deformation in these samples, and [010](100) has not been identified as an active slip system in plagioclase.

Another feature of note in the SL3 sample is a very fine band of grains that comprises a preferred orientation domain that was derived from an originally twinned grain whose two orientations appear orange and blue-purple (Fig. 4.12; similar to the pseudomorphic grain shown in Fig. 3.14). The grains in this band fall, in part, within a single large clinozoisite grain, and partly outside of that grain. This texture shows that a twinned plagioclase grain existed before the clinozoisite formed, although it was almost certainly originally a Ca-bearing species of plagioclase (as it crystallised in a gabbro), and so the commonly-observed twin signature in most CPO domains is most likely preserved from original parent grains, rather than a feature produced by deformation. Texture strength (M-Index; Skemer et al., 2005) of albite grains within the clinozoisite is calculated to be relatively low, at 0.14, compared to 0.13 (i.e. almost identical) in the part of the band that falls outside the clinozoisite (Table 4.1). Misorientation angle distribution plots are also very similar. The main difference in the albite grains is grain size and shape, with those inside the clinozoisite having a mean grain diameter of 18.9 μm and a mean aspect ratio of 1.49 (as calculated using MTEX; grains < 10 pixels removed; see Appendix 2), and those outside having a mean diameter of 26.4 μm and a mean aspect ratio of 1.78. Grain elongation can occur during diffusion creep, e.g. Wheeler (2009), and curved boundaries and triple-junction angles observed in the albite grains that lie outside of the clinozoisite also suggest some late-stage annealing has occurred.

By SL4, many regions of albite contain no distinguishable CPO domains (e.g. Fig. S4.1). Where they do exist (Fig. 4.13; Fig. 4.14), texture strength has weakened further (Table 4.1). Pole figures reveal a large spread in their maxima (Fig. 4.13c; Fig. 4.14c). The presence of a minor subgrain wall population remains. Figure 4.14b shows a WBV magnitude map (see section 3.4.5; Wheeler et al., 2009), which can be considered to be a proxy for dislocation density.

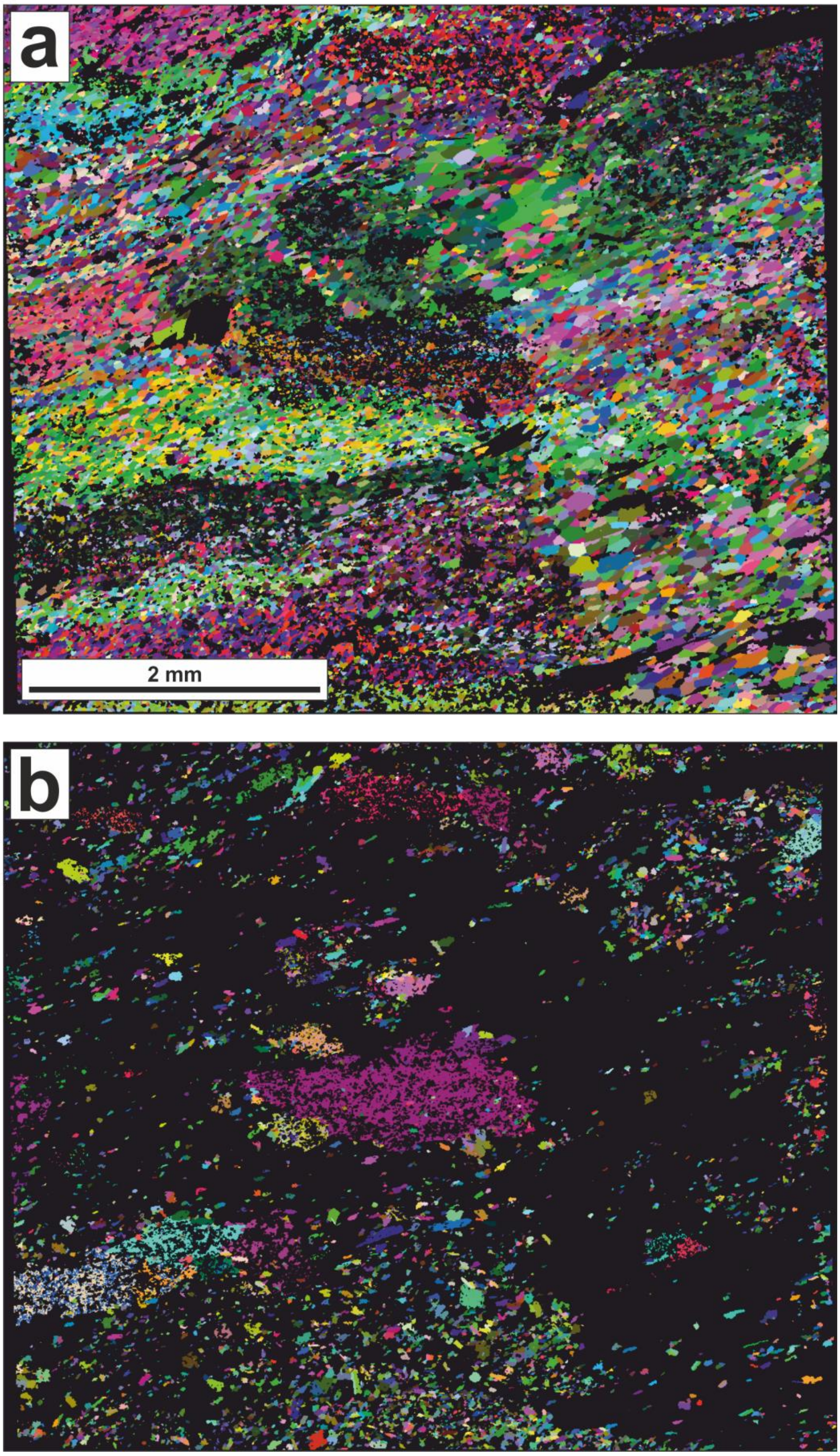

Figure 4.10 *a) All-Euler EBSD map of albite grains at SL3. Albite retains distinct CPO domains. b) All-Euler map of clinozoisite grains. Clinozoisite sometimes appears as large single crystals with many albite inclusions i.e. poikiloblasts (see Fig. 4.12 for detail); this is not observed at other strain levels.*

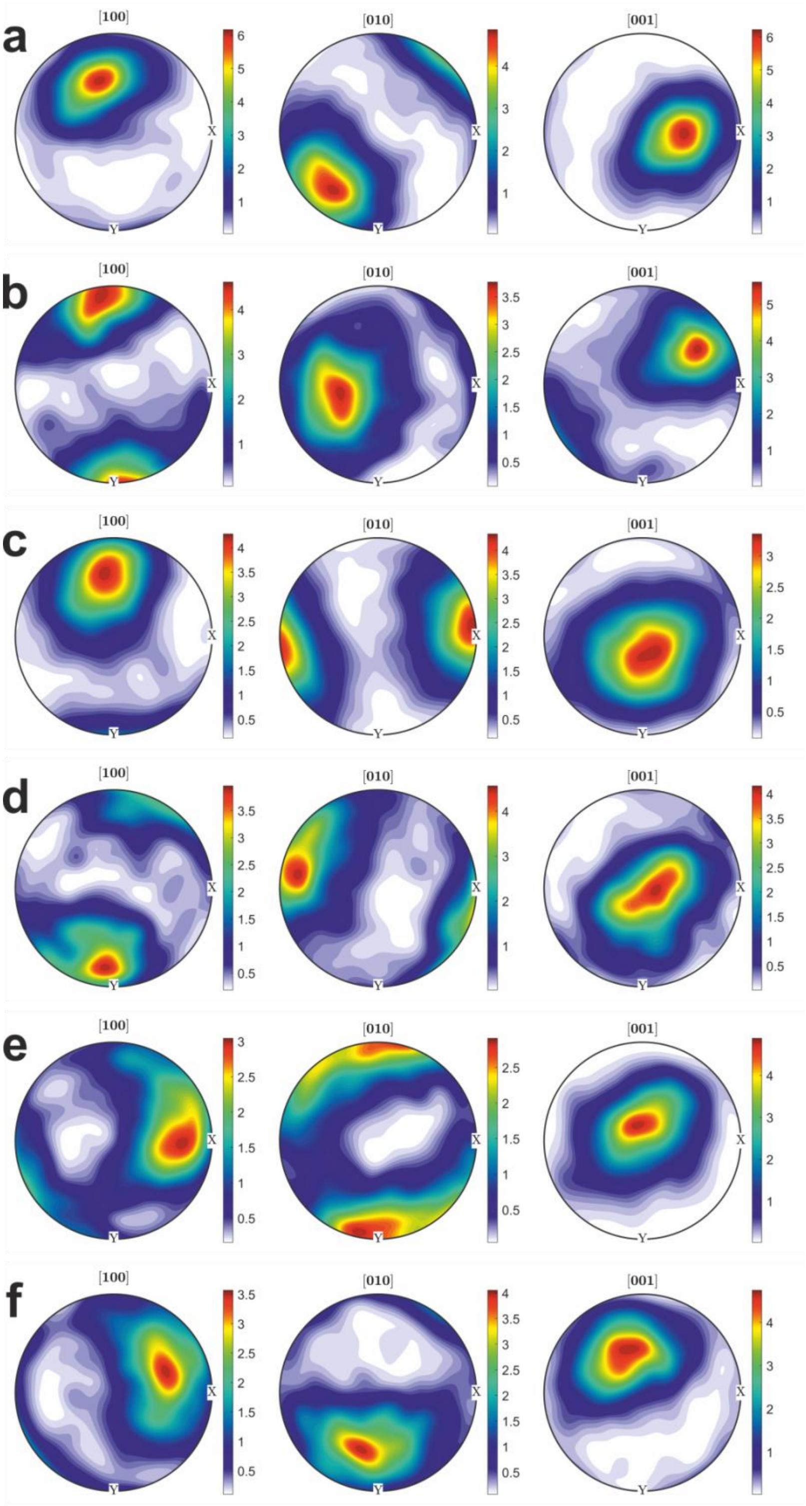

Figure 4.11 *Pole figures constructed from the different-coloured (All-Euler scheme) CPO domains observed at SL3, as shown in Figure 4.10. Half-width 10°. a) purple domain (top left of Fig. 4.10), b) pink domain (half way down left hand side of Fig. 4.10), c) green-orange domain directly below pink domain (left side of Fig. 4.10), d) thin green domain above blue-red domain (bottom left of Fig. 4.10), e) blue-red domain (bottom left of Fig. 4.10), f) green sliver below blue-red domain (bottom left of Fig. 4.10).*

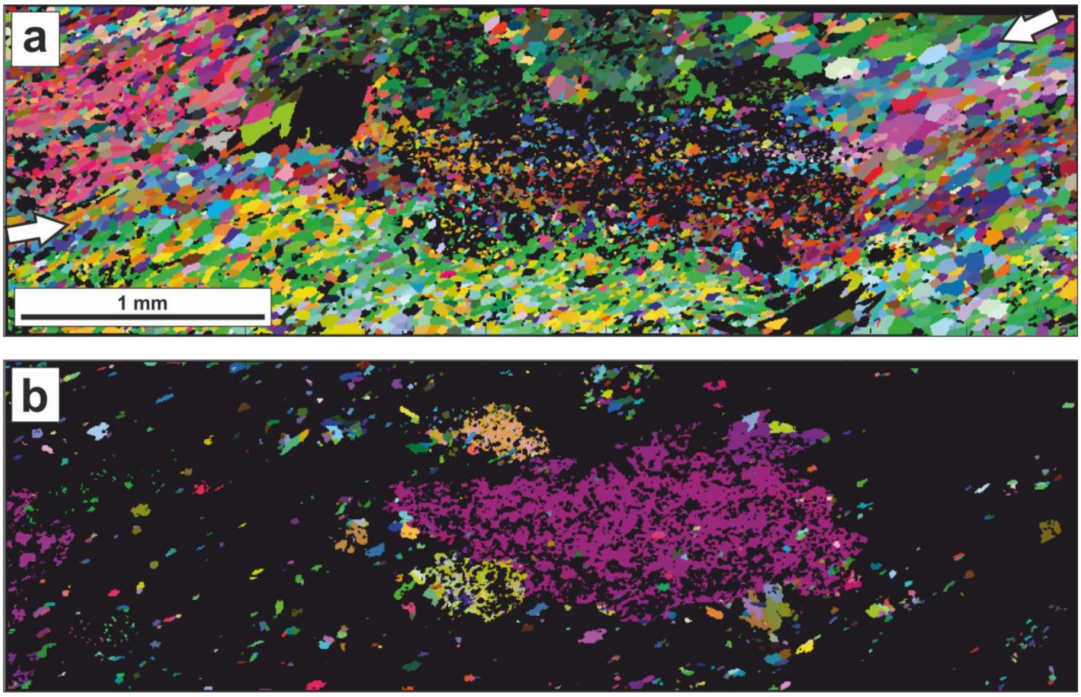

Figure 4.12 *All-Euler maps showing an albite CPO domain with blue-orange twin signature that falls part inside and part outside of a large clinozoisite grain. White arrows define ends of the twinned domain of interest. a) Albite distribution, b) Clinozoisite distribution. Relative grain relationships show that i) a twinned plagioclase grain existed before the clinozoisite formed (but was probably Ca-bearing originally); ii) the twin signature that is often observed within CPO domains at all strain levels is inherited from original Ca-bearing parent grains, as are the CPO domains themselves; iii) there is no difference between texture strength in albite grains within or outside of the clinozoisite; iv) albite grains probably grew by late-stage textural annealing where there was no other phase impeding growth.*

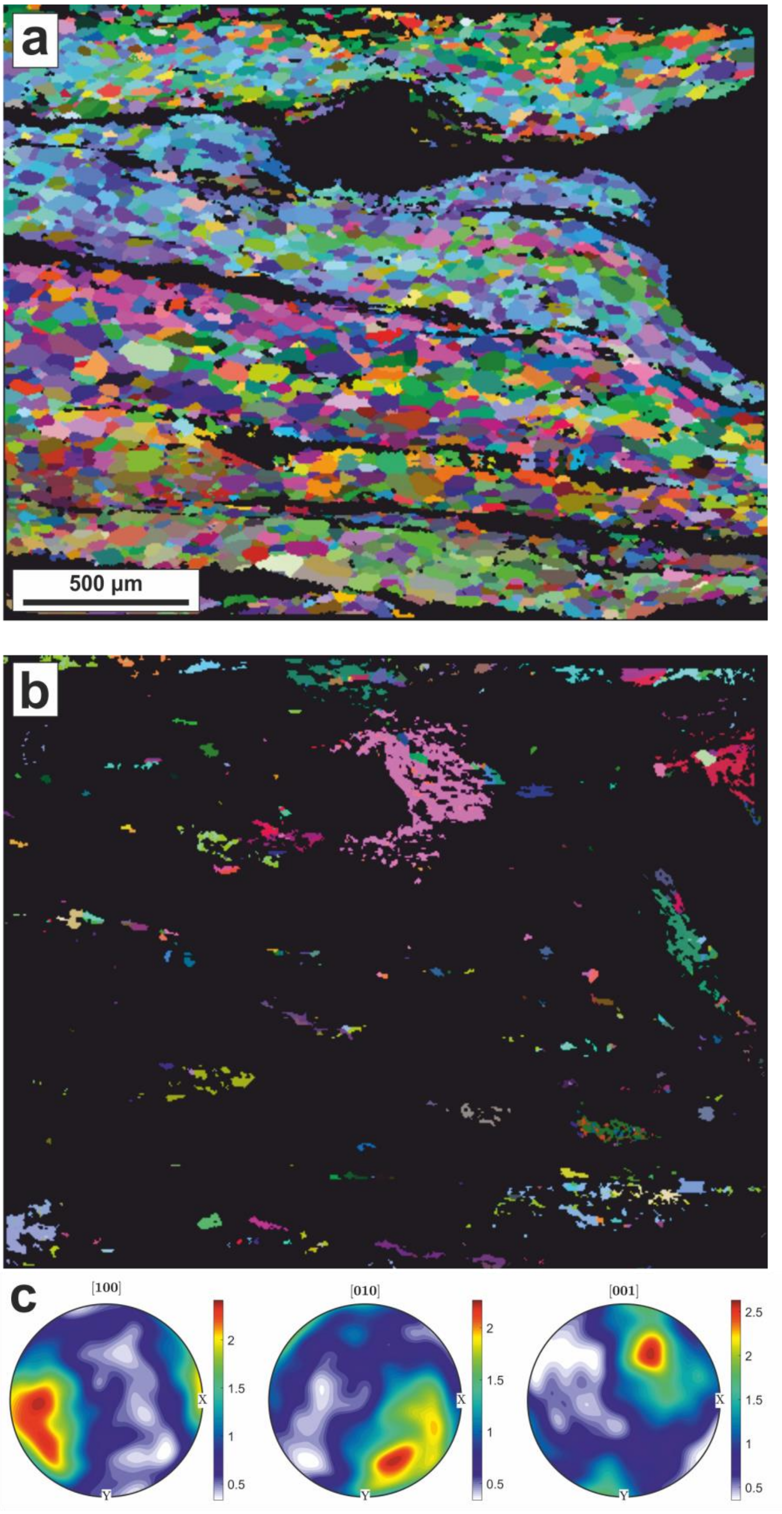

Figure 4.13 *a) All-Euler EBSD map of albite at SL4. A light blue CPO domain is observed, although in general at SL4 such domains are often absent in the albite grains (e.g. region below blue domain). b) All-Euler EBSD map of clinozoisite distribution. c) Pole figure constructed from the light blue domain in (a). Half width = 10°.*

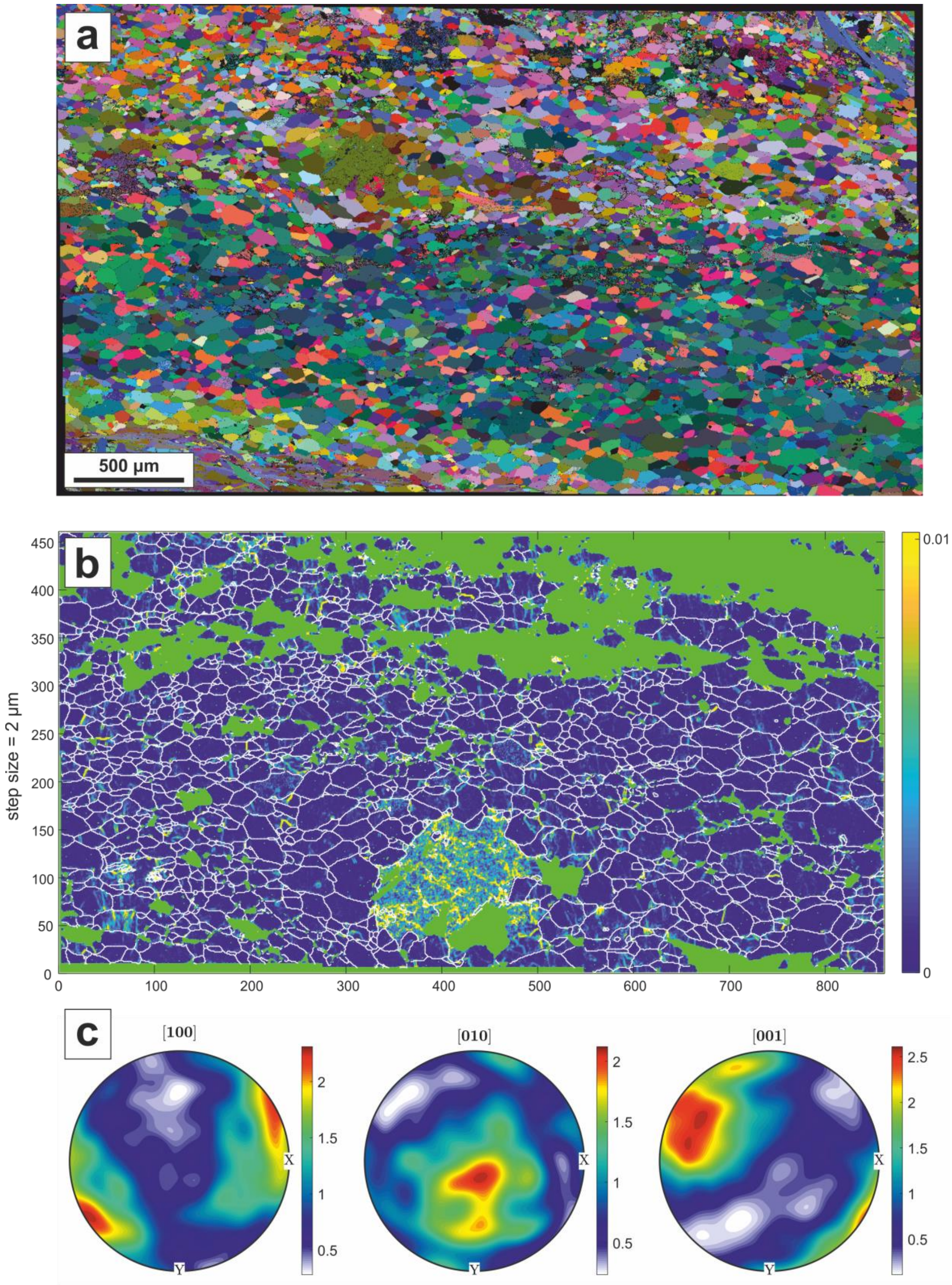

Figure 4.14 *a) All-Euler map showing CPO domain at SL4. b) WBV magnitude map showing high intragranular distortion in large grain, interpreted as a porphyroclast remnant with a signature attributed to a replacement reaction (see Chapter 3). The WBV plot also shows consistent, subparallel subgrain walls in small grains, which may be a signature of a small influence of dislocation creep. c) Pole figure from CPO domain (lower band of colour in (a)). Half width = 10°.*

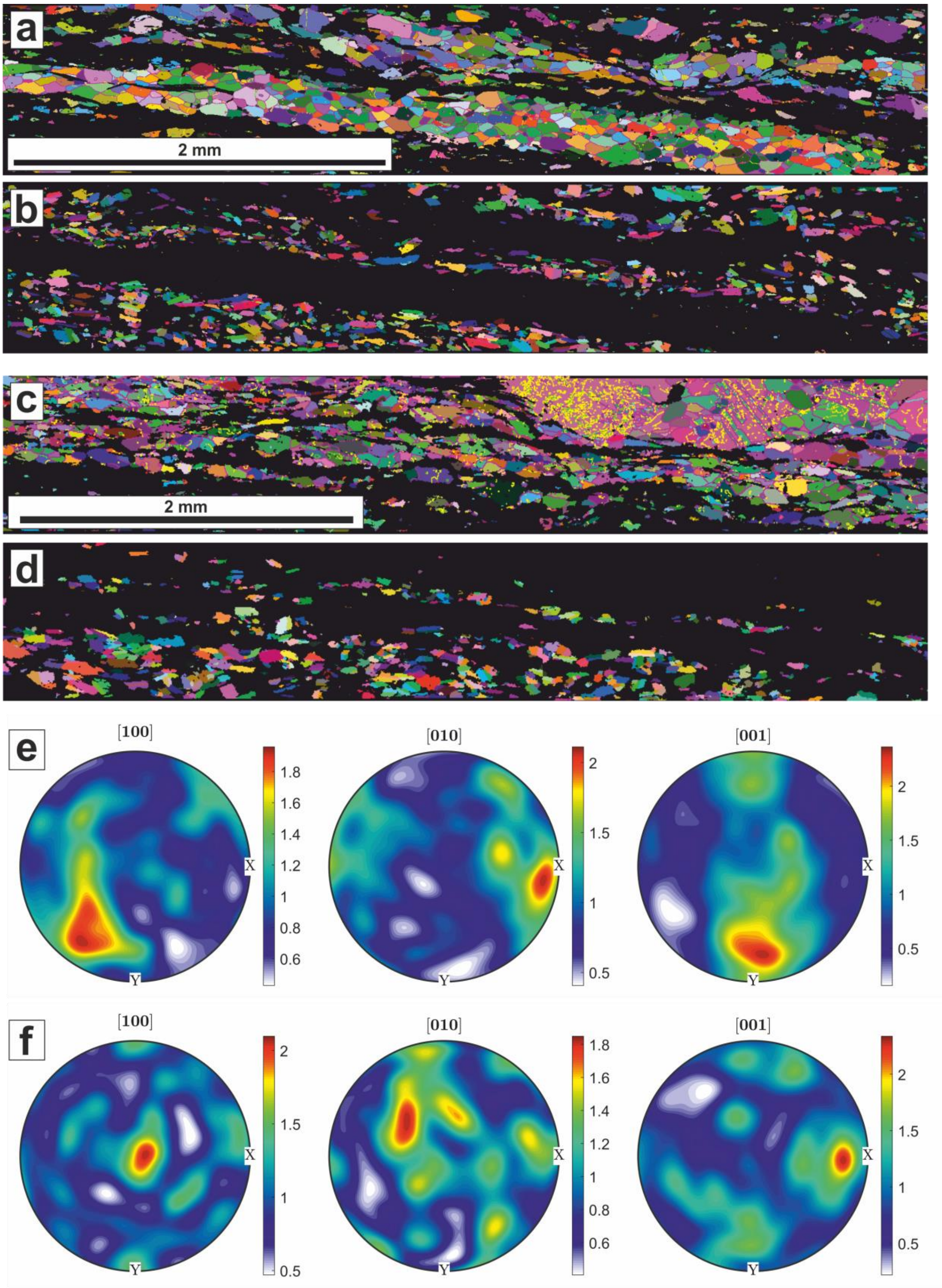

Figure 4.15 *All-Euler EBSD maps of albite (a and c) and clinozoisite (b and d) in two subareas at SL5. No obvious CPO domains are observed in the albite grains. Pole figures for albite in e) and f) are calculated as one-point-per-grain from regions a) and c) respectively.*

Subgrain walls appear as yellow lines within grains in the WBV plot (Fig. 4.14b). Their presence may indicate a minor influence of dislocation creep during deformation (Fig. 1.2). The large grain with a mottled yellow colour in Figure 4.14b is a remnant of the large albite porphyroclasts observed at the lowest strains, and interpreted to be the product of an interface-coupled dissolution-precipitation reaction (Putnis, 2009); see Chapter 3 for a detailed description of this process. At SL5, no CPO domains were observed in bands of albite grains (Fig. 4.15). Large mafic porphyroclasts are no longer present.

4.5.3.1.1 Albite misorientation angle distributions

Low-angle misorientations found in the distorted porphyroclast remnants at SL1 led to a large peak in the misorientation angle distribution (MAD) at misorientations < 10° (Fig. 4.16a). The misorientations between the porphyroclastic parent grains and the small grain population produce a separate peak at closer to 40°. The neighbour-pair distribution is skewed towards lower angles (Fig. 4.16a). At SL2, an MAD plot from the light blue CPO domain in Figure 4.7 shows a dominant peak at around 50°, with another small peak at very low misorientations betraying the continued presence of a minor population of low-angle boundaries (Fig. 4.16b). The neighbour- and random-pair distributions in Figure 4.16b are identical, indicating all of the grains in the light blue CPO domain are derived from the same parent. CPO domains at SL3 show a very similar distribution to those at SL2, although there is a slight shift towards higher misorientations, and there is a greater population of angles that tend towards random (Fig. 4.16c). MAD plots from SL4 show a wide peak that is shifted to around 60°, and noticeably skewed towards random (Fig. 4.16d). At SL5, MAD analysis shows both neighbour- and random-pair distributions tend to random (Fig. 4.16e–f).

4.5.3.2 Clinozoisite microstructures

At SL1, clinozoisite grain shapes suggest growth along pre-existing boundary features within albite-rich regions (Fig. 4.17). Albite inclusions within clinozoisite share a low angle relationship with one another, and with surrounding albite, suggesting they are all derived from the same parent. The albite boundary features being exploited could be (micro)fractures, subgrain walls, or a mixture of both (see discussion). Part of an albite porphyroclast remnant, which contains abundant subgrain boundaries, can be observed in the bottom right quadrant of Figure 4.17. SL1 is the only strain level at which clinozoisite does not show a significant crystallographic (and shape) preferred orientation (Fig. 4.18a).

Clinozoisite is the most common second phase in the two-phase matrix at SL2 (Fig. 4.7b). Clinozoisite abundance is variable but it is relatively well-mixed with (i.e. homogeneously-distributed within) albite grains in the matrix. In regions close to, or between, mafic porphyroclasts, clinozoisite can occur in mostly monophase regions, in which albite grains fill interstices (see in particular streaks of clinozoisite between clinopyroxene porphyroclasts in the lower part of Fig. 4.7b; also Fig. 4.18). Clinozoisite grains are elongate along the [010] axis (Deer et al., 2013). The elongate grains are, in general, aligned with the foliation and so define a strong shape and crystallographic preferred orientation. A 180° twin rotation about (001) is commonly observed in the elongate clinozoisite grains, despite twinning being rare in general in the epidote minerals, and normally about (100) when observed (Deer et al., 2013). At the lowest strains, clinozoisite can be seen to grow along twin planes in albite, and to inherit that twin plane (Fig. 4.19), suggesting many of the small clinozoisite grains nucleated along such boundaries (possibly in microcracks), and their positions have subsequently been adjusted/rotated after a grain size reduction of albite followed by pressure solution of albite and associated GBS, which are processes that are enhanced at finer grain sizes. Rotation of elongate clinozoisite to form a combined SPO and CPO is reflected in the strong clusters in pole figures constructed from clinozoisite grains in samples deformed to strains higher than SL1 (Fig. 4.20).

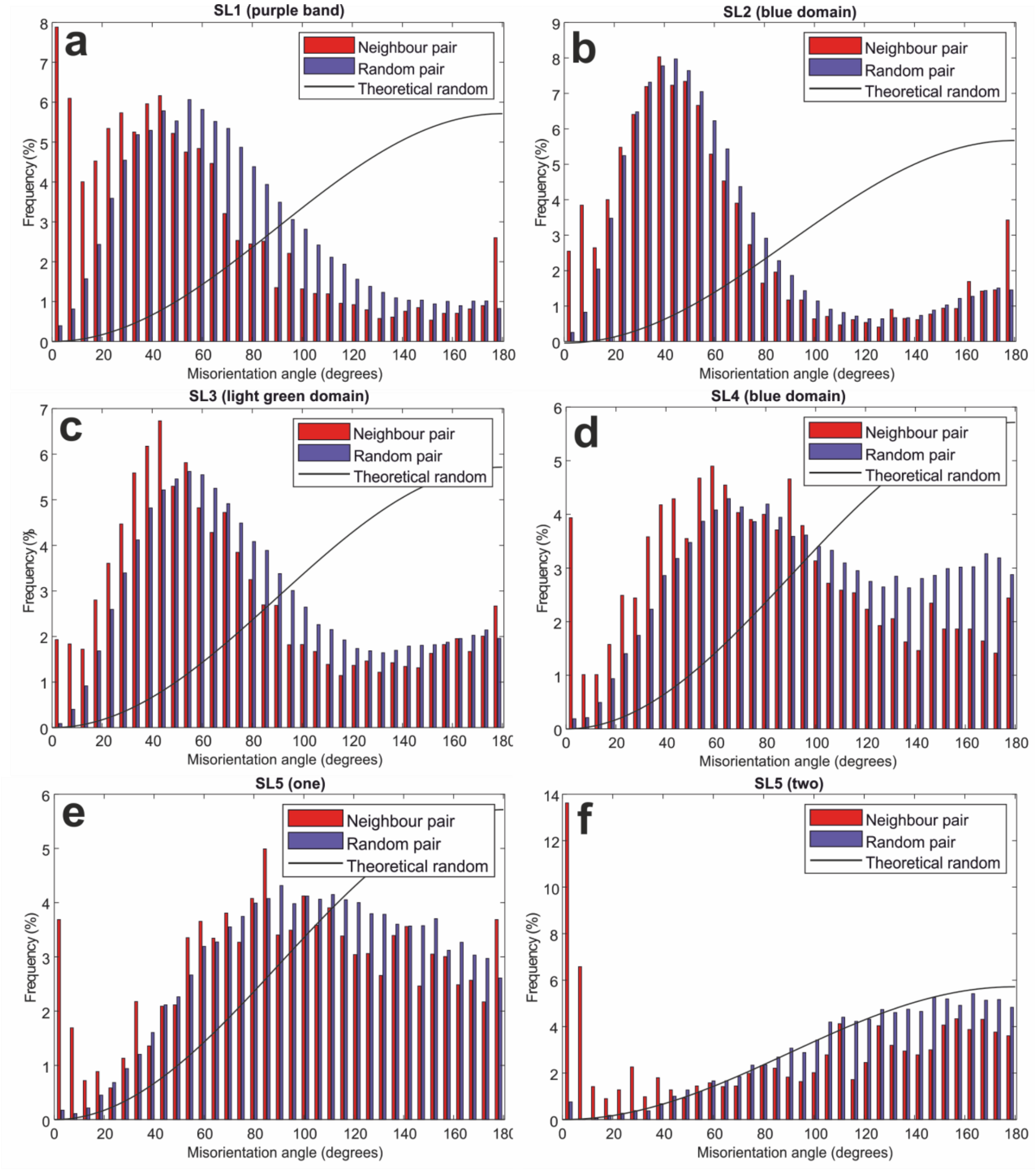

Figure 4.16 *Evolution of albite misorientation angle distributions with increasing strain. a) The SL1 plot contains a prominent low angle boundary peak due to presence of abundant subgrain boundaries. The peak in neighbour-pair high angle boundaries lies at 40° but the overall distribution of high-angle grain boundaries (HAGBs) is skewed towards low angles. The slight mismatch between neighbour- and random-pair distributions suggests the presence of >1 original grain. b) The SL2 plot shows that neighbour- and random-pair distributions are almost identical, indicating grains from a single CPO domain (i.e. originally all part of the same parent). The peak in HAGB distribution is again at 40°, but distribution is no longer skewed towards lower angles. A noticeable but less significant subgrain population remains. c) At SL3 the distribution is similar to SL2, but contains an increased population of higher-angle HAGBs (i.e. randomisation of grain orientations). A minor subgrain population remains. d) At SL4, the peak in HAGB distribution is*

noticeably diminished and shifted to a maximum around 60°. Overall distribution is significantly skewed towards random. A significant subgrain population is present. e) At SL5, some signature of a texture remains in the distribution, but the peak is shifted to some 80–100°, with a separate but significant peak at low angles. f) Also by SL5, many albite regions have no CPO (i.e. grains are randomly oriented); however, subgrain boundaries remain prominent in the microstructure.

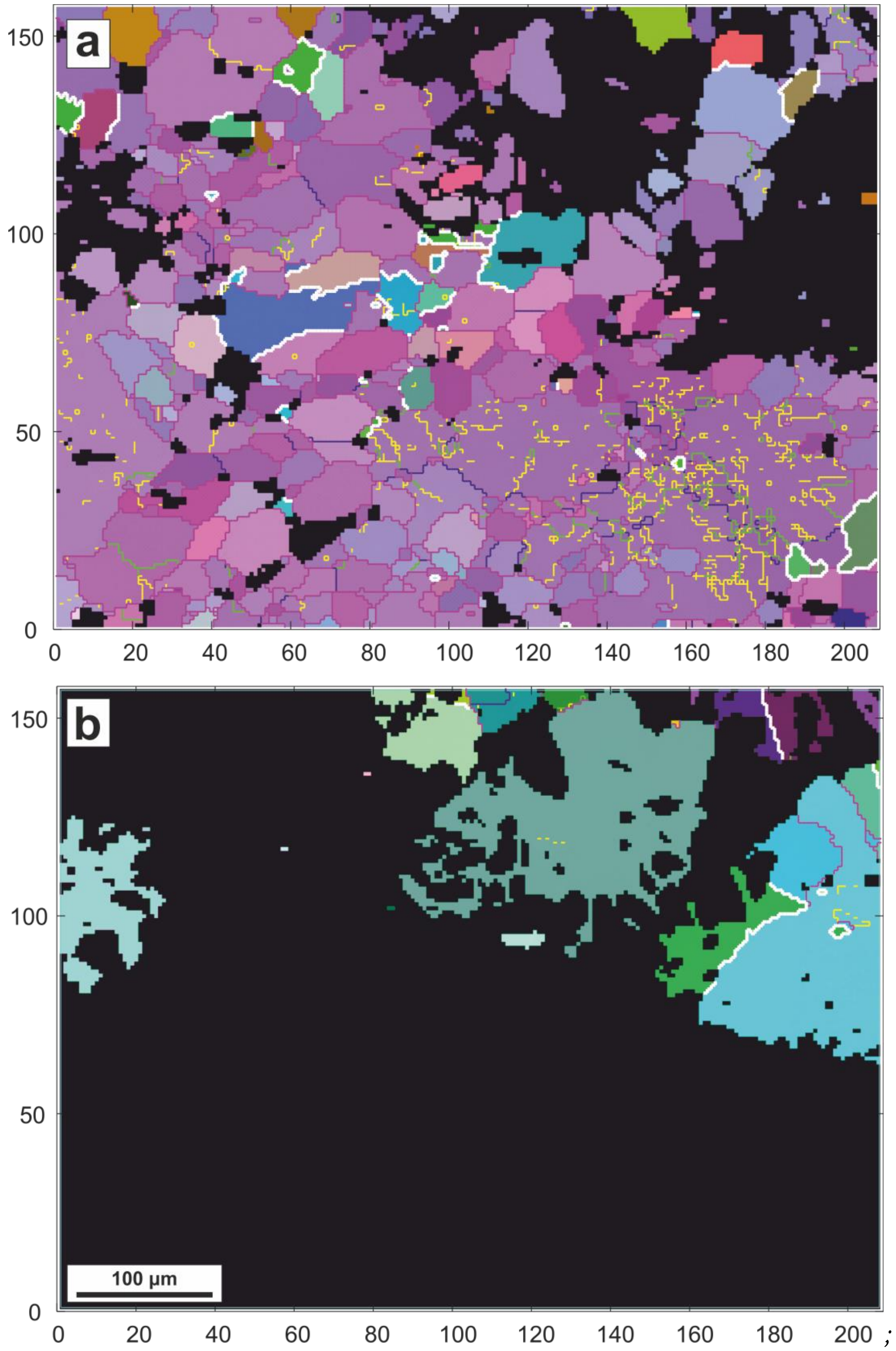

Figure 4.17 *All-Euler maps showing clinozoisite growth structures at SL1. a) Albite grains, with (sub)grain boundaries coloured with respect to misorientation: yellow > 2°, blue > 5°, light green > 10°, fuchsia > 15°, plus 180° twin planes in white). b) Clinozoisite has grown around pre-existing feldspar, which is now albite. Albite inclusions and other grains share an orientation, so are derived from the same parent. Clinozoisite habit suggests growth along pre-existing 'weaknesses' in the albite.*

The behaviour of clinozoisite is very similar in all samples above SL1. Some of the mm-scale clinozoisite grains observed at SL3 show rather different behaviour to clinozoisite found in other samples. The twinning common to clinozoisite grains in other samples is rarely observed, and instead, mm-scale crystals show evidence of abundant low-angle misorientations and intracrystalline distortion, identified by the smooth change in All-Euler colours (Fig. 4.21). Indexing of distorted clinozoisite is relatively poor. An albitic CPO domain, coloured mainly green and brown, which is incorporated within the large clinozoisite grain, has a relatively strong texture (MI = 0.25; Table 4.1) compared to an adjacent blue-orange domain beneath the clinozoisite grain (MI = 0.14; Table 4.1).

4.5.3.3 Microstructure and texture evolution

Montages of multiple maps were collected across mm-scale regions at each strain level. 153 maps (SL1 = 25 maps, SL2 = 41 maps, SL3 = 36 maps, SL4 = 36 maps, SL5 = 15 maps) were selected at random to investigate links between mean grain size, mean grain

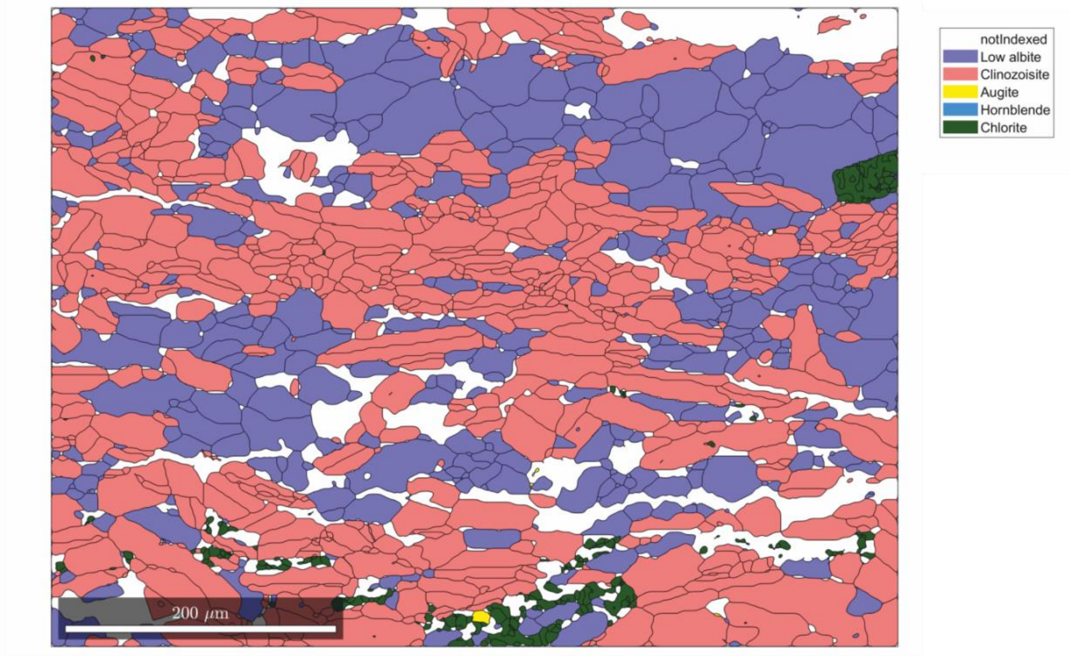

Figure 4.18 *EBSD phase map, showing that at SL2, tightly packed clinozoisite grains surround albite grains with an interstitial grain shape, suggesting albite has dissolved to leave clumps of clinozoisite. This suggests rigid rotation of clinozoisite grains in a soluble albite matrix probably accounts for the observed clinozoisite CPO/SPO. However, the clinozoisite grains often fit tightly together, so there may have been some exchange of material (i.e. grain growth) between clinozoisite grains as well. This figure produced using MTEX 5.0. As the original image was quite pixelated, grain boundaries have been smoothed to remove a 'stair-step' effect, although the effect can still be seen on some twin boundaries in clinozoisite that are flat planes (i.e. straight lines in map view) in reality.*

elongation (aspect ratio) and clinozoisite (a proxy for second phase) abundance, per map. All parameters were calculated using MTEX, following the code presented in Appendix 2. In general, aspect ratio is found to decrease with increasing grain size across the range of strain levels, although within each strain level, there is no clear increase or decrease. Aspect ratios of albite grains at SL5 are significantly larger than those at SL1, and average grain diameter is also noticeably smaller (Fig. 4.22a). Mean albite grain sizes are reduced with increasing clinozoisite abundance at all strain levels (Fig. 4.22b). Increased clinozoisite content with increasing strain, as measured using QEMSCAN (Fig. 4.4f), has a direct impact on grain size, with albite grains from all maps processed at SL1 having a mean diameter of 29.3 μm, while mean diameter of albite grains of maps collected from SL5 samples is calculated to be 23.6 μm (Fig. 4.22b). Increased clinozoisite abundance also leads to an increase in mean aspect ratio, with significant differences between the lowest and highest strain levels (Fig. 4.22c).

Texture strength within identifiable domains decreases with increasing strain level (Table 4.1; Fig. 4.22d), as expected for deformation in diffusion creep, e.g. Karato and Wu (1993); Kilian et al. (2011). There is a large range in texture strength values calculated from CPO domains in samples deformed at SL2, which also show variability in grain size and shape, and clinozoisite abundance. These data therefore provide an opportunity for analysis of the links between albite grain morphology, clinozoisite abundance and texture strength. Six adjacent CPO domains (Fig. S4.2) were processed using MTEX, to calculate average grain size, aspect ratio, clinozoisite abundance and texture strength (Table 4.2; Fig. 4.23). Grain size appears to have a significant effect on texture strength, with relatively small increases in mean grain diameters leading to a drastic reduction in the calculated M-index (Fig. 4.23a). Clinozoisite abundance has a similarly significant impact on texture strength, with increased clinozoisite abundance resulting in a higher M-index value (Fig. 4.23b). There appears to be no correlation between aspect ratio and texture strength (Fig. 4.23c).

The purple domain is unique in that clinozoisite content varies within it, so the two sub-regions can also be compared. Texture strength calculated from albite grains within the very high clinozoisite region (58%) is 0.74, whereas in the low clinozoisite region (16%), texture strength in the purple domain is 0.58. Grain size and shape are also affected by clinozoisite abundance, with mean grain diameter rising from 16.8 μm to 22.8 μm, and mean aspect ratio falling from 2.16 to 1.90 outside the high clinozoisite part of the domain.

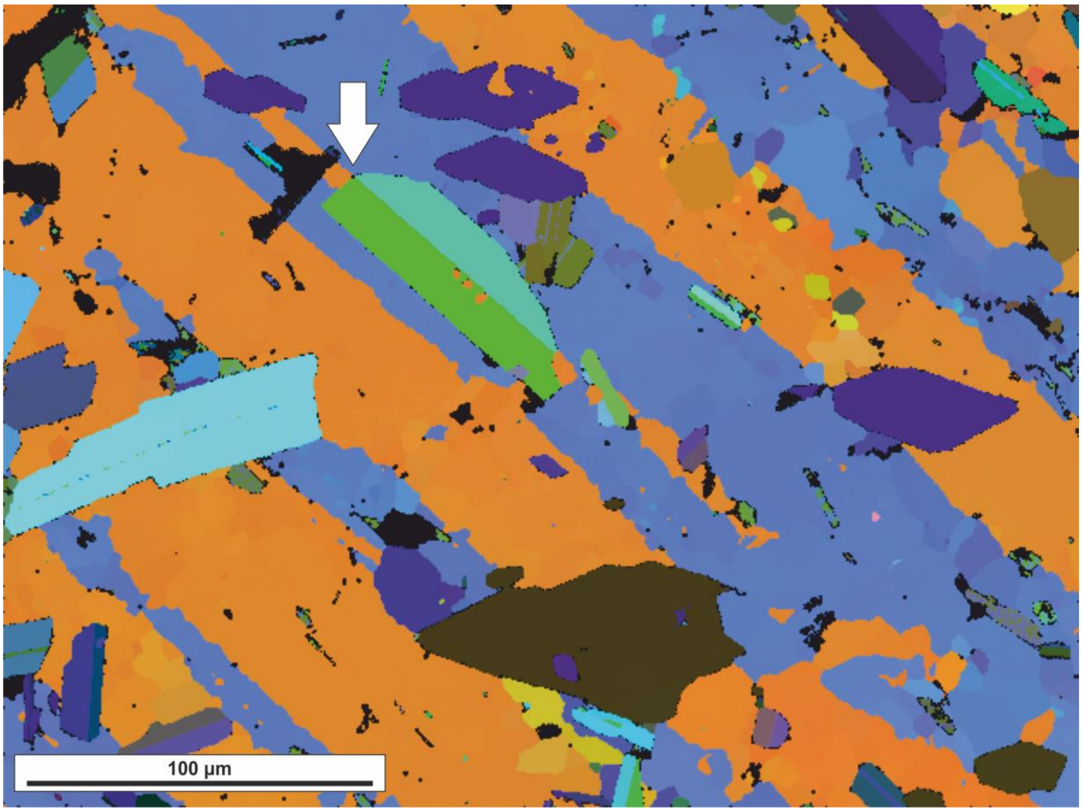

Figure 4.19 *All-Euler EBSD map showing a green-aqua clinozoisite grain that has inherited a twin plane (white arrow) from twinning in a Ca-bearing plagioclase parent. The orange-blue twin pattern has been inherited by smaller albite grains during pseudomorphic replacement. Three small albite inclusions in the clinozoisite grain show the same orientation as the orange twin segments.*

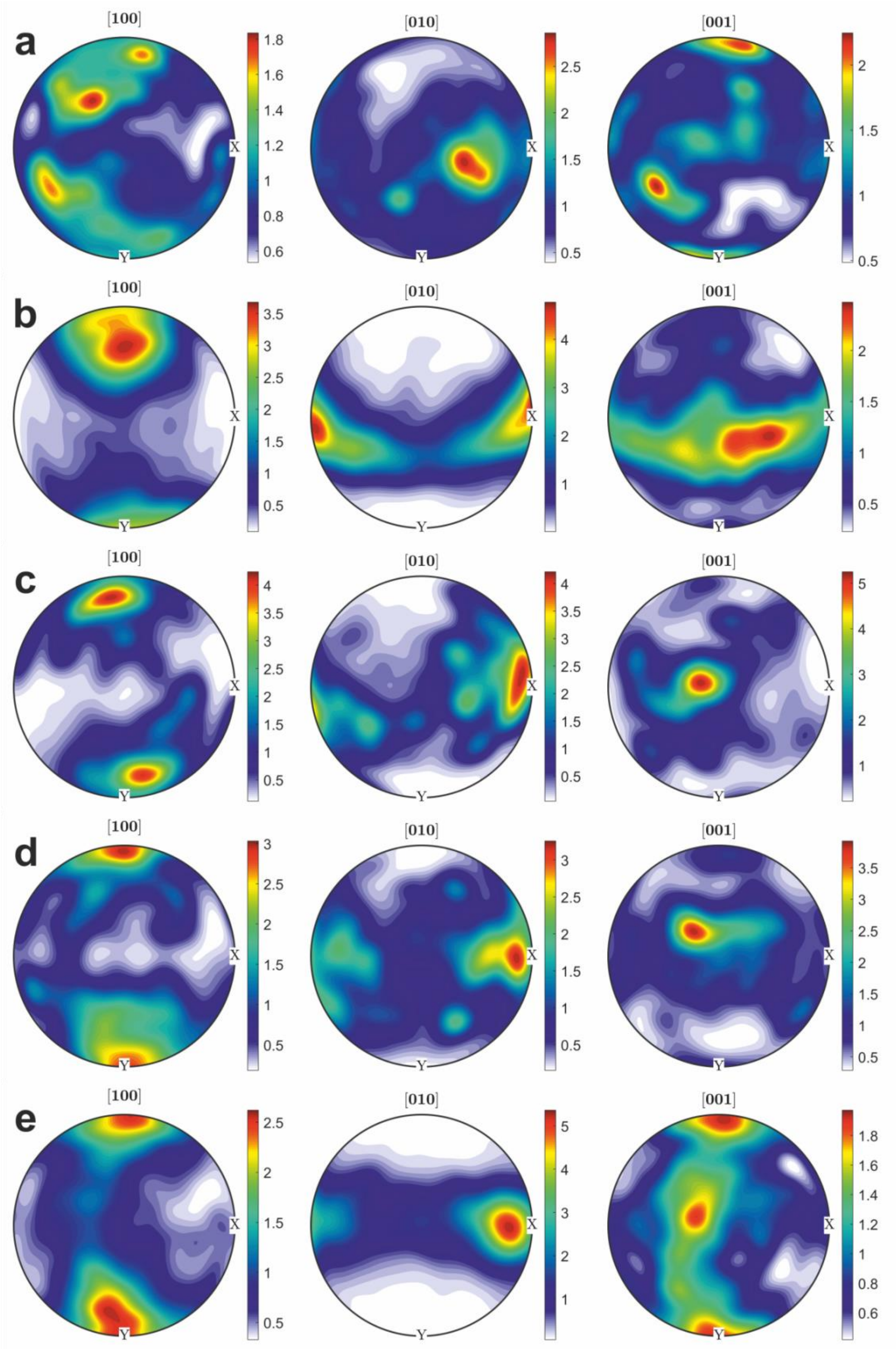

Figure 4.20 *Pole figures constructed from clinozoisite grains found in samples at different strain levels (SLs). a) SL1, from entire map shown in Fig. 4.5, b) SL2, from mixed matrix region shown in Fig. 4.7, c) SL3, from entire map shown in Fig. 4.10, d) SL4, from entire map shown in Fig. 4.13, e) SL5, from entire map in Fig. 4.15. At SL1, no significant CPO is observed. After SL1, [010] (the long axis of the elongate clinozoisite grains) is consistently aligned with foliation. [100] and [001] form either discrete maxima or girdles.*

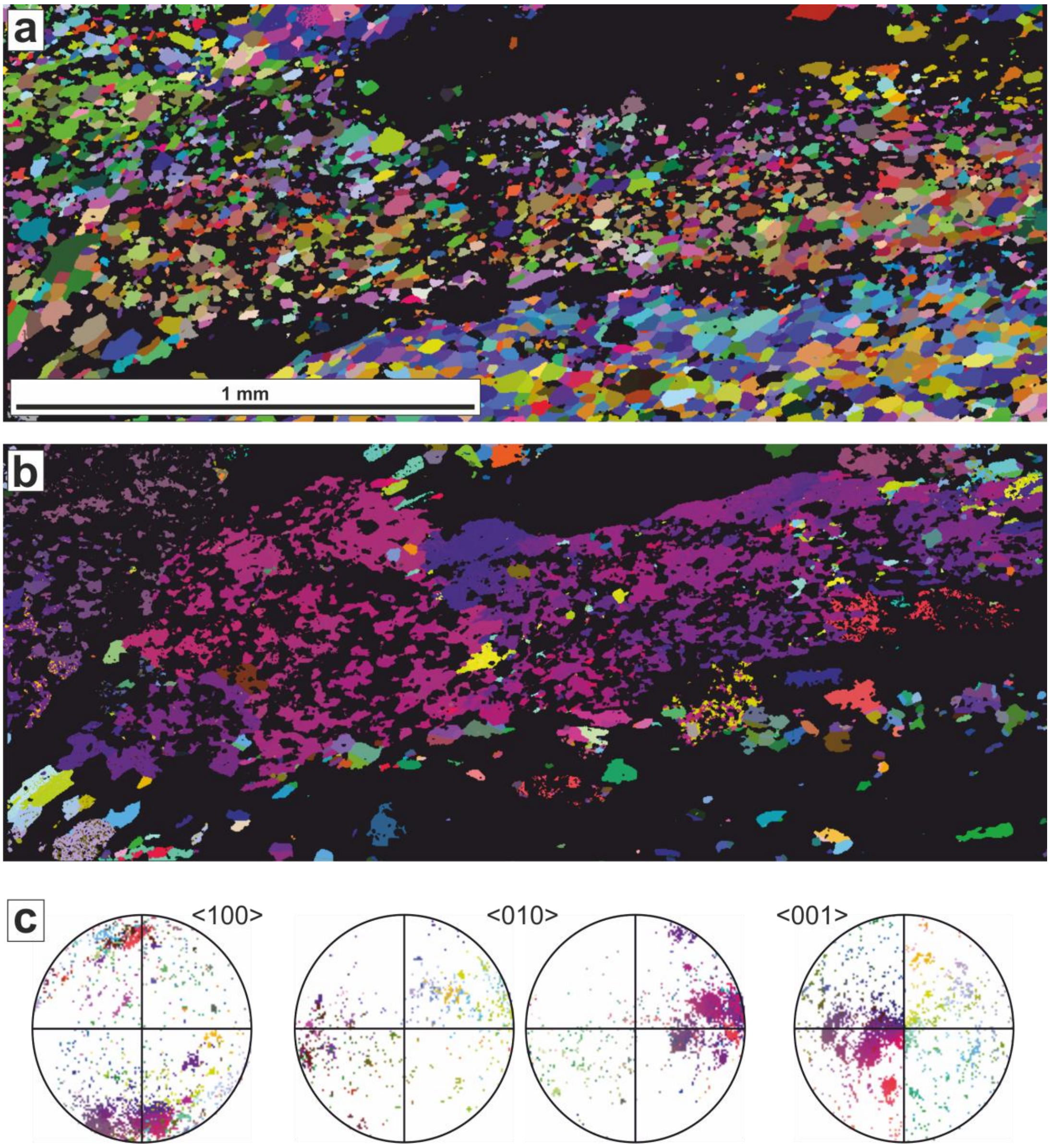

Figure 4.21 *A mm-scale distorted clinozoisite grain observed at SL3. a) All-Euler EBSD map of albite grains that surround the distorted clinozoisite; b) All-Euler EBSD map showing the clinozoisite grain. The slight differences in colour are taken as evidence of lattice distortion due to the presence of dislocations (i.e. crystal plastic deformation); c) pole figures constructed from clinozoisite EBSD data. The clusters of closely-associated colours support the interpretation that the clinozoisite deformed plastically.*

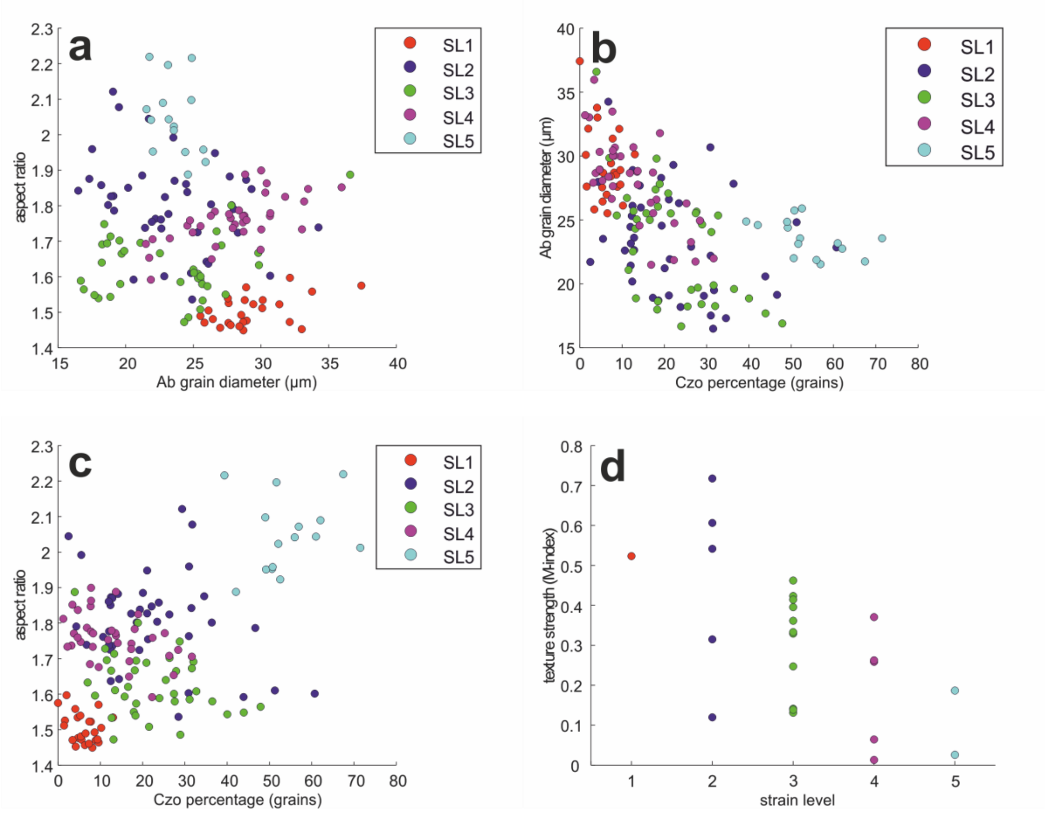

Figure 4.22 a) Aspect ratio as a function of grain size. There is no strong correlation in each subset. Overall aspect ratio decreases with increased grain size, which may suggest textural annealing after grain flattening during pressure solution. b) Grain size as a function of clinozoisite abundance. There is a strong correlation between mean albite grain size and the percentage of clinozoisite; with increasing clinozoisite abundance, albite grains become smaller in every subset. This suggests the secondary phase influenced albite evolution by inhibiting grain growth, which can preserve the lifetime of diffusion creep (Pearce and Wheeler, 2011). c) Aspect ratio as a function of clinozoisite abundance. At the lowest strain (SL1), when clinozoisite is least abundant and not well mixed, aspect ratios are smallest. With increased mixing (SL2–4) there is a wide scatter, probably due to heterogeneities in the degree of mixing. At the highest strain (SL5), where clinozoisite is most abundant, aspect ratios in albite are distinctly higher – clinozoisite abundance (and mixing?) appears to have an effect on grain shape. This may be due to enhanced dissolution of albite at phase boundaries. Note that pressure shadow grains are not included in plots.

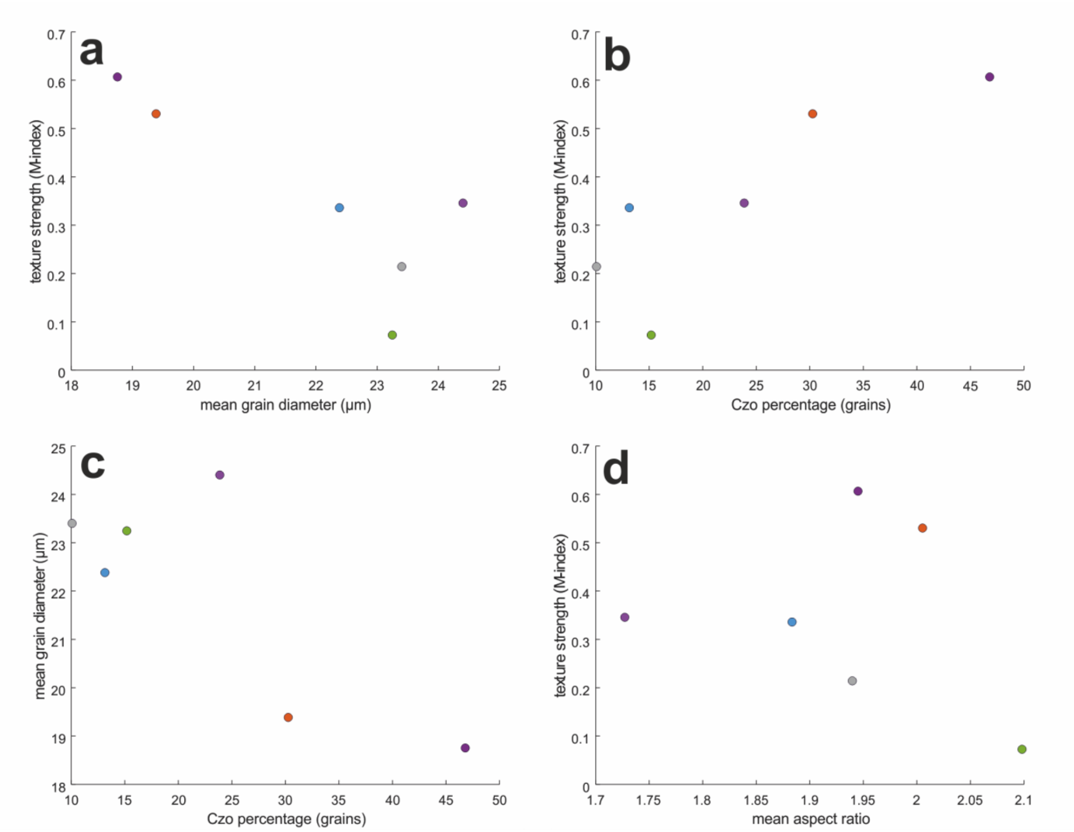

Figure 4.23 *Texture strength of CPO domains at SL3 as a function of a) grain size, b) clinozoisite abundance and d) aspect ratio. c) shows the relationship between clinozoisite abundance and grain size. Colours correspond to the colour of domains in Fig. S4.2.*

4.6 Discussion

4.6.1 Fracturing and plasticity in albite at low temperatures

The mineral assemblage present in all samples indicates deformation occurred at greenschist facies conditions in the middle crust (Winter, 2001). This range of P–T conditions (300–450 °C, less than 900 MPa; see Prior and Wheeler, 1999) mean that intracrystalline processes such as dislocation climb and recovery are expected to be restricted in plagioclase. This is because the volume diffusion of vacancies necessary for dislocations to climb is temperature-dependent (Tullis and Yund, 1985). Because of this lack of low-temperature plastic behaviour, most studies of crystal plasticity in plagioclase focus on amphibolite or higher P–T conditions. Kruse et al. (2001) studied anorthositic gabbros that were deformed naturally at ~700 °C and below 900 MPa. At these conditions, porphyroclastic grains in orientations preferentially aligned for slip on the dominant [001](010) system produced small recrystallized grains by subgrain rotation. However, in porphyroclastic grains not preferentially aligned for slip on that system, microfracturing was the dominant mechanism that created new small grains, despite the relatively high temperatures. Tullis and Yund (1987) performed deformation experiments on albite that showed feldspar commonly deforms by cataclastic flow over a wide range of P–T conditions, due to restrictions on dislocation motion (Tullis and Yund, 1985), and due to its two excellent cleavages on (010) and (001). Their results showed a pressure dependence on dominant deformation mechanism, with high confining pressures supressing fracture on cleavages and promoting dislocation creep, e.g. at 1–1.5 GPa, samples underwent cataclastic flow at 500–650 °C, transitional behaviour was observed at 700–850 °C and steady-state dislocation creep dominated at temperatures $\geq$ 900 °C. The experiments were performed at strain rates of 10^{-6} s^{-1}, some 8–10 orders of magnitude faster than commonly expected natural strain rates, which promotes fracturing behaviour, so fracture behaviour may be an artefact of experimental conditions. However, abundant evidence also exists for fracturing in feldspar throughout the crust. Stünitz et al. (2003) experimentally deformed gem-quality plagioclase at 900 °C, 1 GPa confining pressure and strain rates of 10^{-7} s^{-1}, and found deformation bands and fractures were important sites of glissile dislocation generation, from which they concluded that fracturing may help to induce crystal plastic deformation. Additionally, Stünitz et al. (2003) suggested that grain fragments generated by fracturing may act as nuclei for new grains during dynamic recrystallization, so the two deformation mechanisms may be coupled.

Deformation by cataclastic flow within feldspar crystals can result in the flattening of grains and the development of CPOs, due to extensive grain-scale faulting on feldspar's two good cleavages, which results in any subsequent movement on the grain-scale faults simulating slip on those planes (Tullis and Yund, 1987). Thus, the CPO domains observed in the fine-grained albitic matrix of the samples studied here do not have to be derived by dislocation creep. In previous analysis of similar samples, Prior and Wheeler (1999) suggested that each CPO domain could be derived from original mm-scale single crystals, rather than dislocation creep, on the basis that measured CPOs varied from domain to domain, and the triclinic symmetry observed in individual domains did not match the kinematics of deformation. Prior and Wheeler (1999) do not provide a mechanism for grain size reduction; see section 3.6.2.3 for a discussion of possible mechanisms. Jiang et al. (2000) showed, in a detailed analysis of similar samples, that there was no unique orientation relationship between measured CPOs and the kinematic axes, which would be expected if they were produced by dislocation creep. In particular, Jiang et al. (2000) noted that no CPO domain displayed a cluster of (010) poles around the pole to foliation, which is commonly observed for plastically-deformed plagioclase (Ji and Mainprice, 1988; Satsukawa et al., 2013). Jiang et al. (2000) took the lack of subgrains observed optically, and the lack of low-angle peaks in misorientation angle distribution plots as supporting evidence that dislocation creep was not significant.

Strain Level	Sample	Band	n	Misorientation Index
1	2.3c4	light purple	2080	0.52
2	3A	light blue	1440	0.61
2	3A	dark purple	1861	0.72
2	3A	pink above dark purple	936	0.31
2	3A	pink below dark purple	2683	0.54
2	3A	greyish random	886	0.12
3	3.7bTWO	light green	2822	0.42
3	3.7bTWO	below light green	820	0.41
3	3.7bTWO	red-blue	1710	0.33
3	3.7bTWO	above red-blue	804	0.36
3	3.7bTWO	below red-blue	946	0.40
3	3.7bTWO	twinned within Czo	816	0.14
3	3.7bTWO	twinned outside Czo	357	0.13
3	3.7bTWO	pink above twin	1015	0.33
3	3.7bTWO	pink top left	2200	0.46
3	3.7bONE	within Czo	1353	0.07
4	5.1aONE	light blue	720	0.26
4	5.1aONE	above light blue	450	0.26
4	5.1aTWO	one e.g. of random	3883	0.01
4	5.1bONE	upper band	1571	0.06
4	5.1bONE	lower region	844	0.37
5	6.1ONE	main band (no obvious CPO)	3165	0.19
5	6.1TWO	no clear domain	2861	0.03

Table 4.1 *Evolution of texture strength, as quantified using the Misorientation Index of Skemer et al. (2005), in albite CPO domains with increasing strain. Texture strength was calculated using the MTEX code found in Appendix 2. See also Fig. 4.21d.*

The data collected for this study broadly match the observations made in Prior and Wheeler (1999) and Jiang et al. (2000), in that most of the CPO domains do not align with the kinematic framework to suggest they were produced by dislocation creep, but some additional features of note can also be observed in the new data. Specifically, evidence for (010) poles aligned with the pole to foliation can be seen in a number of CPO domains (Fig. 4.6 and Fig. 4.8a, which are well-aligned for slip on [001](010), and Fig. 4.11e, which is well-aligned for slip on [100](010)). It must be noted, however, that the samples used in this study were originally gabbroic, and it is common for (010) (and less commonly (001)) crystallographic planes to align to form a foliation during magmatic flow (Satsukawa et al., 2013), so this could be an orientation inherited from an original igneous texture. Bearing in mind that each individual CPO domain is interpreted to be derived from a single crystal, however, it would seem there was not a particularly strong magmatic texture in the original gabbro, or more of the domains might be expected to show this alignment.

Also apparent in this study's samples are noticeable populations of subgrain boundaries, which were not observed by Jiang et al. (2000), where their absence was used to support the notion that dislocation creep activity was negligible. The misorientation angle distribution plots presented in Figure 4.16 show that subgrains can be observed at all strain levels. These low-angle boundaries, which are present in the population of new small grains (which are undistorted when first formed, see Chapter 3), are not interpreted to be a product of imperfect topotactic growth, because the new small grains did not form by interface-coupled replacement. Thus, although cataclasis was the dominant mechanism of initial grain size reduction and fluid infiltration (Chapter 3), the samples display evidence that dislocation creep may played a minor role in the subsequent microstructural evolution of the metagabbros.

One or more slip systems with the [010] Burgers vector may have been active during deformation of the albite grains. In the WBV analyses detailed in Chapters 3 and 6, the [010] Burgers vector was commonly observed to be present in subgrain walls, and the same Burgers vector is found in subgrain walls seen at higher strain, although it is not the only one present, e.g., Figure 3.10. Some pole figures show the [010] direction to be close to, or aligned with, the lineation direction, e.g., Figure 4.11c, in which (100) could conceivably act as the glide plane. Shigematsu and Tanaka (2000) analysed fine-grained plagioclase in ultramylonites deformed at low temperature (below 500 °C) and used TEM to identify at least six Burgers vectors contributing to crystal plasticity at these conditions, with no influence from the [001](010) system that dominates deformation at high temperatures. Although [010] is not identified as one of the active Burgers vectors, the results of Shigematsu and Tanaka (2000) do suggest that i) crystal plasticity is possible at low temperature and ii) different slip systems are active at different temperatures in plagioclase. It should be noted, however, that these authors did not discuss the idea that observed texture may be developed through inheritance during chemical change, which should be considered in the analysis of recrystallized plagioclase (see Chapter 3).

Deformation mechanism maps constructed for wet albite of grain sizes similar to those observed in the metagabbros (~50 μm), deforming at 450 °C and natural stresses (~100 MPa), were presented in Rybacki and Dresen (2004a). The deformation mechanism maps suggest that, under these conditions, albite will deform under a small influence from dislocation creep (~10–20%, calculated from the ratio of strain rates for each deformation mechanism), which increases with grain size (Fig. 1.2). This assertion is backed up by the intracrystalline distortion observed in large pressure shadow grains (Fig. 4.9), which is not regarded to have formed by imperfect topotaxy during interface-coupled replacement, as pressure shadow grains are assumed to be produced by a 'classic' precipitation mechanism. Variation in the density of subgrain walls is observed between different CPO domains, which possibly reflects how well-oriented initial mm-scale grains were for slip on a common plagioclase system, with cataclasis being more dominant in grains poorly oriented for slip (Stünitz et al., 2003). Variation in fracturing vs. plastic deformation in the original gabbros may explain the observed differences in clinozoisite distribution. In grains where plasticity and subgrain formation were dominant, there may have been less space for clinozoisite to nucleate and grow, so that small, sparse clinozoisite grains formed. Conversely, fluid influx into the original gabbros may have been greater in grains that experienced cataclasis, meaning clinozoisite may have been able to nucleate more freely and grow as large grains, incorporating albite fragments as inclusions, as seen in Figures 4.14b and 4.21b.

Despite the potential small influence of dislocation mobility, the most likely explanation for the CPO domains observed here is inheritance from large single crystals. As evidence for brittle deformation is common, it is likely that Ca-bearing plagioclase parent grains broke down through a combination of cataclasis and reaction to a more albitic composition (see Chapter 3). On grain size reduction, the dominant deformation mechanism in the metagabbros switched to fluid-assisted diffusion creep (pressure solution), which modified, but preserved, the CPO domains, so the observed inherited texture domains have been produced by a combination of brittle and viscous processes.

4.6.2 Weakening of an inherited texture during pressure solution

The CPO domains observed in the fine-grained albitic matrix are concluded to be inherited from large Ca-bearing parent plagioclase single crystals (Chapter 3). The observed grain size reduction of albite porphyroclasts in SL1 (and by inference the Ca-bearing parent grains), by a few orders of magnitude, at higher strains would profoundly affect the deformation behaviour of the deforming metagabbros. Deformation mechanism maps (Fig. 1.2; Rybacki and Dresen, 2004b), for example, show that, in wet plagioclase at 450 °C and a strain rate of 10^{-14} s^{-1}, a grain size reduction from a few hundred µm to a few tens of µm would induce a transition from dominantly grain-size insensitive to grain-size sensitive creep, which in the hydrated conditions of the middle crust, is termed pressure solution (Gratier et al., 2013; Rutter, 1983; Wheeler, 1992). Pressure solution, and its high-temperature equivalent in the absence of fluids, grain boundary diffusion creep, must occur with simultaneous GBS, to maintain continuity during grain shape change (Elliott, 1973). GBS results in grain rotations, which is why diffusion creep is often cited as the dominant deformation mechanism in the absence of a strong texture in highly deformed rocks, (e.g., Kilian et al., 2011; Menegon et al., 2013; Rosenberg and Stünitz, 2003) (although see section 5.2 for an overview of possible limitations to these arguments).

		n Ab	n Czo	% Czo (grains)	MI	JI	mean diameter (µm)	mean aspect ratio
top pink	all	523	164	23.9	0.35	10.2	24.4	1.73
purple	all	2078	1828	46.8	0.61	22.2	18.8	1.95
	high Czo	724	1005	58.1	0.74	35.4	16.8	2.16
	low Czo	628	120	16.0	0.58	18.7	22.8	1.90
light blue	all	509	77	13.1	0.34	12.3	22.4	1.88
	tail (tentative)	153	41	21.1	0.18	6.6	20.8	1.75
	rest of band	325	44	11.9	0.46	18.3	22.1	1.94
pink-brown	all	2150	933	30.3	0.53	10.7	19.4	2.01
light purple	light purple	857	96	10.1	0.21	4.1	23.4	1.94
	beneath light purple	419	75	15.2	0.07	2.2	23.2	2.10

Table 4.2 *CPO domain data from individual albite domains at SL2. See Fig. S4.2 for images of all CPO domains.*

In this study's samples, there is a clear trend of texture weakening with increasing strain (Table 4.1). This can also be seen in the MAD plots, as the peak in both neighbour-pair and random-pair plots gradually shifts towards higher angles with increasing strain (Fig. 4.16). Neighbour-pair and random-pair populations exhibit the same behaviour, because all grains are derived from the same parent, and so have undergone the same deformation history (Wheeler et al., 2001). The inherited CPO domains persist to high strains (SL3 and 4), probably because the initial texture was very strong, having been derived from a single large crystal. At the margins of domains, grains from each domain can be seen to mix with one another; a good example of this is the tail of the light blue domain in Figure S4.2e. The mixing of grains from domains above and below the light blue domain results in the outline of the left half of the domain in that field of view becoming difficult to define. Some of the grains must have moved – presumably with limited rotations, as they retain an orientation close to the bulk domain – at least as far as their own diameter into an adjacent domain during sliding. As domains continue to thin with increasing strain, it is straightforward to see that mixing of adjacent domains could lead to an overall randomisation of grain orientations. The signature of two original domains could still be picked up, however, by observation of a systematic shift between neighbour-pair and random-pair orientations in the MAD plots (see methods). Another indication that rotations may have been somewhat limited during initial pressure solution is the albite twin signature (a 180° rotation about (010)) that is identifiable by a peak at 180° in the neighbour-pair distribution of the lower strain (SL1 and 2) MAD plots. This peak is absent or very limited at higher strains (Fig. 4.16).

Some of the microstructures observed in the metagabbros studied here are ambiguous, and could be interpreted as evidence that dislocation creep dominated deformation. Even at metamorphic grades higher than the greenschist facies conditions described here, microfracturing could produce a CPO (as described by Tullis and Yund, 1987) at high temperatures, particularly if a parent crystal is more favourably oriented with respect to the stress system for fracture than for dislocation creep (Kruse et al., 2001). The associated grain size reduction could result in a switch to deformation dominantly by diffusion creep, which has been shown to be able to preserve any pre-existing CPO to quite high strains (Wheeler, 2009), so that inherited parent grain orientations could be preserved. In such a scenario, CPO domains could form and be preserved without any major influence of dislocation creep, as they are interpreted to have formed in the studied samples. In rocks interpreted to have deformed at higher grade conditions, however, where dislocation creep is expected to be active, such a process could easily be overlooked.

4.6.3 The influence of a second phase on microstructural evolution

4.6.3.1 Clinozoisite growth and initial distribution

At SL1, clinozoisite grains can be observed to grow around, and incorporate as inclusions, albite grains which share orientations with one another, and the surrounding porphyroclasts and adjacent small matrix grains (Fig. 4.17). This suggests the clinozoisite exploited pre-existing planes of weakness in the small albite grain population during growth. The pre-existing planes of weakness could be a network of (micro)fractures, or subgrain walls (see Fig. 2.3). In some samples, clinozoisite grains can be observed to grow much larger than average (e.g. Fig. 4.12b; Fig. 4.21b). This suggests spatial variations in the pre-existing network of fractures or subgrains, which can be explained by some original plagioclase grains being more preferentially oriented for (micro)crushing or plastic behaviour to occur than others. It is not possible from the observations made here to distinguish which process is more likely to have occurred, and it is possible that both played a role in initial albite grain size reduction, and thus the initial growth and distribution of clinozoisite (Kruse et al., 2001). The heterogeneous distribution of fine-grained clinozoisite in the matrix may reflect differences in composition or zoning in original Ca-bearing plagioclase grains (Jiang et al., 2000).

4.6.3.2 Evolution of clinozoisite distribution with strain

Clinozoisite is observed to become progressively more abundant with increasing strain, relative to other phases (Fig. 4.4). At SL2, clinozoisite is distributed heterogeneously throughout the sample, but always occurs as a predominantly two-phase mixture with albite (Fig. 4.7). Clinozoisite can also be seen to form strain caps around mafic porphyroclasts at SL2, and locally occurs in monophase bands where local stresses may have been very high (e.g. between two rigid mafic porphyroclasts, see Figs. 4.4b and 4.9b for clear examples). The difference between well-mixed albite and clinozoisite in the matrix and the development of clinozoisite strain caps or almost monomineralic bands adjacent to rigid mafic porphyroclasts, suggests the solubility of albite was increased at locally high stresses. A local difference in albite solubility is supported by the interstitial grain shapes albite has in these regions. Clinozoisite is strongly aligned in the densely-packed regions, with shared crystal orientations being deflected around mafic porphyroclasts. In parts of the matrix not influenced by mafic clasts, clinozoisite also displays strong CPOs and SPOs (Fig. 4.20). The shared orientations could have developed either by oriented growth or rigid rotation, or a combination of both (Menegon et al., 2008). At SL1, clinozoisite grains are not aligned, but there would have been a differential stress field in these rocks (note how albite porphyroclast fragments are aligned in Figure 3.15, indicating dextral shear). This observation suggests that alignment was not produced through oriented growth. At higher strains, pole figures tend to show girdles rather than discrete maxima (Fig. 4.20b–e), which suggests rigid-body rotation occurred to align the long axis of grains – [010] – with the foliation plane, rather than oriented growth, which produces grains with a more-pronounced lineation. In regions where clinozoisite is tightly packed, clinozoisite boundaries can be seen to overlap, so some exchange of material between grains probably also occurred to produce intergrowth. In addition, 180° twinning about (001) is routinely observed in the clinozoisite grains in these samples, when clinozoisite is not commonly observed to twin (Deer et al., 2013), and twinning is normally oriented about (100) when it is observed. The Gressoney metagabbros display evidence that twinning in clinozoisite is inherited from growth along twin planes in initial plagioclase (Fig. 4.19). This suggests that clinozoisite orientation at the time of initial growth was aligned within Ca-bearing plagioclase grains that have completely broken down to fine-grained albite, which has subsequently deformed by fluid-assisted diffusion creep, meaning the current alignment of clinozoisite to foliation cannot be an original orientation. It is highly likely, then, that rigid-body rotation has caused their observed parallelism. Mainprice and Nicolas (1989) showed that during rigid-body rotation in simple shear, elongate particles can rotate indefinitely, but tend to be statistically oriented parallel to the flow plane, as their rotation velocities temporarily become zero in this orientation, which explains why the clinozoisite grains are predominantly aligned with foliation.

The impact of phase-mixing during deformation is currently a much-debated topic in the rock deformation community, due to its potential role in limiting grain growth and strain localisation in the crust, which may be fundamental to the development of plate tectonics (Bercovici and Ricard, 2012; Cross and Skemer, 2017). De Bresser et al. (1998, 2001) questioned the generally-accepted notion that grain size reduction (GSR) by dynamic recrystallization can lead to rheological weakening and strain localisation due to the switch from grain-size insensitive (GSI) to grain-size sensitive (GSS) creep. Those authors proposed that dynamic recrystallization leads to a steady-state balance between GSR and grain growth in the boundary field between dislocation and diffusion creep, and that significant rheological weakening only results if GSR occurs by other mechanisms, or if grain growth is inhibited. Platt and Behr (2011) put forward a counter-argument that GSR by dynamic recrystallization could play a fundamental role in rheological weakening of the lithosphere, because lithospheric-scale shear zones probably evolve at approximately constant stress, which means that material weakening by grain size reduction results in an increase in strain rate, not a decrease in stress. The weakening that occurs by grain size reduction and a subsequent switch in deformation mechanism could be permanent, because rates of dislocation motion, dislocation density, and recrystallized grain size would all stay the same at constant stress,.

Inhibition of grain growth can result from phase mixing. Cross and Skemer (2017) performed torsion experiments to high strains to help characterise phase mixing during the generation of ultramylonites. Monophase polycrystalline domains in the original samples were stretched and thinned to form compositional banding of only one or two grains width, which increased the influence grain boundary pinning and led to GSR below the critical limit of the deformation mechanism field boundary. At $\gamma > 17$, the monolayers necked to complete phase mixing to produce ultramylonites. In our samples, the breakdown of porphyroclasts led to a homogeneous grain size and mixing of phases with increasing strain (Fig. 4.2, Fig. 4.4). However, in detail, albite and clinozoisite never actually formed a completely homogeneous mix. Fine banding (with a width of about 3 or 4 grains, so on the order of hundreds μm) of relatively pure albite and a clinozoisite -mafic mixture persists to the highest strain levels (Fig. 4.4e, Fig. 4.5d, Fig. 4.15). The studied samples appear to have reached the critical stage where GSS creep dominates deformation (leading to the weakening of texture through rotations associated with GBS), but not quite to the stage where complete homogenisation occurs.

Despite incomplete mixing of albite and clinozoisite, the relationship between second phase (clinozoisite) abundance and albite grain size is clear (Fig. 4.22b). Albite-albite boundaries are typically lobate and grain shape (aspect ratio) appears to have some dependence on clinozoisite abundance (although grain elongation may be more dependent on amount of strain the sample has seen), which suggests grain growth by textural annealing has occurred. The twinned albite CPO domain in Figure 4.12 shows obvious differences in grain shape and size within and outside (larger grains with lobate boundaries) of the clinozoisite grain. There is no doubt the presence and abundance of clinozoisite had a direct effect on the grain size of albite, and probably extended the time over which diffusion creep could dominate deformation in in clinozoisite-rich regions of the samples (Pearce and Wheeler, 2011).

The exact mechanism of phase mixing during deformation can be difficult to determine. Metamorphic reactions play a key role in the creation of new phases, e.g. Newman et al. (1999), and that is clearly the case in our samples, with the albite and clinozoisite mixture being produced by the decomposition of Ca-bearing plagioclase and clinopyroxene (clinozoisite is locally observed to contain Fe-rich patches; Fig. 4.2) at greenschist facies. However, further modification of this assemblage during deformation is also observed, with clinozoisite clusters becoming rarer at higher strains, and clinozoisite grains becoming aligned to foliation.

In general, grain boundary sliding tends to be invoked in explanations of phase mixing, e.g. Hiraga et al. (2010), but this can occur via multiple mechanisms, such as grain switching, subgrain rotation recrystallization, or dissolution and precipitation (Cross and Skemer, 2017). In the pressure solution field, dissolution and precipitation is the mechanism most likely to control mixing by dictating where grains disappear and grow. Kilian et al. (2011) observed the precipitation of K-feldspar grains at opening sites along grain boundaries in disintegrating quartz aggregates, which pinned the quartz grain size, promoted GBS and led to a transition from dislocation to diffusion creep. Platt (2015) described a model whereby, regardless of initial grain size mechanism, a transition to grain boundary diffusion creep with GSR, accompanied by GBS, opens up voids between existing grains that are filled by diffusion and precipitation of a new phase to lead to grain mixing, similar to the mechanisms involved in creep cavitation (Fusseis et al., 2009; Menegon et al., 2015). In this study's samples, it is unclear whether precipitation of material leads to phase mixing. Clinozoisite is interpreted to have mainly formed prior to GSS deformation, from the observed twin planes that appear to have been inherited during initial greenschist-facies metamorphism of Ca-bearing plagioclase (Fig. 4.19). Precipitation of albite into pressure shadows tends to form bands of predominantly monophase material, accompanied by localised actinolite grains (e.g. top of Fig. 4.7; Fig. 4.9), and clinozoisite appears to be left behind in strain caps and sites of high local stress where albite has likely been removed by dissolution (Fig. 4.7), so overall dissolution and precipitation processes in fact appear to unmix rather than mix albite and clinozoisite in this case. It is possible that dissolution, and thus boundary sliding, is enhanced at albite-clinozoisite phase boundaries, so initial distribution of albite and clinozoisite in a fine-grained matrix may facilitate grain boundary diffusion creep.

4.6.3.3 Effect of clinozoisite on albite morphology and texture

Figure 4.22a shows that aspect ratio of albite is not particularly dependent on grain size at each strain level, although trends show a slight decrease in aspect ratio with increasing grain size. There is a big difference in grain shape between the smallest and largest strains, with grains at SL5 being smaller and more elongate than those at SL1. This implies that deformation processes have had more influence on grain size/shape than grain growth by textural annealing. Aspect ratios of albite grains are clearly influenced by clinozoisite content, which increases with increasing strain (Fig. 4.22c). This is because dissolution of albite was enhanced at phase boundaries, leading to more intense flattening of grain shapes during pressure solution.

Figure 4.22b shows that clinozoisite abundance has an influence on albite grain size. This is most likely a signature of boundary pinning by clinozoisite phase boundaries during grain growth in albite (Herwegh et al., 2011). In support of this, note the clear difference in albite grain size in monophase bands derived from pressure shadows (note pressure shadow grains are not plotted on Fig. 4.22b). In these larger grains, clear signatures of a switch to deformation dominated by dislocation creep (i.e. intragranular distortion and the presence of subgrain boundaries) are observed. These observations indicated that shear deformation took place close to the boundary zone between GSI and GSS creep, so the presence of a second phase, inhibiting grain growth, affected dominant deformation mechanism and thus the rheology of the deforming rocks.

Adjacent preferred orientation domains must have experienced the same deformation history. The wide range of texture strength between domains measured at SL2 therefore provides further insight into the effect of clinozoisite on the evolving microstructure. Texture strength per domain falls rapidly with quite small increases in mean grain size (Fig. 4.23a), and increases rapidly with increasing clinozoisite abundance (Fig. 4.23b). Figure 4.23c shows there is also a clear link between mean grain diameter and clinozoisite abundance. These observations suggest that clinozoisite not only inhibited growth in the albite grains, but also inhibited rotations in those grains during diffusion creep, allowing texture strength to be preserved. Where clinozoisite abundance is minor, albite grains are freer to rotate and slide, so mixing of domains and associated weakening of texture occurs, along with grain growth. Thus, although the presence of a secondary phase is understood to activate and enhance diffusion creep in polymineralic rocks, the results of this study show that it can also inhibit the texture weakening that is normally associated with diffusion creep and associated GBS, by enhancing dissolution-precipitation and allowing rapid grain shape change to proceed, thereby limiting the need for grain rotations.

4.7 Conclusions

- A strong (single-crystal) inherited CPO can be preserved to high strain by grain boundary diffusion creep, so interpretation of CPO domains must be treated with care, as their presence is open to misinterpretation without careful analysis

- The possibility of low-temperature plasticity in feldspar is typically overlooked (e.g., Jiang et al., 2000) and further detailed investigation is required to fully understand its deformation behaviour in the middle crust. In particular, studies that elucidate the activity of the [010] Burgers vector would help develop our understanding of how feldspar deforms at relatively low temperatures
- Secondary phases produced during metamorphic reactions may inhibit grain growth to promote GSS creep, but their presence may also limit texture modification by inhibiting the rotations normally associated with diffusion creep and grain boundary sliding

4.8 Supplementary figures.

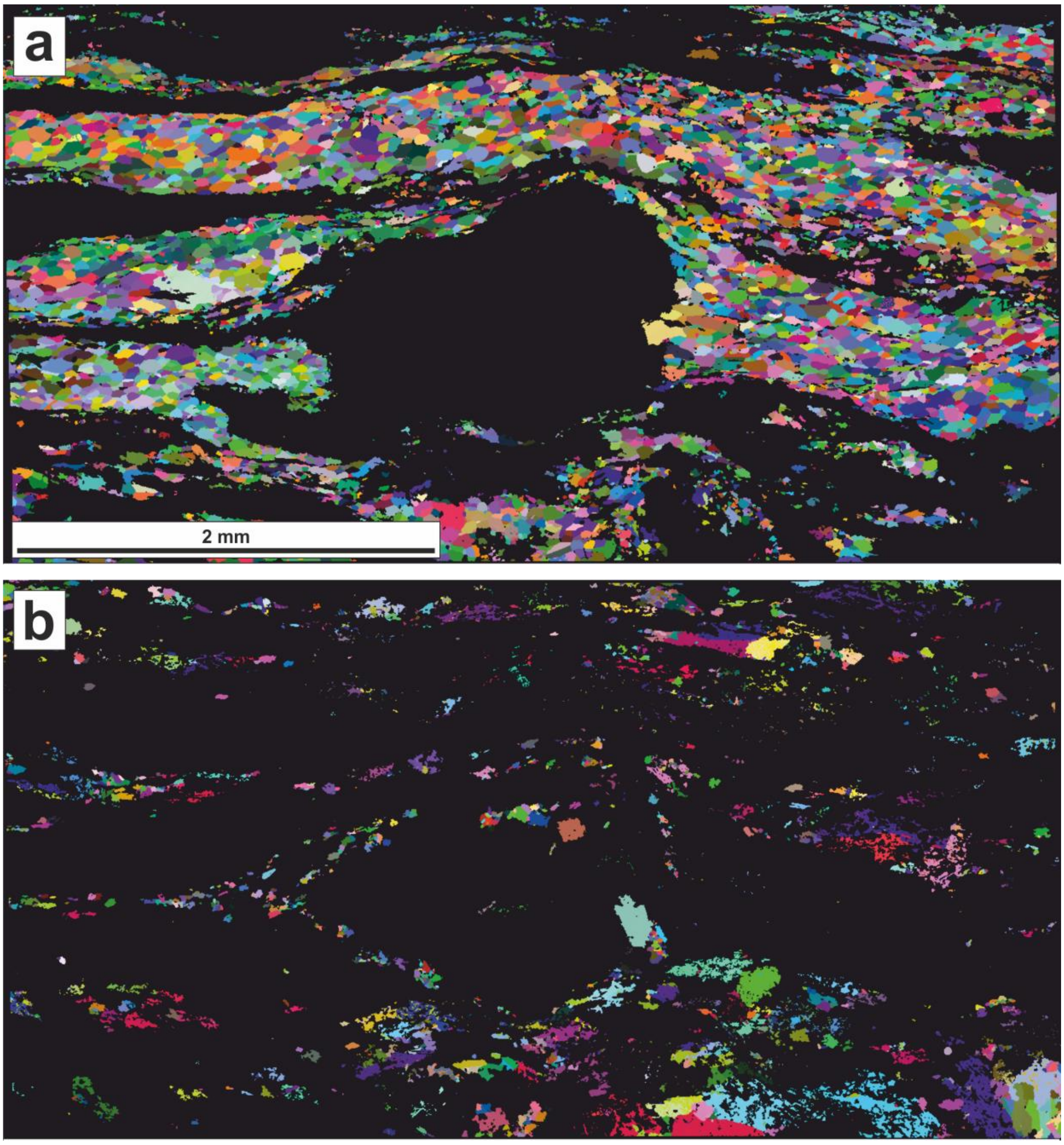

Figure S4.1 *An All-Euler EBSD map from SL4. a) Albite showing a lack of distinct CPO domains, b) Clinozoisite grains also show a lack of preferred orientation.*

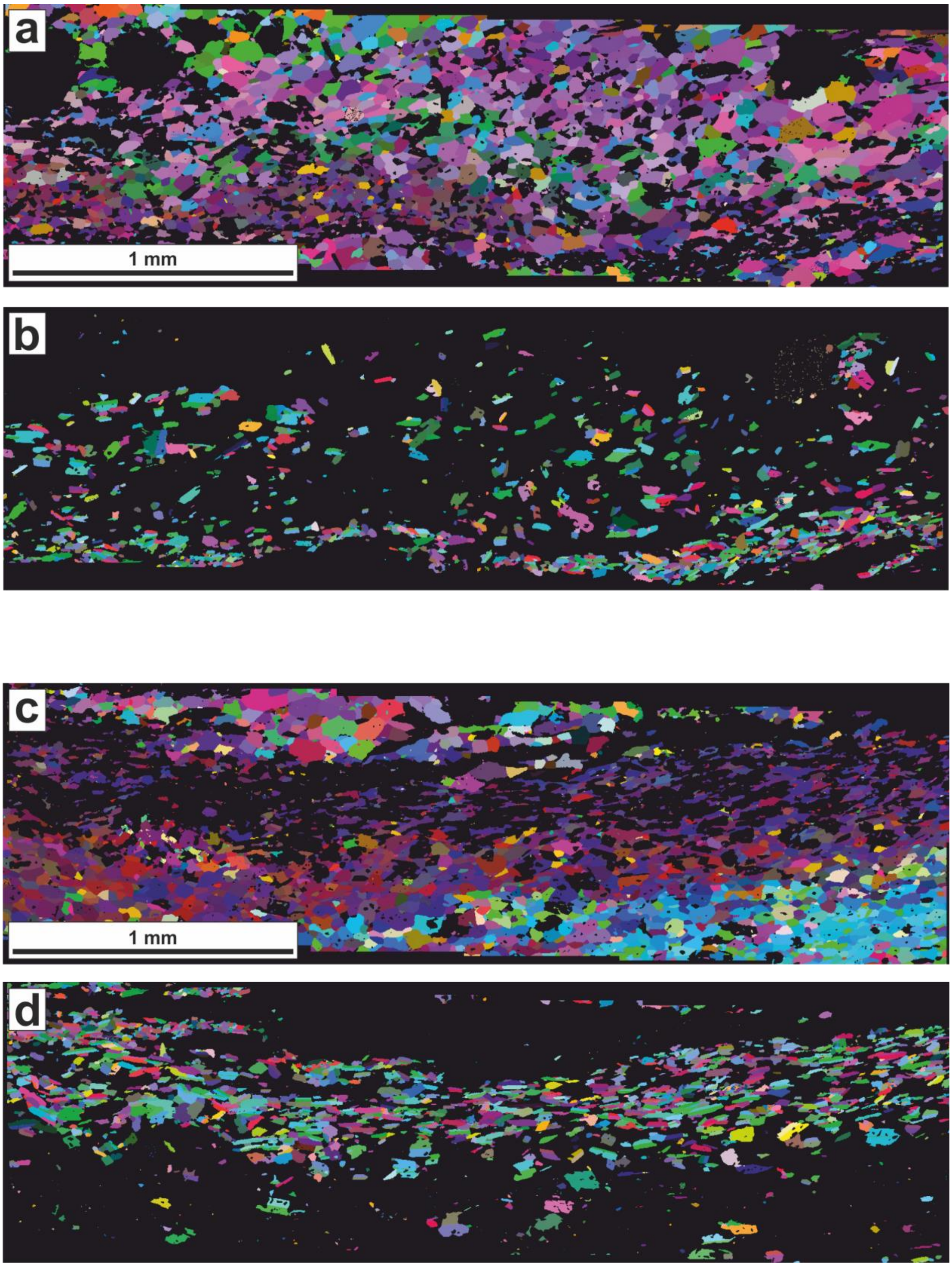

Figure S4.2 *Albite CPO domains from SL2 in detail. These domains were used to extract data in Table 4.2 and plot graphs in Fig. 4.23.*

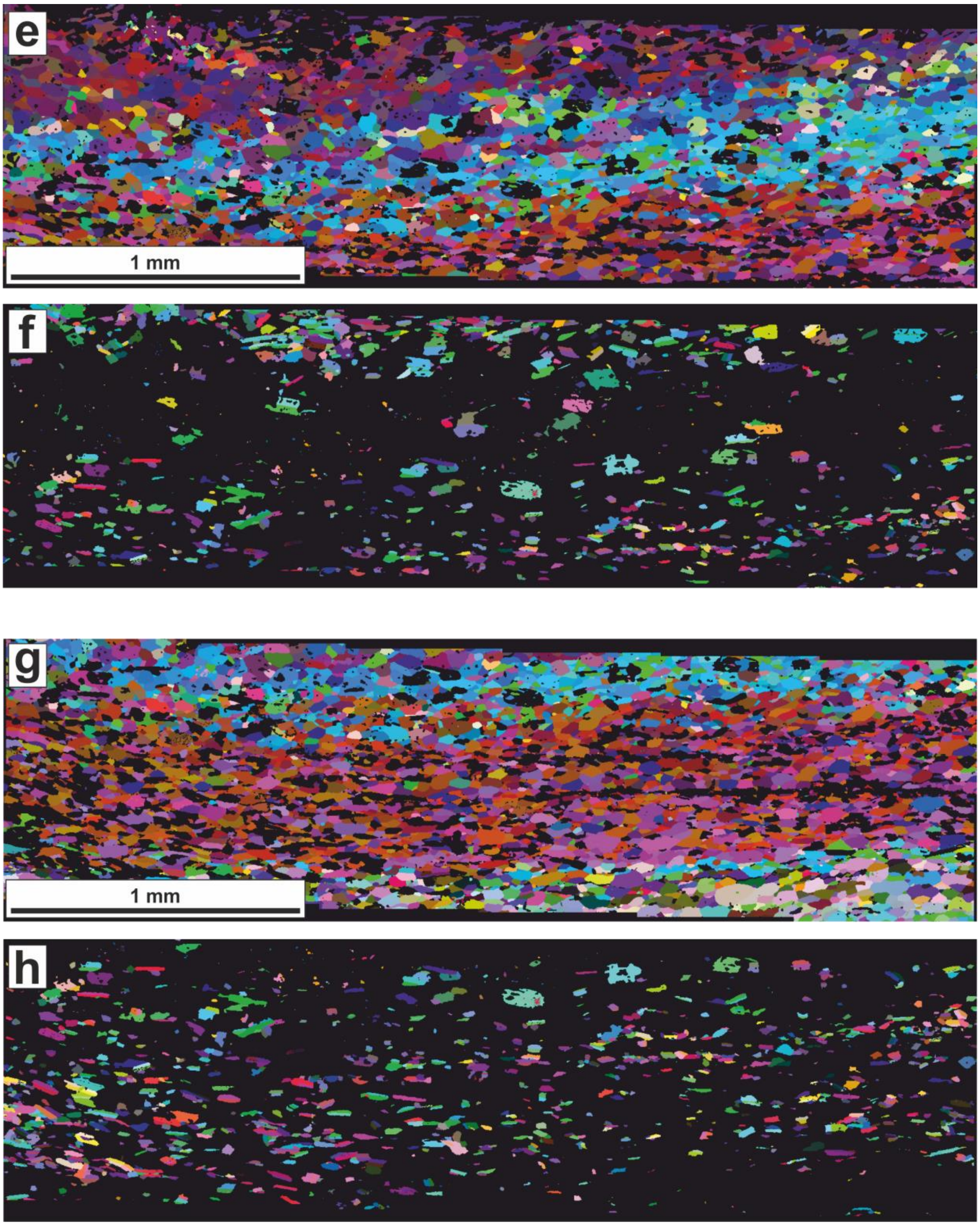
e
1 mm
f
g
1 mm
h

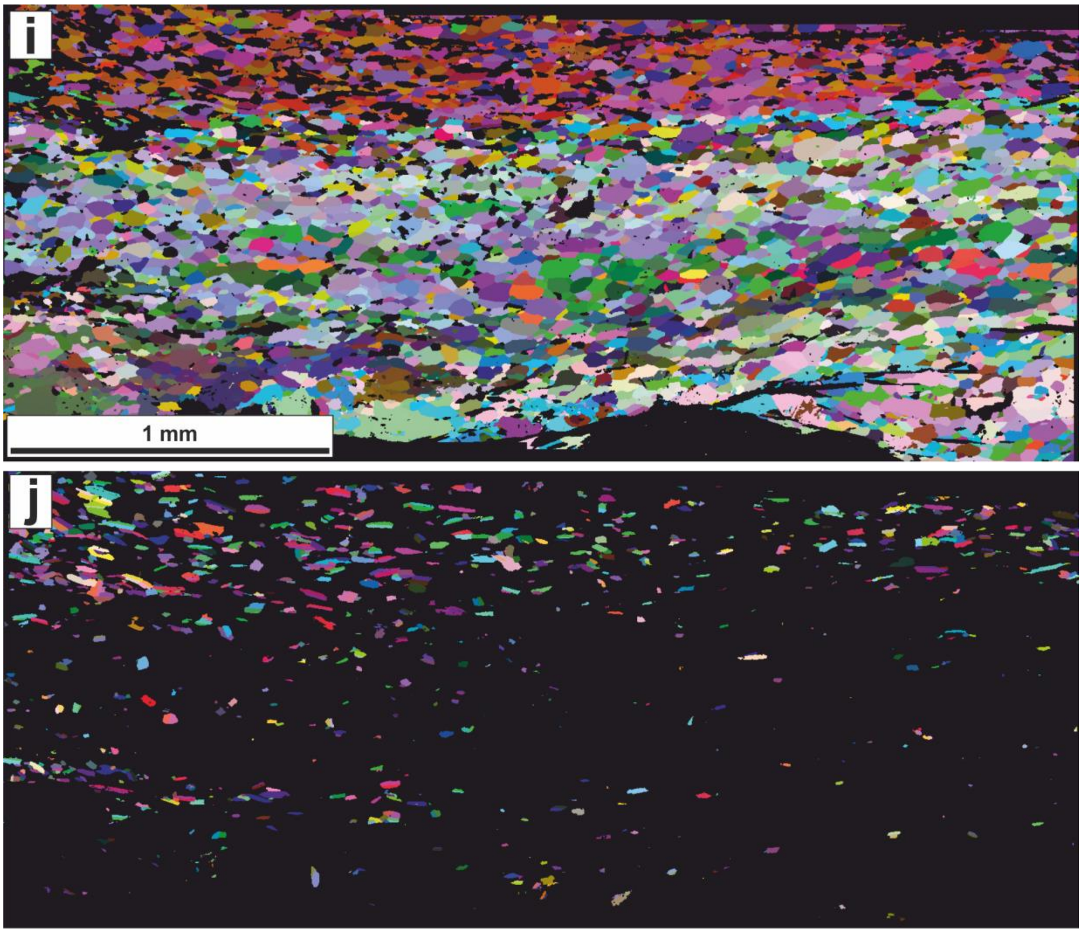
i
1 mm
j

Chapter 5 The influence of porphyroclasts on microstructural evolution during diffusion creep

5.1 Abstract

Diffusion creep is a fundamental deformation mechanism of Earth materials, but the way a microstructure evolves during diffusion creep remains poorly understood. Diffusion creep has traditionally been regarded to weaken or destroy any pre-existing crystallographic preferred orientation in rocks, although recent work has shown that the grain rotations that occur during diffusion creep become inhibited with grain elongation at increasing strain, and some authors have postulated a preferred orientation can actually develop during diffusion creep. In this study, the results of numerical simulations of diffusion creep which investigate the influence of porphyroclasts on microstructural evolution during diffusion creep are presented. DiffForm, a MATLAB®-based modelling suite designed to simulate deformation by diffusion creep, was used to explore the microstructural evolution of a fine-grained matrix containing a single large grain, in both pure and simple shear. The results of the modelling show that the presence of a large grain has a significant effect on the microstructural evolution of a fine-grained matrix undergoing diffusion creep. In particular, rotations of matrix grains are strongly influenced by the rotation direction and velocity of the large grain, especially the matrix grains that lie adjacent to the large grain. The rotation direction of large grains does not have to be simply either synthetic or antithetic; rotation directions can change due to interactions with the matrix, and the overall evolution of grain rotations in a rock undergoing diffusion creep is complex. The results of the study also show that large grains create stress heterogeneities that focus the effects of diffusion creep. The stress heterogeneities can result in the alignment of grain boundaries, which can lead to a profound drop in strength of a material.

5.2 Introduction

The geodynamic behaviour of the Earth is dependent on the physico-chemical properties of the Earth material being deformed, which itself is dependent on that material's metamorphic and deformation history. A rock's microstructure (texture) contains detailed information about the deformation and metamorphic processes that were operative during its history, provided geologists can correctly interpret the microstructural features. One aspect of textural interpretation that remains elusive is exactly how a microstructure evolves during diffusion creep.

Diffusion creep is a fundamental process in the Earth, both in mantle (Hiraga et al., 2010; Hirth and Kohlstedt, 1995; Karato and Wu, 1993) and crustal (Kilian et al., 2011; Rosenberg and Stünitz, 2003; Rybacki and Dresen, 2000; Rybacki et al., 2006) materials. In the mid-to-upper crust (to a depth of some 20 km), water is abundant; e.g., in the fractured upper crust, an interconnected, fluid-filled network of pores characteristically makes up on the order of 1 vol%, and the crust behaves hydrologically like a homogeneous infinite aquifer; porosity vanishes below the brittle-viscous transition (~12–15 km depth) but water remains adsorbed to grain boundaries, and occurs in hydrous phases and fluid inclusions (Bucher and Stober, 2010). In the presence of fluid, diffusion-dominated deformation is termed pressure solution or dissolution-precipitation creep (Menegon et al., 2008; Rutter, 1976; Rutter, 1983; Wheeler, 1992; Wintsch and Yi, 2002), but the processes are the same (Elliott, 1973). Diffusion creep is often postulated as the dominant deformation mechanism in rocks that lack other microstructural signatures. In particular, the presence or absence of a crystallographic preferred orientation (CPO) is commonly used to distinguish deformation by dislocation creep (during which a CPO is developed due to slip on specific crystallographic planes and in specific crystallographic directions; Karato et al., 2008) and diffusion creep, where a CPO is traditionally not expected to develop, and any pre-existing CPO is expected to weaken or be destroyed by rotations associated with the grain boundary sliding (GBS) that is required for the material to maintain continuity during grain shape change (Elliott, 1973). Indeed, the dominant deformation mechanism by which the mantle deforms is inferred from its observed seismic anisotropy (or lack thereof), which is interpreted to be a product of crystal alignment (e.g., Karato et al., 2008).

Recent advances in our understanding of how diffusion creep operates in rocks have brought some of these ideas into question. Jiang et al. (2000) showed that an inherited CPO could be preserved to high strain in albite during diffusion creep. The microstructural data presented in Chapter 4 of this thesis showed such inheritance results in a banded, CPO texture, in which individual CPO domains are incrementally weakened but preserved to high strains during pressure solution. Imon et al. (2004) analysed microstructures found in amphibolites from the Ryoke metamorphic belt and concluded that dissolution-precipitation creep produced the observed CPO, by preferential dissolution of original amphibole at grain boundaries sub-parallel to foliation and nucleation and anisotropic growth of new amphibole in a stress field. Similar dissolution-precipitation processes have been observed to develop CPOs in clinoamphiboles under low-pressure metamorphic conditions from Spain (Díaz Aspiroz et al., 2007). Getsinger and Hirth (2014) performed shear deformation experiments on powdered basalt to assess fabric development in amphibole grains during diffusion creep, concluding that CPO development in amphibole occurs by oriented grain growth and rigid grain rotation during such experiments, and that CPOs are likely to develop by the same mechanisms in natural lower crustal shear zones. Gómez Barreiro et al. (2007) deformed synthetic anorthite aggregates experimentally in torsion under Newtonian creep (i.e. diffusion creep) conditions and observed the development of a strong CPO, suggesting the presence or absence of a CPO cannot by itself be used to infer the dominant deformation mechanism (and associated rheology) of a deforming material. Sundberg and Cooper (2008) analysed experimentally-deformed harzburgite to show that interface-reaction-controlled diffusion creep, and associated phase boundary migration, can lead to the development of strong CPOs in the near absence of mobile dislocations in polyphase upper mantle material. Miyazaki et al. (2013) performed uniaxial creep experiments on forsterite in the diffusion creep regime, which resulted in the development of a CPO by rotation of grains due to grain boundary sliding accommodated by diffusion, leading them to suggest that diffusion creep may be the primary mechanism by which the mantle flows.

Numerical models have also yielded results that suggest diffusion creep can lead to the development or preservation of CPOs. Bons and den Brok (2000) showed that reaction-controlled dissolution-precipitation creep (DPC) can lead to the development of CPOs, as long as grain dissolution and growth rates are influenced by crystallographic anisotropy, and DPC is accompanied by rigid-body rotation. Wheeler (2009) used a numerical model to show that seismic anisotropy could be preserved during diffusion creep in a monophase material due to the suppression of grain rotations during deformation. Grain rotations were inhibited by slight elongation of grains, which occurred when diffusion creep rates were fast compared to grain growth rates. Grain elongation occurs during diffusion creep as dissolution at faces experiencing highest normal stress and precipitation at faces experiencing lowest normal stress causes 'flattening' of grains, e.g., Rutter (1983). Grain growth, or annealing, results in more equiaxed grains, so if this is fast compared to diffusion creep, grain elongation is inhibited (Wheeler, 2009). Thus the link between diffusion creep and CPO development, preservation and/or annihilation remains ambiguous.

On the subject of grain elongation in diffusion creep, Elliott (1973) noted that if the strain path is co-axial and grains do not rotate, then they will become more elongate, diffusion paths will get longer, and so the process becomes self-exhausting, except that:

1) even on a coaxial strain path, grains continuously rotate with respect to each other because of GBS, which brings different faces into contact, so newly precipitated parts of grains will become subject to dissolution and thus tend to remain equiaxed; and
2) for the most part, coaxial deformation is a rare case, only occurring locally within a body of deforming rock, and a typical non-coaxial strain path will tend to keep grains equiaxed.

However, Wheeler (2009) showed that grain elongations do not have to be very large before they significantly impact rotations in monophase aggregates. Most rocks, though, are polyphase. Microstructural evolution within a polyphase sample depends strongly on how the different phases interact, e.g., Jessell et al. (2009). The viscosity of a polymineralic rock undergoing pressure solution can be much lower than its monomineralic counterparts (Wheeler, 1992). Also, secondary phases may enhance the solubility of the primary phase in a fine-grained matrix (e.g. see chapter on two phase mixing and figure of region where all albite has been 'squeezed out' of a high strain area between clinopyroxene porphyroclasts. Grain boundary diffusion creep is also more efficient in small grains due to the reduced length of diffusion pathways, so grain size differences between phases will have an effect. Variation in grain size within a sample may have a local effect on distribution of stress, and therefore how a given microstructure responds to an imposed far-field stress. Many of the factors that control how the microstructure of a polyphase rock may evolve during diffusion creep remain to be tested. Here, the first attempt at modelling the influence of a large second-phase grain sitting in a finer-grained matrix of a monophase, polycrystalline material deforming by diffusion creep, is presented. The model tracked changes in the microstructure as it evolved along both coaxial (pure shear) and non-coaxial (simple shear) strain pathways. The starting geometry for the model was inspired by the evident large porphyroclasts and heterogeneous strain documented in Chapters 3 and 4 of this thesis and in many other studies. The way in which grain rotations, and the angular velocities of those rotations, changed during deformation, and thus how a CPO may be developed or modified, is reported. An analysis of how differential stress within the sample evolved as deformation proceeded is also presented. Grain rotations in the model resulted in the partitioning of initial orientations into smaller subsets of shared orientation, which may be analogous to the development of the domainal CPOs that were observed in the fine-grained matrix of metagabbros presented in Chapter 4.

5.3 Methods

The MATLAB®-based modelling suite DiffForm was utilised for the analysis (Berton et al., 2011; Berton et al., 2006; Ford et al., 2004; Ford et al., 2002; Wheeler, 2009; Wheeler and Ford, 2008). A rigorous treatment of the fundamental mathematics which DiffForm employs to model microstructural evolution in diffusion creep can be found in Wheeler and Ford (2008) and Wheeler (2009). The intention here is to attempt to describe how DiffForm works in a way accessible to non-mathematicians, to emphasise the physical processes that are being modelled.

The most fundamental link between stress (a physical property) and diffusion (a chemical process) comes from the driving force for diffusion, which is the gradient in chemical potential. At an interface, chemical potential is given by:

$$\mu = F + \sigma_n V \tag{5.1}$$

where σ_n is compressive normal stress across the interface, F is the molar Helmholtz free energy of the solid, V is the molar volume of the solid and μ is the chemical potential of the solid in an adjacent ‘phase’ in which it can dissolve (the ‘phase’ is actually the grain boundary region). From the equation, it can be seen that as normal stress increases on an interface, the chemical potential of the material composing that interface will also increase, i.e. it will dissolve more readily. Thus grain boundaries under higher normal stress will have a higher chemical potential than grain boundaries under lower normal stress, which in turn results in a gradient in chemical potential along grain boundaries, and between different boundaries of the same grain. This gradient is what drives diffusion of material resulting in shape change. Variations in normal stress can then give rise to gradients along interfaces (enabling Coble creep) and within grains (enabling Nabarro-Herring creep).

It has been shown (Wheeler, 1987) that the distribution of stress (i.e. the chemical potential) along a boundary evolves to a parabolic shape, the result of which being that material can be dissolved or precipitated at all points along the boundary. The flux, and therefore the current (i.e. the flux × the boundary width; Wheeler and Ford, 2008), can be determined at any point along the boundary, so dissolution and precipitation rates can be calculated for a given imposed normal stress. Utilising the dissolution and precipitation rates at grain boundaries, the divergence speed of any two adjacent grains can be calculated, and because grains are rigid and do not experience internal deformation, the relative motions of grains must be equivalent to their relative velocity plus a rotation around a reference point. As no internal deformation is assumed by the model, overgrowths must be either of constant width or wedge-shaped.

A set of simultaneous equations are solved to determine instantaneous velocities of grains, and stresses along each boundary. After each strain increment is applied, the microstructure is modified by repositioning grain boundaries in the middle of overgrowths and regions where dissolution has occurred. Triple junctions that overlap at any stage, which represent the neighbour switching events common to GBS (Ashby and Verrall, 1973), are redrawn. The resultant microstructure is then used to solve for new velocities and stresses. Note that stress is not actually imposed on the model; instead an average strain rate tensor is imposed, for which the simultaneous equations are then solved to predict the average stress and the local stresses on grain boundaries which drive shape change.

To test how a large secondary phase might impact the microstructural evolution of a fine-grained monophase matrix deforming by diffusion creep, the initial grain geometry shown in Figure 5.1 was used. This topology is roughly analogous to a garnet-mica schist, or to the mafic porphyroclasts observed within the fine-grained albite matrix in the metagabbroic samples presented in Chapter 4, with a porphyroclastic secondary phase embedded in a finer-grained matrix whose grains show a shape-preferred orientation. The net is simplified to highlight the effect of the porphyroclast on matrix-grain evolution. The possible effects of matrix grain periodicity compared to the heterogeneity of grain shape and size found in natural samples is discussed below.

The two phases are arbitrary in the model, but ‘K values’ for each phase must be defined: in a grain boundary, the flux of a component is multiplied by the grain boundary width to calculate the chemical current of that component, and it is the current rather than the flux which determines growth and dissolution rates of phases (Wheeler, 1992). The net chemical current along a grain boundary is a function of the ‘conductances’ of all components that comprise the system. K values relate to the ‘resistances’ (or the inverse of the ‘conductances’) of each component to dissolution or growth by diffusion along the grain boundary (Wheeler, 1992). K values at phase boundaries are set to zero, which ensures phases do not interact during deformation and the porphyroclast is essentially inert.

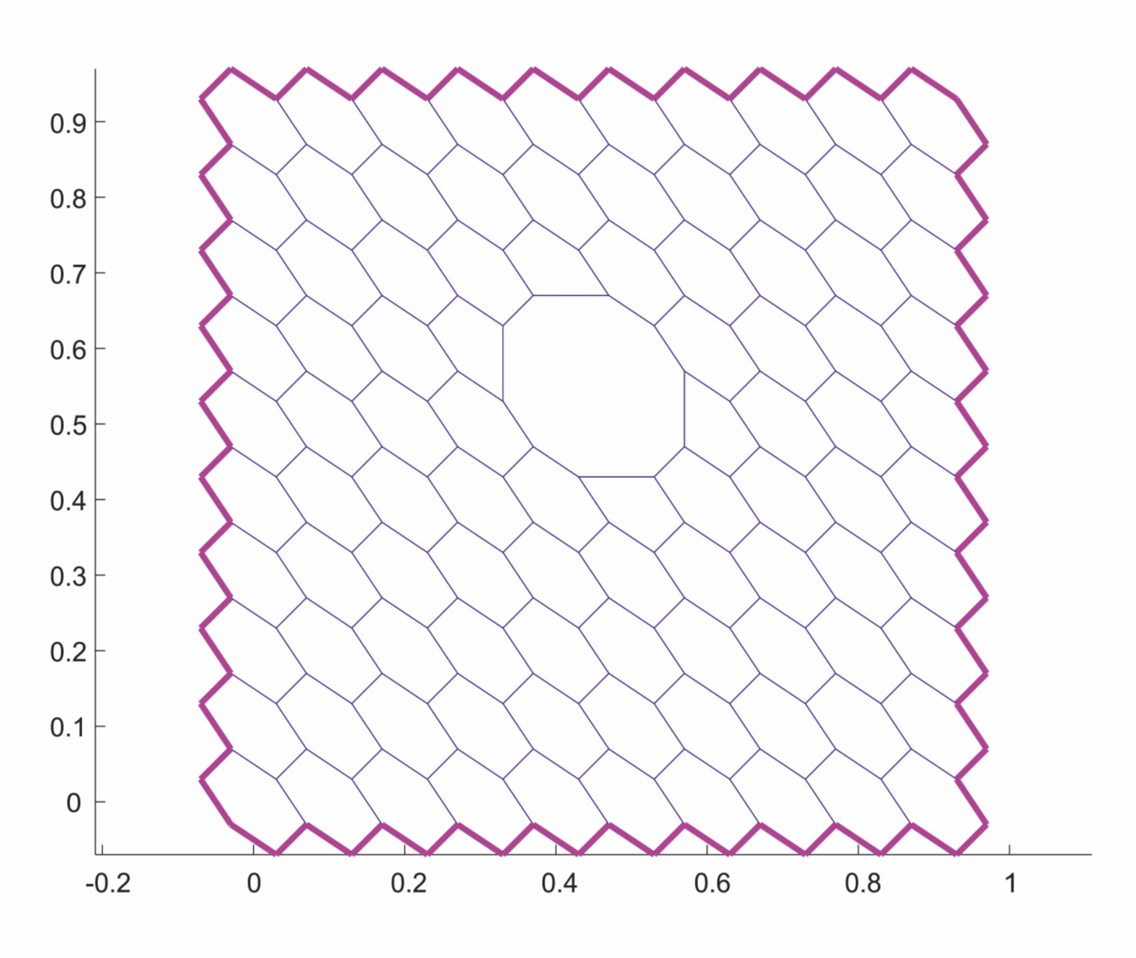

Figure 5.1 *Starting geometry of model runs. The large central grain is defined to be a different phase, although grain size is considered to have more of an effect on microstructural evolution. Scale is arbitrary in the model.*

The starting net was set up to undergo 200 increments of either pure or simple shear at a strain of 0.5 per time step, with a time step length of 0.01. Multiplying strain by time step length results in a strain of 0.5% being imposed on the model per time step (i.e. 50% strain would be achieved after 100 time steps). Time step length, and therefore strain rate, are arbitrary as there is a linear relationship between angular velocity and strain rate in the model, so faster strain rates simply mean the microstructural evolution occurs more quickly, but the final microstructure produced is identical (see Wheeler, 2009, for more details).

5.4 Results

5.4.1 Pure shear

The pure shear experiment terminated at 130 time steps, i.e. achieved a strain of 65%. Numerical experiments performed using DiffForm sometimes terminate because of problems with the evolving topology of the net (neighbour switching in particular). If these occur at the edge of the net as represented in the model, there are a number of scenarios and some are difficult to deal with, hence the program fails (Wheeler pers. comm.). Four strain increments of the microstructural evolution are presented in Figure 5.2a–d (readers are referred to M5.1 in the digital appendix at the back of this thesis for an animation of the entire experiment). Grains in Figure 5.2 are coloured by finite rotation they have undergone from their original orientation, in degrees. Note that the colour scale changes for each plot to accommodate larger finite rotations as deformation proceeds. Figure 5.2a shows that, by a strain of about 0.16, most matrix grains have rotated about the same amount as the porphyroclast (~15°), with the exception of a row of grains whose rotations appear to be subdued by their alignment with the long axis of the porphyroclast (at an angle of approximately 125° to the direction of maximum shortening) and so have only rotated some 10°. Figure 5.2b shows a similar trend, with distinct regions of the matrix undergoing different finite rotations depending on their geometric relation to the porphyroclast. The band of lowest rotations sits at 120° to the maximum shortening direction. By a strain of about 0.49 (Fig. 5.2c), the band has flattened to around 110° with respect to the maximum shortening direction, but the

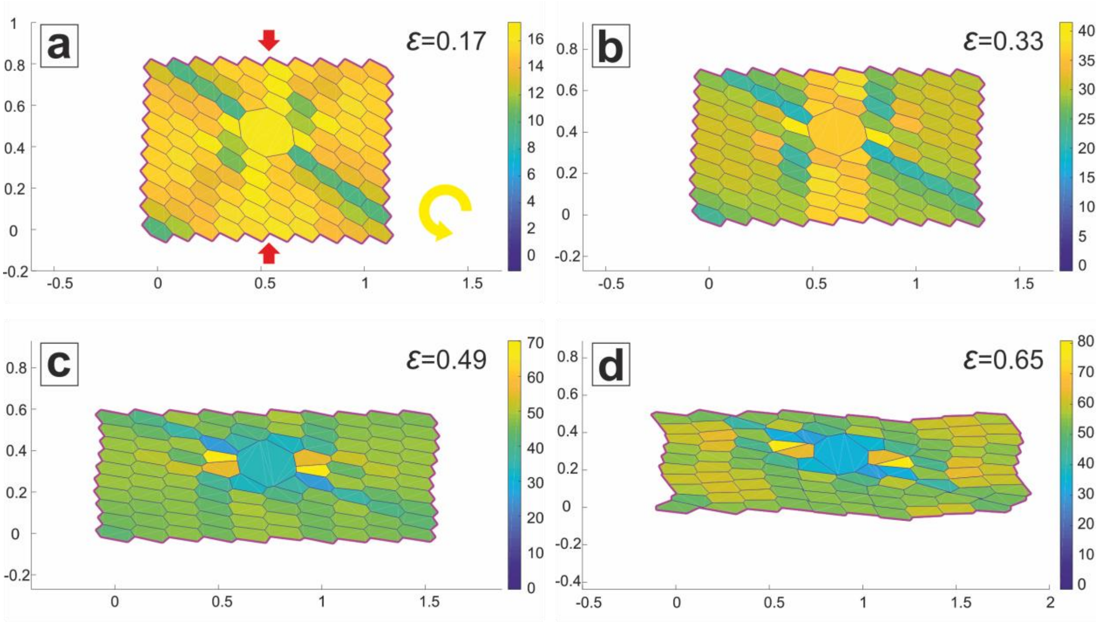

__Figure 5.2__ Results of the pure shear experiment at four strain increments. The model terminated at a strain of 0.65. Grains are coloured by finite rotation with respect to starting orientation in degrees (anticlockwise positive; yellow arrow in (a)). Red arrows in (a) show direction of shear. Note change in scale for each strain increment; colour scale was altered so unique features can be seen at each stage. For a movie of the full evolution of the model to failure, see M5.1 in the digital appendix at the back of this thesis.

influence of the porphyroclast is no longer apparent along the entire band. Instead, most matrix grains that do not neighbour the porphyroclast have rotated more (some 45°) than the porphyroclast itself (closer to 35°), and matrix grains that neighbour the porphyroclast either have lower or higher finite rotations than the bulk matrix. By the last stage, a 'sliding surface' (shear band??) that links up across multiple grains has formed (this is best seen in the animation in the online supplementary information), at an angle of 105° to the maximum shortening direction (Fig. 5.2d). The sliding surface is composed of aligned boundaries of grains that undergo the smallest rotations in the early stages of deformation, so its existence is clearly related to the presence of the porphyroclast. By the time the model fails, it has undergone a longitudinal strain of roughly 0.65 (the model retains a constant area).

Figure 5.3a shows the finite rotations of each grain with respect to their initial orientation, with the rotation behaviour of the porphyroclast highlighted as a thick red line. Notably, most matrix grain rotations tend to steadily increase in an anticlockwise direction with strain (anticlockwise rotation is defined as positive). This is probably an effect of the orientation of the strong shape fabric in the matrix with respect to the direction of maximum shortening, and more variation in rotations would be expected in more heterogeneous samples. The porphyroclast begins rotating in the same, anticlockwise, direction as the matrix grains, but at a strain of about 35% its direction of rotation reverses. This is reflected in the angular velocity plot (Fig. 5.3c), where porphyroclast rotation initially accelerates, before stabilising at around 60° per arbitrary time unit at a strain of approximately 0.1, then slowing and reversing rotation direction at a strain of 0.35. The porphyroclast then begins to accelerate in the new rotation direction, before stabilising at around 30° per time unit, and finally reverses rotation direction again just before the model terminates. Overall, the matrix grains experience a less unstable rotation journey, with the majority of grains rotating at a fairly consistent angular velocity of around 50° per time unit, until a strain of around 0.45, when the rotational steady-state destabilises and nearly all grain rotations slow down, before the matrix grain population undergoes a wide range of accelerations/decelerations at a strain of about 0.6, just before the model terminates. The spread in angular velocities prior to the destabilisation phase is due to the influence of the porphyroclast on matrix grains adjacent to it, which undergo quite different behaviour than the bulk matrix.

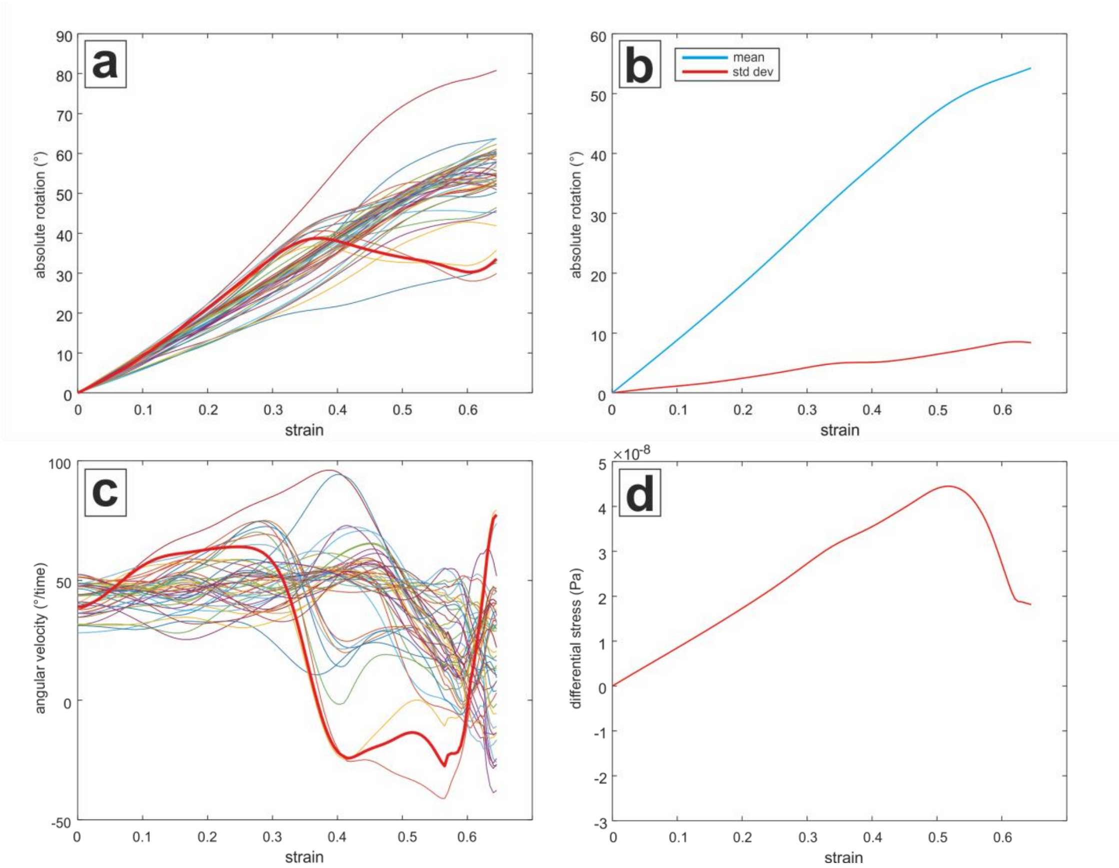

Figure 5.3 *a) Absolute rotation in degrees of each grain as a function of increasing strain in the pure shear model (anticlockwise positive). The thick red line tracks rotation of the porphyroclast. b) Mean and standard deviation of all grain rotations in the pure shear model. c) Angular velocity of all grains as a function of strain in the pure shear model. Thick red line tracks the angular velocity of the porphyroclast. d) Evolution of differential stress (i.e. strength evolution of the deforming microstructure) during the model run.*

Mean rotation is positive (i.e. clockwise), and there is a suggestion that the microstructure may be asymptotically approaching a rotational steady-state as per Wheeler (2009), but termination of the model makes this difficult to be sure of (Fig. 5.3b). The development of the sliding surface by grain boundary alignment has a profound effect on the strength of the model. The differential stress applied to the net steadily increases with increasing deformation until a critical point, just after a strain of 0.5, is reached (Fig. 5.3d), i.e. just after the 'destabilisation' of the microstructure is observed in the angular velocities. As the model 'fails', the differential stress evolves along a stress-strain path reminiscent of typical rock deformation laboratory experiments stressed to brittle failure (e.g. the room temperature experiments performed by Tullis and Yund (1992); see their Fig. 2). The stress-strain curve shows the strength of the material, which initially allows differential stress to increase, is lost just after a strain of 0.5, which indicates material failure.

5.4.2 Simple shear

The dextral simple shear experiment does not undergo the same material failure, and so completes all 200 time steps, i.e. achieves 100% strain. As for pure shear, the colour scheme in Figure 5.4 shows finite rotation of grains, in degrees. Note that the colour scale changes between plots to accommodate higher-angle finite rotations. The influence of the porphyroclast on matrix grain rotations is quite different to that observed in pure shear, but equally significant. The porphyroclast begins to rotate in a clockwise direction, i.e. synthetically to the imposed shear strain direction. The rotation of the porphyroclast influences a row of grains perpendicular to the shape fabric to rotate in the same direction as itself (Fig. 5.4a–d; readers are referred to M5.2 in the digital appendix at the back of this thesis for an animation of the entire experiment). Rotation of these grains results in neighbouring grains forming two rows parallel to the first (i.e. perpendicular to original shape fabric) that rotate in the opposite direction. The

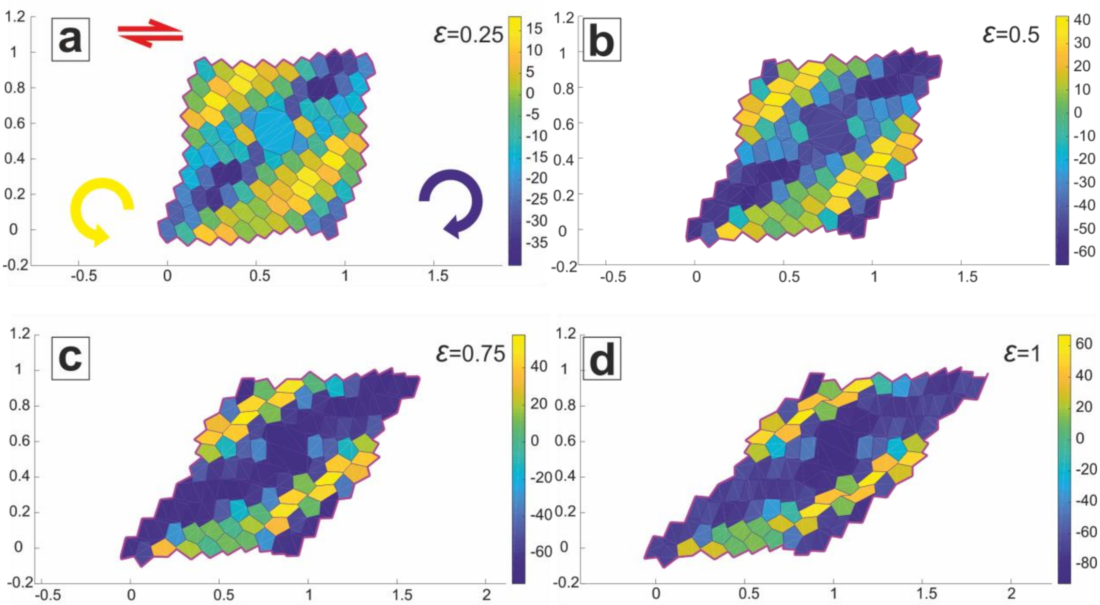

Figure 5.4 *Results of the simple shear experiment at four strain increments. The model terminated at a strain of 1.08. Grains are coloured by finite rotation with respect to starting orientation in degrees (anticlockwise positive, yellow arrow in (a); clockwise negative, blue arrow in (b)). Red arrows in (a) show direction of shear. Note change in scale for each strain increment; colour scale was altered so unique features can be seen at each stage. For a movie of the full evolution of the model to failure, see M5.2 in the digital appendix at the back of this thesis.*

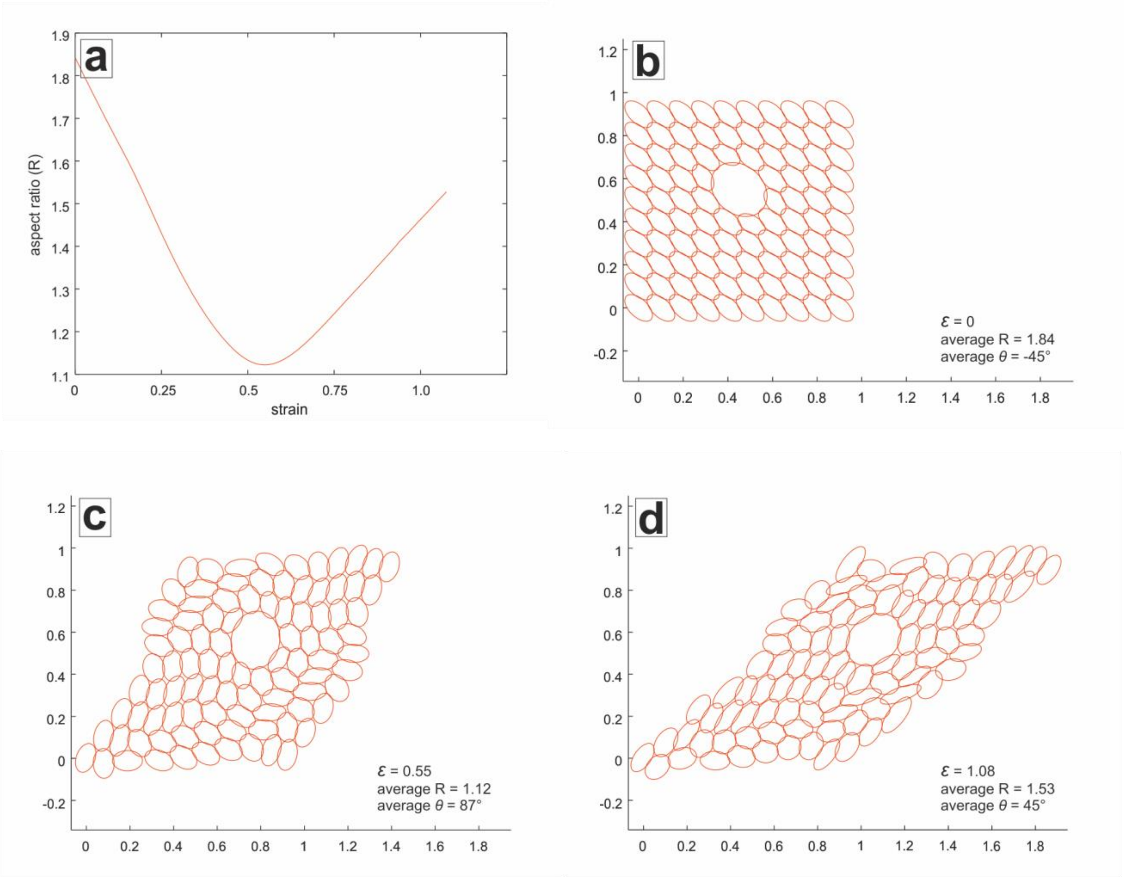

Figure 5.5 *a) Aspect ratio evolution during dextral simple shear. b) Best fit ellipses to grains in the starting net have an average aspect ratio of 1.84, and the average angle of grain long axes to the horizontal is 45° clockwise. c) At a strain of 0.55 (half way through the model run) average aspect ratio of the best fit ellipses drops to 1.12, and on average long axes have rotated to almost vertical (87°). d) When the model run terminates, best fit ellipses have an average aspect ratio of 1.53, and long axes have continued to rotate to an average of 45° to the horizontal.*

initial shape preferred orientation in the matrix is completely wiped out with increasing strain. The average aspect ratio of the grains decreases from >1.8 at the start of the experiment to a minimum of 1.12 at 110 time steps, before increasing again to 1.53 by the end of the run (Fig. 5.5a, which shows aspect ratio evolution throughout the full model run; 215 time steps). The average orientation of the long axis of grains rotates synthetically with increasing shear strain (Fig. 5.5b–d), i.e. clockwise, but the change in average aspect ratio shows this is not simply due to rigid body rotation; grains shorten in directions parallel to the highest normal stress, and lengthen in directions perpendicular to the highest normal stress.

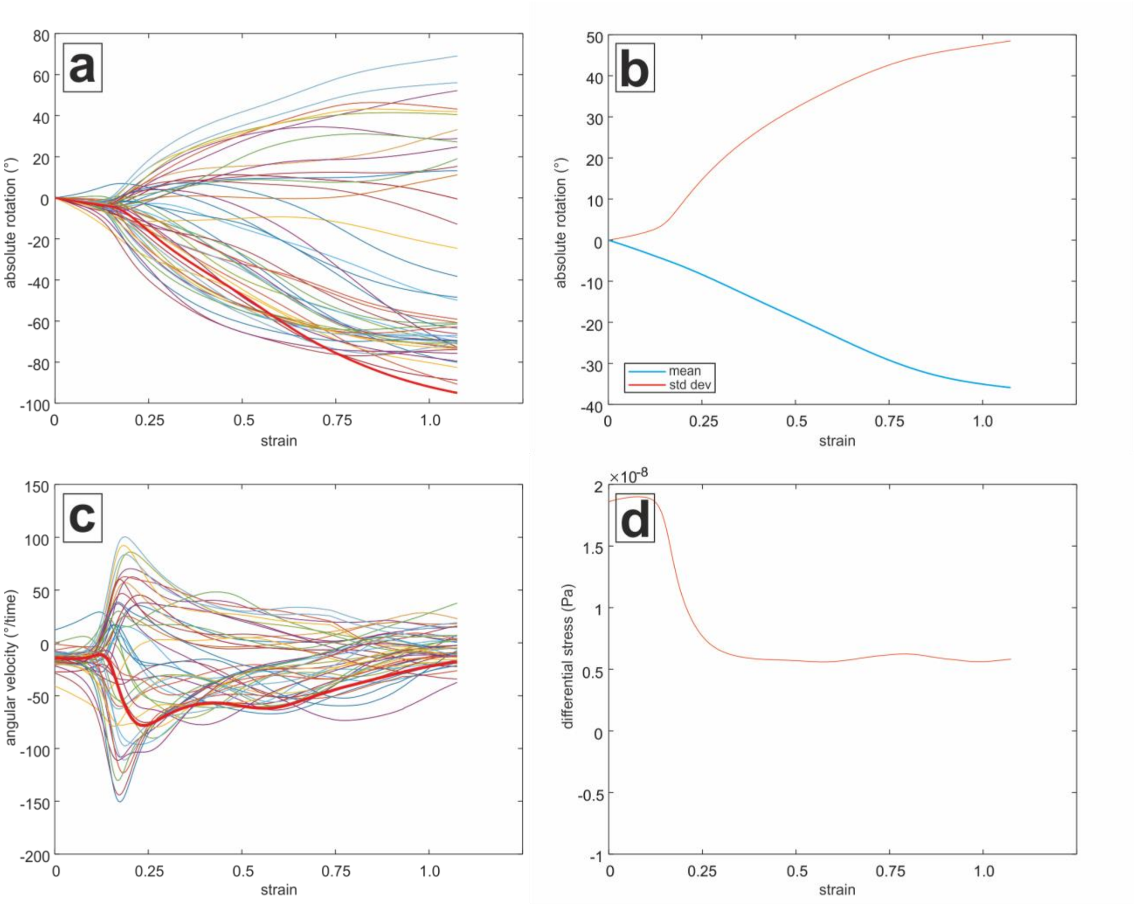

Figure 5.6 *a) Absolute rotation in degrees of each grain as a function of increasing strain in the dextral simple shear model (anticlockwise positive). The thick red line tracks rotation of the porphyroclast. b) Mean and standard deviation of all grain rotations in the simple shear model. c) Angular velocity of all grains as a function of strain in the simple shear model. Thick red line tracks the angular velocity of the porphyroclast. d) Evolution of differential stress (i.e. strength evolution of the deforming microstructure) during the model run.*

Most grains retain their initial rotation direction for the duration of the experiment. Finite rotations are quite small until a strain of around 0.18, by which point critical strain is achieved and grain rotations balloon out in both rotation directions (Fig. 5.6a). Individual grain rotations, and the mean rotation, tend to flatten with increasing strain, suggesting a rotational steady-state is achieved (Fig. 5.6a–b). This is reflected in the angular velocity plot (Fig. 5.6c), which shows a huge increase in rotational velocity in both rotation directions from a strain of around 0.15, which initially subsides relatively quickly after peak velocities are reached at a strain of around 0.2, and then the angular velocities of most grains flatten off at a strain of around 0.4 and gradually evolve towards zero, i.e. grain rotations evolve to some kind of stable steady state (Wheeler, 2009). Matrix grain rotations are clearly influenced by the porphyroclast, as they broadly follows the same pathway in both finite rotation and angular velocity plots (Figs. 5.6a and c). The differential stress evolution plot shows a constant value until a strain of about 0.15 when it drops suddenly indicating a decrease in strength in the net, which correlates with the sharp increase in the angular velocity of the porphyroclast (and therefore all grains). As grain rotations stabilise, so the differential stress curve also stabilises, indicating the strength of the net has stabilised at a new, but lower, value.

5.5 Discussion

5.5.1 Grain rotations

Grain rotations during diffusion creep occur in a very dynamic environment, where rotations have a measurable impact on adjacent grains. In particular, rotations of porphyroclastic grains can have significant effects on the surrounding matrix. Rotations of porphyroclastic grains are generally assumed to be either synthetic or antithetic to shear (Griera et al., 2013). The results presented here suggest a more complex picture, where rotation directions actually change through time as porphyroclast and matrix grains interact, and stress within the entire system evolves. In the model, the stress evolution influences chemical potential, which influences grain shape change, which, in turn, influences rotation direction. More detailed work on the evolution of grain rotations to very high strains would give valuable insight into how finite strain microstructures should be interpreted.

Matrix grain rotations are clearly influenced by the porphyroclastic grain. In pure shear, the porphyroclast appears to act as a destabilising force on the microstructure by suppressing the rotations of specific grains, which leads to a plane of weakness within the net that is caused by aligned grain boundaries. The inference here is that a rock comprised of grains with a homogeneous grain size may be stronger than those with a bimodal distribution of sizes when deforming by diffusion creep, because large grains act to focus the microstructural modifications inherent in diffusion creep into specific areas, which can result in the development of mechanical heterogeneities that weaken the bulk rock.

5.5.2 Preservation or formation of a CPO

It is well documented that shape preferred orientations can develop by diffusion creep (e.g., Díaz Aspiroz et al., 2007; Getsinger and Hirth, 2014; Imon et al., 2004), and it has been shown that inherited CPOs can be retained during diffusion creep deformation (Chapter 4; Jiang et al., 2000; Wheeler, 2009). In the pure shear experiment, a CPO would not be expected to develop from a random initial texture, as the rotations of all grains follow the same path. However, if there was an initial CPO in the matrix grains of such a rock, it would be largely preserved, albeit weakened, by the diffusion creep deformation. A more heterogeneous initial grain geometry would be expected to evolve quite differently so more work is required in this area.

In simple shear, the story is more complex but follows the same trend; a rock with no initial crystallographic alignment would not develop one during diffusion creep deformation. However, if an initial CPO did exist, crystallographic alignment would also be observed in the final geometry, but the original CPO would have been split into two domains – one that shares an orientation related to rotations in the same direction as the porphyroclast, and another that shares a different orientation, related to rotations that are antithetic to porphyroclast rotation but are equivalent to one another, so a shared orientation is preserved. This may be one explanation for the development of the CPO domains observed in Chapter 4.

5.5.3 Strength evolution

The importance of grain rotations is shown to relate to more than just a rock's microstructure. A microstructure influences the physical properties of a deforming material and the experimental results clearly indicate that the strength of a rock deforming by diffusion creep is influenced by grain rotations. When rotations are large and fast, the microstructure can be interpreted to 'destabilise', with an associated drop in strength, in both pure and simple shear. The critical degree of rotation needed to cause destabilisation of the overall microstructure appears to be dictated by how rapid the rotation of a large grain is within a fine-grained matrix. Again it must be stressed that it is the heterogeneity in the microstructure that causes these effects.

To understand the low stress values in Figures 5.3d and 5.6d, note that 'legacy' values of various coefficients are used in the program. These were introduced arbitrarily during program development (Wheeler, pers. comm.) and have not been changed subsequently. They do not affect the predictions of microstructure, since these depend on finite strain and are independent of strain rate, or the angular velocities, since these scale with strain rate. Consider the flow law for a microstructure made of notional spherical grains. Coble (1963) treated diffusion creep of spherical grains of diameter a to find the (Newtonian) viscosity, η, expressed as the first term below (where Coble's equation has been rewritten in terms of shear stress, following eqn. 7.14 of Poirier, 1985). Subsequent terms in the equation below recast this flow law into a form using the parameters defined in DiffForm input files, which are as follows. Wheeler (1992) found it useful to use Onsager diffusion coefficients L $(= Dc/RT)$ to describe diffusion creep.

With just one soluble phase, the mathematics is simplified. When multiplied by grain boundary width w, $A = wL$ describes the overall ease of diffusion along a boundary (eqn. 4 in Wheeler, 1992). The matrix inverse of A (eqn. 5 in Wheeler, 1992) is useful for multicomponent systems, but here the second phase is set to be almost insoluble (almost, so as to avoid infinities in the code). So, with one soluble phase, with a formula identical to the mobile chemical component, $K = 1/A$ (eqn. 6 of Wheeler, 1992). So:

$$\eta = \frac{1}{141}\frac{kTa^3}{Dw\Omega} = \frac{1}{141}\frac{kTa^3}{Dw\Omega} = \frac{1}{141}\frac{RTa^3}{Dw\mathrm{V}} = \frac{1}{141}\frac{a^3}{wL\mathrm{V}^2} = \frac{1}{141}\frac{Ka^3}{\mathrm{V}^2}$$

where k is Boltzmann's constant, T is temperature, w is grain boundary width, D is the diffusion coefficient, Ω is atomic volume and V is molar volume.

In the DiffForm input file for Figures 5.3d and 5.6d parameters used are:

Average grain area for soluble phase $G = 0.01$ m^2

Diameter of equivalent circle $a = ((4/\pi)G)^{1/2} = 0.112$ m

$\mathrm{V} = 3.683 \times 10^{10}$ m^3/mol

K[SiO2, SiO2]= 2×10^{18} Pa.s m^3 mol^{-2}

So

$\eta = 1.469 \times 10^{-8}$ Pa.s

For simple shear (Figs. 5.4–5.6), the shear strain rate is $\dot{\varepsilon} = 0.5$ s^{-1}, so the equivalent differential stress (twice the shear stress) is 1.5×10^{-8} Pa. This value is in the right order of magnitude for the numerical prediction for the initial microstructure (1.9×10^{-8} Pa), but is slightly low. It is slightly low because elongate grains are stronger than equant grains of equivalent area; e.g. Elliott (1973) showed that at constant stress, grain elongation results in a decrease in strain rate.

Wheeler (2010) discussed anisotropic rheology during diffusion creep, with particular reference to a periodic microstructure constructed of a single irregular hexagonal grain shape. The results of Wheeler (2010) showed that anisotropy occurred in two orthogonal strong directions, and two orthogonal weak directions that lie at 45° to the strong directions. The model runs in this study were set up so that grain boundaries had zero viscosity, and, under these conditions, the weak directions have low strength. The porphyroclast was expected to have some effect on the strength of the starting geometry, but it seems to have been minor. The geometry of the elongate hexagons that comprised our initial microstructure meant that the direction of imposed pure shear happened to be aligned with the weak directions. As finite grain rotations occurred, the strength of the microstructure increased as the weak directions rotated away from parallelism with the imposed shear stress (Fig. 5.3d).

A periodic microstructure can create spurious results in models of diffusion creep, as discussed below. In pure shear, alignment of matrix grain boundaries is considered to lead to the observed drop in strength. Could the periodicity in the starting net be the reason for boundary alignment and associated failure/strength drop? This is not expected to be the case, as Wheeler (2009) saw sliding surfaces develop due to boundary alignment in a starting net with heterogeneous grain geometry during diffusion creep that affects the strength of the net in the same way (Wheeler, pers. comm.). Thus, boundary alignment is a natural product of diffusion creep deformation; it is shown here that porphyroclastic grains will influence where boundary alignment (and therefore sample weakening) will occur.

5.5.4 The effect of a periodic matrix

Although many natural rocks do exhibit an SPO, the geometry of the matrix grains in the start net used here is somewhat artificial. Such periodicity of grain shape can cause problems in diffusion creep modelling because the neighbour switches that occur as a natural product of diffusion-accommodated grain boundary sliding (Ashby and Verrall, 1973) all occur at the same time throughout the microstructure. Such synchronised grain switching is unrealistic and thus will produce unrealistic deformation behaviour. The advantage of a mostly-periodic matrix, however, is that it is easy to identify heterogeneity in matrix behaviour that is a product of (in this case) the porphyroclastic grain, which is why such a starting geometry was chosen. The limitations of such a microstructure being rigorously compared to real-world examples are clear, so further work on more realistic, heterogeneous starting geometries is necessary to elucidate the effects of large grains on stress, grain rotations, and other aspects of textural evolution in real rocks.

5.6 Conclusions

1) The presence of porphyroclastic grains has a significant effect on the microstructural evolution of a fine-grained matrix undergoing diffusion creep
2) Rotations of matrix grains are strongly influenced by rotation of porphyroclasts, especially matrix grains that lie adjacent to porphyroclasts

3) The rotation direction of a porphyroclastic grain does not have to be simply either synthetic or antithetic; rotation directions can change due to interactions with the matrix, and the overall evolution of grain rotations in a rock undergoing diffusion creep is complex
4) The presence of porphyroclastic grains is unlikely to influence formation of a CPO. A pre-existing CPO can be largely preserved, and depending on the shear geometry may undergo splitting into smaller domains due to the influence porphyroclast rotation has on matrix grains
5) Porphyroclasts create stress heterogeneities that focus the effects of diffusion creep. This can result in the alignment of grain boundaries, which can lead to a profound drop in strength of a material
6) The velocity of a rotating porphyroclast can lead to the destabilisation of grain rotations in a fine-grained matrix, which results in a significant drop in the strength of a material deforming by diffusion creep. Recovery of the microstructure from destabilisation, by eventual slowing of rotations to a steady-state, destabilises the strength of the material, but at a value lower than the original.

Chapter 6 Application of the Weighted Burgers Vector algorithm to high-angular resolution EBSD datasets

6.1 Abstract

Electron backscatter diffraction (EBSD) has a resolution limit which depends on the angular precision of the technique. The relatively new method of processing EBSD data known as high-angular resolution EBSD (HR-EBSD) improves the angular precision of the technique from 1° to < 0.006°, meaning information regarding intragranular distortions (elastic strains and rotations) can be extracted from the data in unparalleled detail. This study investigates, for the first time, how HR-EBSD processing can enhance the information gathered by the Weighted Burgers Vector algorithm, which calculates 3D information on which slip systems were active in plastically-deformed crystals from 2D EBSD data. EBSD data from naturally-deformed albite and experimentally-deformed olivine were utilised for the study. The results of the study show that applying the Weighted Burgers Vector technique to HR-EBSD-processed data allowed fine detail of intragranular distortion to be resolved in EBSD datasets, that could not be resolved prior to HR-EBSD processing. However, the WBV technique is fast, and extracts the same bulk information from conventional EBSD as it does from HR-processed datasets, albeit with less precision. For most of the traditional analyses performed with EBSD data, the more time-consuming and computing-intensive step of HR-processing may be unnecessary.

6.2 Introduction

The traditional resolution limits of EBSD depend on a) the angular precision of the technique, and b) the activation volume in the sample that interacts with the electron beam, which affects spatial resolution but will not be discussed further here (see review of EBSD technique in methods chapter). The absolute orientation of a crystal measured by conventional EBSD is accurate to ~1° (Humphreys, 2001; Wilkinson et al., 2006a). The accuracy of relative orientations of data points collected within a single grain is often the most important aspect of EBSD measurements, so that subgrain structures and intracrystalline distortion can be calculated to a high degree of certainty. The lowest misorientations between pixels are the least reliable (Humphreys, 2001; Prior, 1999), and it is the sum of orientation noise and the actual misorientations that is measured. Very small intragranular misorientations become increasingly difficult to measure with accuracy, as shown schematically in Figure 6.1.

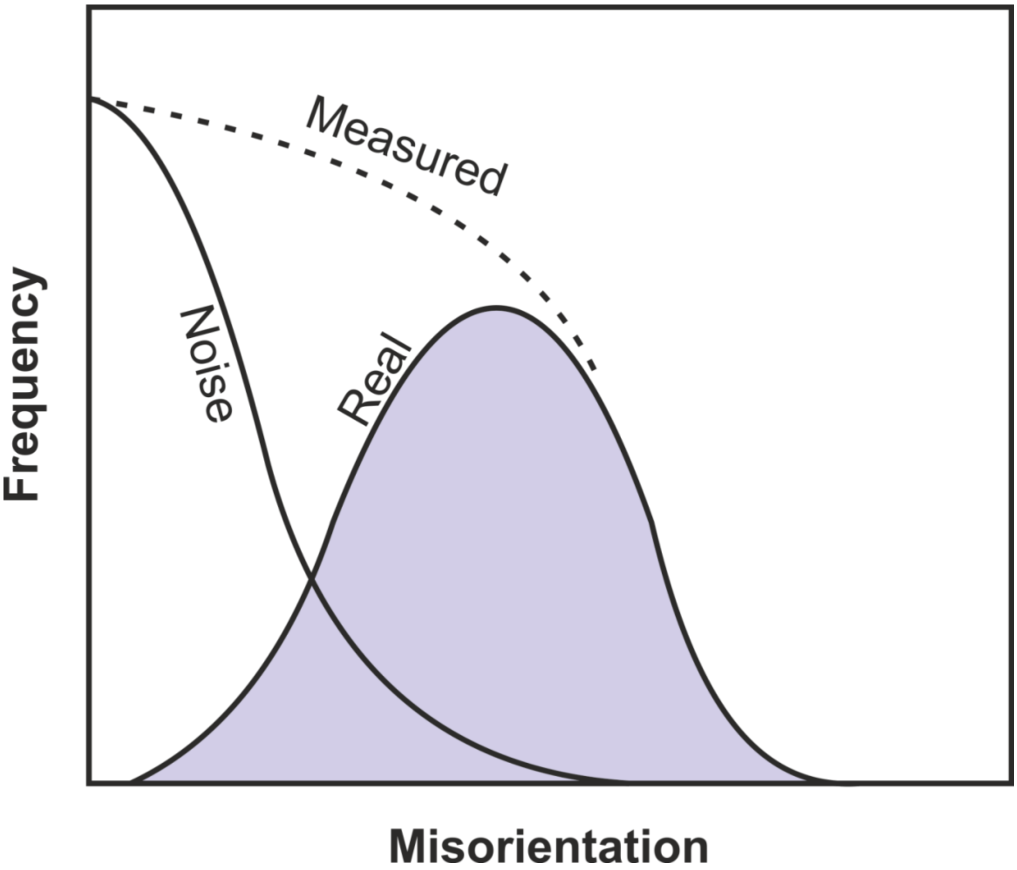

Figure 6.1 *Schematic figure showing that noise increases relative to real EBSD orientation measurements at lower misorientations. Redrawn from Humphreys (2001).*

As the EBSD technique has evolved, methods have been developed to extract additional information from EBSD datasets. One such method is the high-angular resolution EBSD (HR-EBSD) technique (Wilkinson et al., 2006b), which works by comparing conventional EBSD diffraction patterns using cross-correlation procedures, to increase the angular resolution of the data by two orders of magnitude (see methods), which allows information on lattice rotations and strains to be gathered (Britton and Hickey, 2018). An alternative method is the Weighted Burgers Vector (Wheeler et al., 2009), which can be used to calculate estimates of dislocation densities and the likely Burgers vector population using conventional 2D EBSD data (see methods). The Weighted Burgers Vector has never been systematically applied to HR-EBSD-processed data, so the two techniques are combined here for the first time. The results are compared against WBV data calculated from the same EBSD maps without application of the HR-EBSD algorithm.

The techniques are found to be complementary, because the HR-EBSD technique sharpens intragranular distortion features within the map data, meaning those features that the WBV can reveal are resolved in finer detail. Combining the two techniques can provide 3D information about the geometry of dislocation interactions, which currently cannot be gathered by other methods from 2D EBSD map data. It should also be noted that the bulk information extracted from conventional and HR-processed EBSD datasets is essentially the same, so, given the time and computing constraints of HR-EBSD, that technique may be unnecessary for many of the traditional applications of EBSD data.

6.3 Methods

6.3.1 HR-EBSD

The HR-EBSD technique was developed because the typical angular precision of conventional EBSD is about 0.5–1°, which is orders of magnitude too large to analyse elastic strains in most materials (Wilkinson et al., 2006a). Essentially, HR-EBSD works by measuring very small changes in the geometry of a deformed crystal through cross correlation of the diffraction patterns generated by EBSD (Britton et al., 2013). Small shifts in the zone axes of diffraction patterns can be identified using the cross-correlation procedure, which record angular changes due to residual elastic strains and local misorientation down to levels of < 0.006°. Misorientations are identified by the rotation of features in a diffraction pattern with respect to their position in the reference diffraction pattern, while elastic strains are observed as a change in angles between lattice plane features in the diffraction pattern of interest and the reference pattern (e.g. a change in distance between identified zone axes in each pattern). Because lattice rotations (i.e. misorientations) and elastic strains cause independent changes in the diffraction patterns, they can be analysed independently (Britton et al., 2013).

The albite EBSD dataset (Fig. 6.2a), used in the comparison that follows, was collected on an FEI Quanta650 FEG-SEM equipped with a Nordlys S detector and the Oxford Instruments Aztec software package in the Department of Earth Sciences at the University of Oxford. A 14 mm working distance, 70° specimen tilt, 30 kV accelerating voltage and 10 nA beam current were used for collection under low vacuum (50 Pa water vapour) conditions. Step size was 0.2 μm and no binning was used during data collection to preserve diffraction pattern quality. HR-EBSD data are collected in exactly the same way as conventional EBSD, but the diffraction patterns generated at each pixel are stored and decomposed into multiple regions of interest, to which the cross-correlation procedure is applied, comparing each region of interest in each pattern to the corresponding region of interest in a selected reference pattern (Britton and Wilkinson, 2011; Wilkinson et al., 2006b). The saved diffraction patterns were split into 100 distinct regions of interest.

The comparison of WBV results obtained from conventional and HR-EBSD datasets was also performed using an olivine sample, because (i) unlike plagioclase, slip systems in olivine are limited and well-constrained (Wallis et al., 2016), and (ii) the olivine sample used for analysis was known to have deformed by dislocation creep (Wallis et al., 2016), unlike the albite in this study. The olivine dataset used in the comparison (Fig. 6.2b) was collected from a single crystal of San Carlos olivine that was experimentally deformed in a Paterson apparatus at the University of Minnesota, in triaxial compression, at 1000 °C and 388 MPa differential stress, to a finite strain of 8%. The crystal was oriented so that the primary compressive stress roughly bisected the [010] and [001] crystallographic planes EBSD data were collected on the same FEI Quanta650 SEM at the University of Oxford, using essentially the same operating conditions, with a working distance between 8.4–11.9 mm, and a step size of 1.25 μm (Wallis et al., 2016).

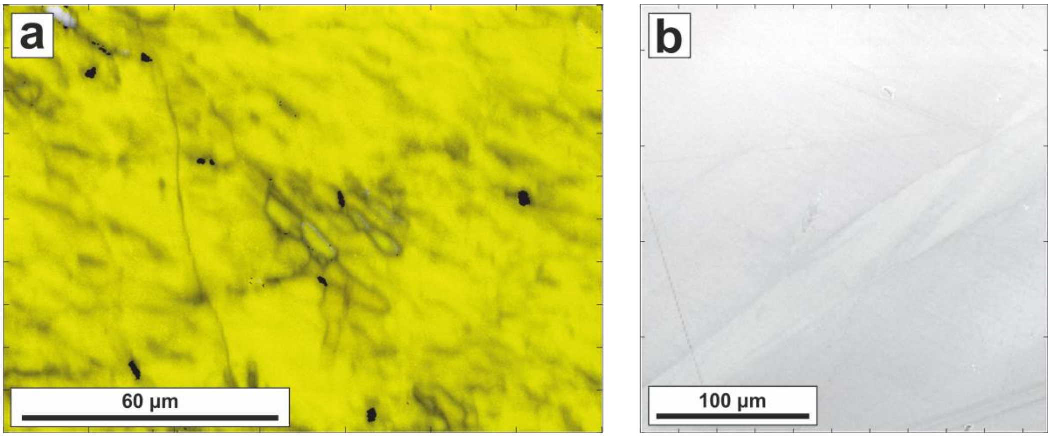

Figure 6.2 *a) All-Euler overlay on band contrast map of the albite sample used in this study, from the naturally deformed, low strain Gressoney metagabbros detailed in Chapter 3. b) All-Euler overlay on band contrast map of the single crystal San Carlos olivine sample used in this study, which was experimentally deformed in triaxial compression, at 1000 °C and 388 MPa differential stress, to a finite strain of 8%.*

6.3.2 Weighted Burgers Vector

The Weighted Burgers Vector algorithm is described in detail in section 3.4.5. As the name suggests, it is a vector quantity calculated from 2D map data, and so has a magnitude and a direction, which provide an estimate a lower bound on the magnitude of the dislocation density tensor, and 3D information about dislocation types present (i.e. directions of likely Burgers vectors), respectively (Wheeler et al., 2009). The WBV data presented here was calculated from a square region of 9 pixels, with the calculated WBV value being assigned to the central point.

6.4 Results

For the comparison of the two techniques, the WBV algorithm was first applied to conventional EBSD maps of the two samples, and then the WBV algorithm was applied to the *same* data, after it had been processed by the HR-EBSD technique.

6.4.1 Albite

The WBV can be used to calculate the net Burgers vector content of a given region of interest in an EBSD map by an integration around the edge of the area. Wheeler et al. (2009) first suggested such an integration would reduce the effect of noise within the data, and this has been confirmed in unpublished numerical experiments (Wheeler, pers. comm.). When the integral WBV is calculated around a loop, a histogram is generated which shows lengths of the WBV calculated at each pixel within the loop. WBVs of the smallest magnitude are those most prone to error, and should thus be discarded; hence the histogram provides a simple way to threshold minimum and maximum reliable WBV magnitude values.

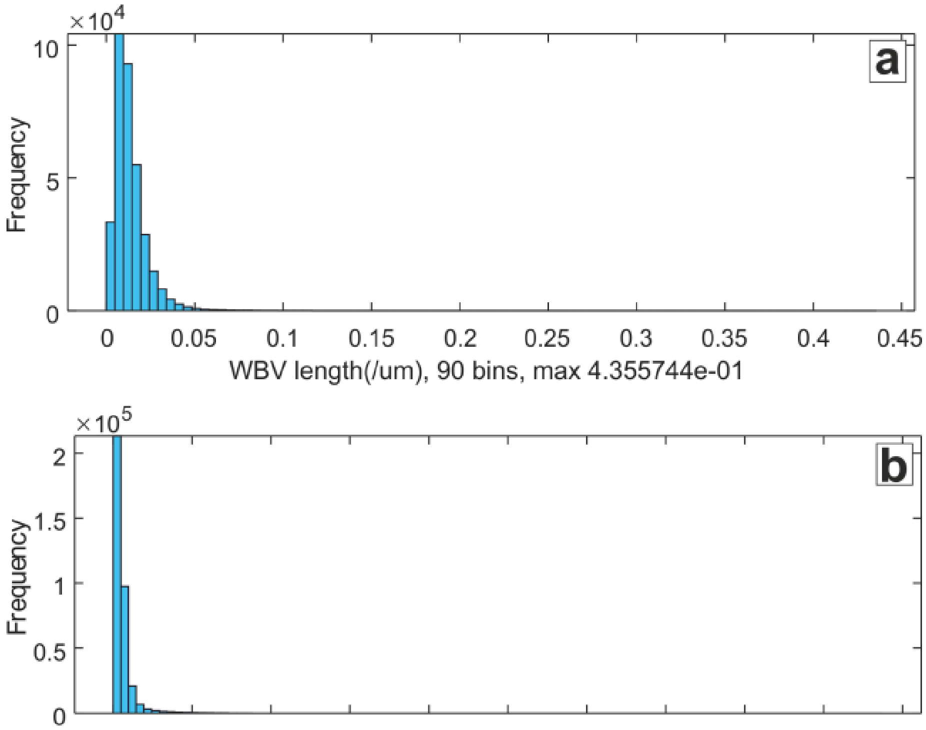

Figure 6.3 *a) Frequency histogram of WBV magnitudes calculated for the conventional EBSD map of albite. b) Frequency histogram of WBV magnitudes calculated for the HR-EBSD map of albite. Note the greater maximum WBV magnitude calculated from the HR-EBSD dataset.*

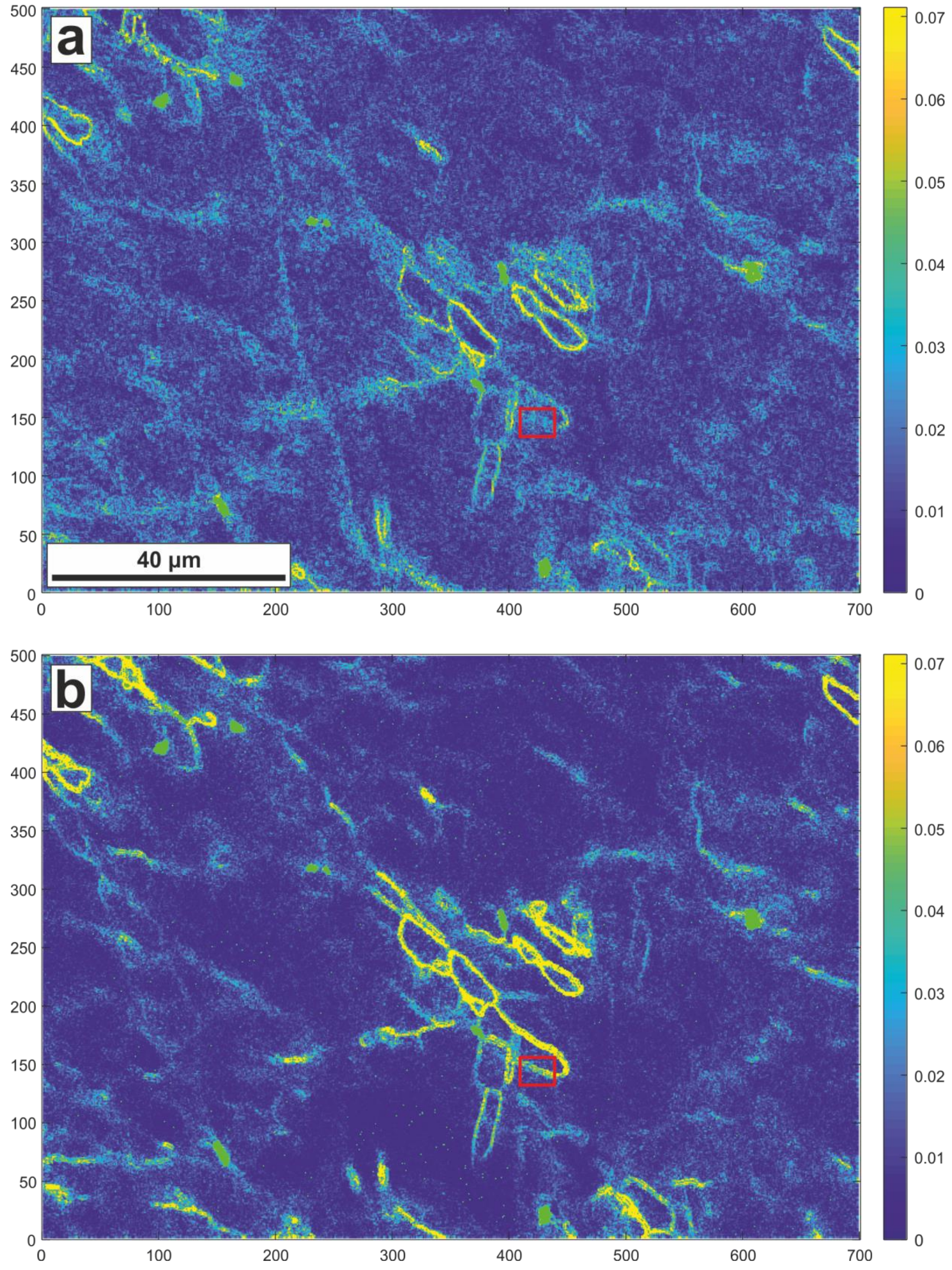

Figure 6.4 *a) WBV magnitude map of albite from conventional EBSD dataset, thresholded between 0.02 and 0.07* μm^{-1}*. b) WBV magnitude map of the same area using HR-EBSD-processed data, using the same thresholds. Intracrystalline features are more sharply defined in the HR-EBSD-processed map. Red boxes show the position of data presented in Fig. 6.7.*

When the WBV is calculated, frequency histograms of WBV magnitude are automatically generated (e.g. Figs. 6.3 & 6.8), which can be used to remove noise from a WBV magnitude map by thresholding minimum and maximum values. The main peak in the histogram is predominantly composed of noise, so most of the peak should be removed. The histogram generated by the conventional EBSD map of albite suggests a minimum value of 0.02 μm^{-1} and a maximum value of around 0.07 μm^{-1} should be used (Fig. 6.3; note different x axis scales). The histogram shows that the highest value for WBV magnitude actually occurs at a little under 0.45 μm^{-1}. However, using this value as a maximum when plotting WBV magnitude maps means intracrystalline features containing lower magnitude WBVs do not show up well in such maps, so a lower maximum value is recommended. Thresholding at the values stated above and plotting the WBV magnitude on to the albite map results in certain intracrystalline features, such as subgrain walls, emerging in the magnitude map (Fig. 6.4a). The WBV directions of pixels with the highest magnitudes can also be plotted using the IPF colour scheme (key in inset). The maximum magnitude used for this plot was increased to 0.45 μm^{-1}, to include all of the longest WBVs, as these are the most accurate (Fig. 6.5a). This is because the WBV is calculated from orientation gradients, which, in turn, relate to misorientations (angles and axes) between the point of interest and adjacent pixels. Low dislocation densities lead to smaller misorientations, bigger errors on misorientation axes and hence bigger errors in WBV. There is a clear dominance of blue pixels in the image, which corresponds to the [010] Burgers vector. This is not a Burgers vector that has been identified to be part of a common slip system in plagioclase, suggesting the observed intracrystalline distortion is a product of other processes. See Chapter 3 for a full discussion of these ideas.

The accuracy of the integral WBV depends on the angular resolution of the EBSD data (Piazolo et al., 2015), which suggests applying the WBV to HR-processed EBSD datasets should yield more accurate results. The histogram produced by integration of the HR-processed data shows the maximum WBV magnitude calculated for a single pixel has more than doubled, although the peak in the histogram has not shifted to higher values (Fig. 6.3b). Using the same threshold values as applied to the conventional EBSD dataset (min = 0.02, max = 0.07 μm^{-1}), more detail, with sharper boundaries, can be observed in the magnitude plot. The noise, apparent in the background of the HR-EBSD magnitude plot as stippling of colour, is reduced compared to the conventional EBSD dataset (Fig. 6.4b), and the same dominant central feature is resolved in sharper detail. Plotting WBV directions using the IPF colour

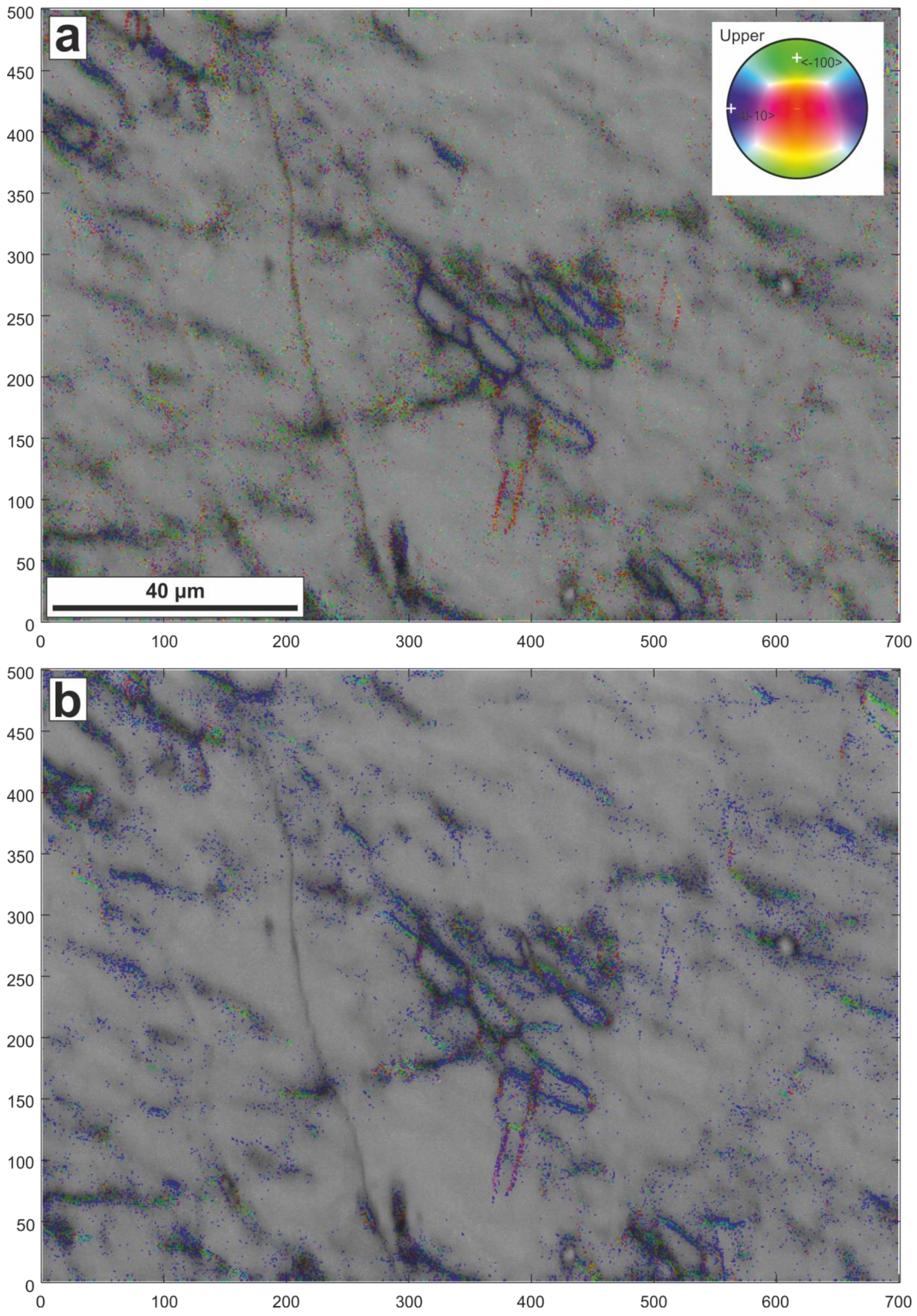

Figure 6.5 *WBV direction plots of a) conventional and b) HR-EBSD albite data. Noise reduction during HR-EBSD processing removes many single pixels with a range of IPF colours (i.e. orientations), leaving dominantly blue (i.e. the [010] crystallographic direction) WBV orientations in both linear features and isolated pixels.*

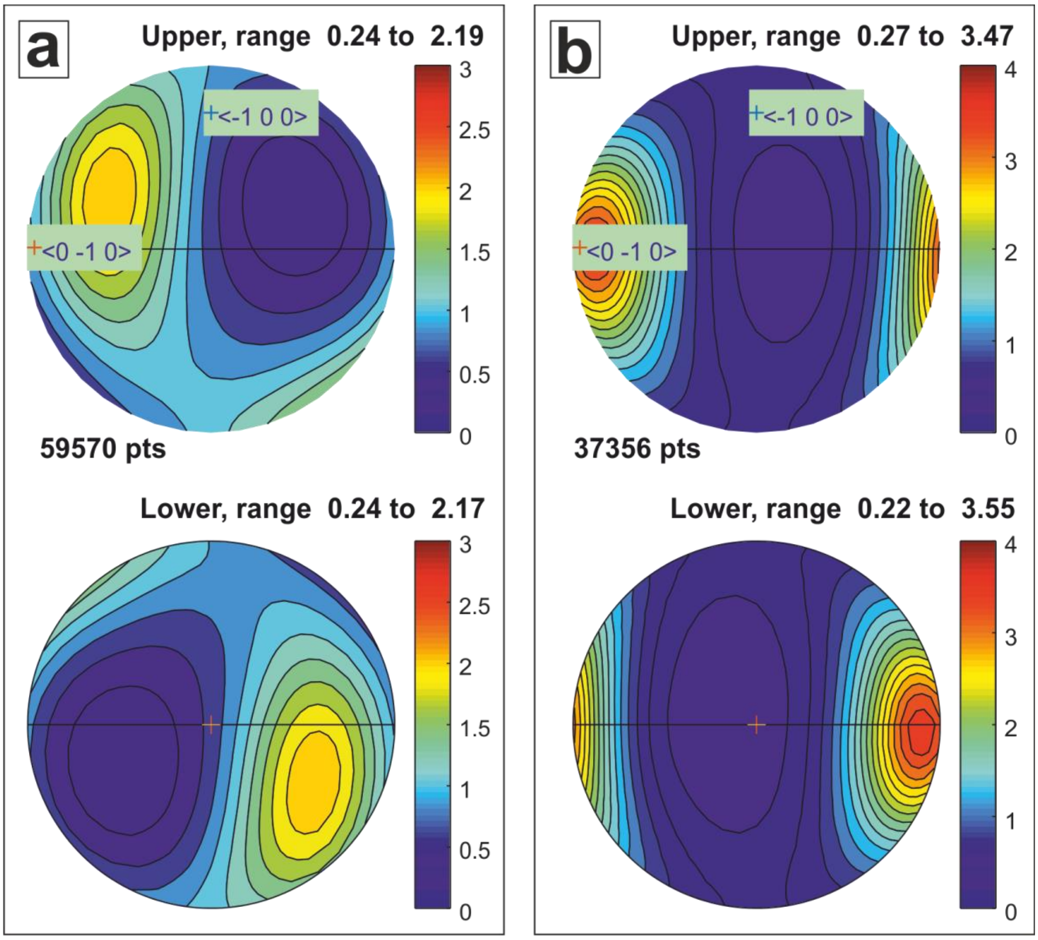

Figure 6.6 *Contoured IPF plots of the WBV directions plotted on the maps in Fig. 6.5. a) a range of directions are calculated from the conventional EBSD data. b) a clear maxima centred on the [010] crystallographic direction can be observed.*

scheme shows a stronger dominance of the 'blue' (i.e. [010]) crystallographic direction within the central feature (Fig. 6.5b). In addition, the WBV calculated for isolated pixels tends to be dominated by the [010] direction, unlike the isolated pixels plotted from the conventional EBSD data, which have a much wider spread (compare Figs. 6.5a & b). Contoured IPF plots confirm the dominance of the [010] Burgers vector in the HR-processed dataset (Fig. 6.6).

A close-up of part of a prominent looping feature in the HR-EBSD dataset that is not picked out in the conventional EBSD dataset serves to reinforce the extra detail that can be gathered using HR-EBSD data (Fig. 6.7; see box in Figs. 6.4a and b for location; map grid reference: [415 440 135 150]). Figures 6.7a and c show WBV magnitude maps, thresholded between 0.005 and 0.05 μm^{-1}, for the conventional and HR-EBSD datasets, respectively. In the conventional EBSD dataset, no linear feature can be determined, in contrast to a clear linear feature (subgrain wall?) visible in the HR-EBSD dataset.

Likewise, in WBV direction IPF plots (both thresholded between 0.02 and 0.5 μm^{-1}, no regular directional feature is observed in the conventional EBSD dataset (Fig. 6.7b), but a clear feature with WBVs consistently oriented in the [010] crystallographic direction is resolved (Fig. 6.7d); indeed, systematic changes in orientation *within* the linear feature – from the edges to the centre of the line – can also be observed.

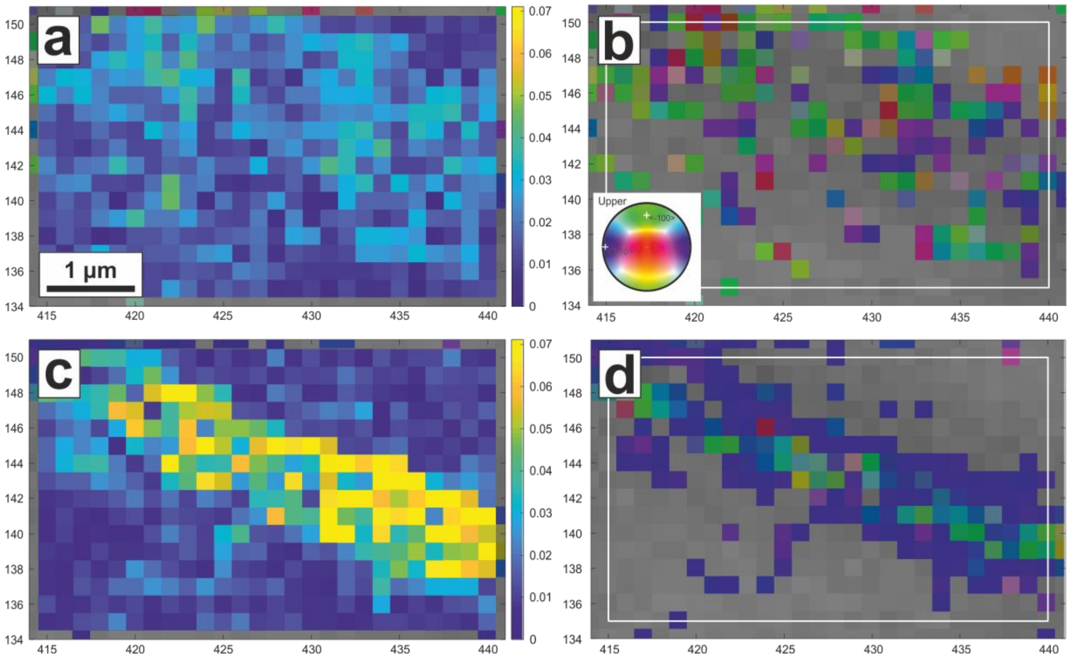

Figure 6.7 *Close-up of the region identified by the red box in Figs. 6.4a&b. In a) and b), from the conventional EBSD dataset, no linear feature is resolved, whereas after HR-EBSD processing a linear feature can be observed in both the c) WBV magnitude and d) WBV direction plots. Not only is the feature identifiable in the HR plots, some degree of detail within the line can be resolved, e.g. there is a systematic shift in orientation from either edge to the centre of the feature.*

6.4.2 Olivine

Studies of Burgers vector populations are generally focused on materials that are known or expected to have deformed by dislocation creep. The lattice distortion observed in the albite sample is not thought to be a product of dislocation creep (see Chapter 3 for a full discussion of these ideas). Therefore, a crystal with limited and well-known slip systems, olivine, was employed to explore the effects of HR-EBSD on WBV output further. Previous work on this olivine sample has shown that slip systems with [100] and [001] Burgers vectors dominate plastic deformation in the sample (Wallis et al., 2016; Wallis et al., 2017). The histograms of WBV magnitude calculated for the olivine dataset show the same general trend as the albite dataset; i.e. the peak is much narrower in the HR-EBSD processed dataset, due to removal of noise (Fig. 6.8).

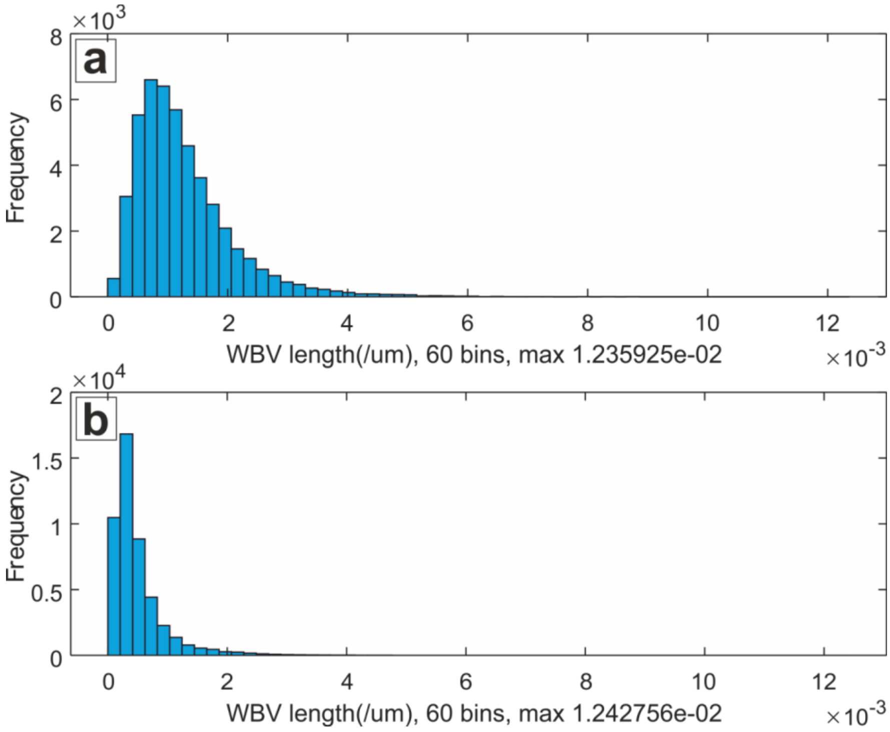

Figure 6.8 *a) Frequency histogram of WBV magnitudes calculated for the conventional EBSD map of olivine. b) Frequency histogram of WBV magnitudes calculated for the HR-EBSD map of olivine. Note almost identical maximum WBV magnitude calculated from each dataset. This differs from the albite histograms presented in Fig 6.3.*

In the albite dataset, HR-EBSD processing results in an increase in the largest WBV magnitude by a factor of two. This does not occur in the olivine dataset, with the largest WBVs in the conventional and HR-processed maps measured to be within 7×10^{-6} μm^{-1} of each other. For an equal comparison of the two maps, threshold values of 0.001 and 0.004 μm^{-1} were chosen (although note there may still be a step size bias), which results in the conventional EBSD map being somewhat noisy, although some intracrystalline features can be observed (Fig. 6.9a). Applying threshold values of 0.002 and 0.01 μm^{-1} to the conventional EBSD data makes the subparallel NE–SW trending lines stand out more clearly (Fig. 6.10a), but none of the more subtle features that can be observed in the HR-processed map (Fig. 6.9b) emerge. In the HR-processed map, sets of structures similar to those presented in Figure 6.5 of Wallis et al. (2017) can be resolved. Their 'Set 1', which trends NE–SW is very clear in this map, and less clear but observable is a second set of structures that trends WNW–ESE (Fig. 6.8b). If a lower maximum threshold of 0.002 μm^{-1} is used, the 'Set 2' structures become clearer in the map (Fig. 6.10b). Thus, the bulk information gathered by plotting the WBV magnitude from both datasets is similar, but the HR-processed dataset provides greater fine detail.

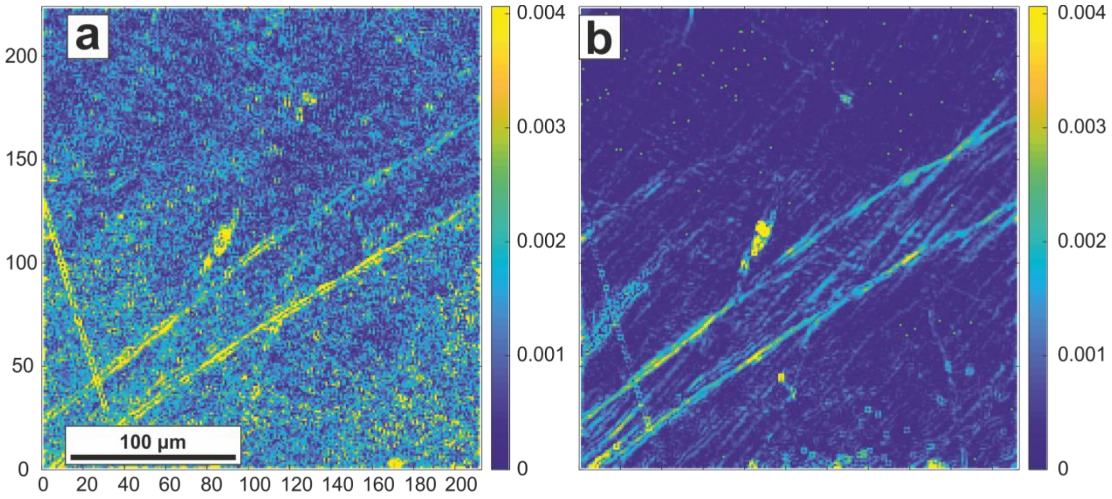

Figure 6.9 *WBV magnitude maps plotted from the a) conventional EBSD and b) HR-EBSD datasets of olivine. The conventional dataset contains lots of noise which obscures some of the fine detail that can be observed in the HR-processed data.* Thresholding between 0.001 and 0.014 µm^{-1} was applied to the WBV direction plots (Fig. 6.11). Similar to the albite data, a lack of resolution in the conventional EBSD dataset means subtle features are not identified, although a comparison of the two plots shows the main features (Set 1) share the same bulk orientations in each map. Red pixels correspond to the [001] direction in the IPF colour scheme. It is difficult to

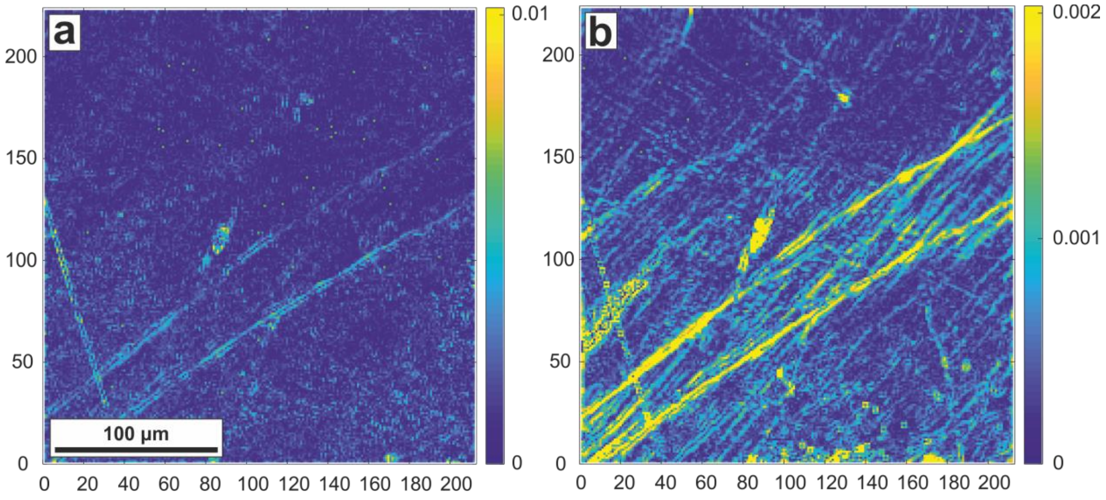

Figure 6.10 *WBV magnitude maps of the olivine dataset plotted with different threshold values. a) Conventional EBSD data plotted between 0.002 and 0.01 µm^{-1}. Much of the noise observed in Fig. 6.9a is removed, although fine scale features observed in the HR-processed data are still not resolvable. b) HR-EBSD data plotted between 0.001 and 0.002 µm^{-1}. The 'Set 2' structures are much clearer when the data are plotted within these bounds (compare with Fig. 6.9b).*

differentiate structures of any other colour (i.e. direction) from the noise, although in the top part of the map rows of blue pixels associated with the Set 2 structures of Wallis et al. (2017) can be seen (Fig. 6.11a). In the HR-EBSD dataset, Set 2 structures are completely lacking in the WBV direction plots, probably because they are below the minimum magnitude threshold (see future developments below). The Set 1 structures, however, are more sharply resolved, to a detail where the orientation of dominant Burgers vectors in subgrain walls can be seen to vary when different dislocation sets interact (Fig. 6.11b).

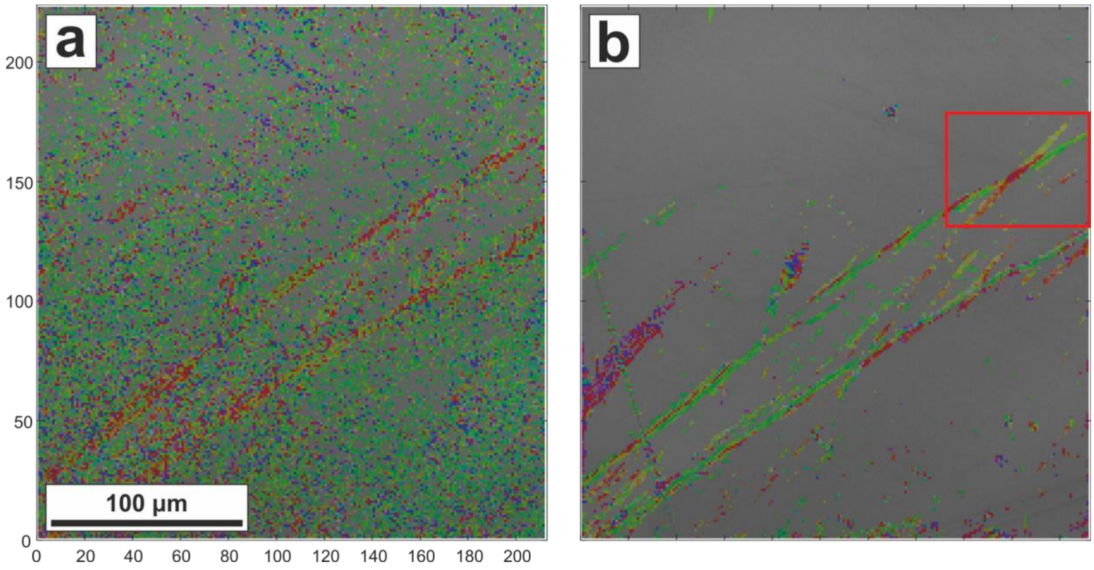

Figure 6.11 *WBV direction plots of a) conventional and b) HR- EBSD olivine data. Noise in the conventional dataset again obscures detail that can be picked out after HR-processing. See text for further discussion.*

Figure 6.12a shows a zoomed region of the olivine dataset (grid ref: [155 212 133 177]) where dominantly green (i.e. the [100] direction) and dominantly yellow (i.e. a set of dislocation structures of mixed character) pixels merge to dominantly red (i.e. the [001] direction). WBV directions can be plotted as arrows on to EBSD maps, which can provide additional information on the geometric compatibility between dislocation structures when they intersect (Fig. 6.12b). Arrows represent Burgers vector directions in sample space (i.e. which way the Burgers vectors point in Cartesian space, with x and y being the map axes and z plotting perpendicular to the map plane), and as they are 3D representations can point in to or out of the map plane, which is not easily visualised in the 2D map plane. 3D representations of the calculated WBV directions can be constructed, as shown in Figure 6.13. The 3D plots are currently also quite difficult to visualise, but it can be seen that the WBVs making up the green line (i.e. [100]) plot into the plane of the map, and the orange-yellow WBV plot out of the plane of the map.

Where they intersect, the [001] Burgers vector (red) dominates, and is oriented sub-parallel to the map plane. The WBV directions of the two lines are gradually deflected in to the overlapping zone, resulting in a switch in dominance to the [001] orientation. The 3D structure of the WBV can be more easily visualised in a movie of the 3D plot, as can be seen in M6.1 in the digital appendix at the back of this thesis.

6.5 Discussion

The information gleaned from EBSD can only ever be as detailed as the resolution of the data. It is broadly accepted that the HR-EBSD processing technique increases the angular resolution of EBSD data by two orders of magnitude (Britton et al., 2013; Britton and Hickey, 2018). The analysis presented here shows that if the WBV analytical technique is applied to HR-EBSD data, additional detail can be gathered from EBSD maps that is likely to be unresolvable in conventional EBSD datasets.

HR-EBSD removes much of the low-angle noise inherent in EBSD data collection (Fig. 6.1). Because of this, the range of WBV magnitudes calculated per map area is narrower (compare Fig. 6.3a & b, and Fig. 6.8a & b). A smaller range of WBV magnitudes means that a magnitude threshold can be set within closer limits, and is applied to refined data, which, in turn, means more detail can be resolved within WBV magnitude plots (compare Fig. 6.4a & b, and Fig. 6.9a & b).

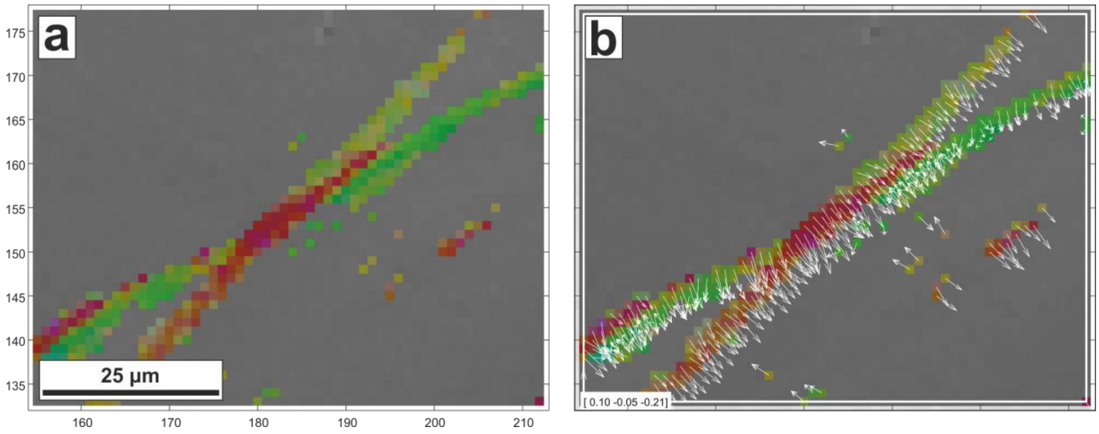

Figure 6.12 *Detail of interacting dislocation sets shown in Fig. 6.11. a) WBV directions plotted using the IPF colour scheme. b) Vector plot of calculated WBVs superposed as white arrows on the IPF map.*

In the albite IPF maps, the conventional EBSD dataset shows a wide range of orientations in WBV directions calculated for isolated pixels (Fig. 6.5a). In the HR-processed map, most of the spread has disappeared from the population of isolated pixels, which are dominated by the [010] direction. This switch may be due to HR-processing removing noise that prevents the [010] direction from being resolved in the conventional dataset, but the exact reason for the amplification of the [010] signal remains unclear, and more work is needed in this area to test these effects.

Additional fine detail can be resolved using HR-processed EBSD data in the looping dislocation sets in the albite map. The zoomed region shown in Figure 6.7 shows that there are actually three sets of parallel dislocation structures within what looks like a single structure in the conventional EBSD dataset (or in some areas is not resolved at all). The dislocation sets have alternating [010], [100] and [010] WBV directions, and the map shows that HR-processing can provide detail on how sets of dislocations with different Burgers vectors can contribute to the same intracrystalline features; a level of detail which is not resolvable in the conventional EBSD dataset.

6.5.1 Geometric compatibility of dislocation sets

The way in which intracrystalline dislocation structures interact during crystal plasticity exerts fundamental controls on deformation (strain hardening vs. strain weakening) and recrystallization (dominance of subgrain formation vs. grain boundary migration) behaviour in crystalline materials. The ability to carry out quantitative analysis of dislocation types, distributions and densities is therefore one of the key contributions that the EBSD technique has made to our understanding of the deformation behaviour of rocks (Wallis et al., 2016). Wallis et al. (2017) investigated dislocation interactions within the same olivine sample that was used in this study. During the original deformation experiments, the olivine was oriented to preferentially activate slip in the [100] and [001] directions, and those authors found that the dislocation sets that run NE–SW in the olivine maps are of mixed character, but composed dominantly of [100] and [001] screw dislocations, and (001)[100] edge dislocations. The WBV analysis of olivine in this study concurs with the results of that study (i.e. the same Burgers vectors dominate the sample), and also provides additional geometrical information on the influence of dislocation sets when they interact. For dislocation creep to efficiently accommodate large strains in a deforming crystal, it is understood that both glide and climb/cross-slip of dislocations must be achieved, e.g., Tullis (2002). Recovery by climb (of edge dislocations) or cross-slip (of screw dislocations) is particularly important in overcoming the tangling that occurs when dislocations of more than one slip system intersect. The WBV analysis shown in Figures 6.12 and 6.13 appears to show that the sets of (dominantly screw, although subgrain walls cannot be solely composed of screw dislocations; Wallis et al., 2017) dislocations intersect, which could potentially lead to tangling. The dominant Burgers vector, as calculated by the WBV, is observed to change across the intersection (Fig. 6.13, see M6.1 in the digital appendix at the back of this thesis).

One explanation for this change could be that the dislocation set switches to a new crystallographic plane, which is the definition of cross-slip. This observation suggests that information about the cross-slip of dislocations (i.e. one aspect of the 3D geometric compatibility of dislocation lines) could be resolved in detail from 2D EBSD data using a combination of the HR-EBSD and WBV processing techniques. As the viscosity of materials deforming by dislocation creep depends on whether creep is glide- or recovery-controlled, the ability to characterise the microphysical intracrystalline processes that occur during creep by this method could be fundamental to increasing our understanding about how the Earth's mantle (and other Earth materials) deforms. Mantle deformation exerts fundamental controls on the movement of tectonic plates, so is important in fully understanding many macroscale geological processes, from plate subduction and associated large magnitude, tsunamigenic earthquakes, to basin evolution and the associated formation of oil reservoirs. Although similar information can be gleaned from TEM, we are unaware of any other combination of EBSD-based methods that can extract similar information from 2D EBSD data. As EBSD is a well-established and relatively straightforward technique, there is vast potential for the combination of WBV and HR-EBSD processing to push our knowledge of such microphysical processes forward.

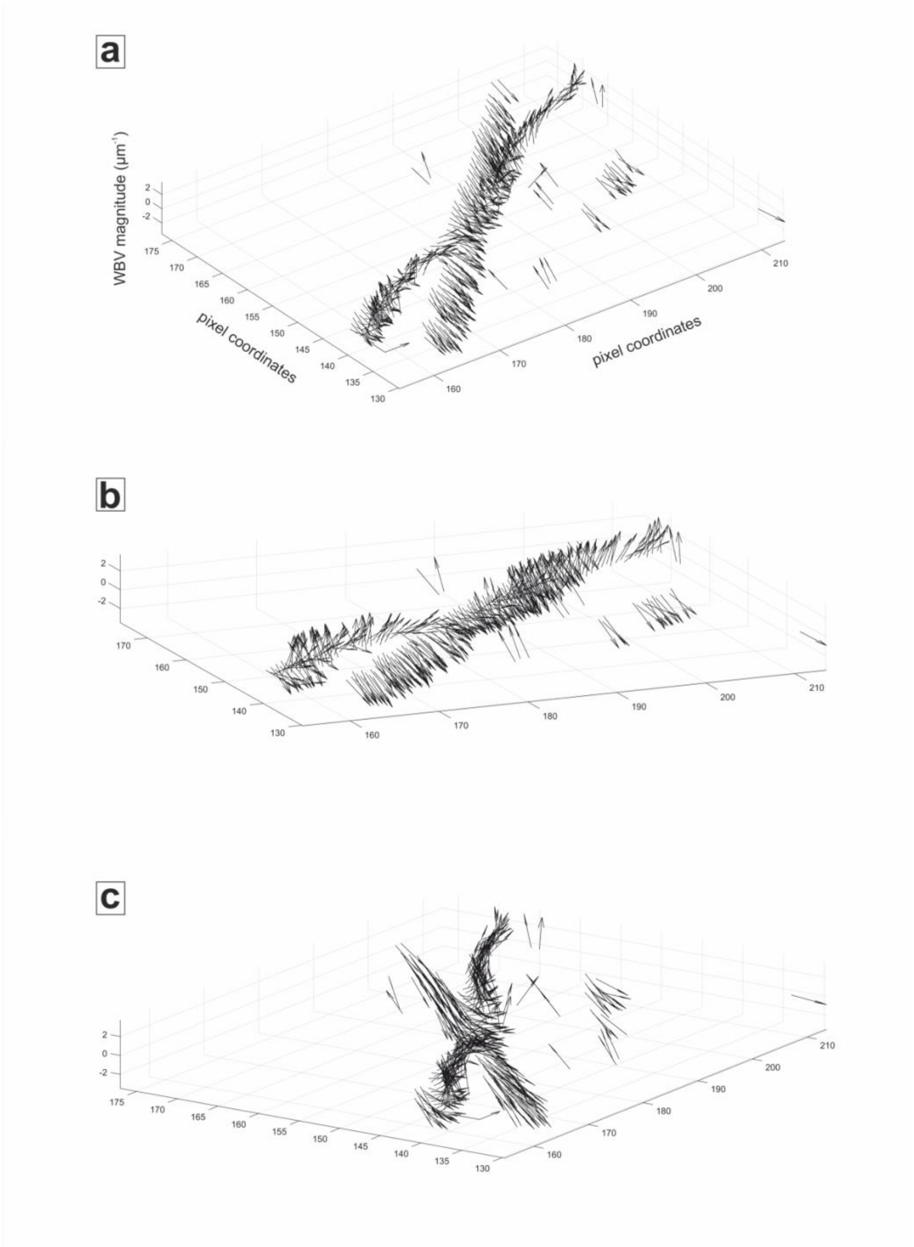

Figure 6.13 *The WBV calculation attributes all lattice curvature recorded in EBSD maps to the presence of geometrically necessary dislocations (GNDs). The algorithm constrains both a lower bound magnitude of the dislocation density tensor, and the directions of the Burgers vectors that are most likely to comprise the GND population, from measured lattice curvature (Wheeler et al., 2009), so is itself a vector which can be plotted in 3D. This figure shows a 3D vector plot of all WBVs calculated from the intersecting dislocation sets shown in Fig. 6.12. The two dislocation sets are observed to be roughly perpendicular, with dominant directions merging as they intersect. a), b) and c) show the same plot from different angles, so the interaction between the two sets can be clearly seen. The numbers on the x and y axes in the plots are EBSD map coordinates, in pixels, and the scale on the z axis is WBV magnitude (*μm^{-1}*). A 3D movie of this plot, M6.1, can be found in the digital appendix at the back of this thesis.*

6.6 Conclusions:

1. The WBV technique allows 3D information on Burgers vector populations present in the microstructure to be extracted from 2D EBSD data. Applying this technique to HR-EBSD processed data allowed fine detail of intragranular distortion to be resolved in EBSD datasets.
2. Information on the interaction between dislocation sets, which could not be extracted by either technique alone, was resolved in the olivine dataset. Such information on dislocation interactions from EBSD datasets could help to better constrain the rheological behaviour of materials deforming by crystal plasticity.
3. The WBV technique is fast, and extracts the same bulk information from conventional EBSD as it does from HR-processed datasets, albeit with less precision. For most of the traditional analyses performed with EBSD data, the more time-consuming and computing-intensive step of HR-processing may be unnecessary.
4. HR-EBSD and WBV processing are complimentary techniques that can be used to gather information, which is currently unavailable via other methods, from 2D EBSD datasets, regarding the microphysical intracrystalline processes that control the rheology of Earth materials deforming by dislocation creep.

Chapter 7 Summary and suggestions for future work

The previous four chapters of this thesis have described individual packages of work, and the conclusions of each work package are presented in the relevant chapter. The main findings of each piece of work will be summarised here, and related back to the thesis aims as listed in Chapter 1. The implications of the findings in this thesis to the wider field of rock deformation will then be discussed, and suggestions for future work will be presented.

7.1 Summary of results

In Chapter 1, it was stated that the feldspars are the most common group of minerals in the Earth's mid to lower crust, and so control crustal rheology, but their deformation behaviour remains relatively poorly understood. Complex interactions between metamorphism and deformation occur in plagioclase feldspar, so multiple processes can work consecutively or in tandem to reduce plagioclase grain size in deforming rocks, and promote strain localisation into discrete zones of shear. Grain size reduction can lead to a switch in the dominant deformation mechanism in shear zones, promoting grain size-sensitive creep by (fluid-assisted) grain boundary diffusion creep. This deformation mechanism is relatively poorly understood, as it leaves few microstructural indicators.

In Chapter 3, the relationship between metamorphism and deformation in plagioclase was explored using naturally-deformed, greenschist-facies, albite-rich metamorphosed gabbros from the Gressoney Shear Zone, NW Italian Alps. The plagioclase in the original gabbros would have been Ca-bearing, but a complete lack of Ca was recorded in all chemical analyses of the albite. This indicates a greenschist-facies metamorphic transition from Ca-plagioclase to albite went to completion in the samples, generating both porphyroclasts of albite, and a population of small, new albite grains. For this to have occurred in mm-scale porphyroclasts, the transition must have been very efficient, implying fluid-enhanced kinetics. Initial fracturing of the feldspar opened fluid pathways. Microstructural analysis suggests different amounts of fluid availability, which varied with different degrees of fracturing, influenced whether porphyroclasts or new grains formed. EBSD was used to extract crystallographic orientation data in low-strain samples from both albitic porphyroclasts and associated populations of small grains. The EBSD data showed that small grains that neighbour porphyroclasts tend to share common orientations with the porphyroclasts. Preserved twin orientations in altered porphyroclasts suggest that crystallographic orientation was inherited from parent Ca-bearing plagioclase. These observations, that a fluid-assisted metamorphic reaction, which preserved parent crystallographic information, occurred, suggest that the porphyroclasts underwent interface-coupled replacement reactions (Putnis, 2009). Replacement reactions have been shown to be common in feldspar (Engvik et al., 2008; Plümper and Putnis, 2009). These types of reactions occur in a nm-thin film of fluid (Hövelmann et al., 2009), and thus it was concluded that they were the dominant transformation mechanism in plagioclase porphyroclasts, where fracturing, and therefore fluid availability, was limited.

As energy dispersive spectroscopy (EDS) showed a complete lack of Ca in both grain populations in all studied areas, the system lacked a chemical driving force for 'neocrystallisation' of fine-grained albite from the porphyroclasts. Where fracturing (and therefore fluid availability) was more abundant, sub-µm-scale Ca-plagioclase fragments may have acted as nuclei upon which albite could precipitate to generate the bands of small grains that are observed to run through porphyroclasts. However, the orientation relationship between porphyroclasts and small grains must also be explained, the frictional sliding and grain rotations associated with cataclastic grain size reduction would be unlikely to have preserved an orientation. EBSD processing revealed porphyroclast lattices were highly distorted, whereas small grains were observed to be nominally strain free. Replacement reactions can load product grains with growth dislocations and other defects during imperfect topotactic growth, due to mismatches between lattice parameters (Jain et al., 1997; van der Merwe, 1991), resulting in grains with a high dislocation density produced by a chemical, rather than mechanical, process. Thus, although the exact mechanism of small grain nucleation remains unclear, the differences in internal distortion between the porphyroclasts (high dislocation density) and the new, µm-scale grains (low dislocation density) suggest that the small grains are likely to have grown at the expense of the porphyroclasts. Grain boundary segments that separate the porphyroclastic and µm-scale grains require growth of small grains into porphyroclasts by grain boundary migration, which implies boundary migration occurred as a response to the stored strain energy in the porphyroclasts. The mechanism of topotactic replacement in feldspar during fluid-assisted, interface-coupled replacement reactions, has been observed to produce grains with a high defect density (Hövelmann et al., 2009). The results of this study suggest this mechanism of defect production could provide a driving force for recrystallization (i.e. a grain size reduction and associated changes in strength) in response to stored strain energy, even in the absence of crystal plastic deformation.

Chapter 3 focuses on low strain metagabbros, where abundant porphyroclasts are preserved. In Chapter 4, microstructural data from a suite of metagabbros at five different strain levels are presented, which show how inherited CPO domains become modified during fluid-assisted grain boundary diffusion creep (pressure solution) in the albite-rich matrix. The inherited CPO domains are interpreted to have been produced by the complete replacement of albite porphyroclast remnants by the growth of small strain-free grains, as described in Chapter 3. On grain size reduction, a switch in dominant deformation mechanism, from grain-size-insensitive to grain-size-sensitive creep, can occur. In the middle crust, where fluids are abundant, pressure solution is likely to dominate viscous deformation, and this occurred in the Gressoney metagabbros. In the studied samples, each CPO domain was produced from a single crystal, so originally had a texture strength of 1 on the M-Index (Skemer et al., 2005), which provides an opportunity to assess how pressure solution modified texture in the domains with increasing strain. In the samples, an increase in strain clearly led to texture weakening, as observed qualitatively by maxima in pole figures becoming more diffuse. Texture weakening was quantified using both the M-Index (Table 4.1), which lowered significantly in individual CPO domains with increasing strain, and misorientation angle distribution plots, which became skewed to higher angles with increasing stain and finally followed the theoretical random distribution.

Nearly all rocks are polyphase materials, so understanding how different phases have interacted during deformation is fundamental to our overall picture of the geodynamic behaviour of the Earth. At greenschist facies, Ca-bearing plagioclase breaks down to albite plus new Ca-Al-bearing phase(s), which in mafic rocks, is normally an epidote mineral (clinozoisite in our samples). At the lowest strains, albite and clinozoisite are not well-mixed, but mixing increases with strain (although never becomes completely homogeneous). Strain caps of clinozoisite and pressure shadows of albite suggest solubility of albite was increased in regions of locally high stress. Albite grain size was observed to be smaller with increasing clinozoisite abundance, which may be due to the inhibition of textural annealing at albite-clinozoisite boundaries (albite-albite boundaries tend to be lobate and exhibit 120° triple junctions). Inhibition of grain growth may have extended the time over which grain-size-sensitive creep dominated deformation in the samples. Aspect ratios of albite grains increased with increasing clinozoisite content towards higher strains, which may be due to enhanced dissolution of albite at albite-clinozoisite boundaries, creating more pronounced flattening in albite during pressure solution. At the same strain level, a higher abundance of clinozoisite within an albite

CPO domain preserved texture strength, which may have happened because second phases tend to inhibit the grain rotations normally associated with diffusion creep.

Many questions remain about how microstructures evolve during diffusion creep, because very few characteristics of diffusion creep have been identified, and it is often the absence of indicators of other mechanisms that has led investigators to suggest a dominance of diffusion creep during deformation. Numerical simulations of diffusion creep can provide insight into its effects on microstructural evolution (Ford et al., 2004; Ford et al., 2002; Wheeler, 2009). In Chapter 5, a numerical simulation of grain boundary diffusion creep, DiffForm, was used to investigate the effects of porphyroclasts on the microstructural evolution of matrix grains during pure and simple shear. A starting geometry in which a large grain is surrounded by small matrix grains was set up to undergo 200 increments of either pure or simple shear, and the finite rotations and angular velocities of all grains were tracked during deformation. In the model runs, rotations of matrix grains are strongly influenced by rotation of the porphyroclast in both shear geometries, but the rotation direction of the porphyroclast changes depending on how the surrounding matrix behaves, showing there is a feedback between the two populations. Although there is no reason why the presence of porphyroclasts may influence CPO formation in rocks deforming by diffusion creep, pre-existing CPOs can be preserved to high strains during grain boundary diffusion creep (Wheeler, 2009; see also Chapter 4). The results of the simple shear model show a pre-existing CPO in a fine-grained matrix may be split into smaller domains as sets of matrix grains undergo different-sense rotations depending on their interactions with a porphyroclast. This may have occurred in the small CPO domains observed in the naturally deformed metagabbros at strain levels 2–4, as presented in Chapter 4. The model results suggest that in both pure and simple shear, changes in the angular velocity of a rotating porphyroclast can lead to the destabilisation of rotations of matrix grains, which is associated with a strength drop. Restabilisation of rotations to a steady-state is concomitant with a restabilisation in material strength, but the new strength of the material is lower than it was prior to destabilisation.

The work presented here is primarily an EBSD investigation into naturally deformed rocks. The information about deformation histories and processes that can be extracted by the EBSD technique depends on the resolution of EBSD data. High-angular resolution (HR-) EBSD processing is a cutting edge method that can be used to increase the angular resolution of EBSD datasets. The Weighted Burgers Vector (WBV) is also a relatively new innovation that was developed to extract 3D information about dislocation populations in deformed materials from 2D EBSD maps. The WBV has never previously been applied to HR-EBSD datasets so, finally, in Chapter 6, the results of a comparison of the information that the WBV can extract from conventional and HR-EBSD processed datasets are presented. Datasets of both feldspar and olivine are compared. In both cases, HR-EBSD processing enhanced WBV output by refining intracrystalline deformation features, allowing fine detail about Burgers vector populations to be extracted in HR-EBSD datasets that is obscured by noise prior to HR-processing. It should be noted, however, that in general the information extracted on Burger's vector populations is the same, so unless very specific questions, such as the interactions between sets of dislocations, aim to be addressed by EBSD studies, the extra time-consuming and computing-intensive step of HR-processing may be unnecessary.

7.2 Implications

Fluid-mediated, interface-coupled replacement reactions are common, especially in fluid-rich regions of the middle crust (Putnis and John, 2010), and can be responsible for the albitisation of plagioclase on a regional scale (Engvik et al., 2008; Hövelmann et al., 2009; Plümper et al., 2017; Plümper and Putnis, 2009). As replacement reactions can produce distorted crystals, resultant mineral grains can appear to have undergone crystal-plastic deformation (Spruzeniece et al., 2017), thus it is possible that their influence could long have been overlooked or misinterpreted. With a clear view of the microstructures that develop during replacement reactions, criteria can be identified to distinguish between the effects of replacement reactions and traditional plastic deformation (see Chapter 3, and Spruzeniece et al., 2017). Observation of the signature of transient microporosity, the production of CPO domains that do not match expected distributions with respect to the kinematic axes, and the observation of unexpected Burger's vectors in dislocation populations are, taken together, all good indicators of replacement reactions.

Species of feldspar exist along a temperature-dependent solid solution, so they are prone to react during vertical movement in the crust. Because all species of feldspar share a similar crystallographic structure, imperfect topotactic replacement is common (Engvik et al., 2008; Hövelmann et al., 2009; Plümper and Putnis, 2009). This could be an important, and as yet overlooked, mechanism for loading feldspar (and similar families of minerals) with defects and dislocations at conditions where high dislocation densities are not expected, i.e. where slip systems for a given material are not expected to be active. Loading a crystal with a high dislocation density leads to material weakening, and/or grain size reduction, and is therefore associated with a drop in strength. Thus, replacement reactions may exert controls on the strength of the crust. Shear zones are localised regions of high strain, and replacement reactions and subsequent grain size reduction by the processes detailed in this thesis may contribute to the development of shear zones and strain localisation in the crust. This in turn implies such processes may exert controls on where seismogenic crustal faults develop.

In general, (fluid-assisted) diffusion creep remains a relatively poorly understood deformation mechanism. A better understanding of the mechanism is important because diffusion creep is interpreted to be how much of the Earth's crust (Getsinger and Hirth, 2014; Montési and Hirth, 2003b; Platt and Behr, 2011) and mantle (Hiraga et al., 2010; Karato and Wu, 1993; Miyazaki et al., 2013; Wheeler, 2009) deforms. For example, the upper crust is commonly classified to be the brittle part of the lithosphere (Fig. 1.1a), but this neglects the fact that fluid-assisted diffusion creep, or pressure solution, operates alongside fracturing to relax stress between fracture events, which exerts controls on the magnitude and recurrence intervals of seismic events (Gratier et al., 1999). Fluid-assisted diffusion creep also works to develop folds and cleavage in upper crustal rocks, meaning the upper crust in fact exhibits both brittle and viscous behaviour (Gratier et al., 2013). Pressure solution plays an important role in the diagenesis of sedimentary rocks, exerting an influence on reservoir quality, but controversy remains over whether effective stress or temperature has the greater influence on how efficient the deformation mechanism is (Worden et al., 2018).

The observation that inherited CPOs can be preserved to high strains during fluid-assisted diffusion creep is important for our understanding of processes in the deep Earth, because our current understanding of mantle deformation relies on the presence (dislocation creep) or absence (diffusion creep) of seismic anisotropy (Karato et al., 2008; Mainprice, 2015; Wheeler, 2009). Wheeler (2009) showed that seismic anisotropy can be preserved during diffusion creep, because grain rotation rates decrease through time when microstructural change by diffusion creep dominates change due to grain growth in a single phase aggregate. The observation that grain rotations can be inhibited by the presence of a second phase, made in Chapter 4, adds weight to this argument, as most real rocks are multiphase aggregates, and supports the assertion made by Wheeler (2009) that the link between seismic anisotropy and deformation mechanism in the subsurface must be made with caution. The observation that differences in grain size can have a profound effect on the strength of an aggregate during diffusion creep, due to complex interactions between grains of different sizes (Chapter 5), also indicates more work is needed to fully understand how this common deformation mechanism works in real rocks.

7.3 Suggestions for future work

In Chapter 3, a grain size reduction that occurs in conjunction with interface-coupled replacement reactions is described. Orientation relationships between porphyroclasts and small grains indicate that small grains grow at the expense of the more distorted porphyroclasts. However, the exact nucleation mechanism of the small grains remains unclear. Nuclei may precipitate from fluid, or may develop from small (sub-micron scale?) regions of undistorted porphyroclast that form during topotactic replacement. This could be tested experimentally by creating distorted replacement reaction products similar to those detailed in Spruzeniece et al. (2017) and allowing them to anneal to see if this leads to an overall grain size reduction. Deformation experiments on grains produced by replacement reactions are lacking from the literature. As replacement reactions can weaken product grains by loading them with defects, how those grains respond to subsequent deformation will yield important information on how such weakening may affect the strength of the crust. One current limitation is the size of grains currently produced synthetically in the lab, however many examples of rocks showing evidence of grains that have undergone interface-coupled replacement have been cited in the literature, so tests on natural samples would be a good place to start.

The presence of the [010] Burger's vector observed in abundance in porphyroclastic grains in Chapter 3 requires further investigation. Here, its presence was attributed to non-crystal plastic mechanisms, although low temperature plasticity of plagioclase has been reported to activate different slip systems than those expected at higher temperatures (Shigematsu and Tanaka, 2000). Low temperature deformation experiments on single crystals, carried out under high confining pressures to suppress the fracture that is common on the two good plagioclase cleavages, could provide insight into whether slip in the [010] direction can be activated under some conditions.

Additional future work on how the distribution of phases affects grain parameters and texture strength could be carried out following the procedures set out in Herwegh et al. (2011), where the impact of spatial distribution of second phases is quantified using interparticle distance measurements, and the potential degree of boundary pinning is assessed using the Zener parameter (Z = second-phase size/second-phase volume fraction; Herwegh and Berger, 2004). Alternatively, a modified version of the phase boundary density technique outlined in Cross and Skemer (2017) using total phase boundary-length, as calculated in MTEX from EBSD maps of known area, could be used (see Appendix 4 for script).

The results of the diffusion creep modelling presented in Chapter 5 are preliminary, because of the periodicity of matrix grain shapes, which may produce artificial effects if neighbour switching occurs at many grain junctions simultaneously. Starting geometries that have more heterogeneous grain shapes should be tested for comparison. The models were set up to explore the effect of different grain sizes on microstructural evolution during diffusion creep. However, as detailed in Wheeler (2009), diffusion creep does not happen in isolation, and other processes that modify a microstructure that may inhibit the effect of diffusion creep, e.g. grain growth, can operate in parallel. There is a need to understand the process of diffusion creep more fully, and to do so it is necessary to develop the capacity of the DiffForm modelling suite to incorporate multiple processes occurring in tandem. Work to couple the modelling of diffusion creep using DiffForm with grain growth using Elle (Jessell et al., 2001) is in its preliminary stages (Piazolo et al., 2018).

Some of the substructures that can be observed in the WBV magnitude map are not observed in the WBV direction maps. For example, the Set 2 structures of Wallis et al. (2016) are just about resolvable in Figure 9b, but cannot be resolved in Figure 11b. Thresholding at lower minimum values brings out some of the Set 2 substructure (e.g. Fig. 10), but the amount of noise that remains in the map at those threshold levels makes it difficult to distinguish specific structures. Because the WBV directions for each pixel are stored, one future addition to the WBV functionality could be to display WBV at all pixels where it is within a certain angle (e.g., 5/10°) of a specific crystallographic direction, regardless of calculated magnitude. This may help to resolve subtle structures that are 'buried' within the noise (provided they do not have the same direction as noisy pixels), and may provide additional information about the characteristics of sets of dislocation structures with different dominant Burgers vectors.

The 3D distribution of WBV directions as arrows is a useful tool but remains somewhat hard to visualise. Applying the IPF colour scheme to arrows on these plots may help to distinguish where and how dominant Burgers vectors change along a dislocation structure, and when two or more dislocation structures intersect. The 3D movies of these plots are a useful tool, but could be enhanced by the same colour scheme.

The work contained in this thesis has shown that feldspar in mid-crustal gabbroic rocks undergo a multitude of changes due to metamorphism, deformation, interaction with fluids, and competition between deformation mechanisms. Nowhere were attempts made to understand similar interactions that are known to occur in granitic rocks, although interface-coupled replacement reactions (Engvik et al., 2008), phase mixing (Viegas et al., 2016), and pressure solution (Menegon et al., 2008) are all known to occur commonly in those rocks. The analytical methods used here could equally be applied to metamorphosed granites, and in so doing help to widen the view presented here of the Earth's middle crust as a dynamic, evolving environment.

References

Anders, M.H., Laubach, S.E., Scholz, C.H., 2014. Microfractures: A review. Journal of Structural Geology 69, 377-394.

Ashby, M., 1970. The deformation of plastically non-homogeneous materials. Philosophical Magazine 21, 399-424.

Ashby, M.F., Verrall, R.A., 1973. Diffusion-accommodated flow and superplasticity. Acta Metallurgica 21, 149-163.

Bachmann, F., Hielscher, R., Schaeben, H., 2010. Texture Analysis with MTEX – Free and Open Source Software Toolbox. Solid State Phenomena 160, 63-68.

Bercovici, D., Ricard, Y., 2012. Mechanisms for the generation of plate tectonics by two-phase grain-damage and pinning. Physics of the Earth and Planetary Interiors 202-203, 27-55.

Berton, J.R., Durney, D.W., Wheeler, J., 2011. Diffusion-creep modelling of fibrous pressure shadows II: influence of inclusion size and interface roughness. Geological Society, London, Special Publications 360, 319.

Berton, J.R., Durney, D.W., Wheeler, J., Ford, J.M., 2006. Diffusion-creep modelling of fibrous pressure-shadows. Tectonophysics 425, 191-205.

Bestmann, M., Piazolo, S., Spiers, C.J., Prior, D.J., 2005. Microstructural evolution during initial stages of static recovery and recrystallization: new insights from in-situ heating experiments combined with electron backscatter diffraction analysis. Journal of Structural Geology 27, 447-457.

Bestmann, M., Prior, D.J., 2003. Intragranular dynamic recrystallization in naturally deformed calcite marble: diffusion accommodated grain boundary sliding as a result of subgrain rotation recrystallization. Journal of Structural Geology 25, 1597-1613.

Bons, P.D., den Brok, B., 2000. Crystallographic preferred orientation development by dissolution–precipitation creep. Journal of Structural Geology 22, 1713-1722.

Bons, P.D., Elburg, M.A., Gomez-Rivas, E., 2012. A review of the formation of tectonic veins and their microstructures. Journal of Structural Geology 43, 33-62.

Britton, B., Holton, I., Meaden, G., Dingley, D., 2013. High angular resolution electron backscatter diffraction: measurement of strain in functional and structural materials. Microsc. Anal 27, 8-13.

Britton, T.B., Hickey, J.L.R., 2018. Understanding deformation with high angular resolution electron backscatter diffraction (HR-EBSD). IOP Conference Series: Materials Science and Engineering 304, 012003.

Britton, T.B., Wilkinson, A.J., 2011. Measurement of residual elastic strain and lattice rotations with high resolution electron backscatter diffraction. Ultramicroscopy 111, 1395-1404.

Brodie, K.H., Rutter, E.H., 1985. On the Relationship between Deformation and Metamorphism, with Special Reference to the Behavior of Basic Rocks, in: Thompson, A.B., Rubie, D.C. (Eds.), Metamorphic Reactions: Kinetics, Textures, and Deformation. Springer New York, New York, NY, pp. 138-179.

Bucher, K., Stober, I., 2010. Fluids in the upper continental crust. Geofluids 10, 241-253.

Bürgmann, R., Dresen, G., 2008. Rheology of the Lower Crust and Upper Mantle: Evidence from Rock Mechanics, Geodesy, and Field Observations. Annual Review of Earth and Planetary Sciences 36, 531-567.

Carpenter, M.A., 1994. Subsolidus Phase Relations of the Plagioclase Feldspar Solid Solution, in: Parsons, I. (Ed.), Feldspars and their Reactions. Springer Netherlands, Dordrecht, pp. 221-269.

Champness, P., 1977. Transmission electron microscopy in earth science. Annual Review of Earth and Planetary Sciences 5, 203-226.

Cherniak, D.J., 2010. Cation Diffusion in Feldspars. Reviews in Mineralogy and Geochemistry 72, 691-733.

Coble, R.L., 1963. A Model for Boundary Diffusion Controlled Creep in Polycrystalline Materials. Journal of Applied Physics 34, 1679-1682.

Cowie, P.A., Scholz, C.H., Roberts, G.P., Faure Walker, J.P., Steer, P., 2013. Viscous roots of active seismogenic faults revealed by geologic slip rate variations. Nature Geoscience 6, 1036-1040.

Cross, A.J., Skemer, P., 2017. Ultramylonite generation via phase mixing in high-strain experiments. Journal of Geophysical Research: Solid Earth 122, 1744-1759.

Czaplińska, D., Piazolo, S., Zibra, I., 2015. The influence of phase and grain size distribution on the dynamics of strain localization in polymineralic rocks. Journal of Structural Geology 72, 15-32.

De Bresser, J., Ter Heege, J., Spiers, C., 2001. Grain size reduction by dynamic recrystallization: can it result in major rheological weakening? International Journal of Earth Sciences 90, 28-45.

De Bresser, J.H.P., Peach, C.J., Reijs, J.P.J., Spiers, C.J., 1998. On dynamic recrystallization during solid state flow: Effects of stress and temperature. Geophysical Research Letters 25, 3457-3460.

Deer, W.A., Howie, R.A., Zussman, J., 2013. An introduction to the rock-forming minerals, 3rd ed. Mineralogical Society, UK.

Díaz Aspiroz, M., Lloyd, G.E., Fernández, C., 2007. Development of lattice preferred orientation in clinoamphiboles deformed under low-pressure metamorphic conditions. A SEM/EBSD study of metabasites from the Aracena metamorphic belt (SW Spain). Journal of Structural Geology 29, 629-645.

Dimanov, A., Dresen, G., Xiao, X., Wirth, R., 1999. Grain boundary diffusion creep of synthetic anorthite aggregates: The effect of water. Journal of Geophysical Research: Solid Earth 104, 10483-10497.

Drury, M.R., Urai, J.L., 1990. Deformation-related recrystallization processes. Tectonophysics 172, 235-253.

Elliott, D., 1973. Diffusion Flow Laws in Metamorphic Rocks. GSA Bulletin 84, 2645-2664.

Engler, O., Randle, V., 2009. Introduction to Texture Analysis: Macrotexture, Microtexture and Orientation Mapping. Taylor and Francis.

Engvik, A.K., Putnis, A., Fitz Gerald, J.D., Austrheim, H., 2008. Albitization of Granitic Rocks: The Mechanism of Replacement of Oligoclase by Albite. The Canadian Mineralogist 46, 1401-1415.

Fitz Gerald, J., Stünitz, H., 1993. Deformation of granitoids at low metamorphic grade. I: Reactions and grain size reduction. Tectonophysics 221, 269-297.

Ford, J.M., Ford, N.J., Wheeler, J., 2004. Simulation of grain-boundary diffusion creep: analysis of some new numerical techniques. Proceedings of the Royal Society of London. Series A: Mathematical, Physical and Engineering Sciences 460, 2395.

Ford, J.M., Wheeler, J., Movchan, A.B., 2002. Computer simulation of grain-boundary diffusion creep. Acta Materialia 50, 3941-3955.

Fossen, H., 2016. Structural geology. Cambridge University Press.

Fusseis, F., Regenauer-Lieb, K., Liu, J., Hough, R.M., De Carlo, F., 2009. Creep cavitation can establish a dynamic granular fluid pump in ductile shear zones. Nature 459, 974.

Gardner, R., Piazolo, S., Evans, L., Daczko, N., 2017. Patterns of strain localization in heterogeneous, polycrystalline rocks – a numerical perspective. Earth and Planetary Science Letters 463, 253-265.

Getsinger, A.J., Hirth, G., 2014. Amphibole fabric formation during diffusion creep and the rheology of shear zones. Geology 42, 535-538.

Getsinger, A.J., Hirth, G., Stünitz, H., Goergen, E.T., 2013. Influence of water on rheology and strain localization in the lower continental crust. Geochemistry, Geophysics, Geosystems 14, 2247-2264.

Giannuzzi, L.A., Stevie, F.A., 1999. A review of focused ion beam milling techniques for TEM specimen preparation. Micron 30, 197-204.

Gómez Barreiro, J., Lonardelli, I., Wenk, H.R., Dresen, G., Rybacki, E., Ren, Y., Tomé, C.N., 2007. Preferred orientation of anorthite deformed experimentally in Newtonian creep. Earth and Planetary Science Letters 264, 188-207.

Gower, R.J.W., Simpson, C., 1992. Phase boundary mobility in naturally deformed, high-grade quartzofeldspathic rocks: evidence for diffusional creep. Journal of Structural Geology 14, 301-313.

Gratier, J.-P., Dysthe, D.K., Renard, F., 2013. The role of pressure solution creep in the ductility of the Earth's upper crust. Advances in Geophysics 54, 47-179.

Gratier, J.-P., Renard, F., Labaume, P., 1999. How pressure solution creep and fracturing processes interact in the upper crust to make it behave in both a brittle and viscous manner. Journal of Structural Geology 21, 1189-1197.

Griera, A., Llorens, M.-G., Gomez-Rivas, E., Bons, P.D., Jessell, M.W., Evans, L.A., Lebensohn, R., 2013. Numerical modelling of porphyroclast and porphyroblast rotation in anisotropic rocks. Tectonophysics 587, 4-29.

Grove, T.L., Baker, M.B., Kinzler, R.J., 1984. Coupled CaAl-NaSi diffusion in plagioclase feldspar: Experiments and applications to cooling rate speedometry. Geochimica et Cosmochimica Acta 48, 2113-2121.

Hacker, B.R., Christie, J.M., 1990. Brittle/Ductile and Plastic/Cataclastic Transitions in Experimentally Deformed and Metamorphosed Amphibolite, The Brittle-Ductile Transition in Rocks. American Geophysical Union, pp. 127-147.

Hansen, L.N., Zimmerman, M.E., Dillman, A.M., Kohlstedt, D.L., 2012. Strain localization in olivine aggregates at high temperature: A laboratory comparison of constant-strain-rate and constant-stress boundary conditions. Earth and Planetary Science Letters 333-334, 134-145.

Herwegh, M., Berger, A., 2004. Deformation mechanisms in second-phase affected microstructures and their energy balance. Journal of Structural Geology 26, 1483-1498.

Herwegh, M., Linckens, J., Ebert, A., Berger, A., Brodhag, S.H., 2011. The role of second phases for controlling microstructural evolution in polymineralic rocks: A review. Journal of Structural Geology 33, 1728-1750.

Hildyard, R.C., Prior, D.J., Mariani, E., Faulkner, D.R., 2009. Crystallographic preferred orientation (CPO) of gypsum measured by electron backscatter diffraction (EBSD). Journal of Microscopy 236, 159-164.

Hiraga, T., Miyazaki, T., Tasaka, M., Yoshida, H., 2010. Mantle superplasticity and its self-made demise. Nature 468, 1091-1094.

Hirth, G., Kohlstedt, D.L., 1995. Experimental constraints on the dynamics of the partially molten upper mantle: Deformation in the diffusion creep regime. Journal of Geophysical Research: Solid Earth 100, 1981-2001.

Hirth, G., Tullis, J., 1992. Dislocation creep regimes in quartz aggregates. Journal of Structural Geology 14, 145-159.

Hövelmann, J., Putnis, A., Geisler, T., Schmidt, B.C., Golla-Schindler, U., 2009. The replacement of plagioclase feldspars by albite: observations from hydrothermal experiments. Contributions to Mineralogy and Petrology 159, 43-59.

Hull, D., Bacon, D., 2011. Introduction to Dislocations (Fifth Edition). Butterworth-Heinemann, Oxford.

Humphreys, F.J., 2001. Review Grain and subgrain characterisation by electron backscatter diffraction. Journal of Materials Science 36, 3833-3854.

Humphreys, F.J., 2004. Characterisation of fine-scale microstructures by electron backscatter diffraction (EBSD). Scripta Materialia 51, 771-776.

Humphreys, J., Beanland, R., Goodhew, P.J., 2014. Electron microscopy and analysis. CRC Press.

Imon, R., Okudaira, T., Kanagawa, K., 2004. Development of shape- and lattice-preferred orientations of amphibole grains during initial cataclastic deformation and subsequent deformation by dissolution–precipitation creep in amphibolites from the Ryoke metamorphic belt, SW Japan. Journal of Structural Geology 26, 793-805.

Jain, S.C., Harker, A.H., Cowley, R.A., 1997. Misfit strain and misfit dislocations in lattice mismatched epitaxial layers and other systems. Philosophical Magazine A 75, 1461-1515.

Jessell, M., Bons, P., Evans, L., Barr, T., Stüwe, K., 2001. Elle: the numerical simulation of metamorphic and deformation microstructures. Computers & Geosciences 27, 17-30.

Jessell, M.W., Bons, P.D., Griera, A., Evans, L.A., Wilson, C.J.L., 2009. A tale of two viscosities. Journal of Structural Geology 31, 719-736.

Ji, S., Mainprice, D., 1988. Natural deformation fabrics of plagioclase: implications for slip systems and seismic anisotropy. Tectonophysics 147, 145-163.

Jiang, Z., Prior, D.J., Wheeler, J., 2000. Albite crystallographic preferred orientation and grain misorientation distribution in a low-grade mylonite: implications for granular flow. Journal of Structural Geology 22, 1663-1674.

Karato, S.-i., Jung, H., Katayama, I., Skemer, P., 2008. Geodynamic Significance of Seismic Anisotropy of the Upper Mantle: New Insights from Laboratory Studies. Annual Review of Earth and Planetary Sciences 36, 59-95.

Karato, S.-I., Paterson, M.S., FitzGerald, J.D., 1986. Rheology of synthetic olivine aggregates: Influence of grain size and water. Journal of Geophysical Research 91, 8151.

Karato, S.-i., Wu, P., 1993. Rheology of the Upper Mantle: A Synthesis. Science 260, 771-778.

Kilian, R., Heilbronner, R., Stünitz, H., 2011. Quartz grain size reduction in a granitoid rock and the transition from dislocation to diffusion creep. Journal of Structural Geology 33, 1265-1284.

Kruse, R., Stünitz, H., 1999. Deformation mechanisms and phase distribution in mafic high-temperature mylonites from the Jotun Nappe, southern Norway. Tectonophysics 303, 223-249.

Kruse, R., Stünitz, H., Kunze, K., 2001. Dynamic recrystallization processes in plagioclase porphyroclasts. Journal of Structural Geology 23, 1781-1802.

Law, R.D., 1990. Crystallographic fabrics: a selective review of their applications to research in structural geology. Geological Society, London, Special Publications 54, 335-352.

Loewenstein, W., 1954. The distribution of aluminum in the tetrahedra of silicates and aluminates. American Mineralogist: Journal of Earth and Planetary Materials 39, 92-96.

Logan, J.M., Dengo, C.A., Higgs, N.G., Wang, Z.Z., 1992. Chapter 2 Fabrics of Experimental Fault Zones: Their Development and Relationship to Mechanical Behavior, in: Evans, B., Wong, T.-f. (Eds.), International Geophysics. Academic Press, pp. 33-67.

Mainprice, D., 2015. Seismic Anisotropy of the Deep Earth from a Mineral and Rock Physics Perspective. 487-538.

Mainprice, D., Bachmann, F., Hielscher, R., Schaeben, H., 2014. Descriptive tools for the analysis of texture projects with large datasets usingMTEX: strength, symmetry and components. Geological Society, London, Special Publications 409, 251-271.

Mainprice, D., Nicolas, A., 1989. Development of shape and lattice preferred orientations: application to the seismic anisotropy of the lower crust. Journal of Structural Geology 11, 175-189.

Martelat, J.-E., Schulmann, K., Lardeaux, J.-M., Nicollet, C., Cardon, H., 1999. Granulite microfabrics and deformation mechanisms in southern Madagascar. Journal of Structural Geology 21, 671-687.

Maruyama, S., Liou, J.G., Suzuki, K., 1982. The peristerite gap in low-grade metamorphic rocks. Contributions to Mineralogy and Petrology 81, 268-276.

Matthews, J., 1975. Epitaxial growth. Academic Press, New York.

Matthews, J.W., Blakeslee, A.E., 1974. Defects in epitaxial multilayers: I. Misfit dislocations. Journal of Crystal Growth 27, 118-125.

Mehl, L., Hirth, G., 2008. Plagioclase preferred orientation in layered mylonites: Evaluation of flow laws for the lower crust. Journal of Geophysical Research 113.

Menegon, L., Fusseis, F., Stünitz, H., Xiao, X., 2015. Creep cavitation bands control porosity and fluid flow in lower crustal shear zones. Geology 43, 227-230.

Menegon, L., Pennacchioni, G., Spiess, R., 2008. Dissolution-precipitation creep of K-feldspar in mid-crustal granite mylonites. Journal of Structural Geology 30, 565-579.

Menegon, L., Stünitz, H., Nasipuri, P., Heilbronner, R., Svahnberg, H., 2013. Transition from fracturing to viscous flow in granulite facies perthitic feldspar (Lofoten, Norway). Journal of Structural Geology 48, 95-112.

Miranda, E.A., Hirth, G., John, B.E., 2016. Microstructural evidence for the transition from dislocation creep to dislocation-accommodated grain boundary sliding in naturally deformed plagioclase. Journal of Structural Geology 92, 30-45.

Miyazaki, T., Sueyoshi, K., Hiraga, T., 2013. Olivine crystals align during diffusion creep of Earth's upper mantle. Nature 502, 321-326.

Montési, L.G., Hirth, G., 2003a. Grain size evolution and the rheology of ductile shear zones: from laboratory experiments to postseismic creep. Earth and Planetary Science Letters 211, 97-110.

Montési, L.G.J., Hirth, G., 2003b. Grain size evolution and the rheology of ductile shear zones: from laboratory experiments to postseismic creep. Earth and Planetary Science Letters 211, 97-110.

Mukai, H., Austrheim, H., Putnis, C.V., Putnis, A., 2014. Textural Evolution of Plagioclase Feldspar across a Shear Zone: Implications for Deformation Mechanism and Rock Strength. Journal of Petrology 55, 1457-1477.

Newman, J., Lamb, W.M., Drury, M.R., Vissers, R.L.M., 1999. Deformation processes in a peridotite shear zone: reaction-softening by an H2O-deficient, continuous net transfer reaction. Tectonophysics 303, 193-222.

Noiriel, C., Renard, F., Doan, M.-L., Gratier, J.-P., 2010. Intense fracturing and fracture sealing induced by mineral growth in porous rocks. Chemical Geology 269, 197-209.

Passchier, C.W., Trouw, R.A., 2005. Microtectonics. Springer Science & Business Media.

Pearce, M.A., Wheeler, J., 2011. Grain growth and the lifetime of diffusion creep deformation. Geological Society, London, Special Publications 360, 257-272.

Pearce, M.A., Wheeler, J., Prior, D.J., 2011. Relative strength of mafic and felsic rocks during amphibolite facies metamorphism and deformation. Journal of Structural Geology 33, 662-675.

Piazolo, S., Bestmann, M., Prior, D.J., Spiers, C.J., 2006. Temperature dependent grain boundary migration in deformed-then-annealed material: Observations from experimentally deformed synthetic rocksalt. Tectonophysics 427, 55-71.

Piazolo, S., Bons, P.D., Griera, A., Llorens, M.G., Gomez-Rivas, E., Koehn, D., Wheeler, J., Gardner, R., Godinho, J.R.A., Evans, L., Lebensohn, R.A., Jessell, M.W., 2018. A review of numerical modelling of the dynamics of microstructural development in rocks and ice: Past, present and future. Journal of Structural Geology.

Piazolo, S., Montagnat, M., Grennerat, F., Moulinec, H., Wheeler, J., 2015. Effect of local stress heterogeneities on dislocation fields: Examples from transient creep in polycrystalline ice. Acta Materialia 90, 303-309.

Pirrie, D., Butcher, A.R., Power, M.R., Gottlieb, P., Miller, G.L., 2004. Rapid quantitative mineral and phase analysis using automated scanning electron microscopy (QemSCAN); potential applications in forensic geoscience. Geological Society, London, Special Publications 232, 123-136.

Platt, J.P., 2015. Rheology of two-phase systems: A microphysical and observational approach. Journal of Structural Geology 77, 213-227.

Platt, J.P., Behr, W.M., 2011. Grainsize evolution in ductile shear zones: Implications for strain localization and the strength of the lithosphere. Journal of Structural Geology 33, 537-550.

Plümper, O., Botan, A., Los, C., Liu, Y., Malthe-Sørenssen, A., Jamtveit, B., 2017. Fluid-driven metamorphism of the continental crust governed by nanoscale fluid flow. Nature geoscience 10, 685.

Plümper, O., Putnis, A., 2009. The Complex Hydrothermal History of Granitic Rocks: Multiple Feldspar Replacement Reactions under Subsolidus Conditions. Journal of Petrology 50, 967-987.

Poirier, J., 1985. Creep of crystals. Cambridge University Press, Cambridge.

Prior, D.J., 1999. Problems in determining the misorientation axes, for small angular misorientations, using electron backscatter diffraction in the SEM. Journal of Microscopy 195, 217-225.

Prior, D.J., Wheeler, J., 1999. Feldspar fabrics in a greenschist facies albite-rich mylonite from electron backscatter diffraction. Tectonophysics 303, 29-49.

Prior, D.J., Wheeler, J., Peruzzo, L., Spiess, R., Storey, C., 2002. Some garnet microstructures: an illustration of the potential of orientation maps and misorientation analysis in microstructural studies. Journal of Structural Geology 24, 999-1011.

Putnis, A., 2002. Mineral replacement reactions: from macroscopic observations to microscopic mechanisms. Mineralogical Magazine 66, 689-708.

Putnis, A., 2009. Mineral Replacement Reactions. Reviews in Mineralogy and Geochemistry 70, 87-124.

Putnis, A., 2015. Transient Porosity Resulting from Fluid–Mineral Interaction and its Consequences. Reviews in Mineralogy and Geochemistry 80, 1-23.

Putnis, A., John, T., 2010. Replacement Processes in the Earth's Crust. Elements 6, 159-164.

Putnis, A., Putnis, C.V., 2007. The mechanism of reequilibration of solids in the presence of a fluid phase. Journal of Solid State Chemistry 180, 1783-1786.

Qian, G., Li, Y., Gerson, A.R., 2015. Applications of surface analytical techniques in Earth Sciences. Surface Science Reports 70, 86-133.

Randle, V., 2009. Electron backscatter diffraction: Strategies for reliable data acquisition and processing. Materials Characterization 60, 913-922.

Reddy, S., Wheeler, J., Cliff, R., 1999. The geometry and timing of orogenic extension: an example from the Western Italian Alps. Journal of Metamorphic Geology 17, 573-590.

Reddy, S.M., Wheeler, J., Butler, R.W.H., Cliff, R.A., Freeman, S., Inger, S., Pickles, C., Kelley, S.P., 2003. Kinematic reworking and exhumation within the convergent Alpine Orogen. Tectonophysics 365, 77-102.

Rosenberg, C.L., Stünitz, H., 2003. Deformation and recrystallization of plagioclase along a temperature gradient: an example from the Bergell tonalite. Journal of Structural Geology 25, 389-408.

Rutter, E., 1976. The kinetics of rock deformation by pressure solution. Philosophical Transactions of the Royal Society of London A: Mathematical, Physical and Engineering Sciences 283, 203-219.

Rutter, E.H., 1983. Pressure solution in nature, theory and experiment. Journal of the Geological Society 140, 725-740.

Rutter, E.H., Brodie, K.H., 1988. The role of tectonic grain size reduction in the rheological stratification of the lithosphere. Geologische Rundschau 77, 295-307.

Rutter, E.H., Maddock, R.H., Hall, S.H., White, S.H., 1986. Comparative microstructures of natural and experimentally produced clay-bearing fault gouges. pure and applied geophysics 124, 3-30.

Rybacki, E., Dresen, G., 2000. Dislocation and diffusion creep of synthetic anorthite aggregates. Journal of Geophysical Research: Solid Earth 105, 26017-26036.

Rybacki, E., Dresen, G., 2004a. Deformation mechanism maps for feldspar rocks. Tectonophysics 382, 173-187.

Rybacki, E., Dresen, G., 2004b. Deformation mechanism maps for feldspar rocks. Tectonophysics 382, 173-187.

Rybacki, E., Gottschalk, M., Wirth, R., Dresen, G., 2006. Influence of water fugacity and activation volume on the flow properties of fine-grained anorthite aggregates. Journal of Geophysical Research: Solid Earth 111.

Satsukawa, T., Ildefonse, B., Mainprice, D., Morales, L.F.G., Michibayashi, K., Barou, F., 2013. A database of plagioclase crystal preferred orientations (CPO) and microstructures - implications for CPO origin, strength, symmetry and seismic anisotropy in gabbroic rocks. Solid Earth 4, 511-542.

Seward, G.G.E., Prior, D.J., Wheeler, J., Celotto, S., Halliday, D.J.M., Paden, R.S., Tye, M.R., 2002. High-temperature electron backscatter diffraction and scanning electron microscopy imaging techniques: In-situ investigations of dynamic processes. Scanning 24, 232-240.

Shannon, R.D., Rossi, R.C., 1964. Definition of Topotaxy. Nature 202, 1000-1001.

Shigematsu, N., Tanaka, H., 2000. Dislocation creep of fine-grained recrystallized plagioclase under low-temperature conditions. Journal of Structural Geology 22, 65-79.

Sibson, R.H., 1994. Crustal stress, faulting and fluid flow. Geological Society, London, Special Publications 78, 69-84.

Simpson, C., 1985. Deformation of granitic rocks across the brittle-ductile transition. Journal of Structural Geology 7, 503-511.

Skemer, P., Katayama, I., Jiang, Z., Karato, S.-i., 2005. The misorientation index: Development of a new method for calculating the strength of lattice-preferred orientation. Tectonophysics 411, 157-167.

Smith, J.V., 1956. The powder patterns and lattice parameters of plagioclase felspars. I. The soda-rich plagioclases. Mineralogical Magazine and Journal of the Mineralogical Society 31, 47-68.

Spruzeniece, L., Piazolo, S., Maynard-Casely, H.E., 2017. Deformation-resembling microstructure created by fluid-mediated dissolution-precipitation reactions. Nat Commun 8, 14032.

Stünitz, H., 1993. Transition from fracturing to viscous flow in a naturally deformed metagabbro. Defects and processes in the solid state: geoscience applications: the Mc-Laren volume (Developments in Petrology, Vol. 4). Amsterdam, Elsevier Science, 121-150.

Stünitz, H., 1998. Syndeformational recrystallization–dynamic or compositionally induced? Contributions to Mineralogy and Petrology 131, 219-236.

Stünitz, H., Fitz Gerald, J., 1993. Deformation of granitoids at low metamorphic grade. II: Granular flow in albite-rich mylonites. Tectonophysics 221, 299-324.

Stünitz, H., Fitz Gerald, J.D., Tullis, J., 2003. Dislocation generation, slip systems, and dynamic recrystallization in experimentally deformed plagioclase single crystals. Tectonophysics 372, 215-233.

Stünitz, H., Tullis, J., 2001. Weakening and strain localization produced by syn-deformational reaction of plagioclase. International Journal of Earth Sciences 90, 136-148.

Sundberg, M., Cooper, R.F., 2008. Crystallographic preferred orientation produced by diffusional creep of harzburgite: Effects of chemical interactions among phases during plastic flow. Journal of Geophysical Research 113.

Svahnberg, H., Piazolo, S., 2010. The initiation of strain localisation in plagioclase-rich rocks: Insights from detailed microstructural analyses. Journal of Structural Geology 32, 1404-1416.

Thielmann, M., Rozel, A., Kaus, B.J.P., Ricard, Y., 2015. Intermediate-depth earthquake generation and shear zone formation caused by grain size reduction and shear heating. Geology 43, 791-794.

Tomus, D., Ng, H.P., 2013. In situ lift-out dedicated techniques using FIB–SEM system for TEM specimen preparation. Micron 44, 115-119.

Tullis, J., 2002. Deformation of Granitic Rocks: Experimental Studies and Natural Examples. Reviews in Mineralogy and Geochemistry 51, 51-95.

Tullis, J., Dell'Angelo, L., Yund, R.A., 1990. Ductile shear zones from brittle precursors in feldspathic rocks: The role of dynamic recrystallization. 56, 67-81.

Tullis, J., Yund, R., 1992. Chapter 4 The Brittle-Ductile Transition in Feldspar Aggregates: An Experimental Study, in: Evans, B., Wong, T.-f. (Eds.), International Geophysics. Academic Press, pp. 89-117.

Tullis, J., Yund, R.A., 1985. Dynamic recrystallization of feldspar: a mechanism for ductile shear zone formation. Geology 13, 238-241.

Tullis, J., Yund, R.A., 1987. Transition from cataclastic flow to dislocation creep of feldspar: Mechanisms and microstructures. Geology 15, 606-609.

Tullis, J., Yund, R.A., 1991. Diffusion creep in feldspar aggregates: experimental evidence. Journal of Structural Geology 13, 987-1000.

Urai, J.L., Means, W.D., Lister, G.S., 1986. Dynamic recrystallization of minerals. 36, 161-199.

van der Merwe, J.H., 1991. Misfit dislocation generation in epitaxial layers. Critical Reviews in Solid State and Materials Sciences 17, 187-209.

Vdovin, V., 1999. Misfit dislocations in epitaxial heterostructures: Mechanisms of generation and multiplication. PHYSICA STATUS SOLIDI A APPLIED RESEARCH 171, 239-250.

Vernon, R.H., 2018. A practical guide to rock microstructure. Cambridge University Press, Cambridge, UK.

Viegas, G., Menegon, L., Archanjo, C., 2016. Brittle grain-size reduction of feldspar, phase mixing and strain localization in granitoids at mid-crustal conditions (Pernambuco shear zone, NE Brazil). Solid Earth 7, 375-396.

Wallis, D., Hansen, L.N., Ben Britton, T., Wilkinson, A.J., 2016. Geometrically necessary dislocation densities in olivine obtained using high-angular resolution electron backscatter diffraction. Ultramicroscopy 168, 34-45.

Wallis, D., Hansen, L.N., Britton, T.B., Wilkinson, A.J., 2017. Dislocation Interactions in Olivine Revealed by HR-EBSD. Journal of Geophysical Research: Solid Earth 122, 7659-7678.

Warren, J.M., Hirth, G., 2006. Grain size sensitive deformation mechanisms in naturally deformed peridotites. Earth and Planetary Science Letters 248, 438-450.

Wenk, H.R., Christie, J.M., 1991. Comments on the interpretation of deformation textures in rocks. Journal of Structural Geology 13, 1091-1110.

Wheeler, J., 1987. The significance of grain-scale stresses in the kinetics of metamorphism. Contributions to Mineralogy and Petrology 97, 397-404.

Wheeler, J., 1992. Importance of pressure solution and coble creep in the deformation of polymineralic rocks. Journal of Geophysical Research 97, 4579.

Wheeler, J., 2009. The preservation of seismic anisotropy in the Earth's mantle during diffusion creep. Geophysical Journal International 178, 1723-1732.

Wheeler, J., 2010. Anisotropic rheology during grain boundary diffusion creep and its relation to grain rotation, grain boundary sliding and superplasticity. Philosophical Magazine 90, 2841-2864.

Wheeler, J., 2014. Dramatic effects of stress on metamorphic reactions. Geology 42, 647-650.

Wheeler, J., Butler, R.W., 1993. Evidence for extension in the western Alpine orogen: the contact between the oceanic Piemonte and overlying continental Sesia units. Earth and Planetary Science Letters 117, 457-474.

Wheeler, J., Ford, J.M., 2008. Diffusion creep, in: Bons, P.D., Koehn, D., Jessell, M.W. (Eds.), Microdynamics Simulation. Springer-Verlag, Berlin Heidelberg, p. 405.

Wheeler, J., Jiang, Z., Prior, D.J., Tullis, J., Drury, M.R., Trimby, P.W., 2003. From geometry to dynamics of microstructure: using boundary lengths to quantify boundary misorientations and anisotropy. Tectonophysics 376, 19-35.

Wheeler, J., Mariani, E., Piazolo, S., Prior, D., Trimby, P., Drury, M., 2009. The weighted Burgers vector: a new quantity for constraining dislocation densities and types using electron backscatter diffraction on 2D sections through crystalline materials. Journal of microscopy 233, 482-494.

Wheeler, J., Prior, D., Jiang, Z., Spiess, R., Trimby, P., 2001. The petrological significance of misorientations between grains. Contributions to Mineralogy and Petrology 141, 109-124.

White, S., 1977. Geological significance of recovery and recrystallization processes in quartz. Tectonophysics 39, 143-170.

Wilkinson, A.J., Britton, T.B., 2012. Strains, planes, and EBSD in materials science. Materials Today 15, 366-376.

Wilkinson, A.J., Meaden, G., Dingley, D.J., 2006a. High-resolution elastic strain measurement from electron backscatter diffraction patterns: new levels of sensitivity. Ultramicroscopy 106, 307-313.

Wilkinson, A.J., Meaden, G., Dingley, D.J., 2006b. High resolution mapping of strains and rotations using electron backscatter diffraction. Materials Science and Technology 22, 1271-1278.

Winter, J.D., 2001. An introduction to igneous and metamorphic petrology. Prentice hall New Jersey.

Wintsch, R., Yi, K., 2002. Dissolution and replacement creep: a significant deformation mechanism in mid-crustal rocks. Journal of Structural Geology 24, 1179-1193.

Worden, R.H., Armitage, P.J., Butcher, A.R., Churchill, J.M., Csoma, A.E., Hollis, C., Lander, R.H., Omma, J.E., 2018. Petroleum reservoir quality prediction: overview and contrasting approaches from sandstone and carbonate communities. Geological Society, London, Special Publications 435, 1.

Yardley, B.W.D., Bodnar, R.J., 2014. Fluids in the Continental Crust. Geochemical Perspectives 3, 1-127.

Yund, R.A., 1986. Interdiffusion of NaSi—CaAl in peristerite. Physics and Chemistry of Minerals 13, 11-16.

Appendix I

QEMSCAN® supplementary material

I) Key

	Mineral Name
⬜	Background
🟦	Plagioclase
🟨	Diopside
🟦	Actinolite
🟩	Hornblende
🟥	Epidote
⬜	Quartz
🟧	Rutile
🟪	Zircon
🟩	Chlorite
🟫	Titanite
⬛	Others
⬛	Unclassified

II) Species Identification Protocol (SIP) parameters used to identify minerals in the QEMSCAN® analysis presented in Chapter 4.

Albite (A)

Must Have Concentration Elements	Al	>= 9.7 < 25
Must Have Concentration Elements	Na	>= 3.8 < 17
Must Have Concentration Elements	Si	>= 36.2 < 67
May Have Concentration Elements	Ba	< 5.1
May Have Concentration Elements	C	< 13.4
May Have Concentration Elements	Ca	< 12.3
May Have Concentration Elements	Ce	< 9.9
May Have Concentration Elements	Fe	< 6.9
May Have Concentration Elements	K	< 13.9
May Have Concentration Elements	O	< 37
May Have Concentration Elements	S	< 4.3

Albite_Std

Must Have Concentration Elements	Al	>= 13 < 26
Must Have Concentration Elements	Na	>= 4 < 17
Must Have Concentration Elements	Si	>= 39 < 59
May Have Concentration Elements	Ba	< 6
May Have Concentration Elements	Ca	< 7
May Have Concentration Elements	Ce	< 8
May Have Concentration Elements	K	< 5
May Have Concentration Elements	O	< 50

Epidote (A)

Must Have Concentration Elements	Al	>= 10 < 35
Must Have Concentration Elements	Ca	>= 22 < 36
Must Have Concentration Elements	Si	>= 25 < 38
May Have Concentration Elements	Ba	< 7
May Have Concentration Elements	C	< 7
May Have Concentration Elements	Ce	< 7
May Have Concentration Elements	Fe	< 17
May Have Concentration Elements	Mg	< 5
May Have Concentration Elements	Mn	< 5
May Have Concentration Elements	O	< 27

Epidote

Must Have Concentration Elements	Al	>= 24 < 37
Must Have Concentration Elements	Ca	>= 12 < 27
Must Have Concentration Elements	Si	>= 23 < 37
May Have Concentration Elements	C	< 5
May Have Concentration Elements	Ce	< 5
May Have Concentration Elements	O	< 27

Diopside (A)

Must Have Concentration Elements	Ca	>= 19 < 36
Must Have Concentration Elements	Mg	>= 9 < 20
Must Have Concentration Elements	Si	>= 34 < 56
May Have Concentration Elements	Ce	< 8
May Have Concentration Elements	Fe	< 9
May Have Concentration Elements	O	< 23

Actinolite (A)

Must Have Concentration Elements	Ca	>= 9 < 18
Must Have Concentration Elements	Fe	>= 4 < 13
Must Have Concentration Elements	Mg	>= 12 < 24
Must Have Concentration Elements	O	>= 15 < 35
Must Have Concentration Elements	Si	>= 35 < 55
May Have Concentration Elements	Ba	< 8
May Have Concentration Elements	C	< 8
May Have Concentration Elements	Ce	< 8

Magnesiohornblemde (A)

Must Have Concentration Elements	Al	>= 4 < 13
Must Have Concentration Elements	Ca	>= 9 < 19
Must Have Concentration Elements	Mg	>= 12 < 23
Must Have Concentration Elements	Si	>= 32 < 53
May Have Concentration Elements	Ba	< 7
May Have Concentration Elements	C	< 7
May Have Concentration Elements	Ce	< 7
May Have Concentration Elements	Fe	< 15
May Have Concentration Elements	Ni	< 5
May Have Concentration Elements	O	< 28
May Have Concentration Elements	Zn	< 5

Chlorite (Cham20)

Must Have Concentration Elements	Al	>= 10 < 21
Must Have Concentration Elements	Fe	>= 5 < 12
Must Have Concentration Elements	Mg	>= 21 < 29
Must Have Concentration Elements	O	>= 10 < 41
Must Have Concentration Elements	Si	>= 15 < 30
May Have Concentration Elements	C	< 10
May Have Concentration Elements	Ce	< 5
May Have Concentration Elements	Cl	< 10

Chlorite (Cham30)

Must Have Concentration Elements	Al	>= 9 < 21
Must Have Concentration Elements	Fe	>= 9 < 16
Must Have Concentration Elements	Mg	>= 16 < 24
Must Have Concentration Elements	O	>= 10 < 41
Must Have Concentration Elements	Si	>= 15 < 30
May Have Concentration Elements	C	< 10
May Have Concentration Elements	Ce	< 5
May Have Concentration Elements	Cl	< 10

Appendix II

Sample semi-quantitative EDS data collected on a Philips XL30 tungsten filament SEM, showing a complete lack of detectable Ca in all analysed grains. Results are normalised and presented in wt%.

Porphyroclast 1

	C	Na	Al	Si	O	Total
Spectrum 1	5.32	7.63	8.55	25.27	53.23	100
Spectrum 2	6.92	7.07	7.83	23.53	54.66	100
Spectrum 3	4.74	7.57	8.96	25.94	52.79	100
Spectrum 4	5.53	7.32	8.49	25.15	53.5	100
Spectrum 5	5.66	7.17	8.3	25.21	53.67	100
Spectrum 6	6.68	7.29	7.95	23.69	54.39	100
Spectrum 7	5.97	7.06	8.33	24.71	53.92	100
Spectrum 8	5.23	7.21	8.44	25.78	53.33	100
Spectrum 9	5.46	7.25	8.27	25.52	53.5	100
Spectrum 10	6.34	7	8.4	24.06	54.21	100

Porphyroclast 2

	C	Na	Al	Si	O	Total
Spectrum 1	5.96	7.16	8.46	24.55	53.87	100
Spectrum 2	5.51	7.05	8.52	25.33	53.58	100
Spectrum 3	5.81	7.23	8.71	24.54	53.71	100
Spectrum 4	5.96	7.26	8.2	24.72	53.86	100
Spectrum 5	5.36	7.07	8.64	25.47	53.45	100
Spectrum 6	5.43	7.45	8.18	25.52	53.41	100
Spectrum 7	5.83	7.22	8.07	25.08	53.8	100
Spectrum 8	5.8	7.09	8.42	24.9	53.78	100
Spectrum 9	5.77	7.09	8.47	24.93	53.75	100
Spectrum 10	5.32	6.98	8.76	25.5	53.44	100

Selected small grains

	C	Na	Al	Si	O	Total
Spectrum 1	6.24	7.44	8.3	24.04	53.98	100
Spectrum 2	5.69	7.34	8.54	24.83	53.6	100
Spectrum 3	7.37	6.6	7.76	23.11	55.16	100
Spectrum 4	5.08	7.1	8.93	25.68	53.21	100
Spectrum 5	4.88	7.84	8.8	25.67	52.8	100
Spectrum 6		8.13	10.87	32.03	48.98	100
Spectrum 7	7.37	6.68	7.88	22.95	55.12	100
Spectrum 8		8.17	10.57	32.26	49	100
Spectrum 9	5.94	7.19	8.71	24.35	53.81	100
Spectrum 10	6.17	7.16	8.21	24.42	54.04	100
Spectrum 11	6.51	6.86	8.06	24.15	54.42	100
Spectrum 12	6.26	7.12	8.25	24.25	54.12	100
Spectrum 13		8.37	10.77	31.95	48.9	100
Spectrum 14	5.83	7.24	8.23	24.92	53.77	100
Spectrum 15	7.02	6.76	7.85	23.52	54.84	100
Spectrum 16	6.62	6.98	8.25	23.72	54.43	100
Spectrum 17	6.27	7.2	8.1	24.31	54.11	100
Spectrum 18	5.53	7.54	8.54	24.98	53.41	100
Spectrum 19	5.46	7.24	8.68	25.16	53.46	100
Spectrum 20	5.21	7.52	8.69	25.4	53.17	100
Spectrum 21	5.89	7.22	8.22	24.86	53.82	100
Spectrum 22	5.47	7.3	8.83	24.98	53.42	100
Spectrum 23	5.33	6.88	8.61	25.67	53.5	100
Spectrum 24	7.43	7.01	7.68	22.82	55.06	100
Spectrum 25	6.94	7.42	8.15	22.99	54.5	100
Spectrum 26		8.73	10.23	32.21	48.83	100
Spectrum 27	6.13	7.42	8.35	24.19	53.91	100
Spectrum 28	6.28	7.03	8.31	24.23	54.16	100
Spectrum 29	6.82	6.91	7.97	23.67	54.63	100
Spectrum 30	5.66	6.97	8.49	25.16	53.72	100

Appendix III

MatLab® script for the MTEX analysis carried out in Chapter 3.

```
%% check data has loaded correctly
plot (ebsd)

%% grain reconstruction
[grains,ebsd.grainId,ebsd.mis2mean] =
calcGrains(ebsd,'angle',10*degree); %%define minimum misorientation
% angle
%% check grains have plotted correctly
figure
plot(grains)

%% ***ALL EULER PLOT***
% we have to set up a crystal symmetry first, as it defines the
% fundamental region for the Euler angles
cs = crystalSymmetry('-1'); %% i.e. triclinic for albite

% this defines the Euler colors on the orientation map
oM = BungeRGBOrientationMapping(cs);
color = oM.orientation2color(ebsd('L').orientations);
figure
plot(ebsd('L'),color) %% ‘L’ is short for Low albite – only plotting
% one phase
hold on
plot(grains('L').boundary)
hold off
title('All Euler plot')

% NB - we are plotting using 'ebsd' variable but grain boundaries %
% come from cleaned 'grains' variable, can generate white speckles
% in grains

%% ***CREATING SUBSETS FROM POLYGONS***

% once EBSD has been plotted, can use the 'poly' command to define a
% polygon of any shape which you can then work with, e.g. to test
% texture strength in a single CPO domain

poly = selectPolygon;

% will get a cursor on a plot so you can define polygon of any shape
% using mouse click. when finished use right arrow to join polygon
% and cursor will disappear
% ***NB - CANNOT HAVE CONCAVE SURFACES*** will grow grains in this
instance

%% to use only EBSD data from inside the polygon
% create new EBSD variable called ebsd_poly

ebsd_poly = ebsd(inpolygon(ebsd,poly));
% figure
% plot(ebsd_poly) % plot to check okay
% **need to reload original if you want to access it again**
```

```
%% calculate grains for new polygon
[grains_poly,ebsd_poly.grainId,ebsd_poly.mis2mean] =
calcGrains(ebsd_poly('indexed'),...
    'threshold',10*degree);
figure
plot(ebsd_poly('L'))
hold on
plot(grains_poly.boundary('L'),'edgecolor','k','linewidth',.5)
hold off

%% ***TEXTURE STRENGTH***
% to calculate texture strength need to first calculate the ODF
% (orientation distribution function)

% compute optimal halfwidth from the mean orientations of grains
psi = calcKernel(grains_poly('L').meanOrientation);

% compute the ODF with the kernel psi
odf = calcODF(ebsd_poly('L').orientations,'kernel',psi);

%% texture index i.e. J-index can be plotted if ODF has been
% calculated
JIpoly = textureindex(odf);

%% M-Index of Skemer et al 2005 can be plotted if ODF has been
% calculated
% NB - as both these use the odf, they're only using the phase the
% odf was calculated from
MIpoly = calcMIndex(odf);

% mean aspect ratio
AspRatMn = mean(grains_poly('l').aspectRatio);

%% grain equivalent diameter and mean (M)
grnDiam = 2 * equivalentRadius(grains_poly('l'));
M = mean(grnDiam);
```

Appendix IV

MatLab® script for calculating phase boundary density (after Cross and Skemer, 2017).

```
%% load EBSD data into MTEX
% detect grains
[grains,ebsd.grainId] = calcGrains(ebsd,'threshold',10*degree);
% and visualise phase boundaries of interest
figure
plot(grains.boundary('l','cl'),'linecolor','r','linewidth',1.5)

%% calculate phase boundary length in map units (um)
phsBndryLength = sum(grains.boundary('l','cl').segLength);

%% smooth
grains = smooth(grains,2);

% recalculate smoothed length
smooveBndryLength = sum(grains.boundary('l','cl').segLength);
%%
% can also calculate total length of grain boundaries in the whole
map
totalGBlength=sum(grains.boundary.segLength);

%% calculate number of pixels in map
numPix = length(ebsd);

%% calculate step size of map in um
stepMatrix = ebsd.unitCell; % gives step units in matrix, need to
% calc absolute value of difference between first value in each
% column
x=stepMatrix(1,1);
y=stepMatrix(1,2);
stepSize=abs(x)+abs(y);

%% calcuate area of map in um^2
mapArea = numPix*(stepSize^2);

%% calc phase boundary density of Cross and Skemer 2017
% density = phase boundary length (m) / map area (m^2)
% first convert values to m:
pBL = smooveBndryLength*10^-6;
A = mapArea*10^-12;
% then
d= pBL/A % units m/m^2
```

Appendix V

Electronic appendix (see CD at the back of this thesis)

Included in Appendix V are:
1. Supplementary movies
2. PDF copy of the thesis

Figure captions for supplementary movies:

M5.1. *Evolution of microstructure undergoing diffusion creep during pure shear. Grains are coloured by finite rotation, in degrees.*

M5.2. *Evolution of microstructure undergoing diffusion creep during simple shear. Grains are coloured by finite rotation, in degrees.*

M6.1. *Animation of the 3D orientations of Burger's vectors in intersecting dislocation sets in olivine. Burger's vector directions are deflected towards each other as the sets of dislocations cross.*